

ELECTROACTIVE POLYMER FILM DYNAMICS

Thesis submitted for the degree of

Doctor of Philosophy

at the University of Leicester

by

Mark John Brown B.Sc. (Leicester)

Department of Chemistry

University of Leicester

September 1999



UMI Number: U594561

All rights reserved

INFORMATION TO ALL USERS

The quality of this reproduction is dependent upon the quality of the copy submitted.

In the unlikely event that the author did not send a complete manuscript and there are missing pages, these will be noted. Also, if material had to be removed, a note will indicate the deletion.



UMI U594561

Published by ProQuest LLC 2013. Copyright in the Dissertation held by the Author.
Microform Edition © ProQuest LLC.

All rights reserved. This work is protected against
unauthorized copying under Title 17, United States Code.



ProQuest LLC
789 East Eisenhower Parkway
P.O. Box 1346
Ann Arbor, MI 48106-1346

ABSTRACT

Electroactive polymer film dynamics

by Mark J. Brown

The crystal impedance technique was used to study, *in situ*, electroactive polymer film dynamics. An equivalent circuit transmission line model was applied to extract physical characteristics of polymer films in solution in terms of their shear storage (G') and loss (G'') moduli. This model comprises three components that describe the surface roughness features of the quartz oscillator, the overlaying viscoelastic polymer film and the contacting electrolyte solution.

Crystal impedance measurements were made on poly(3-hexylthiophene) (PHT) films, exposed to propylene carbonate electrolyte solutions, that were electrochemically maintained at different fixed potentials (corresponding to a range of film oxidation states) and at different temperatures. The p-doped film is substantially softer than the undoped film and G' and G'' can show maxima at partial p-doping. Spectra recorded at a range of frequencies, corresponding to the fundamental (10 MHz) and higher harmonics (30 MHz to 110 MHz), indicate that PHT shear moduli are frequency dependent; substantial increases in shear modulus are found upon increasing perturbation frequency. Film shear modulus values also exhibited temperature dependence, increased temperature corresponding to a decrease in shear modulus value. The role of solvent upon electroactive polymer film dynamics was explored by exposing PHT films to polar (propylene carbonate) and non-polar (dichloromethane) media. p-Doped films were highly swollen in the polar solvent and relatively compact in the non-polar medium, these trends being reversed for undoped films.

Thin PHT films were also found to exhibit mechanical resonance effects. This is a special situation in which the mechanical shear deformation across the polymer film corresponds to one quarter of the acoustic wavelength in that medium. The new phenomenon of peak splitting was also observed at film resonance. This data indicates spatial variation of the PHT film shear modulus.

MEMORANDUM

The work in this thesis is original except where reference or acknowledgement has been made. The project was carried out in the Department of Chemistry, University of Leicester between October 1995 and September 1999.

Mark J. Brown

ACKNOWLEDGEMENTS

I would like to say a big thank you to my supervisor Prof. Rob Hillman for making this study possible and for providing the support, encouragement and enthusiasm that led me through to the completion of this thesis. Thanks too to my second supervisor Andy Abbott for his patience and many helpful suggestions.

To all members past and present of the ARH group I owe a huge debt of gratitude for putting up with me day by day over the years. Thanks Lou, Paul, Lorraine, Sally, Helen, Giblert, Rob, Miggel, Lee, and Ange – you're all great! Also all the staff in the Chemistry Department deserve a special mention including Phil, Gerry, Roy, Anne, Vicky and everybody else who had to put up with the fact that I wanted something every time I saw them.

Many thanks to all my great housemates and friends who made my stay in Leicester enjoyable over the years – Hendo, Lord Clarendon, Lou, Simmo, and John to name a few. Also, many thanks to all my friends at The Centre for Alternative Technology for keeping me sane whilst I finished writing up and aiding me in every way they could. Finally, I would also like to thank my parents for their ever-present love and support.

To my parents

TABLE OF CONTENTS

CHAPTER 1: INTRODUCTION

1.1	INTRODUCTION	1
1.1.1	Modified electrodes	2
1.2	POLYMER MODIFIED ELECTRODES	2
1.2.1	Redox polymers	3
1.2.2	Conducting polymers	5
1.2.3	Applications	6
1.2.3.1	<i>Charge storage and batteries</i>	6
1.2.3.2	<i>Corrosion protection</i>	6
1.2.3.3	<i>Electrochromic devices</i>	7
1.2.3.4	<i>Sensors</i>	7
1.2.3.5	<i>Electrocatalysis</i>	8
1.3	POLY(HETEROCYCLES)	8
1.3.1	The polaron-bipolaron model	8
1.4	POLY(THIOPHENES)	11
1.4.1	Electropolymerisation	11
1.4.2	Electrochemical properties	14
1.4.3	Functionalisation	16
1.4.4	Poly(3-hexylthiophene)	16
1.5	CHARACTERISATION OF ELECTROACTIVE FILMS	17
1.5.1	Electrochemical techniques	18
1.5.1.1	<i>Cyclic voltammetry</i>	18
1.5.1.2	<i>Alternating current (AC) impedance</i>	19
1.5.2	Spectroscopic techniques	20
1.5.2.1	<i>Ultraviolet visible spectroscopy</i>	20
1.5.2.2	<i>Infra-red spectroscopy</i>	21
1.5.2.2.1	Raman spectroscopy	22
1.5.2.3	<i>X-ray photoelectron spectroscopy (XPS)</i>	23
1.5.2.4	<i>Electron spin resonance (ESR)</i>	24
1.5.3	Depth profiling techniques	25
1.5.3.1	<i>Ellipsometry</i>	25

1.5.3.2	<i>X-ray reflectivity</i>	26
1.5.3.3	<i>Neutron reflectivity</i>	26
1.5.4	Surface imaging techniques	27
1.5.4.1	<i>Scanning tunnelling microscopy (STM)</i>	27
1.5.4.2	<i>Atomic force microscopy (AFM)</i>	29
1.5.4.3	<i>Scanning electrochemical microscopy (SECM)</i>	29
1.5.5	Thickness shear mode resonator techniques	30
1.5.5.1	<i>The electrochemical quartz crystal microbalance (EQCM)</i>	30
1.5.5.2	<i>Crystal impedance</i>	30
1.6	OBJECTIVES	31
1.7	REFERENCES	32

CHAPTER 2: THEORY

2.1	BACKGROUND TO THE QUARTZ CRYSTAL MICROBALANCE (QCM)	37
2.1.1	The piezoelectric effect	37
2.1.2	Modes of vibration	39
2.1.3	Frequency-mass relationship	40
2.1.4	The Sauerbrey equation	41
2.1.5	The electrochemical quartz crystal microbalance (EQCM)	42
2.2	NON-IDEAL QCM RESPONSE	42
2.2.1	Viscoelastic effects and overlayer thickness	43
2.2.2	High mass loading	43
2.2.3	Surface roughness	44
2.2.4	Surface stress	44
2.2.5	Interfacial slippage	45
2.2.6	Non-uniform mass distribution	46
2.2.7	Temperature	46
2.3	EQUIVALENT CIRCUIT REPRESENTATIONS	47
2.3.1	Lumped element model	47
2.3.2	Impedance analysis	48
2.3.3	Impedance analysis as a diagnostic tool	51
2.3.4	Transmission line model	53
2.3.5	Comparison of the lumped element and transmission line models	55
2.4	PHYSICAL MODELS	55

2.4.1	Ideal mass layer	55
2.4.2	Finite viscoelastic layer	56
2.4.3	Semi-infinite Newtonian liquid	58
2.5	MULTI-LAYER PHYSICAL MODELS	60
2.5.1	Ideal mass layer + semi-infinite Newtonian liquid	61
2.5.2	Ideal mass layer + finite viscoelastic layer + semi-infinite Newtonian liquid	62
2.5.3	Physical model summary	63
2.6	ACOUSTIC EFFECTS	64
2.6.1	Harmonics	64
2.6.2	Film resonance	65
2.7	POLYMER VISCOELASTICITY	66
2.7.1	Stress and strain	66
2.7.2	The glass-transition	68
2.7.3	Time-temperature equivalence	69
2.7.4	Dynamic experiments	70
2.7.5	Models of viscoelastic behaviour	72
2.8	REFERENCES	73

CHAPTER 3: EXPERIMENTAL

3.1	INTRODUCTION	77
3.2	QUARTZ THICKNESS SHEAR MODE (TSM) RESONATOR PREPARATION	77
3.3	ELECTROCHEMICAL INSTRUMENTATION	77
3.3.1	Temperature control	78
3.4	CRYSTAL IMPEDANCE MEASUREMENT	79
3.4.1	Instrumentation	79
3.4.2	Data acquisition	80
3.4.2.1	<i>Static measurements</i>	80
3.4.2.2	<i>Dynamic measurements</i>	80
3.5	CRYSTAL IMPEDANCE INTERPRETATION	81
3.5.1	Extraction of electrical parameters	82
3.5.2	Extraction of physical parameters	84
3.5.2.1	<i>Uniqueness of data fit</i>	84
3.5.2.1.1	Chemical knowledge	84
3.5.2.1.2	Harmonics	85

3.6	POLY(3-HEXYLTHIOPHENE) DEPOSITION STUDIES	85
3.6.1	Film preparation	85
3.6.2	Estimation of surface coverage	85
3.7	POLY(3-HEXYLTHIOPHENE) OXIDATION STATE STUDIES	85
3.7.1	Static potential control	86
3.7.2	Dynamic potential control	86
3.8	CHEMICALS	87
3.9	REFERENCES	87

CHAPTER 4: RESONANCE EFFECTS IN POLY(3-HEXYLTHIOPHENE) FILMS

4.1	INTRODUCTION	88
4.2	EXPERIMENTAL	89
4.3	RESULTS	89
4.3.1	Impedance analysis	91
4.3.2	Peak splitting	98
4.4	DISCUSSION	101
4.4.1	Data analysis	101
4.4.2	Peak splitting	104
4.5	CONCLUSIONS	106
4.6	REFERENCES	107

CHAPTER 5: MANIPULATION OF ELECTROACTIVE POLYMER FILM VISCOELASTICITY: THE ROLES OF APPLIED POTENTIAL AND FREQUENCY

5.1	INTRODUCTION	108
5.2	EXPERIMENTAL	109
5.3	RESULTS	109
5.3.1	Raw spectra	109
5.3.2	Fitted data	115
5.3.2.1	<i>General observations</i>	<i>115</i>
5.3.2.2	<i>Film thickness and density responses to redox state</i>	<i>116</i>
5.3.2.3	<i>Film shear modulus responses to redox state</i>	<i>119</i>
5.3.2.3.1	Effect of potential	119
5.3.2.3.2	Effect of frequency	122
5.4	DISCUSSION	124

5.4.1	Constitutive relations	124
5.4.2	Frequency dependence of shear modulus	126
5.4.3	Solvent effects	128
5.5	CONCLUSIONS	132
5.6	REFERENCES	132

CHAPTER 6: MANIPULATION OF POLYMER FILM VISCOELASTICITY: THE EFFECT OF TEMPERATURE

6.1	INTRODUCTION	134
6.2	EXPERIMENTAL	134
6.3	RESULTS	134
6.4	DISCUSSION	139
6.4.1	The Williams, Landel and Ferry (WLF) equation	139
6.4.2	Estimation of the glass transition temperature	142
6.5	CONCLUSIONS	145
6.6	REFERENCES	145

CHAPTER 7: MANIPULATION OF POLYMER FILM VISCOELASTICITY: THE ROLE OF SOLVENT

7.1	INTRODUCTION	146
7.2	EXPERIMENTAL	146
7.3	PROPYLENE CARBONATE ELECTROLYTE SOLUTIONS	147
7.3.1	Cyclic voltammetry experiments	147
7.3.2	Potential step experiments	153
7.4	DICHLOROMETHANE ELECTROLYTE SOLUTIONS	155
7.4.1	Cyclic voltammetry experiments	155
7.4.2	Potential step experiments	160
7.5	DATA MODELLING	162
7.5.1	Poly(3-hexylthiophene) films exposed to propylene carbonate	162
7.5.2	Poly(3-hexylthiophene) films exposed to dichloromethane	164
7.6	DISCUSSION	167
7.7	CONCLUSIONS	171
7.8	REFERENCES	172

CHAPTER 8: GENERAL CONCLUSIONS AND SCOPE FOR FUTURE WORK

8.1	GENERAL CONCLUSIONS	173
8.2	FUTURE WORK	175

CHAPTER 1

INTRODUCTION

1.1 INTRODUCTION

The intention of this study is to examine the polymer dynamics of thin electroactive polymer films immobilised on electrode surfaces. Of particular interest are the dependencies of polymer chain mobility upon variables such as temperature, perturbation frequency, oxidation state and the solvent and counter-ion content of the polymer matrix.

The convenience and effectiveness with which electrode properties can be modified via the application of an electroactive overlayer has made this one of the largest areas of electrochemical research in the last decade. The versatility of polymers, providing opportunities for chemical substitution and stability coupled with high concentration of active sites, make them desirable candidates for the fabrication of solid state devices. Of particular interest, due to their high conductivity and charge storage capabilities, are poly(heterocyclic) films.

Successful design of chemically modified electrodes has called upon utilisation of a number of characterisation techniques, including electrochemical, spectroscopic and physical methods. Understanding the correlation between structure, function and dynamics is generally agreed to be of utmost importance. The electrochemical quartz crystal microbalance (EQCM) has made an important contribution to this cause, allowing dynamic, *in situ*, study of the motion of mobile species populations between overlayer and bathing electrolyte via the related change in mass of a rigidly coupled film.

Provided the stipulation of a rigidly coupled overlayer is fulfilled, the EQCM technique offers an invaluable insight into the mechanism of electroactive film redox switching. However, the EQCM ceases to be a valid analytical tool when the modifying overlayer is not rigid or sufficiently thin to allow negligible shear mechanical distortion. In this regime the frequency response becomes a function of not only mobile species populations but also the dynamic properties of the overlaying film itself. In order to extract meaningful information concerning the physical nature of the contacting film it therefore becomes necessary to analyse the entire crystal impedance spectrum in the region of crystal resonance.

Until recently, the examination of crystal impedance spectra has remained relatively simplistic. It has however, provided the ability to discriminate between the presence of rigid

or viscoelastic overlayers. Confirmation of film rigidity can be used to provide the necessary validation of more detailed analyses of mobile species population changes using the EQCM. Detailed analysis of the crystal impedance spectra of non-rigid films has been largely avoided.

Incentive, for excursion into the extra effort required for complex analysis of crystal impedance spectra, is provided by the opportunity to extract quantitative information regarding the physical nature of the modifying film. In particular, it is possible to extract the shear modulus of the overlayer, a parameter that is often used to quantify material rigidity. Shear modulus values are vital to the understanding of diffusional properties of mobile species within the film, known to affect the performance of resultant devices.

In this thesis shear modulus values are obtained for electroactive polymer films exposed to electrolyte solution. Development of the technique has enabled dynamic, *in situ*, thin film material characterisation, under thermal and potential control. This allows procurement of distinctive material properties, such as the dependence of thin film viscoelasticity upon redox state and the timescale upon which these changes can be evoked. Investigation of temperature and frequency dependencies allows the determination of shear modulus master curves, traditionally used to characterise bulk material properties.

1.1.1 Modified electrodes

Fabrication of the first modified electrode was reported in 1975 [1]. Since then, this area of research has understandably attracted a great deal of attention [2, 3]. A coating applied at the electrode surface prohibits contact between the electrode and solution species, limiting charge transfer reactions to those that are mediated by the modifying layer. Hence, the properties of the modifying layer dictate the properties of the resultant electrode. Commonly, electrodes are modified with polymer or metal oxide coatings. Thin films of these materials are generally porous in nature, yielding electrodes with a reactive surface area many times larger than conventional electrodes, leading to current responses that are far in excess of those which would be possible without the modifying film.

1.2 POLYMER MODIFIED ELECTRODES

Electroactive polymeric materials are commonly categorised into two main groups known as redox and conducting polymers [4-7], these are discussed in greater detail in the following sections. Oxidation (p-doping) or reduction (n-doping) of the surface immobilised polymer species necessarily involves the incorporation/expulsion of counter-ion

species to maintain electro-neutrality within the polymer matrix. Counter-ion movement may also be accompanied by the activity driven ingress/egress of neutral species such as solvent or salt. Movement of all these species within the polymer matrix is affected by the nature of the polymer structure. Electrodes that possess a polymer-modifying layer can no longer be considered as 2D interfaces, since reactions occur throughout the film's thickness. Furthermore, motion of solvent, counter-ions and salt upon redox switching will provoke changes to the structure of the film that may affect subsequent electrochemical responses. It is for these reasons that the electrochemical response is not only limited by electrochemical laws but is also subject to the features of structure and morphology common to amorphous polymer systems.

1.2.1 Redox polymers

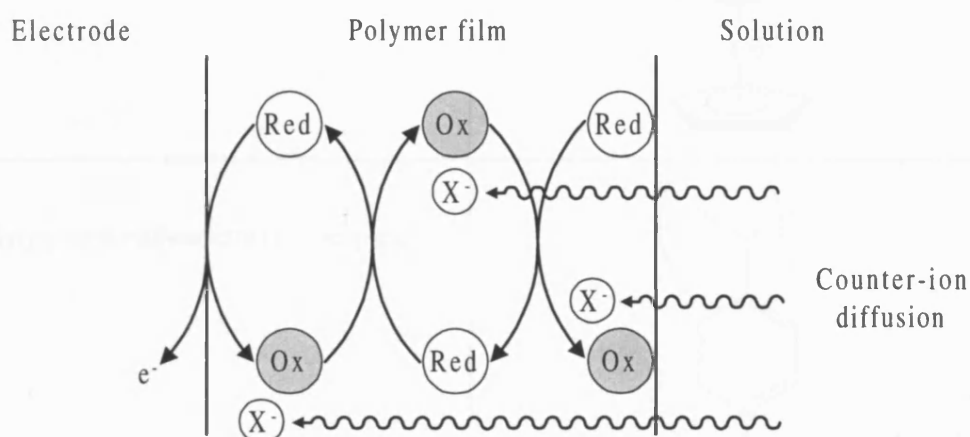


Figure 1.1: A schematic representation of the 'electron hopping' mechanism which occurs in redox polymer modified electrodes.

Redox active polymers consist of an insulating backbone along which are situated discrete redox sites. It has been proposed that redox conversion occurs via an 'electron hopping' mechanism [8], schematically represented in Figure 1.1. Examples of redox polymers can be seen in Table 1.1.

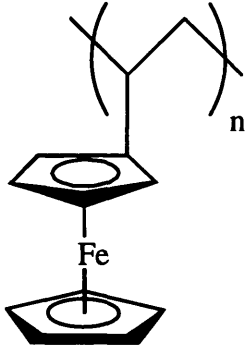
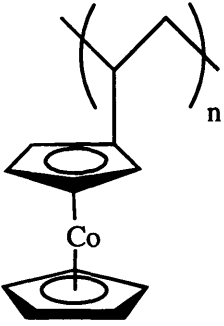
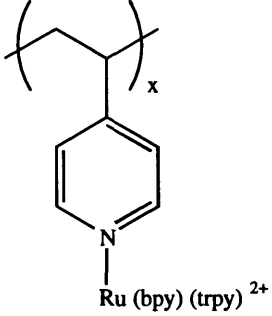
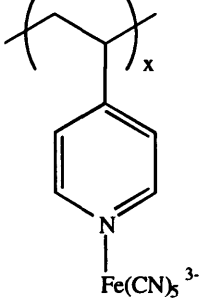
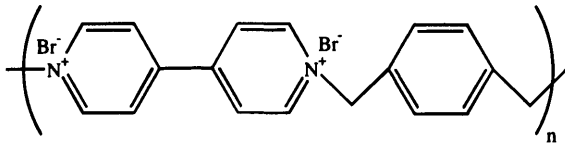
Name	Structure
Poly(vinylferrocene)	
Poly(vinylcobaltocene)	
Poly(pyridyl)ruthenium(II) complex	
Poly(pyridyl)iron(II) complex	
Poly(xylylviologen dibromide)	

Table 1.1: Redox polymer structures.

1.2.2 Conducting polymers

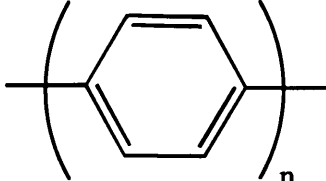
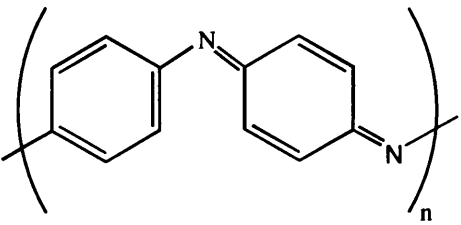
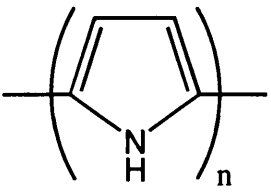
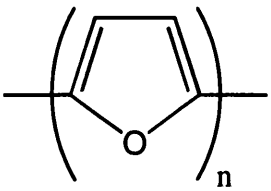
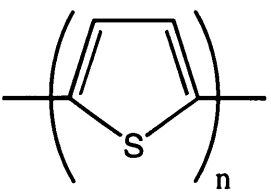
Name	Structure
Poly(acetylene)	
Poly(paraphenylene)	
Poly(aniline)	
Poly(pyrrole)	
Poly(furan)	
Poly(thiophene)	

Table 1.2: Conducting polymer structures [2].

In contrast to redox polymers, the backbone of a conducting polymer consists of a conjugated π -electron system [9]. Oxidation (p-doping) or reduction (n-doping) of redox entities incorporated within conducting polymer chains necessitates the introduction of positive or negative charges into the polymer. In conducting polymers, these charges are stabilised via delocalisation over the conjugated backbone. The ease with which the species

can be oxidised/reduced and the conductivities of the p-doped and n-doped states are dependent on the extent of conjugation of the backbone. Polymers with a π -electron conjugated backbone are essentially insulating in the undoped state and conducting in the doped states. The conductivity of these polymers can be varied over 15 orders of magnitude upon doping, which is dependent upon the movement of polarons and bipolarons along the conjugated backbone, described in further detail in Section 1.3.1. However, defects in the chain structure, discussed in Section 1.4.1, cause a decrease in the mean conjugation length. Moreover, electroactive polymer films are often thicker than the mean polymer chain length. Therefore in order for electrons to move from the polymer/solution interface to the polymer/electrode interface it is necessary for 'electron hopping' to occur at defects, and between polymer chains, in an analogous fashion to that which occurs in redox polymers. These effects cause an overall decrease in the conductivity of the polymer film.

1.2.3 Applications

Electrodes have been modified with polymers incorporating a wide variety of functional groups that specialise their properties for specific performance requirements. An enormous number of possible applications for electroactive polymer modified electrodes have been proposed. Below, some examples of particular interest are briefly outlined.

1.2.3.1 Charge storage and batteries

Electronically conducting polymers have been proposed for use as electrode materials in all-polymer cells, or as cathode materials in lithium batteries [10]. A particular illustrative example can be made of poly(pyrrole), which has been used as cathode material. Upon charging of the cell counter ions are inserted into the poly(pyrrole) film and lithium is deposited at the anode. These processes are reversible and therefore reverse reactions occur upon discharging.

1.2.3.2 Corrosion protection

Thin organic films of electroactive polymers have been used to effectively reduce the rate of corrosion on common metals, such as iron. Electroactive polymers are capable of maintaining the native passive film on the metal's surface as a consequence of a form of anodic protection, which arises from the presence of redox states within the polymer [11]. Examples of electroactive polymers used as corrosion inhibitors include poly(aniline) [12], poly(thiophene) [13], and poly(pyrrole) [14].

1.2.3.3 Electrochromic devices

Electrochromic devices exhibit vast possibility for application in displays and optical shutters [15]. Electroactive polymers often display a colour change upon redox switching. In conducting polymers this is a direct result of changes in the size of the band gap (discussed in Section 1.3.1). The energy difference across the gap is comparable to the energy associated with visible light. Upon redox switching, the size of the gap is altered and is accompanied by a concurrent colour change [16]. Examples of electrochromic polymers include poly(thiophene), poly(aniline) and poly(vinylferrocene).

1.2.3.4 Sensors

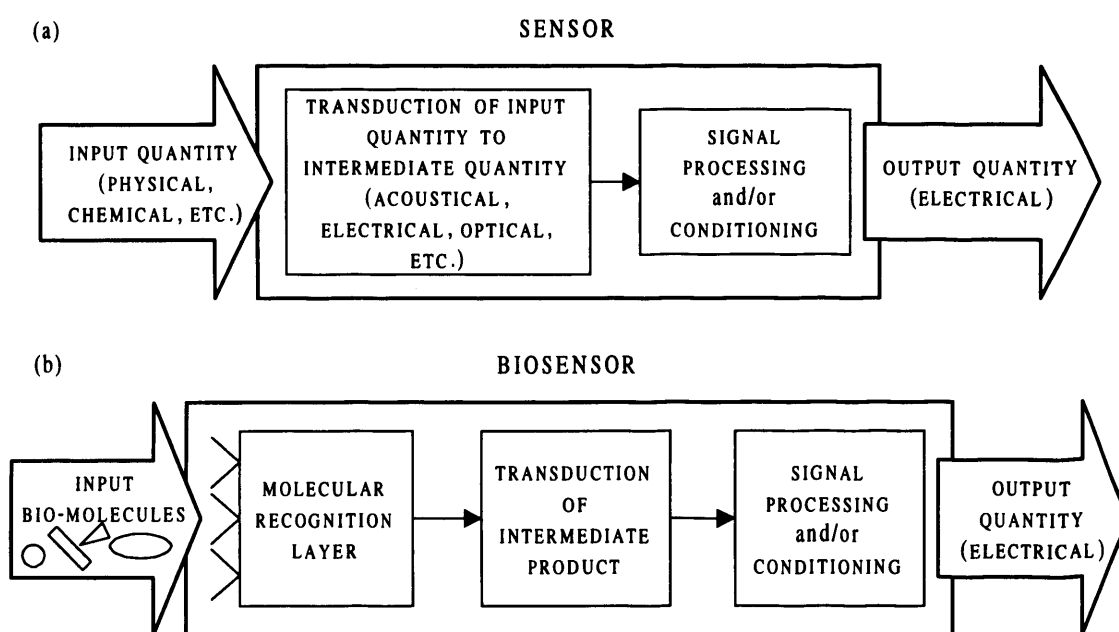


Figure 1.2: Sensor principles. (a) Schematic diagram of a sensor that produces an electrical output in response to the presence of an input quantity. (b) Biosensor comprising the generic device shown in (a) with a molecular recognition layer that has a highly selective response.

Polymer modified electrodes are superb candidates for application as sensors. In most cases, a sensor transduces an input quantity into an electrical signal (Figure 1.2). Charge transfer mediated by a modifying layer provides the scope to fabricate a wide variety of electrodes selective to particular solution species. Functional groups with sites that specifically bind to particular analytes are commonly incorporated into polymer matrices [17]. More specific examples include the incorporation of enzymes [18], and crown ethers [19]. A particular illustrative example is the crosslinking of poly(vinylferrocene) with

glucose oxidase [20], which leads to an electrode with a detectable electrochemical response upon exposure to glucose.

1.2.3.5 Electrocatalysis

The electrode can be used as a source or sink of pure electrons of precisely controllable free energy. Electrochemical oxidation and reduction reactions therefore offer highly desirable synthetic possibilities. Minimisation of the energy input required for a given synthetic goal can be achieved via combination of electrochemical synthesis conditions with catalysed reaction pathways. To this end electroactive polymers such as poly(thiophene) [21], and poly(pyrrole) [22], have been utilised as matrices for electrochemically reactive catalytic sites, such as complexed metal centres. Two general, essentially equivalent, models have been proposed that approximate mediated charge transfer in modified electrodes [23, 24]. Analysis of mediated charge transfer using these models permits mechanistic diagnosis and facilitates determination of parameters, such as diffusion coefficients within the polymer and effective rate constants, which lead the way towards optimisation of electrocatalytic devices.

1.3 POLY(HETEROCYCLES)

Poly(heterocycles) are a particular class of conducting polymer. They comprise aromatic ring monomer repeat units that contain at least one heteroatom. Examples of heterocyclic polymers are given in the bottom half of Table 1.2. Maximum π -orbital overlap, and therefore the maximum degree of conjugation and maximum conductivity is attained in poly(heterocycles) when monomer repeat units are arranged in a planar conformation. Factors that decrease the π -orbital overlap also decrease the mean conjugation length of poly(heterocyclic) films and therefore decrease the polymer conductivity.

1.3.1 The polaron-bipolaron model

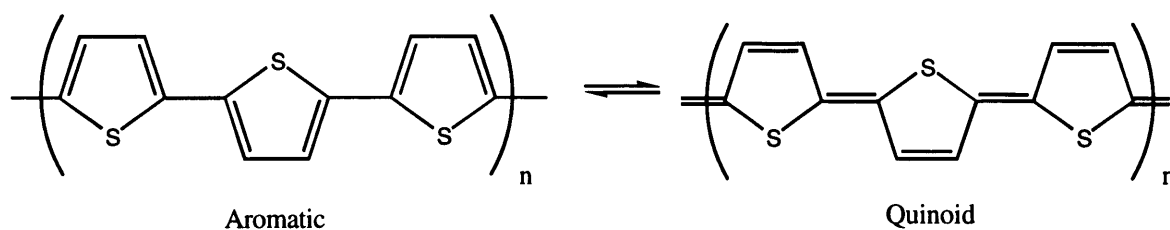


Figure 1.3: Possible limiting electronic structures for polythiophene.

The polaron-bipolaron model is proposed as the mechanism of charge transport in polymers with a non-degenerate ground state. In poly(heterocycles), non-degeneracy of the ground state arises from the fact that the aromatic and quinoid forms of the polymer are dissimilar in energy, which is a consequence of the presence of the heteroatom (Figure 1.3).



Figure 1.4: Possible limiting electronic structures for poly(acetylene).

Polymers which lack the presence of a heteroatom, such as poly(acetylene), often have degenerate ground states, which arise from the energetic equivalence of their electronically resonant forms (Figure 1.4). Charge transport occurs, in these polymers, via the movement of solitons. Detailed discussion of the soliton model lies beyond the scope of this text, the reader is therefore referred to the literature [9].

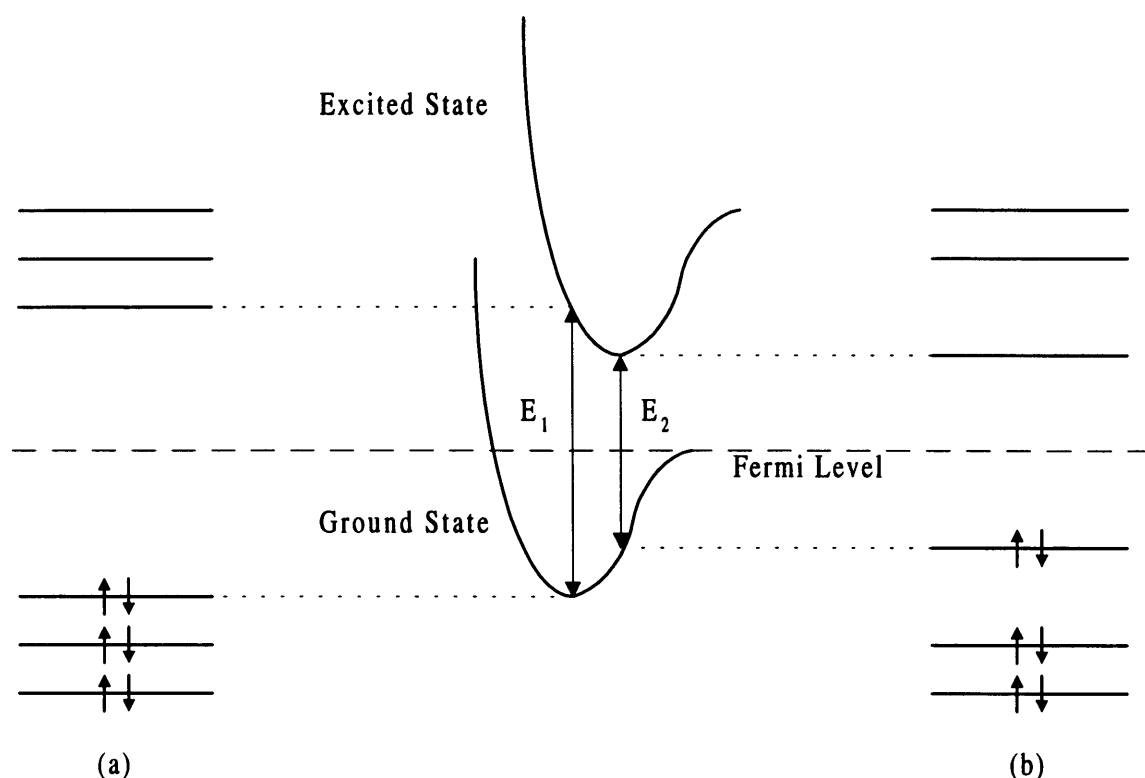


Figure 1.5: Schematic representation of the energy levels of a poly(heterocycle); (a) aromatic, (b) quinoid form.

The energy levels corresponding to the aromatic and quinoid forms of poly(heterocycles) are schematically represented in Figure 1.5. Since the equilibrium positions of the ground and excited states do not coincide, a vertical Frank Condon type transition from the ground

state equilibrium position results in occupation of a vibrationally excited level within the electronically excited state. In order to attain a lower energy, the system relaxes to the more favourable conformation, (i.e. the quinoid form). Alternatively, the molecule can undergo a conformational distortion to the quinoid form prior to the electronic transition.

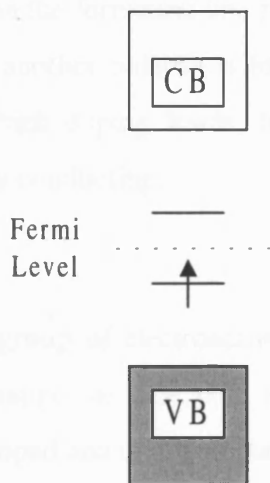


Figure 1.6: Schematic illustration of the band structure of a polaron.

According to Figure 1.5 it is apparent that the quinoid form of a poly(heterocycle) has a lower ionisation energy than the aromatic form. Therefore, upon oxidation, the most energetically favourable conformation is quinoid.

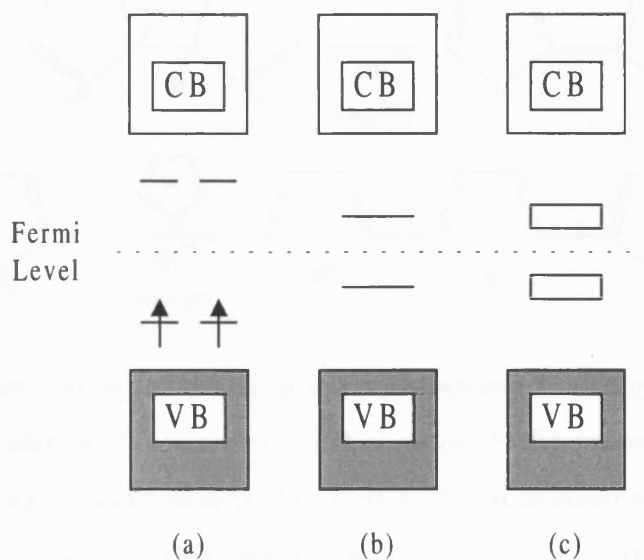


Figure 1.7: Schematic illustration of the band structure of a poly(heterocyclic) chain containing; (a) two polarons, (b) one bipolaron and (c) bipolaronic bands.

Due to the large number of electrons present in polymeric chains, the electronic structure contains a high concentration of electronic levels. These levels are so similar in

energy that they are commonly grouped together and regarded as electronic energy bands. The electronic energy band that is completely filled with electrons is known as the valence band. The unoccupied electronic energy band, usually comprised of antibonding orbitals, is labelled the conduction band. Removal of an electron from the Highest Occupied Molecular Orbital (HOMO) results in the formation of a polaron (Figure 1.6). Upon removal of another electron another polaron is formed (Figure 1.7). Polarons can combine to form bipolarons. At high doping levels, bipolaronic states overlap to form bipolaron bands that are more highly conducting.

1.4 POLY(THIOPHENES)

Poly(thiophenes) are an attractive group of electroactive polymers [9, 25]. They have a reversible doping level in the range of 25-50% and exhibit good chemical and electrochemical stability in both p-doped and undoped states.

1.4.1 Electropolymerisation

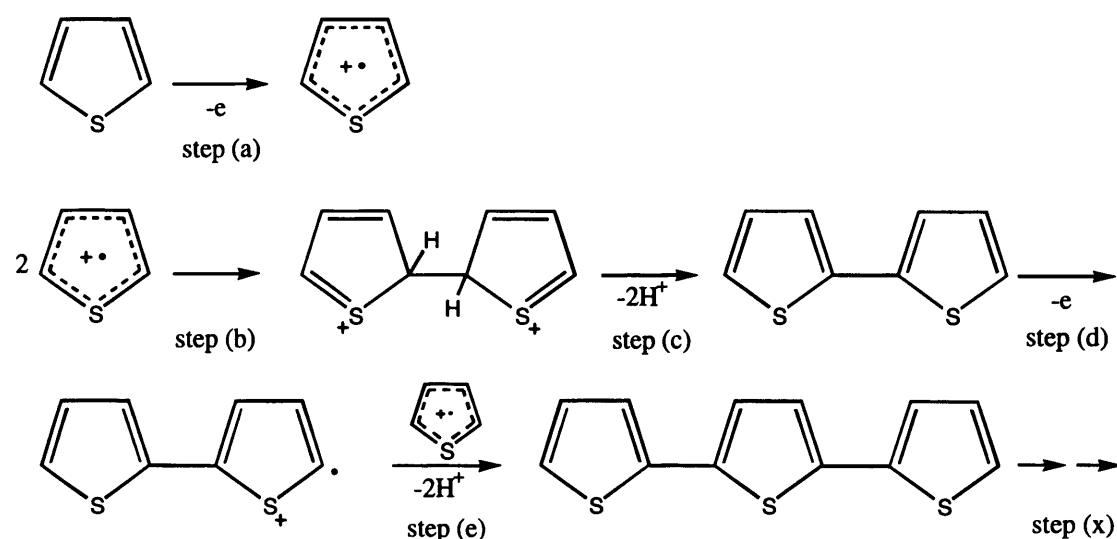


Figure 1.8: Reaction scheme for the electrochemical polymerisation of thiophene and its derivatives: a) oxidation of monomer to radical cation, b) dimerisation of the radical cations, c) proton loss to yield a neutral dimer, d) oxidation of dimer to its radical cation, e) reaction of dimer radical cation with another radical cation, x) oxidised conducting polymer.

Thiophene and numerous β -substituted thiophene derivatives can be polymerised via electrochemical oxidation of the monomer in solution. The generally accepted mechanism for the electrochemical polymerisation reaction of thiophene and its derivatives is shown in

Figure 1.8. The reaction proceeds via an electrochemically stoichiometric mechanism, i.e. two electrons are required per monomer unit for the polymerisation to occur. Polymer film deposition at the electrode surface results from the formation of cation intermediates. The stability of the intermediate is crucial to the efficiency of the polymerisation process. Very stable cation intermediates are able to diffuse away from the electrode surface to form soluble products. Very reactive cation intermediates react with the solvent.

The sensitivity of the radical cation to the nucleophilicity of its environment exerts limitations on the choice of solvent and electrolyte to be used during electrochemical polymerisation of thiophenes. Aprotic solvents are poor nucleophiles, often leading to the choice of propylene carbonate or acetonitrile as the reaction medium. Propylene carbonate is believed to yield more homogeneous films and is therefore used as the deposition medium in this work [25, 26]. Considerations to be taken into account when choosing a suitable supporting electrolyte for the electropolymerization are its solubility, degree of dissociation and nucleophilicity. Tetraalkylammonium salts fulfil these criteria so long as the anion is not a halide, since halides are nucleophilic and can be oxidised by the intermediate radical cation.

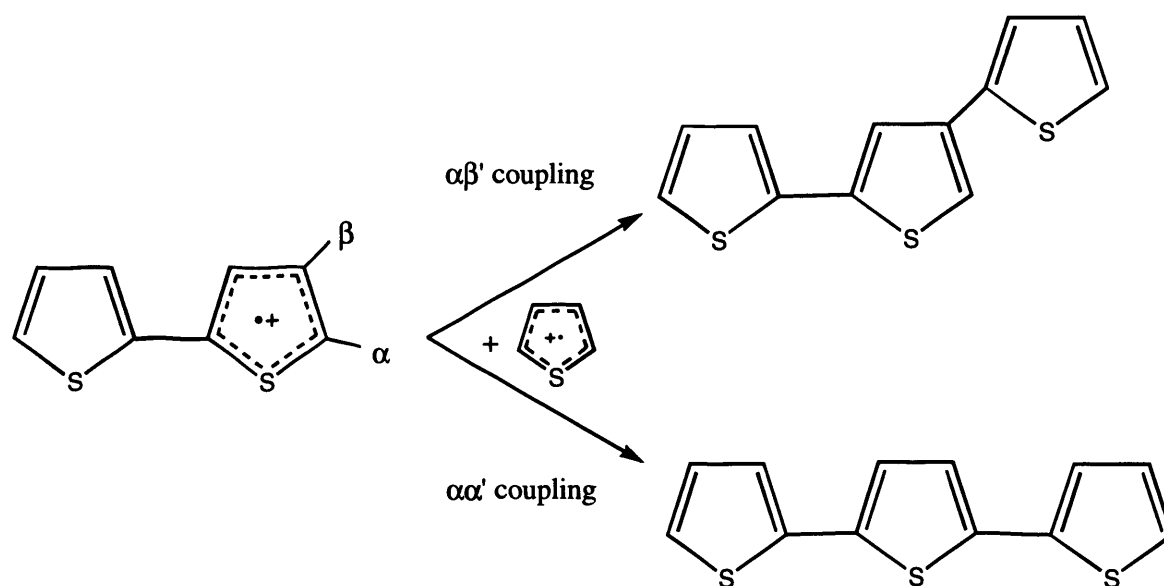


Figure 1.9: Competitive reaction pathways in the electropolymerization of thiophene.

The reaction scheme in Figure 1.8 highlights the predominant reaction mechanism that occurs during the electrochemical polymerisation of heterocycles. This mechanism yields polymers with $\alpha\alpha'$ couplings between monomer units only. Poly(heterocycles) which consist of monomer units linked only with $\alpha\alpha'$ couplings maintain a high degree of conjugation and hence a high conductivity. However, a competitive reaction pathway

which occurs during the electrochemical polymerisation mechanism of some heterocycles introduces $\alpha\beta'$ linkages between monomer units in the polymer backbone. This reaction pathway is shown in Figure 1.9. $\alpha\beta'$ coupling between monomer units result in a loss of conjugation in the polymer backbone, which in turn leads to a less conducting polymer.

Name	Structure	Conductivity / $\Omega^{-1} \text{ cm}^{-1}$
Poly(thiophene)		100
Poly(bithiophene)		1
Poly(terthiophene)		10^{-2}
Poly(3-methylthiophene)		500
Poly(3,4-dimethylthiophene)		0.5
Poly(3-hexylthiophene)		50

Table 1.3 Table displaying common poly(thiophenes) and their electrical conductivity in the p-doped state [25, 29].

Table 1.3 displays some common poly(thiophenes) and details of their conductivity in the p-doped state. Differences between conductivities of all the listed poly(thiophenes) can be rationalised entirely using arguments of π -orbital overlap.

Substituents at the β -position of poly(thiophenes) statistically decrease the probability of forming $\alpha\beta'$ couplings between monomer units in the polymeric chain, see Figure 1.9. $\alpha\beta'$ couplings cause a break in the conjugation and therefore a decrease in the conductivity. Hence the conductivity of poly(3-methylthiophene) is in excess of that of unsubstituted poly(thiophene). It has been shown that poly(3-methylthiophene) has a more regular structure than poly(thiophene) [27, 28].

Substitution of large bulky groups on the β position sterically hinders the formation of a planar polymer configuration and therefore decreases π -orbital overlap and polymer conductivity. This explanation is used to rationalise the relatively low conductivities of poly(3-hexylthiophene) and poly(3,4-dimethylthiophene) in comparison to poly(thiophene).

However, one might expect that the conductivities of poly(bithiophene) (PBT) and poly(terthiophene) (PTT) to be greater than for poly(thiophene). In practice this is not the case, despite the fact that a certain degree of polymer conjugation is guaranteed due to the nature of the monomer structures. The detected decrease in conductivity of PBT and PTT is ascribed to the decrease in the relative reactivity of the α position for conjugated oligomers. Consequently, the stereoselectivity of the polymerisation process is deleteriously affected.

1.4.2 Electrochemical properties

The transition between neutral (undoped) and oxidised (p-doped) poly(thiophenes) is a highly reversible process. The polymer can be cycled between its oxidised and reduced states as depicted in Figure 1.10. p-doped poly(thiophenes) display conductivities which may be several orders of magnitude larger than the corresponding undoped polymer [9].

Oxidation involves removal of electrons from the π orbital of the conjugated polymer backbone, accompanied by the incorporation of charge-compensating anions ('dopant') into the polymer matrix. Generally, the cyclic voltammogram of poly(thiophenes), displays an oxidation current peak, which is symmetrical and well defined with a large residual current plateau. Theoretical works have assigned this plateau to capacitive charging arising from the porous nature of polymer modified electrodes [30]. The large surface-to-volume ratio is assumed to yield a correspondingly high double layer capacitance, which is proportional to the amount of oxidised (conducting) film present. Experimental results also suggest that the current plateau is not Faradaic, as potential induced spectral changes of PT derivatives are limited to the potential region corresponding to the anodic peak of their cyclic voltammograms [31, 32].

In contrast, the reduction peak resulting from the undoping of oxidised poly(thiophenes) is comparatively broad and complex. Several works have highlighted the asymmetry between the cyclic voltammogram of the doping and undoping process. Various interpretations have been proposed, including: structural relaxation and conformational changes [33, 34], distinct oxidation stages with modification in the interactions among charged sites [35-37], differences in the properties of oxidised and neutral polymer [38], and polymer segments having different conjugation lengths [26, 39].

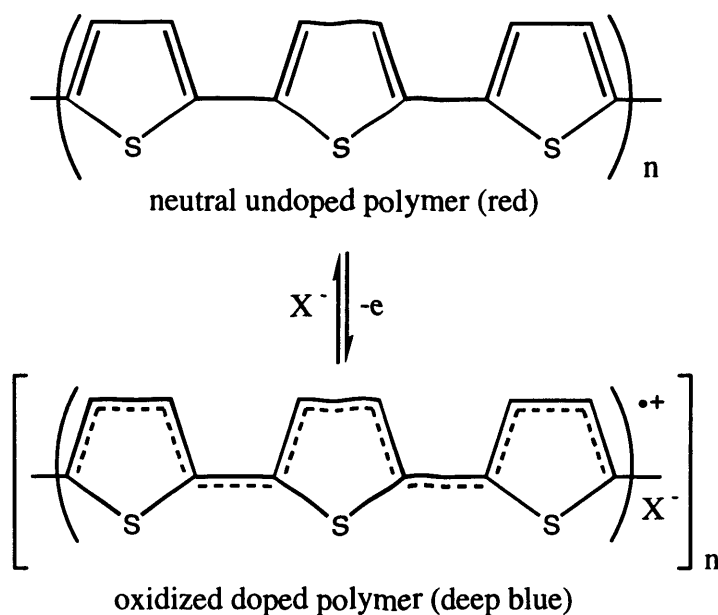


Figure 1.10: Reversible doping of poly(thiophenes).

Oxidation of neutral polythiophene's (PT's) is reported to proceed via polaron and bipolaron states [36, 40]. The two anodic peaks sometimes observed during the electrochemical p-doping process of PT's are usually ascribed to the transition of the main charge carrier from polarons to bipolarons.

Jüttner *et al* have shown that the electrochemical oxidation of freshly electropolymerised poly(3-hexylthiophene) (PHT) films exhibits two anodic peaks [41]. However, when films were held in their fully reduced (undoped) form for periods of 300s the subsequent polymer oxidation showed only one peak shifted to a higher potential. At lower temperatures this effect was shown to be more distinct. The shift of the oxidation peak to higher potentials when the polymer had been held in the reduced form for a period of time has been ascribed to the potential-driven opening of the polymer structure [42, 43]. It is suggested by Otero *et al* that anodic overvoltages supply the electrochemical work

required to open the structure, allowing the incorporation into the film of counter-ions necessary to maintain the electroneutrality of the oxidised polymer.

In summary, complete explanation for the electrochemical behaviour of conducting PTs remains unresolved. It is, however, apparent that the oxidation of PTs is a complex process involving the formation of conjugated cationic chain segments coupled with conformation changes and incorporation of counter-ions and solvent.

1.4.3 Functionalisation

Poly(thiophene) has been functionalised with various pendant groups, usually via addition to the polymeric backbone [21, 25]. The intention of this effort is to tailor the properties of poly(thiophenes) to a multitude of potential technological applications, such as energy storage, electrochromic devices and sensors (discussed in Section 1.2.3). Extended effort has been directed into decreasing the bandgap via rigidification of the π -conjugated backbone [44], optimisation of the conjugation of poly(thiophenes) could lead to extremely efficient electronic conductors. Other examples include thiophenes containing macrocyclic cavities, such as calixarenes [45], for use as ionoresponsive sensors. Incorporation of alkali metal cations causes a twisting of the polymeric backbone and hence a loss of conjugation. Presence of the ion can be detected via the associated change in polythiophene electroactivity.

1.4.4 Poly(3-hexylthiophene)

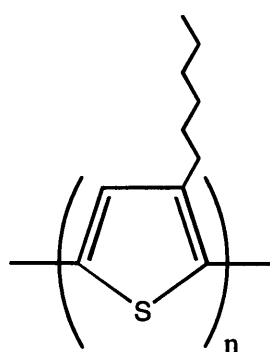


Figure 1.11: Poly(3-hexylthiophene).

Poly(3-alkylthiophenes) are of particular interest. Substitution of an alkyl chain onto the thiophene backbone enhances the solubility of thiophene polymers, allowing their more detailed characterisation using classical analytical techniques and improving processability into applicable devices. Herein, the focus of this discussion is on poly(3-hexylthiophene). The optical and electronic properties of PHT have recently attracted interest for exploitation

in field effect transistors [46], colour sensors for imagers [47], and rechargeable batteries [48].

Rational interfacial design requires an understanding of the relationship between structure, function, and dynamics of the modifying polymer film, exemplified specifically for PHT in a recent electropolymerisation optimisation study [49]. Further to the realisation of this goal are a variety of characterisation techniques, which offer further insight into the structure of electroactive films.

1.5 CHARACTERISATION OF ELECTROACTIVE FILMS

The last decade has seen the development of an immense number of materials, intended for use in a wide variety of novel electrochemically related applications. The chemical and physical properties of these materials possess an intimate relation to device performance, often determining their ability to meet the stringent specifications necessary for a given application. Characterisation of material properties is therefore a crucial goal.

The field of thin film technology has proposed an exceptional requirement for the advent of new characterisation methods, exemplified by the quest to elucidate the structure-function relationships of electroactive polymer films. Thin electroactive films have a multitude of applications, such as batteries, sensors, corrosion protection, electronics and displays. Optimisation of such devices demands techniques that directly analyse the properties of thin films, as these properties are often quite different from those of bulk materials. The development of techniques to quantify thin film characteristics has proven to be demanding. Such instruments require high sensitivity to detect the minute amount of material present in thin films.

Each technique described below is particularly sensitive to different aspects of the structure, bonding or charge transfer mechanisms of surface immobilised electrode species. Methods that permit the study of modified electrodes in solution are termed '*in situ* techniques.' *In situ* techniques offer the desirable prospect of studying active devices in their working environment. The relevance of *ex situ* techniques is often more questionable as the properties of a modifying layer can vary remarkably upon removal from solution.

Important limiting characteristics of any analytical approach are its sensitivity and resolution (i.e. temporal or spatial etc.). The sensitivity imposes a restriction on the minimum amount of analyte for detection. Techniques that have a desirable temporal resolution can be employed on fast time scales and offer the possibility of studying reaction kinetics, whereas non-dynamic techniques are limited to probing thermodynamic equilibria.

The following sections contain a selection of techniques that have been dedicated to the elucidation of electrochemical mechanisms. They are more thoroughly reviewed by Christensen and Hamnett [50].

1.5.1 Electrochemical techniques

1.5.1.1 Cyclic voltammetry

Cyclic voltammetry is a technique which involves sweeping the potential of the working electrode back and forth one or more times between two pre-set limits at a constant sweep rate ν [51, 52]. The current is monitored continuously and presented as a function of the applied potential. Resultant voltammograms (plots of i vs. E) provide invaluable information concerning the presence of electroactive species, either in solution or at the electrode surface. A standard electrochemical cell consists of three electrodes immersed in electrolyte solution: the working electrode (WE), counter electrode (CE), and reference electrode (RE). A potentiostat is used to precisely control the potential applied at the WE with respect to the RE. Current flows between the WE and the CE, usually measured as a potential drop across a measuring resistor. Integration of the current with respect to time yields the charge, a quantity that is directly related to the amount of electroactive species at the surface in the case of adsorbed species.

Cyclic voltammetry is a popular method used to investigate polymer-modified electrodes because it is easy to implement and instantly provides a wealth of information. The overall charge passed upon redox switching can be used to determine the amount of redox entities present within the film. Providing the extent of doping is known this quantity can be used to estimate the unswollen thickness of the polymer film based upon the molecular weight and density of the system under investigation. In summary, cyclic voltammetry is an invaluable technique, capable of detecting less than a monolayer of adsorbed species. However although cyclic voltammetry provides information of the occurrence of processes at the electrode surface, no information is supplied about the identity of the chemical species involved. Nevertheless, cyclic voltammetry is superbly complementary to the techniques described below which offer further insight into the mechanism of electrode reactions.

1.5.1.2 Alternating current (AC) impedance

AC impedance provides one of the most powerful methods used to investigate electrochemical reactions [51, 52]. An AC impedance experiment comprises measuring the current flow as a function of small amplitude sinusoidally applied potentials of varying frequency. The electrical response of an electrochemical system is modelled with an electrical equivalent circuit (see below) consisting of a combination of resistors, capacitors and inductors. In a resistor the current flow is in phase with the applied potential. However, in a capacitor, or an inductor, the current leads, or lags behind, the applied voltage respectively, by a phase angle of 90° . As a result of these relationships, approximate values of the individual components of the circuit can be determined from a plot of the real (resistive) vs. the imaginary (capacitive and inductive) contributions as a function of frequency, known as an 'impedance plot'.

'Randles' circuit, shown in Figure 1.12, represents a simple electrochemical system. The current which flows as a result of redox conversion of electroactive species is analogous to current flowing through a resistor, known as the charge transfer resistance R_{ct} . Charging of the double layer leads to additional current flow that can simply be represented by current flow through a capacitance C_{dl} . Electrolyte solutions give rise to a separate resistance represented by R_{so} . The final component of the circuit is known as the 'Warburg' impedance that represents the electrical impedance arising from diffusion of species to the interface, necessary for the electrochemical reaction to occur.

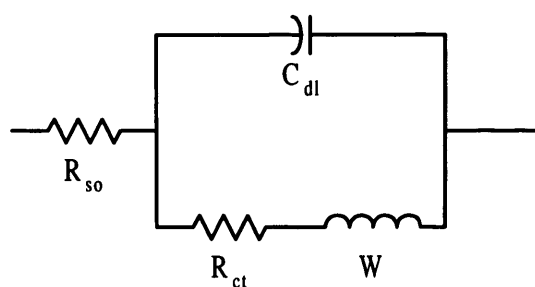


Figure 1.12: 'Randles' equivalent circuit.

The suitability of the model and the magnitude of the various components required within it are more accurately resolved by comparison of the experimentally measured current responses to those supplied by the model.

AC methods have proven most successful when the system of study is mechanistically straightforward and is therefore most easily modelled analytically. With

modern equipment it is possible to explore a dynamic range between 10^{-4} and 10^4 Hz allowing the determination of constants for the reaction steps constituting the model. However, particular attention must be paid to the cell design to ensure that measured impedance arises only from the working electrode. In addition, many electrochemical reactions are too complicated to allow their effective analysis with AC impedance.

The AC impedance technique is analogous to the technique of crystal impedance that is described in Section 1.5.5.2. Both techniques involve monitoring current which flows as a result of a sinusoidally applied alternating potential, and in both cases current responses can be modelled using electrical equivalent circuits. In the case of AC impedance, equivalent circuit representation permits extraction of mechanistic information concerning the electrochemical reaction of interest. Equivalent circuit representation of crystal impedance permits the extraction of quartz crystal electrical parameters, which are directly related to the rheological properties of the overlaying film. Crystal impedance potentials are typically applied at high frequencies ($\geq 10^7$ Hz). At these short time scales electrochemical reactions are 'frozen' and therefore do not affect the crystal impedance response.

1.5.2 Spectroscopic techniques

1.5.2.1 Ultraviolet visible spectroscopy

The energy associated with ultraviolet-visible (UV-vis) radiation is comparable to the energy required for electronic transitions within molecules. UV-vis spectroscopy is therefore used as a probe of molecular electronic energy level structure. The technique can be used to identify band gap structures arising from the polaronic and bipolaronic states of conducting polymers [53], described in Section 1.3.1.

Transmission experiments involve passing the probe light beam directly through the working electrode. Consequently it is necessary for the working electrode to transmit radiation in the UV-vis region of the spectrum. To this end, working electrodes constructed of fine metal gauzes or thin coatings of semiconductors or metals on glass are used. Changes in the detected intensity of transmitted light, due to the presence of chromophores at the electrode surface, are directly related to the amount of those species present. Absorbance versus wavelength spectra are characteristic of the species present at the electrode surface and are therefore used as a means of species identification [54, 55]. Absorbance arising from the supporting electrolyte, such as aqueous electrolytes, can be avoided using a reflectance technique; this however requires an optically smooth sample.

UV-vis spectroscopy exhibits high sensitivity to absorbent species, which can be used to detect monolayers at the electrode surface [56]. The temporal resolution of diode array instruments permits measurement of 240-800 nm spectra every 5 ms. UV-vis spectroscopy can therefore be used to probe the reaction kinetics of charge transfer mechanisms of conducting polymers [57].

1.5.2.2 *Infra-red spectroscopy*

The frequencies of IR radiation are comparable to bond vibrational frequencies within molecules. This phenomenon provokes molecular absorption of specific radiation frequencies within the IR region of the spectrum. An IR absorption spectrum contains spatially averaged information concerning molecular composition, symmetry, bond lengths and force constants. IR spectroscopy is therefore an invaluable technique with respect to the identification of chemical species.

The application of IR spectroscopy *in situ*, to enable investigation of electrochemically manipulated species, has posed various instrumental challenges due to the absorption of IR radiation by most common solvents. Conventionally weak IR sources, coupled with the low sensitivity of standard detectors have contributed to low signal to noise ratios. These problems are overcome by the use of reflectance (as opposed to transmission) approaches, such as internal reflectance (also known as attenuated total reflectance, ATR) and external reflectance spectroscopy. ATR involves the passing of the IR beam through the substrate, thus avoiding absorption of IR radiation by the bathing electrolyte (Figure 1.13).

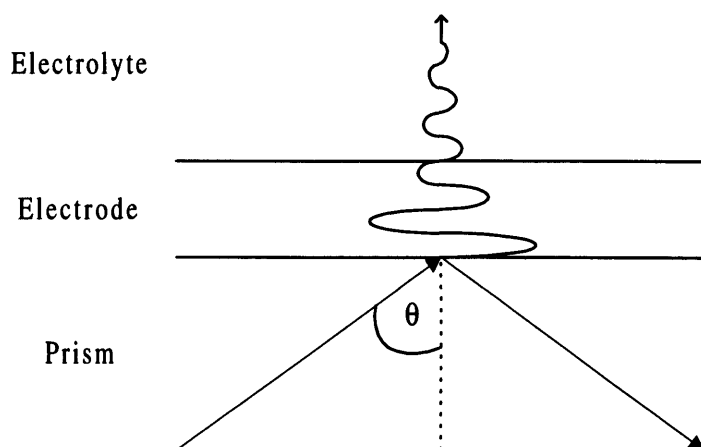


Figure 1.13: Schematic representation of the evanescent wave resulting from the total internal reflection of an electromagnetic ray at an interface.

External reflectance exploits a thin layer cell design, which minimises the path length of the beam in solution. However, electrochemical limitations of the external reflectance approach are presented by the enforced thin layer cell design. Diffusion of species to the thin layer is restricted, and therefore species can soon become depleted during electrochemical experiments. There are three main types of external reflectance techniques which are employed in an attempt to overcome problems of sensitivity [50].

Electrode modulated IR spectroscopy (EMIRS) involves the square wave modulation of the working electrode between a base and working potential, usually at a frequency of ca. 10 Hz. The wavelength range of interest is then slowly scanned. The resulting spectrum is constructed with only the component of reflected light which has the same modulation frequency and phase as the applied potential.

Polarisation modulation infrared reflection-absorption spectroscopy (PM-IRRAS or IRRAS) allows the collection of spectra at a single working potential by modulating the polarisation of the incident IR light. Surface selection rules (SSR) permit the distinction between adsorbed species of constrained orientation utilising polarised light sources. The technique relies upon switching the potential between 'working' and 'rest' states to generate a difference spectrum.

Fourier transform infra red (FTIR) spectroscopy has the main advantage of allowing faster acquisition rates than the two external reflectance approaches described above. As with EMIRS, this technique relies upon potential modulation of the working electrode. However, the modulation can be applied much more slowly than in the EMIRS technique, allowing the study of electrochemically irreversible systems [58-61]. Scan times are typically less than 15 ms; however, it is necessary to collect multiple scans that are co-added and averaged to produce the final spectrum.

1.5.2.2.1 Raman spectroscopy

Raman spectroscopy is comparable to other types of infra-red spectroscopy, inasmuch as it involves the interaction of incident light to cause changes in occupation of vibrational energy levels within the molecules under scrutiny. However, these molecules then re-emit IR radiation in all directions. Raman spectroscopy is advantageous over conventional IR spectroscopy inasmuch as the exciting beam can be UV or visible radiation, and therefore problems associated with absorption due to solvent species are avoided [62, 63]. However, Raman scattering is rather weak. Various methods are employed to enhance the quality of the spectra, such as potential modulation of the working electrode (described in the

previous paragraphs). High intensity lasers are also used, although systems can only be studied if they happen to absorb light at the specific wavelength that the laser produces.

1.5.2.3 X-ray photoelectron spectroscopy (XPS)

X-rays can be used to excite strongly bound core orbital electrons, causing atoms to eject them at high speed [64]. During an XPS experiment these electrons are counted and their respective kinetic energies are determined. The difference in energy between the incident x-ray and the kinetic energy of the ejected electron (or 'photoelectron') is equivalent to the ionisation energy of that electron. As core orbital ionisation energies are largely unaffected by the nature (i.e. bonding) of the molecule they are in, each atom gives rise to a specific photoelectron energy spectrum. XPS is therefore an excellent method to determine the elemental analysis of a substance. It is also possible to acquire information concerning atoms that neighbour the source nucleus utilising instruments with extremely high sensitivity.

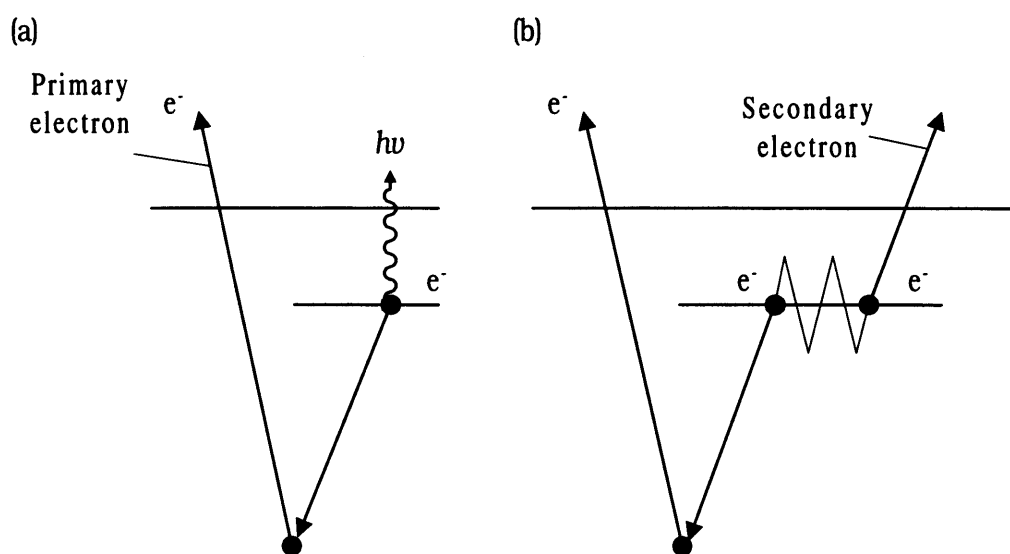


Figure 1.14: Schematic representation of (a) X-ray fluorescence and (b) the Auger effect.

XPS is essentially limited to the study of surface layers. This is because photoelectrons are unable to escape the sample unless they are within a few nanometers of the surface, even though the incident X-rays are able to penetrate into the bulk of the sample. The technique is limited to *ex situ* studies, as vacuum is necessary to avoid absorption by the medium. Even so, the technique has yielded invaluable information concerning the composition of electroactive films [65-69].

X-ray fluorescence and Auger electron spectroscopy (AES) [70], are techniques that are closely related to XPS. Both techniques involve the removal of an electron from a core orbital. The remaining core orbital vacancy is filled, via a secondary photoelectron process, with an electron from a higher energy orbital. The energy released when the electron transition occurs can be emitted as X-ray radiation of a specific wavelength, characteristic of the particular element and hence X-ray fluorescence is observed. Alternatively, the electron falling into the orbital may give up its energy to another electron, which is ejected in the Auger effect (Figure 1.14).

1.5.2.4 Electron spin resonance (ESR)

ESR, otherwise known as electron paramagnetic resonance (EPR), is a spectroscopic method that is used to detect and identify species with a net electronic spin. Net electronic spin is generally characterised by the presence of an unpaired (or paramagnetic) electron.

In the presence of a magnetic field, an unpaired electron may exist in one of two discrete spin states. In an ESR spectrometer the magnetic field is applied in the form of electromagnetic radiation, oscillating at a frequency corresponding to the microwave region of the spectrum. The electron absorbs electromagnetic energy of a specific frequency and is caused to oscillate between its two spin states. Hence, the electron is in resonance with the applied electromagnetic field. Structural information may be extracted from ESR spectra due to interactions between paramagnetic electrons close to each other in space, known as hyperfine couplings.

The main advantages of this technique are that it is extremely sensitive, capable of detecting the presence of approximately 1×10^{12} spins, and that the spectra are relatively easy to interpret. An obvious limitation is that only paramagnetic samples can be investigated. This however, qualifies ESR as an ideal technique to be used to study certain electro-generated electroactive species [71], including polaronic states of conducting polymers.

Short-lived free radicals can be generated and studied *in situ*, usually at the sacrifice of well-defined electrochemistry. The cell design that is necessary to gain *in situ* ESR spectra, incorporates a thin layer design and excludes the reference and working electrodes from the cavity. *Ex situ* generation of radical species permits the use of well defined voltammetric conditions; however, only long lived radical species can be generated in this way.

1.5.3 Depth profiling techniques

1.5.3.1 Ellipsometry

An ellipsometry experiment involves shining a linearly polarised beam of light, at a known incident angle, to the polymer-electrolyte interface (Figure 1.15). An ellipsometer is capable of measuring changes in the polarisation state of the reflected light beam, as well as its intensity. The polarisation of the reflected light is extremely sensitive to the presence and thickness of a film applied to the electrode surface, which leads to a resolution on the order of the order of an Angstrom, when determining film thickness.

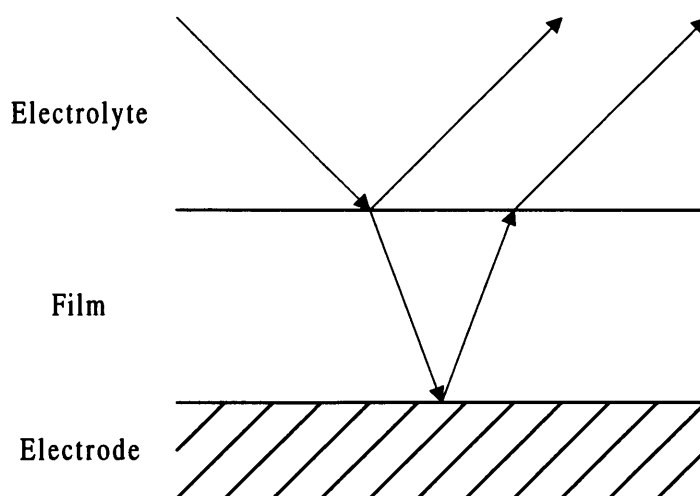


Figure 1.15: Schematic representation of light reflection occurring at electrode/film/electrolyte interfaces.

Ellipsometry can be a spectroscopic technique, hence, the optical properties of the film can be probed within the spectral range of the instrument, which typically ranges from the UV to near-IR regions. Since visible light can be used, problems associated with absorption of light by the electrolyte can be avoided. Modern instruments have enabled spectra to be captured on millisecond time scales, permitting the study of redox switching of electroactive films. Ellipsometry is particularly useful when applied to investigate the potential induced solvent swelling of electroactive polymer films [58, 72-74]. Although ellipsometric data is readily captured, interpretation of the results requires modelling which can be complex and time consuming.

1.5.3.2 X-ray reflectivity

X-rays have a wavelength of comparable magnitude to atomic dimensions. This permits the ‘visualisation’ of species at an atomic level. The theoretical principle of reflection of X-rays within thin films is analogous to that of ellipsometry. X-ray reflectivity permits the determination of thin film parameters such as thickness and density [75], whilst specular X-ray scattering permits the determination of the surface morphology of the layer [76]. In practice, the technique of X-ray reflectivity utilises a collimated X-ray beam, which is reflected off the sample surface. The intensity of the reflected beam is measured as a function of the wavelength or incident angle, which are related according to Equation 1.1:

$$Q = \frac{4\pi \sin \theta}{\lambda} \quad (1.1)$$

where Q is the momentum transfer perpendicular to the interface, and θ and λ are the incident angle and wavelength of the X-ray beam respectively.

X-rays interact with the sample’s electrons and therefore the intensity of the reflected beam can yield information on the nature of the species present. This technique may be applied *in situ*, although typical reflectivity experiments require several hours. Since X-rays predominantly interact with electrons, the results are dominated by the presence of larger atoms of high atomic number. It is possible to apply the technique of X-ray reflectivity *in situ*, to yield information regarding electroactive interfaces [77].

1.5.3.3 Neutron reflectivity

The *in situ* technique of neutron reflectivity is used to analyse the spatial distribution of electroactive films, perpendicular to the electrode surface [75]. The absence of charge on a neutron allows them to be highly penetrating atomic particles. When passing through a sample, neutrons interact with the atomic nucleus, unlike X-rays which interact with electrons. The extent that neutrons interact with specific nuclei, quantified as the scattering length (b), varies randomly from isotope to isotope. These principles allow the spatial distribution of small atoms, such as hydrogen, to be determined, even in the presence of larger nuclei. Neutron reflectivity can provide information which would otherwise be unobtainable using conventional reflectivity techniques which utilise electromagnetic radiation.

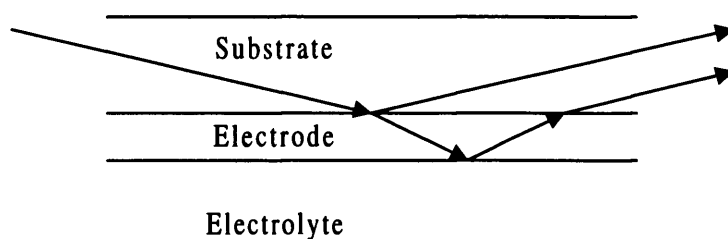


Figure 1.16: Schematic representation of neutron reflection occurring at two interfaces.

The wave behaviour of neutrons is exploited to yield reflectivity profiles, culminating from reflections that occur at multiple interfaces. For reasons of simplicity, Figure 1.16 schematically displays typical neutron reflections occurring at two interfaces. However, investigation of *in situ* modified electrodes involves reflections occurring between three interfaces, i.e., between the substrate, electrode, modifying film and electrolyte [78-80].

Neutron reflectivity profiles are usually measured as a function of momentum transfer, Q , which occur perpendicular to the interface (defined in Equation 1.1), in an analogous fashion to X-ray reflectivity. Extensive modelling is required to extract density information from this data. However fitted results can be verified using isotopic substitutions in either the modifying film or solution species. Typically neutron reflectivity profiles can be acquired in a couple of hours to yield spatial distributions within the sample to a resolution of 10^{-9} m.

1.5.4 Surface imaging techniques

The surface imaging techniques described below permit the study of localised structural and compositional features at surfaces and interfaces. In this respect they are complementary to the depth profiling techniques, such as X-ray and neutron reflectivity (discussed above), which provide laterally, spatially averaged information concerning the structure and composition of thin films.

1.5.4.1 Scanning tunnelling microscopy (STM)

STM provides real space atomic imaging of the structural and electronic properties of both bare and adsorbate-covered electrodes [81-83]. STM exploits the phenomena of quantum mechanical tunnelling. A sharp tip, constructed from a chemically inert conductor, such as W or Pt-Ir, is etched to a diameter much less than 1 micron. During a typical STM experiment the tip is brought extremely close to a conducting surface so that the electronic wavefunctions of the tip and sample overlap. It is then possible for tunnelling to occur,

which is maintained by the application of a potential difference between the tip and the electrode. A 3-dimensional image of surface electron density, commonly interpreted as a topographical image, is constructed by rastering the tip across the electrode surface using extremely precise piezoelectric controllers. There are two conditions of operation known as *constant height* and *constant current* modes, schematically represented in Figure 1.17. Both modes utilise the fact that the tunnelling current is inversely proportional to the distance between the tip and the sample.

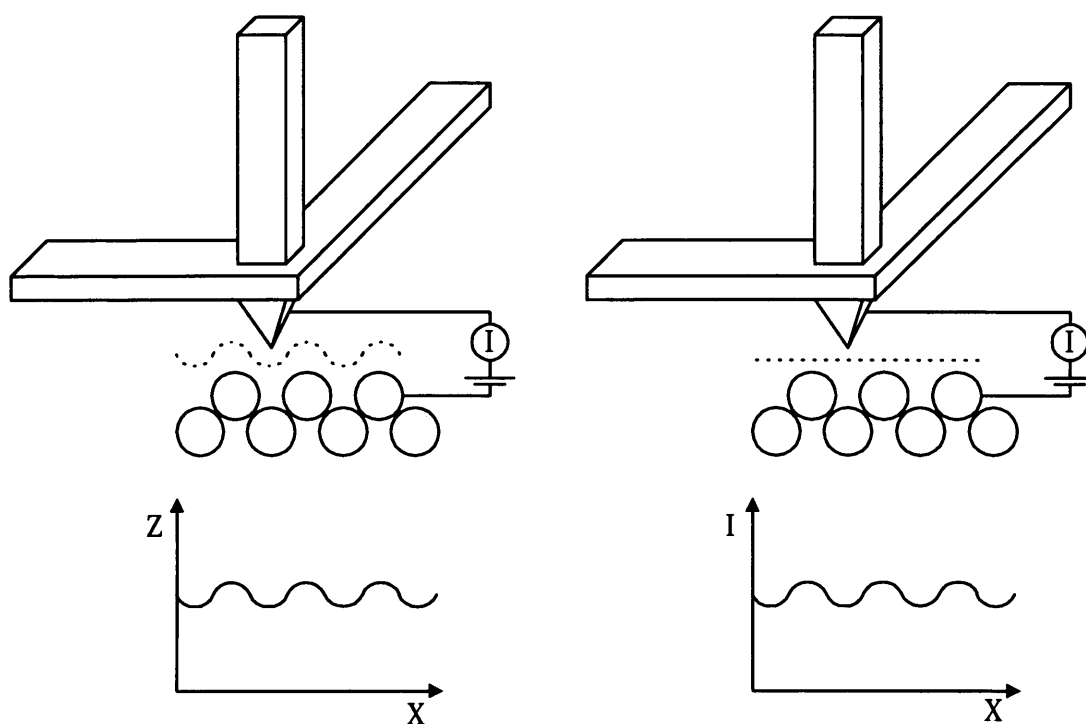


Figure 1.17: Schematic representation of (a) constant current and (b) constant height modes of operation of an STM.

In constant height mode the tip height is maintained steady whilst it is moved laterally across the sample. A surface image is constructed by measuring tunnelling current as a function of the lateral position of the tip. Images can be obtained relatively quickly in this way, although there is a real danger of ‘crashing’ the tip into an ‘atomic mountain’. During constant current mode the tunnelling current is maintained steady, via the use of feedback electronics, which adjust the tip height as it is scanned across the surface. STM has been adapted for use *in situ* and images can be obtained in much less than ten seconds with resolution of 0.1 \AA . However, it is necessary to avoid the major problems of electronic noise and thermal drift.

1.5.4.2 Atomic force microscopy (AFM)

In an analogous fashion to STM, AFM utilises an atomic-scale probe to obtain a surface map of local atomic forces, which are interpreted as a topographical image. Therefore, this technique does not exploit the phenomenon of quantum mechanical tunnelling. The AFM probe detects inter-atomic forces, such as Van der Waals forces and ionic repulsion, between the tip and atoms at the surface of the sample. A distinct advantage this technique offers over STM is that it does not require the sample to be conducting. However a major drawback is that extraction of quantitative spatial information perpendicular to the sample surface is not as straight forward as in the case of STM, because appropriate, well developed, quantitative theory does not yet exist.

Typically, the AFM tip is mounted upon a cantilever spring. This fragile mounting is usually maintained stationary while the sample is tracked beneath it. Both attractive and repulsive inter-atomic forces between the tip and the sample cause the spring to deflect. This deflection is related to the magnitude of the force experience by the tip. In its simplest form, an AFM image is therefore a plot of tip deflection vs. lateral position.

AFM can be applied *in situ* and has yielded some very interesting results when used in conjunction with electrochemical systems [84, 85], such as monitoring molecular adsorption at electrode surfaces [86].

1.5.4.3 Scanning electrochemical microscopy (SECM)

Ultramicroelectrodes have a steady state current which is relatively immune to convection. An ultramicroelectrode can therefore be used to scan the surface of a sample, probing surface electroactivity and local variations in electrochemical kinetics [87].

In an SECM experiment, the position of the ultra microelectrode tip is controlled using highly sensitive positioning devices. In an analogous fashion to STM, constant height and constant current modes of detection are commonly employed. Unlike the STM technique, sample-tip separation is too large for tunnelling to occur.

Advantages of the technique over STM and AFM are that well developed quantitative theory enable relatively easy extraction of quantitative spatial information. Nanometer sized tips permit lateral resolution to be 30-50 nm that enable the detection of single molecules [88]. Almost any conventional electrochemical experiment, including cyclic voltammetry and AC impedance (described in Sections 1.5.1.1 and 1.5.1.2), can be conducted using the SECM, to provide additional spatial resolution. The SECM technique

is therefore an extremely useful technique to map and monitor localised electrochemical activity occurring at modified electrodes [83].

1.5.5 Thickness shear mode resonator techniques

1.5.5.1 The electrochemical quartz crystal microbalance (EQCM)

This technique is discussed in greater detail in the subsequent chapter. Briefly, mass deposited on the surface of a piezoelectric crystal decreases its resonant frequency, consequently permitting the detection of attached mass at the crystal surface to nanogram precision. This dynamic, *in situ* technique is routinely used to study electrochemical deposition of species such as polymers or metals. However, a severe limitation is the inability to distinguish between frequency shifts arising from mass changes due to individual species. Combination of gravimetric and electrochemical data can help elucidate this problem, as can combination with other techniques such as probe beam deflection [89, 90]. A simple frequency-mass relationship can only be applied when the contacting mass is rigidly coupled to the quartz surface. Upon departure from this restraint, it is necessary to employ the crystal impedance technique (see below).

1.5.5.2 Crystal impedance

The crystal impedance technique is discussed extensively in the preceding chapter. Crystal impedance devices are ideally suited to thin film characterisation. Unlike the EQCM, the crystal impedance technique involves detection of the entire impedance curve of the quartz crystal, in the region of crystal resonance. The magnitude and shape of this curve is sensitive to a variety of overlaying film properties, such as mass, density and shear modulus.

In an analogous fashion to AC impedance (described above), crystal impedance spectra are acquired by monitoring the current which results from the application of a sinusoidally oscillating potential over a range of frequencies, typically close to 10 MHz. Crystal parameters are extracted via comparison of experimental data with the theoretical responses of electrical equivalent circuits, in resemblance to the AC impedance technique, whereby information regarding electrochemical reaction processes is also extracted using electrical equivalent circuits.

Crystal impedance electrical equivalent circuits contain lumped or, more accurately, distributed electrical components (see Chapter 2). Alteration of the electrical response of the crystal via the application of a surface perturbation, such as a polymer film overlayer and

contacting electrolyte, is accommodated within the models via the inclusion of additional electrical components. The type and magnitude of the electrical components are related to the physical properties of the surface perturbation. The modelling procedure is complex, however uncertainty can be minimised via the use of multiple oscillation harmonics and comparison of extracted parameters with electrochemical information. These techniques will be described in more detail in the succeeding chapters.

Modern instrumentation permits the acquisition of crystal impedance spectra every second, allowing real time monitoring of physical changes occurring in thin films, which may result from dynamic processes such as film deposition, chemical modification or the diffusion limited ingress/egress of mobile species. High sensitivity permits the detection of submonolayers. Since the technique can be applied *in situ*, and in conjunction with electrochemical apparatus, it is ideally suited to the study of electroactive polymer films.

1.6 OBJECTIVES

The onset of a glass transition (defined in Chapter 2) gives rise to drastic changes in the rheological properties of polymers. It is therefore, a most interesting materials phenomenon to study. The glass transition can be invoked by changes in the temperature or frequency of perturbation of the material under investigation. Investigation of the glass transition region is therefore facilitated when the glass transition temperature, T_g , occurs close to room temperature. Manipulation of material viscoelastic properties is then possible by temperature control, which is easily achieved in this regime, using a standard water bath (see Chapter 3).

To fulfil the intention of this study and gain information concerning the viscoelastic properties of, *in situ*, thin electroactive films in their glass transition region, it is necessary to identify and study an electroactive polymer that has a T_g close to room temperature. An ideal goal, necessary for full characterisation of the materials properties of *in situ* thin electroactive films, would be the acquirement of a modulus master curve (defined in Chapter 2). To achieve this aim, extension of the crystal impedance technique is required to study the viscoelastic properties of *in situ*, electroactive films at a range of frequencies and temperatures.

The careful selection of electroactive polymer and bathing electrolyte yields the opportunity of manipulating film viscoelastic properties by exploiting the interactions between electrolyte and electroactive film. In some cases, the electrolyte may act as a plasticiser, softening and lowering the T_g of the film considerably. In electroactive

polymers, solvent content is known to be affected by the redox state of the film. It is therefore plausible to manipulate the viscoelastic properties of electroactive films, *in situ*, using the application of the applied potential. Counter-ion (dopant) may also affect the viscoelastic properties of the film upon film oxidation. The possibility exists to distinguish between the effects of solvent and dopant incorporation into the film, as motion of these species is known to occur at different rates.

Thin films that are studied using the crystal impedance technique are subject to mechanical resonance effects that have been predicted by theory (discussed in Chapter 2). Film resonance has not previously been observed in electroactive films, *in situ*. The question then arises if electroactive film interfaces are sharp enough for film resonance to be observed at all; this question will be addressed within this study.

In summary, the crystal impedance technique is an ideal candidate to enable the investigation of the phenomena discussed above. However, application of this technique to study the viscoelastic properties of *in situ*, electroactive polymer films in the region of their glass transition, is an entirely novel venture. Significant chemical and technical development is required to fulfil these aims, which is discussed in the succeeding chapters.

1.7 REFERENCES

1. P. R. Moses, L. Wier, and R. W. Murray, *Anal. Chem.* **47**:1882 (1975).
2. Molecular design of electrode surfaces, Wiley, New York, (1992).
3. H. D. Abruna, *Coordination Chemistry Reviews* **86**:135 (1988).
4. G. Wegner, *Angew. Chem. Int. Ed. Engl.* **20**:361 (1981).
5. R. W. Murray, *Annual Review of Materials Science* **14**:145 (1984).
6. A. R. Hillman, in Electrochemical Science and Technology of Polymers, Vol. 1 (R. G. Linford, ed.), Elsevier Applied Science, London, 1987.
7. J. Heinze, *Topics in Current Chemistry* **152**:1 (1990).
8. C. P. Andrieux, J. M. Dumas-Bouchiat, and J. M. Saveant, *J. Electroanal. Chem.* **114**:159 (1980).
9. Handbook of Conducting Polymers, Marcel Dekker, Inc., New York, (1986).
10. D. Linden, Handbook of Batteries, McGraw-Hill, New York, (1995).
11. T. Schauer, A. Joos, L. Dulog, and C. D. Eisenbach, *Prog. Org. Coat.* **33**:20 (1998).
12. P. J. Kinlen, D. C. Silverman, and C. R. Jeffreys, *Synth. Met.* **85**:1327 (1997).
13. F. Beck and R. Schrotz, *Materials Science Forum* **289**:1217 (1998).

14. N. V. Krstajic, B. N. Grgur, S. M. Jovanovic, and M. V. Vojnovic, *Electrochim. Acta* 42:1685 (1997).
15. P. M. S. Monk, R. J. Mortimer, and D. R. Rosseinsky, *Electrochromism*, VCH, Weinheim, (1995).
16. K. Hyodo, *Electrochim. Acta* 39:265 (1994).
17. J. N. Barisci, C. Conn, and G. G. Wallace, *Trends in Polymer Science* 4:307 (1996).
18. S. Mutlu, M. Mutlu, P. Vadgama, and E. Piskin, *Acs Symposium Series* 556:71 (1994).
19. B. Fabre and J. Simonet, *Coordination Chemistry Reviews* 180:1211 (1998).
20. A. L. Nguyen and J. H. T. Luong, *Applied Biochemistry and Biotechnology* 43:117 (1993).
21. S. J. Higgins, *Chem. Soc. Rev.* 26:247 (1997).
22. A. Deronzier and J. C. Moutet, *Coordination Chemistry Reviews* 147:339 (1996).
23. W. J. Albery and A. R. Hillman, *J. Electroanal. Chem.* 170:27 (1984).
24. C. P. Andrieux, J. M. Dumasbouchiat, and J. M. Saveant, *J. Electroanal. Chem.* 169:9 (1984).
25. J. Roncali, *Chem. Rev.* 92:711 (1992).
26. M. A. Sato, S. Tanaka, and K. Kaeriyama, *Synth. Met.* 18:229 (1987).
27. P. A. Christensen, A. Hamnett, and S. J. Higgins, *J. Chem. Soc., Far. Trans.* 92:773 (1996).
28. H. Neugebauer, G. Nauer, A. Neckel, G. Tourillon, F. Garnier, and P. Lang, *J. Phys. Chem.* 88:652 (1984).
29. J. Bargon, S. Mohmand, and R. J. Waltman, *IBM J. Res. Develop.* 27:330 (1983).
30. S. W. Feldberg, *J. Am. Chem. Soc.* 106:4671 (1984).
31. J. Roncali, R. Garreau, A. Yassar, P. Marque, F. Garnier, and M. Lemaire, *J. Phys. Chem.* 91:6706 (1987).
32. J. Roncali, P. Marque, R. Garreau, F. Garnier, and M. Lemaire, *Macromolecules* 23:1347 (1990).
33. J. Heinze, R. Bilger, and K. Meerholz, *Ber. Bunsenges. Phys. Chem.* 92:1266 (1988).
34. J. Guay, A. F. Diaz, J. Y. Bergeron, and M. Leclerc, *J. Electroanal. Chem.* 361:85 (1993).
35. P. Marque and J. Roncali, *J. Phys. Chem.* 94:8614 (1990).
36. X. W. Chen and O. Inganäs, *J. Phys. Chem.* 100:15202 (1996).

37. G. Zotti and G. Schiavon, *Synth. Met.* 31:347 (1989).
38. F. Chao and M. Costa, *Synth. Met.* 39:97 (1990).
39. M. Skompska, *Electrochim. Acta* 44:357 (1998).
40. M. J. Nowak, S. Rughooputh, S. Hotta, and A. J. Heeger, *Macromolecules* 20:965 (1987).
41. K. M. Mangold, K. Morgenschweis, and K. Juttner, *Electrochim. Acta* 44:1865 (1999).
42. T. F. Otero, H. Grande, and J. Rodriguez, *J. Electroanal. Chem.* 394:211 (1995).
43. T. F. Otero, H. J. Grande, and J. Rodriguez, *J. Phys. Chem. B* 101:3688 (1997).
44. J. Roncali, *Chem. Rev.* 97:173 (1997).
45. M. J. Marsella, R. J. Newland, P. J. Carroll, and T. M. Swager, *J. Am. Chem. Soc.* 117:9842 (1995).
46. M. S. A. Abdou, F. P. Orfino, Y. Son, and S. Holdcroft, *J. Am. Chem. Soc.* 119:4518 (1997).
47. K. Tada and K. Yoshino, *Jpn. Appl. Phys., Part 2* 36:L1351 (1997).
48. S. Kuwabata, N. Tsumura, S. Goda, C. R. Martin, and H. Yoneyama, *J. Electrochem. Soc.* 145:1415 (1998).
49. M. Bouachrine and T. Lakhlifi, *J. Chim. Phys.* 95:987 (1998).
50. P. A. Christensen and A. Hamnett, *Techniques and Mechanisms in Electrochemistry*, Blackie Academic and Professional, London, (1994).
51. J. Koryta, J. Dvorak, and L. Kavan, *Principles of Electrochemistry*, John Wiley & Sons, Chichester, (1993).
52. J. Bockris and U. Shahed, *Surface Electrochemistry*, Plenum Press, New York, (1993).
53. S. A. Chen and C. S. Liao, *Synth. Met.* 57:4936 (1993).
54. G. Zotti, R. A. Marin, and M. C. Gallazzi, *Chem. Mater.* 9:2945 (1997).
55. G. Appel, D. Schmeisser, J. Bauer, M. Bauer, H. J. Egelhaaf, and D. Oelkrug, *Synth. Met.* 99:69 (1999).
56. R. M. Bright, D. G. Walter, M. D. Musick, M. A. Jackson, K. J. Allison, and M. J. Natan, *Langmuir* 12:810 (1996).
57. A. R. Hillman and E. F. Mallen, *Electrochim. Acta* 37:1887 (1992).
58. A. Hamnett, P. A. Christensen, and S. J. Higgins, *Analyst* 119:735 (1994).
59. Y. L. Li, J. H. Yang, and J. R. Xu, *J. Appl. Polym. Sci.* 61:2085 (1996).

60. H. Yang, T. H. Lu, K. H. Xue, S. G. Sun, G. Q. Lu, and S. P. Chen, *J. Electrochem. Soc.* 144:2302 (1997).
61. K. Ogura, M. Nakayama, and C. Kusumoto, *J. Electrochem. Soc.* 143:3606 (1996).
62. S. E. J. Bell, M. D. Devenney, J. Grimshaw, S. Hara, J. H. Rice, and J. TrochaGrimshaw, *J. Chem. Soc., Far. Trans.* 94:2955 (1998).
63. J. Bukowska, G. Roslonek, and J. Taraszewska, *J. Electroanal. Chem.* 403:47 (1996).
64. J. M. Hollas, Photoelectron and Related Spectroscopies, Wiley, Chichester, (1992).
65. T. R. I. Cataldi, R. Guascito, and A. M. Salvi, *J. Electroanal. Chem.* 417:83 (1996).
66. T. R. I. Cataldi, G. E. DeBenedetto, and A. Bianchini, *J. Electroanal. Chem.* 448:111 (1998).
67. N. F. Atta, I. Marawi, K. L. Petticrew, H. Zimmer, H. B. Mark, and A. Galal, *J. Electroanal. Chem.* 408:47 (1996).
68. I. G. Casella and E. Desimoni, *Electroanalysis* 8:447 (1996).
69. H. S. O. Chan, C. S. Toh, and L. M. Gan, *J. Mater. Chem.* 5:631 (1995).
70. H. S. Li, M. Josowicz, D. R. Baer, M. H. Engelhard, and J. Janata, *J. Electrochem. Soc.* 142:798 (1995).
71. H. Ping, Z. Q. Xu, and J. T. Lu, *J. Electroanal. Chem.* 405:217 (1996).
72. Suni, II, *J. Appl. Electrochem.* 27:1219 (1997).
73. F. Chao, M. Costa, and A. Tadjeddine, *J. Electroanal. Chem.* 329:313 (1992).
74. A. Hamnett, *J. Chem. Soc., Far. Trans.* 89:1593 (1993).
75. M. Tolan and W. Press, *Z. Kristallographie* 213:319 (1998).
76. E. Chason and T. M. Mayer, *Critical Reviews in Solid State and Materials Sciences* 22:1 (1997).
77. C. A. Melendres, H. You, V. A. Maroni, Z. Nagy, and W. Yun, *J. Electroanal. Chem.* 297:549 (1991).
78. R. M. Richardson, M. J. Swann, A. R. Hillman, and S. J. Roser, *Far. Disc.*:295 (1992).
79. R. W. Wilson, R. Cubitt, A. Glidle, A. R. Hillman, P. M. Saville, and J. G. Vos, *J. Electrochem. Soc.* 145:1454 (1998).
80. J. Penfold and R. K. Thomas, *J. Phys.: Condens. Matter* 2:1369 (1990).
81. K. Itaya, N. Batina, M. Kunitake, K. Ogaki, Y. G. Kim, L. J. Wan, and T. Yamada, *Acs Symposium Series* 656:171 (1997).
82. S. Ando, T. Suzuki, and K. Itaya, *J. Electroanal. Chem.* 412:139 (1996).

83. J. Wang, *Analyst* 117:1231 (1992).
84. Y. Hotta, K. Inukai, M. Taniguchi, and A. Yamagishi, *J. Colloid Interface Sci.* 188:404 (1997).
85. J. C. Brumfield, C. A. Goss, E. A. Irene, and R. W. Murray, *Langmuir* 8:2810 (1992).
86. H. Cai, A. C. Hillier, K. R. Franklin, C. C. Nunn, and M. D. Ward, *Science* 266:1551 (1994).
87. M. V. Mirkin, *Anal. Chem.* 68:A177 (1996).
88. A. J. Bard, F. R. F. Fan, D. T. Pierce, P. R. Unwin, D. O. Wipf, and F. M. Zhou, *Science* 254:68 (1991).
89. M. J. Henderson, A. R. Hillman, and E. Vieil, *J. Electroanal. Chem.* 454:1 (1998).
90. M. J. Henderson, A. R. Hillman, E. Vieil, and C. Lopez, *J. Electroanal. Chem.* 458:241 (1998).

CHAPTER 2

THEORY

2.1 BACKGROUND TO THE QUARTZ CRYSTAL MICROBALANCE (QCM)

2.1.1 The piezoelectric effect

Pierre and Jacques Curie reported the first observation of the piezoelectric effect in 1880. They discovered that applying a stress to the surfaces of certain crystals produced an electrical potential between those surfaces, proportional to the applied stress [1]. This effect is only seen in materials with ionic crystalline structures that do not possess a centre of symmetry, such as quartz, rochelle salt and tourmaline, see Figure 2.1.

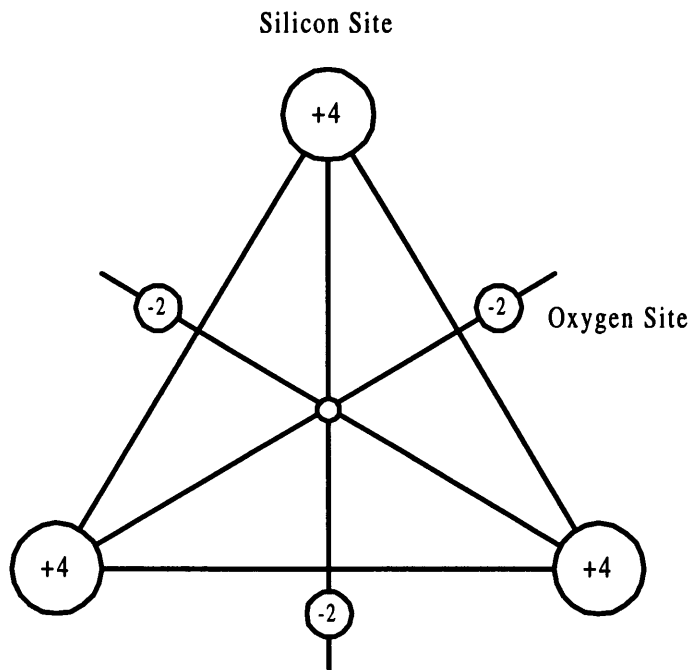


Figure 2.1: Schematic representation of the structure and dipoles of quartz (SiO₂).

The piezoelectric effect is entirely explained using crystal symmetry arguments; distortion of an acentric crystal lattice with an applied stress rearranges electric dipoles within the crystal, giving rise to the net dipole moment responsible for the detected voltage change, see Figure 2.2. The opposite effect is also true and, shortly after their initial discovery, the Curies experimentally verified the *converse piezoelectric effect*, whereby application of a potential

difference across crystal faces causes deformation of the crystal lattice resulting in mechanical strain at the surfaces, see Figure 2.3.

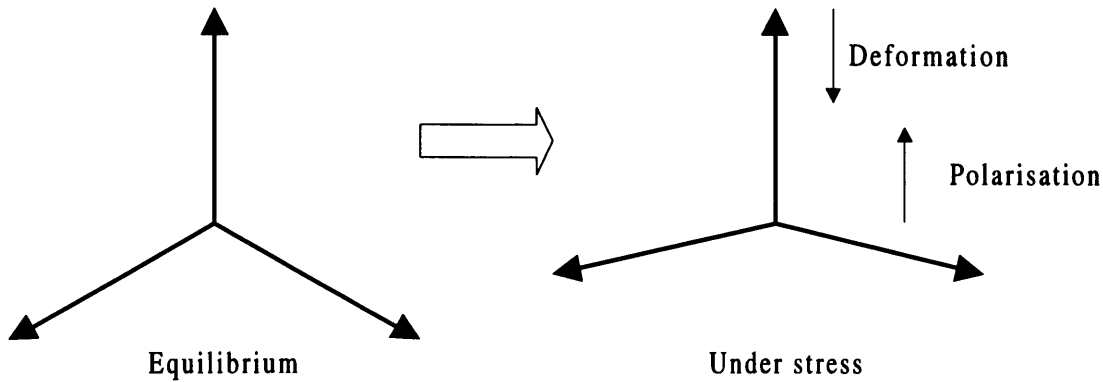


Figure 2.2: Stress induced displacement of centres of gravity leading to formation of electric field.

The converse piezoelectric effect is exploited in quartz thickness shear mode resonators. A voltage with a sinusoidally alternating polarity causes an alternating deformation in the crystal, with opposite potential polarities giving rise to crystal deformations equal in magnitude but opposite in direction. A schematic representation of a thickness shear mode resonator can be seen in Figure 2.4.

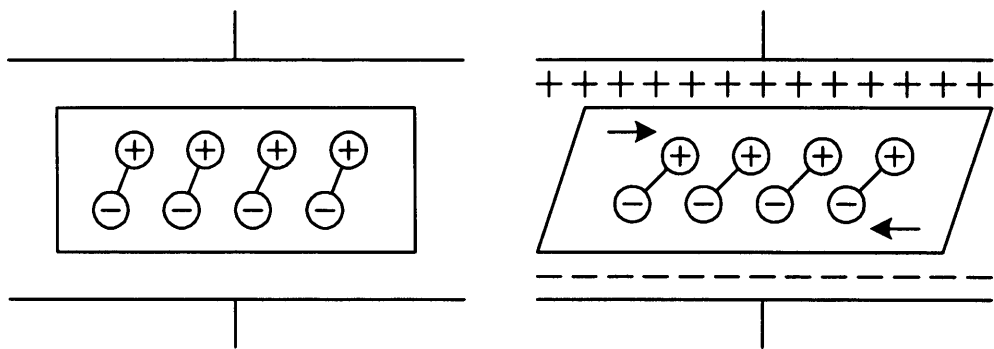


Figure 2.3: Schematic representation of shear motion induced by the converse piezoelectric effect.

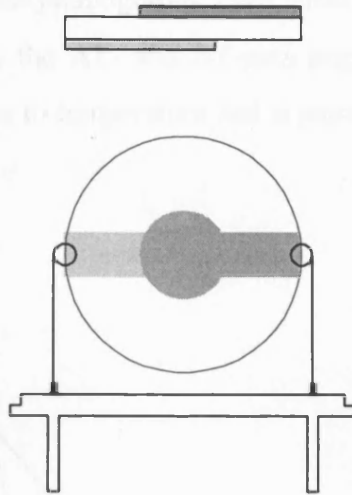


Figure 2.4: Schematic representation of a quartz thickness shear mode resonator.

2.1.2 Modes of vibration

Quartz is the most common material used for the fabrication of thickness shear mode resonators because it is a relatively inexpensive piezoelectric material with good chemical, mechanical and thermal stability properties, making it an ideal candidate for use in highly stable oscillators and frequency control devices. However, quartz in its perfect natural form, see Figure 2.6, exhibits piezoelectric vibrations in many different directions, these are distinguished by their different fundamental motions, known as *modes of vibration* [2]. A desirable mode of vibration, particularly sensitive to mass changes, is the *thickness shear mode*, shown in Figure 2.5.

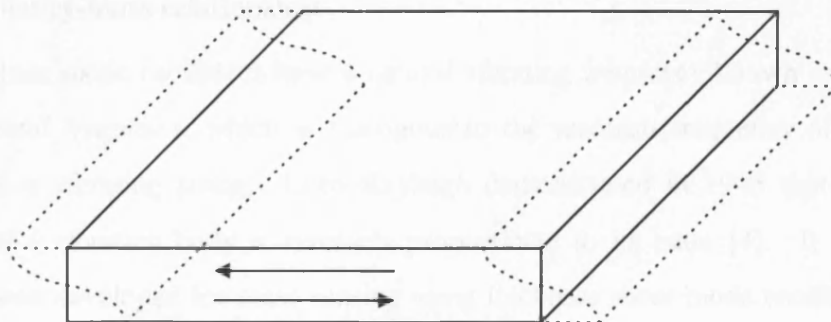


Figure 2.5: Schematic representation of quartz crystal oscillating in its fundamental thickness shear mode [3].

The thickness shear mode of vibration is selected, with suppression of all other modes, using wafers of quartz cut at specific crystallographic orientations. Wafers cut at $35^{\circ} 15'$

and $49^{\circ} 00'$ with respect to the crystallographic axes, yield quartz vibrating in the thickness shear mode and are known as the AT- and BT-cuts respectively. AT-Cut quartz has a resonant frequency less sensitive to temperature and is more commonly used, see Figure 2.6 (also see Section 2.2.7).

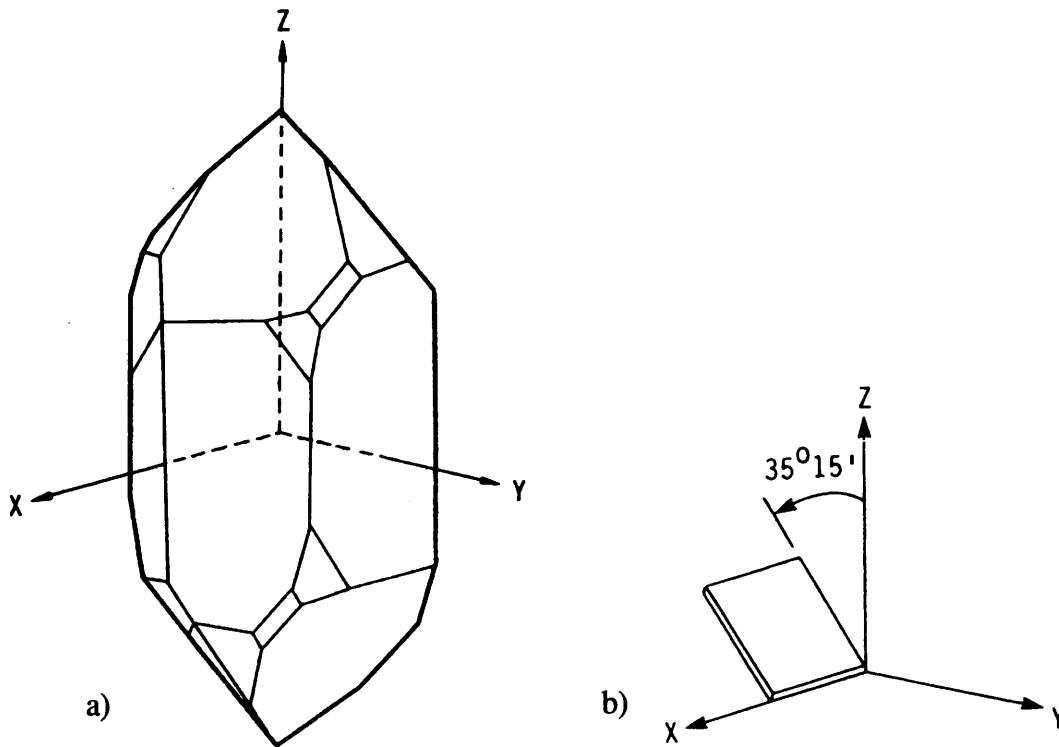


Figure 2.6: a) Assignment of axes to a quartz crystal. b) Cutting angle of AT-cut quartz crystal plate.

2.1.3 Frequency-mass relationship

Thickness shear mode oscillators have a natural vibrating frequency known as the *resonant* or *fundamental frequency*, which is analogous to the resonant frequency of a mass on a spring or to a vibrating string. Lord Rayleigh demonstrated in 1945 that the resonant frequency of a vibrating body is inversely proportional to its mass [4]. It is this theory which has been developed for mass sensing using thickness shear mode oscillators, such as the quartz crystal microbalance (QCM). The QCM applies thickness shear mode resonators to exploit the frequency-mass relationship by exciting and measuring the crystal resonant frequency using a sinusoidally alternating potential.

2.1.4 The Sauerbrey equation

In 1959 Sauerbrey quantified the frequency-mass relationship for an AT-cut quartz crystal, assuming that a sufficiently small change in mass at the crystal surface can be treated as a change in mass of the crystal itself [5].

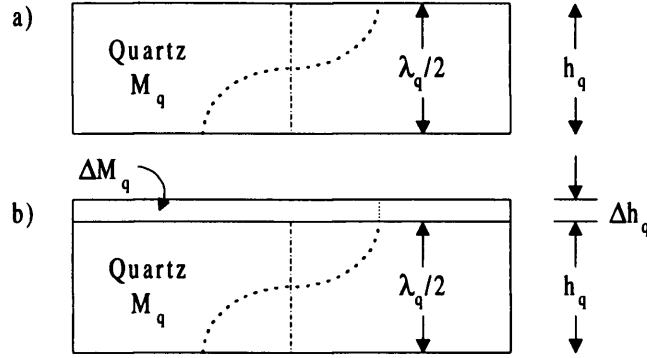


Figure 2.7: Schematic representation of a thickness shear mode (TSM) resonator [2]. (a) At resonance the wavelength, λ_q , is related to the thickness of the quartz plate, h_q . (b) An increase in h_q results in an increase in λ_q (a decrease in the resonant frequency).

The resonant frequency, f_0 , of an AT-cut quartz resonator with a mass M_q and a thickness h_q is given by:

$$f_0 = \frac{V_q}{\lambda_q} = \frac{V_q}{2h_q} \quad (2.1)$$

Where λ_q is the wavelength (equal to $2h_q$) and V_q is the speed of the wave in the quartz. It follows that a change in the thickness of the quartz will affect its resonant frequency, see Figure 2.7.

$$\frac{\Delta f_0}{f_0} = -\frac{\Delta h_q}{h_q} \quad (2.2)$$

A relative increase in the crystal thickness will cause a decrease in the resonant frequency.

This can also be expressed in terms of the crystal mass:

$$\frac{\Delta f_0}{f_0} = -\frac{\Delta M_q}{M_q} \quad (2.3)$$

Combining Equations (2.1) and (2.3) yields:

$$\Delta f_0 = -\left(\frac{2f_0^2}{\rho_q V_q}\right) \frac{\Delta M_q}{A} \quad (2.4)$$

where A is the piezoelectrically active area (cm^2), ρ_q is the density of the quartz (2.648 g cm^{-3}) and V_q is the acoustic velocity of quartz ($3.34 \times 10^5 \text{ cm s}^{-1}$). Substituting numerical values for ρ_q and V_q into Equation 2.4 yields:

$$\Delta f_0 = -2.26 \times 10^{-6} f_0^2 \frac{\Delta M_q}{A} \quad (2.5)$$

Sauerbrey assumed that small, rigid, uniformly distributed masses deposited on the oscillator surface could be treated as a mass change of the oscillator itself. Equation 2.5 can then be written in a more generalised form:

$$\Delta f = -2.26 \times 10^{-6} f_0^2 \frac{\Delta M}{A} \quad (2.6)$$

2.1.5 The electrochemical quartz crystal microbalance (EQCM)

There have been several excellent reviews of the EQCM [6-8]. The quartz crystal microbalance was first reported in 1980 to oscillate in contact with a liquid [9]. In 1985 it was discovered that the resonant frequency shift, upon immersion of the QCM in a liquid, is proportional to the square of the liquid density-viscosity product. The Sauerbrey equation was modified and it was demonstrated that the QCM could be used as a sensitive mass detector *in situ* [10-12]. Since then the QCM has been an invaluable tool to researchers in the study of liquid properties and solid/liquid interfaces [13-15]. Its nanogram sensitivity and short data acquisition time have enabled electrochemical reactions to be studied in terms of the overall reaction, under thermodynamic control, or of the reaction mechanism, under kinetic control [16-19]. The EQCM has been used to study metal ion [20], polymer [21, 22] and metal oxide/hydroxide [23] deposition and dissolution. It also enables determination of mobile species exchange between a modified electrode and its bathing electrolyte [24-31].

2.2 NON-IDEAL QCM RESPONSE

When implementing the Sauerbrey equation to rationalise frequency changes of the (E)QCM in terms of mass changes at the resonator surface, several assumptions are made. In the next section these assumptions, and some physical cases of deviation from them, are described in more detail.

2.2.1 Viscoelastic effects and overlayer thickness

When the QCM is used to investigate overlayers such as polymer films, there is a possibility that these overlayers are not rigid, but exhibit viscoelastic effects [6, 32]. Polymer viscoelastic behaviour is described in more detail in Section 2.7, but it is qualitatively clear that resonator oscillations may distort viscoelastic overlayers, causing motion of the top surface of the film to lag behind that of the lower (driven) surface. In this way energy is dissipated in the film. This leads to deviations from the Sauerbrey equation, an effect first identified by Miller and Bolef in 1968 [33]. The kinetic energy contributed by the moving film, which causes the resonant frequency to decrease, is now no longer linearly proportional to the film's areal mass density; this effect is described in greater detail in Section 2.4.2. Deviations from the Sauerbrey equation become larger for thicker films, as a more appreciable distortion is able to occur in a thicker film. In thin films, the distortion may be negligible. The EQCM is often used to as a gravimetric probe to investigate electroactive polymers. Upon redox switching, counter-ions, solvent and salt may move between the film and the bathing electrolyte. Correlation of the Faradaic charge and concurrent mass change of the electroactive film is a common method for determining the net amounts and directions of movement of charged and neutral mobile species. However, for a viscoelastic overlayer, resonator response is no longer solely a function of overlayer mass; frequency changes are also dependent on the viscoelastic nature of the film. Moreover, incorporation of solvent and counter-ions into a polymer film can lead to plasticization and therefore rheological changes within the film. This highlights the fact that when using the (E)QCM as a simple gravimetric probe it is important to remember that thickness shear mode (TSM) devices directly enable the detection of a *frequency* change and not a *mass* change.

2.2.2 High mass loading

High mass loading results in a significant decrease in oscillator resonant frequency. Upon closer inspection of the Sauerbrey equation (Equation 2.5), it follows that the sensitivity of the resonant frequency to mass changes is reduced, due to the decrease in magnitude of the numerator. It has been shown that the Sauerbrey equation is accurate for mass loading up to 2% of the mass of the quartz crystal [34]. For mass loading in excess of 2% of the crystal mass it is necessary for the shear modulus and density of the film to be known. This is because the assumption that the density and shear modulus of the film are identical to those of the quartz becomes increasingly inaccurate at higher mass loading.

2.2.3 Surface roughness

It was first proposed in 1985, by Schumacher *et al* [35], that QCM surface roughness has a significant effect on the frequency changes of liquid immersed oscillators. In their study it was observed that only 20% of the observed frequency changes of the EQCM were due to induced mass changes at the resonator surface, the remaining frequency shifts being due to liquid confined in pockets on the roughened, oxidised surface. Roughening was confirmed with scanning electron micrographs. Surface roughness effects become important when the oscillator is exposed to a liquid. The high density of liquid trapped within the surface features of the resonator surface can lead to large frequency shifts [36-38]. The mass of the liquid entrapped within the surface features can often be treated as a rigid mass layer when the assumption is made that no movement of the liquid occurs within these features. This assumption is applied in Section 2.5.1 when a physical model of an AT-cut quartz crystal exposed to a liquid overlayer is described. Minimisation of surface roughness effects can be achieved by the use of highly polished quartz crystals.

2.2.4 Surface stress

The bearing of stress to quartz resonators can induce a frequency shift that is unrelated to mass changes at the resonator surface. Stress effects can be induced in quartz crystals by application of hydrostatic, mechanical or thermal forces, which may arise during a typical experiment. These effects are outlined in the following paragraphs.

During most EQCM experiments one face of the quartz resonator is exposed to a column of liquid while the other is exposed to air. Stress induced in this way, due to the hydrostatic pressure exerted by the column of liquid, has been investigated by Heusler *et al* [39]. Hydrostatic pressure is constant throughout a typical EQCM experiment and is therefore not generally considered to have a significant effect on frequency *changes* [6]. The effect can also be minimised by experimental design, for example surface stress induced when operating 10 MHz AT-cut crystals under a column of liquid just a few centimetres deep causes frequency shifts which are negligible.

Mechanically induced stress may arise in crystals when the surface is coated with a film or due to crystal clamping in certain cell designs. Compressive stresses arising in films can act at the film/quartz interface resulting in the generation of stress within the quartz. Eernisse investigated this phenomenon using the “double resonator” method in which he utilised AT- and BT-cut crystals to simultaneously monitor the deposition of various metals [2, 40, 41]. The magnitudes of stress related frequency changes are approximately the same

in both AT- and BT-cut crystals. However, the stress coefficients have opposite signs, thus allowing the determination of stress induced frequency changes and mass induced frequency changes. Stress effects due to metal deposition were found to have a significant contribution only when the layer is a few monolayers thick. At greater thickness, mass-induced frequency shifts are dominant. Materials with lower shear moduli, and therefore greater mobility (such as polymers) are not expected to exhibit significant stress effects.

Clamping the oscillator, necessary in most electrochemical experiments, is another source of stress that remains constant throughout typical experiments and so is generally ignored. This effect can be minimised by clamping the crystal as far away as possible from the piezoelectrically active area [32].

If a quartz resonator is heated from one side, a thermal gradient exists within the quartz. Thermal gradients induce stress within the crystal that can cause significant frequency shifts for large temperature gradients. This phenomenon is known as *thermal shock* and can be avoided by careful experimental design in most cases [2].

When good experimental practice is not sufficient to eliminate stress-induced frequency changes, usage of SC (stress compensated)-cut crystals may be advantageous. SC-cut crystals have a stress related frequency coefficient of zero, therefore stress cannot induce frequency changes in SC-cut crystals. However the high cost of these devices is at present a hindering factor [2].

2.2.5 Interfacial slippage

Interpretation of quartz resonator responses relies on the assumption that there is a “no-slip” boundary condition between the resonator surface and contacting medium. In other words, the displacement of the first layer of the contacting medium at the quartz interface is assumed to be the same as the quartz displacement. This is the case if the interfacial forces of attraction between the quartz and contacting medium are sufficiently large to ensure that the continuity of displacement is maintained across the interface.

Interfacial slip is most likely to have a significant effect on a TSM resonator response when the sensor is placed in a liquid. It has been demonstrated by Thompson *et al* that treatment of the resonator surface with a hydrophobic alkane thiol monolayer has the effect of decreasing measured frequency shifts upon immersion in water, as compared to surfaces coated with a hydrophilic monolayer [42-45]. This has been explained using the argument that the hydrophobic surface provides such a weak interaction with the liquid layer that a discontinuity in displacement at the solid/liquid interface occurs. Unfortunately,

little information was provided on the surface roughness of the crystals used in these experiments and evidence has been provided by Martin *et al* that the alkane thiol monolayer is actually modifying the contact angle of the water [46]. A hydrophilic surface would give rise to a low contact angle and capillary forces drawing the water into the surface features of the resonator would be stronger compared to those of a hydrophobic surface. Hence, it is suggested that the alkyl thiol layer is modifying the extent of liquid trapping in the surface features of the resonator and *not* effecting interfacial slippage.

2.2.6 Non-uniform mass distribution

The sensitivity of quartz TSM resonators varies across the surface of the exciting electrode. Sensitivity is greatest near the centre of the electrode, where the amplitudes of oscillation are greatest, and fall to near zero sensitivity at the edge of the electrode, where amplitude of oscillation is minimal. This has been demonstrated Martin and Harger, who used a tungsten probe to measure surface motion of AT-cut quartz crystal resonators immersed in water [47]. QCM radial sensitivity has also been investigated when the resonator is in contact with a liquid, under electrochemical conditions. Ward *et al* electrodeposited copper [48], and Gabrielli *et al* electrodeposited silver [49], at known positions on the resonator surface and correlated EQCM frequency measurement and electrochemical charge to obtain the measured frequency shift for a mass of known radial position.

Since mass sensitivity is not uniform across oscillator surfaces, the Sauerbrey equation requires that the distribution of a deposited mass layer must be uniform. In reality this is unlikely to be the case. However, as long as the film roughness is not longer than the acoustic wavelength and uniformities are randomly distributed, the Sauerbrey equation will yield an average value of areal mass density of the deposited mass, provided that the departure from uniformity is not severe.

2.2.7 Temperature

It is essential that the temperature at which frequency measurements are made with the QCM is known, as temperature affects many of the assumptions which are made when using the Sauerbrey equation. The response of the quartz itself is affected by temperature, as described in Sections 2.1.2 and 2.2.4. Temperature also significantly affects liquid density and viscosity, and overlayer rheology, which all have a significant effect on resonator response, as described in Sections 2.2.1 and 2.4.2.

2.3 EQUIVALENT CIRCUIT REPRESENTATIONS

Generally, there are two types of equivalent circuit models used to describe AT-cut quartz resonators: the *lumped element* and *transmission line* models. Each of these models will be described in the following sections.

2.3.1 Lumped element model

The electrical response of an AT-cut quartz TSM resonator can be modelled using a series of lumped elements. A series branch consisting of inductive, capacitive and resistive components, with a capacitor in parallel is known as a Butterworth-Van Dyke equivalent circuit (see Figure 2.8).

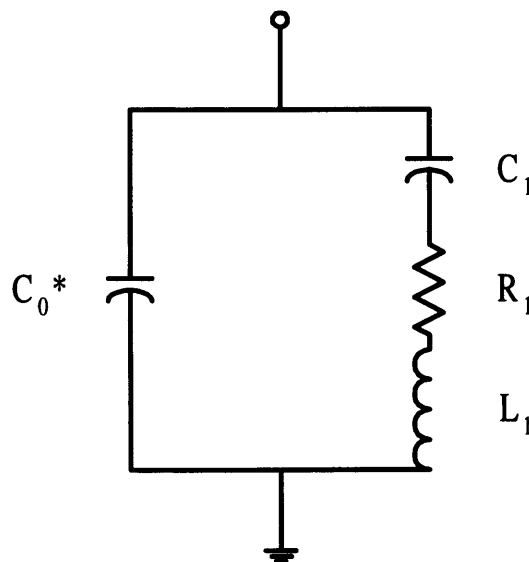


Figure 2.8: Butterworth-Van Dyke equivalent circuit model used to describe the near-resonant electrical characteristics of a TSM resonator.

The components of the series branch correspond to different electromechanical aspects of the quartz resonator. The inductor, L_1 , affects the electrical response in a similar manner to the displaced mass of an oscillating crystal. The capacitor, C_1 , corresponds to energy stored during the oscillation, analogous to mechanical energy stored in the quartz as it is elastically deformed. Non-elastic deformations simultaneously occur whilst the quartz is oscillating; energy lost as heat in this manner is represented by a resistor, R_1 . Non-elastic deformations can arise from internal friction within the quartz, and external losses to the mounting and contacting medium. Together the three series components, L_1 , C_1 , and R_1 , define the electromechanical characteristics of the quartz resonator: they are commonly referred to as

the *motional branch*. The capacitor, C_0^* , attached in parallel to the series branch is given by:

$$C_0^* = C_0 + C_p \quad (2.7)$$

where C_0 represents the static capacitance arising from the gold electrodes attached to the surface of the quartz wafer and C_p represents a parasitic capacitance arising from the geometry of the gold electrodes and the test fixture. The elements of the circuit are given by [50]:

$$C_0 = \frac{\epsilon_{22}A}{h_q} \quad (2.8)$$

$$C_1 = \frac{8K^2 C_0}{(N\pi)^2} \quad (2.9)$$

$$L_1 = \frac{1}{\omega_s^2 C_1} \quad (2.10)$$

$$R_1 = \frac{\eta_q}{\mu_q C_1} \quad (2.11)$$

where ϵ_{22} is the dielectric permittivity; A is the electrode area; h_q is the substrate thickness; K is the quartz electromechanical coupling coefficient; N is the harmonic number; $\omega_s = 2\pi f_s$, where f_s is the series resonant frequency for the unperturbed quartz resonator; η_q is the quartz effective viscosity; and μ_q is the quartz shear stiffness.

2.3.2 Impedance analysis

The fact that well-defined relationships exist between the electrical and mechanical properties of the quartz enables the characterisation of the resonator to be achieved using impedance analysis. A network analyser is used to measure current as a function of applied voltage at a range of frequencies, close to the resonant frequency of the crystal. Each component of the circuit has characteristic impedance. The inductive and capacitive components give rise to impedance that is frequency dependent. Impedance and admittance, the reciprocal of impedance, are often represented using complex numbers, giving rise to real and imaginary components.

$$Y = G_c + jB \quad (2.12)$$

$$|Y| = (G_c^2 + B^2)^{1/2} \quad (2.13)$$

where G_c is the conductance and B is the susceptance. Admittance plots are often used to display quartz resonator admittance information graphically. Figure 2.9 shows an admittance locus of an electrical equivalent circuit of an AT-cut quartz crystal.

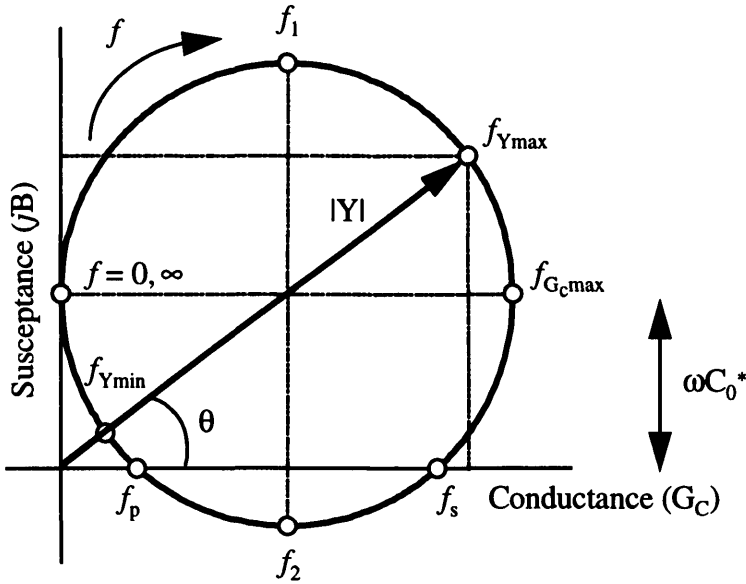


Figure 2.9: Admittance locus for electrical equivalent circuit of AT-cut quartz resonator

At low frequencies the capacitive reactance, $\omega(C_0 + C_1)$, is dominant, and $\theta = 90^\circ$ indicating that the voltage is leading the current. As the frequency is increased from $f = 0$ the magnitude of B reaches a maximum value at f_1 . At frequencies closer to the resonant region, the contribution of the inductive reactance, ωL_1 , increases, opposing the capacitive reactance, until at f_{Ymax} , the maximum admittance magnitude occurs. The maximum of the real admittance component occurs at f_{Gcmax} . The admittance locus crosses the abscissa at two frequencies, the series resonant frequency and the parallel resonant frequency, f_s and f_p , respectively. At these frequencies the reactance and phase angle are zero, the impedance is entirely resistive and resonance occurs. The magnitude of B reaches a minimum at f_2 , so the inductive reactance dominates. Increasing the frequency above f_{Ymin} causes significant decrease in the value of $1/\omega C_0$, increasing the current that flows through the network. Therefore, at extreme frequency values, above and below the resonant frequency, the phase angle is 90° , indicating that the network is mainly capacitive in nature. Another useful way to display this data graphically is to plot the relevant parameter as a function of frequency, as shown in Figure 2.10.

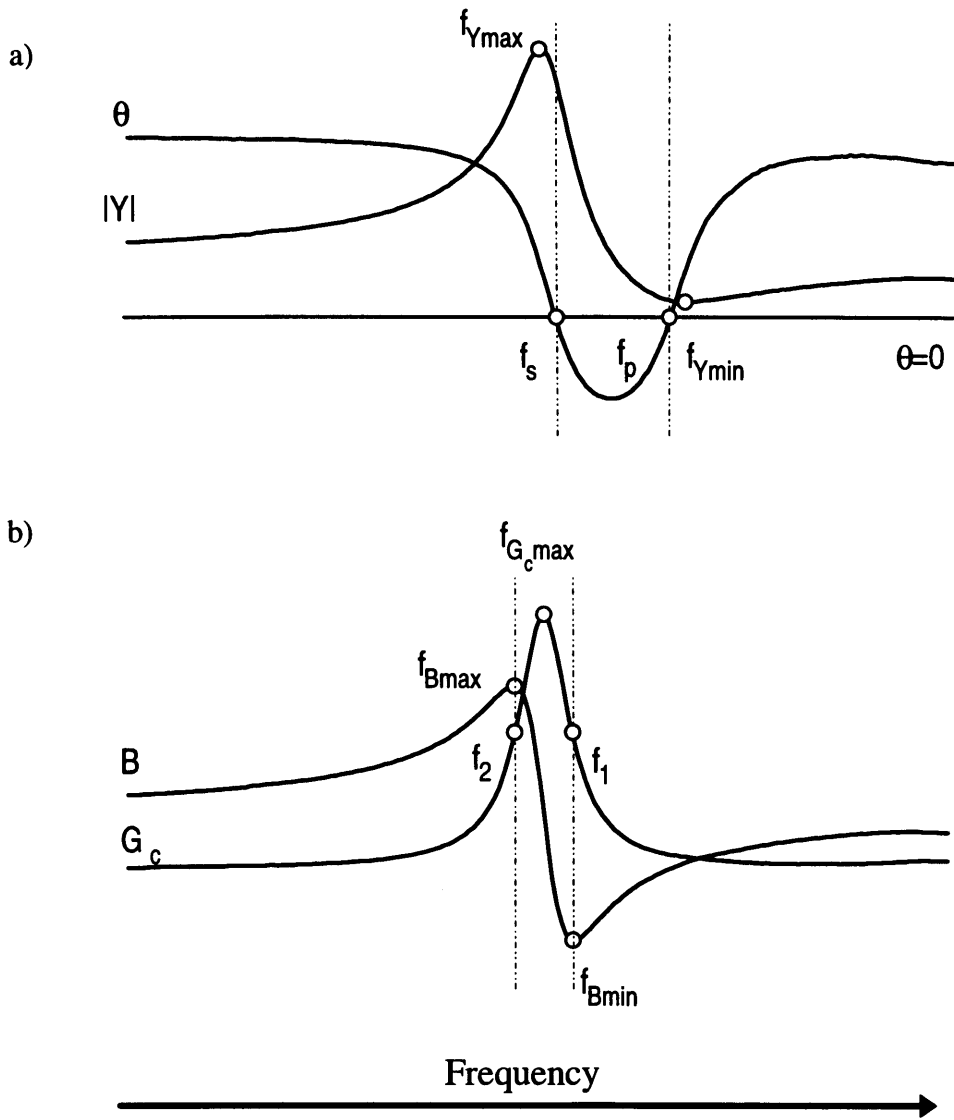


Figure 2.10: (a) Typical $|Y|$ and θ plots in the resonance region of a AT-cut quartz resonator. (b) Typical B and G_c plots in the resonance region of an AT-cut quartz resonator.

The total resonator circuit admittance is given by:

$$Y = j\omega C_0^* + \frac{1}{Z_m} \quad (2.14)$$

where the motional impedance is:

$$Z_m = R_1 + j\omega L_1 + \frac{1}{j\omega C_1} \quad (2.15)$$

and $j = \sqrt{-1}$.

The series and parallel frequencies at which resonance occurs, f_s and f_p , respectively, arise when the sum of capacitive and inductive reactances are zero, giving rise to a purely resistive impedance. The series resonant frequency occurs when the *series* or *motional* reactance is zero, i.e.:

$$j\omega_s L_1 + \frac{1}{j\omega_s C_1} = 0 \quad (2.16)$$

Solving Equation 2.16 for ω_s and noting that $\omega_s = 2\pi f_s$, yields:

$$f_s = \frac{1}{2\pi(L_1 C_1)^{1/2}} \quad (2.17)$$

The parallel resonant frequency occurs when the *total* reactance is zero:

$$f_p = \frac{1}{2\pi} \left[\frac{1}{L_1} \left(\frac{1}{C_1} + \frac{1}{C_0^*} \right) \right]^{1/2} \quad (2.18)$$

2.3.3 Impedance analysis as a diagnostic tool

In Section 2.3.2 it was shown how the unperturbed quartz resonator's electrical response can be approximated using an equivalent electrical circuit. When a surface perturbation is applied to the resonator's surface, such as applying a mass layer or immersing a face of the oscillator in a liquid, piezoelectric coupling relates the additional surface *mechanical* impedance to a concurrent change in the device's *electrical* impedance. With the use of a continuum model, which describes the coupled mechanical displacement and electrical potential [51], these changes in the electrical characteristics of the oscillator can be related to the properties of the perturbing mass or liquid layer. Solving the continuum model can lead to an electrical equivalent circuit that approximates the electrical response of the perturbed crystal. The surface mechanical impedance arising at the quartz surface can be related to the change in the electrical impedance of the quartz oscillator, Z_e , using [52]:

$$Z_e = \frac{N\pi}{4K^2 \omega_s C_0} \left(\frac{Z_s}{Z_q} \right) \quad (2.19)$$

where Z_s and Z_q are the surface mechanical impedance and the characteristic shear wave impedance of quartz, respectively, defined as [53]:

$$Z_s = \frac{T_{xy}}{v_x} \Big|_{y=0} \quad (2.20)$$

$$Z_q = (\rho_q \mu_q)^{1/2} \quad (2.21)$$

T_{xy} is the sinusoidal steady state shear stress (force per unit area in the x-direction on a y-normal plane) occurring in the contacting medium due to the force exerted by the oscillating quartz. v_x is the resulting x-directed surface shear particle velocity. Z_s is a complex quantity and therefore has real and imaginary parts. The real part corresponds to the component of the stress that is in phase with the surface particle velocity: this represents mechanical power dissipation at the surface. The imaginary part corresponds to the component of the stress that is 90° out of phase with the particle velocity: this represents mechanical energy storage [32]. It is possible to represent the complex electrical impedance, Z_e , with lumped electrical components:

$$Z_e = R_2 + j\omega L_2 \quad (2.22)$$

where the electrical resistance, R_2 , represents the real part of Z_e and the electrical impedance represents the imaginary part of Z_e . Using Equation 2.19, R_2 and L_2 can be rewritten as [46]:

$$R_2 = \frac{N\pi}{4K^2\omega_s C_0} \frac{\text{Re}(Z_s)}{Z_q} \quad (2.23)$$

$$L_2 = \frac{N\pi}{4K^2\omega_s^2 C_0} \frac{\text{Im}(Z_s)}{Z_q} \quad (2.24)$$

The electrical equivalent circuits shown in Figure 2.11 are modified Butterworth-Van Dyke circuits. When the quartz oscillator has a surface perturbation the total resonator circuit admittance is still represented by Equation 2.14, but now Z_m is given by:

$$Z_m = (R_1 + R_2) + j\omega(L_1 + L_2) + \frac{1}{j\omega C_1} \quad (2.25)$$

There are many different types of surface perturbation which quartz thickness shear mode resonators are routinely exposed to. In Section 2.4 physical models which are relevant to the study of electroactive polymers films are shown, together with an equation for the surface mechanical impedance, Z_s in that specific case. This equation can be combined with Equation 2.19 to find Z_e for each of those cases.

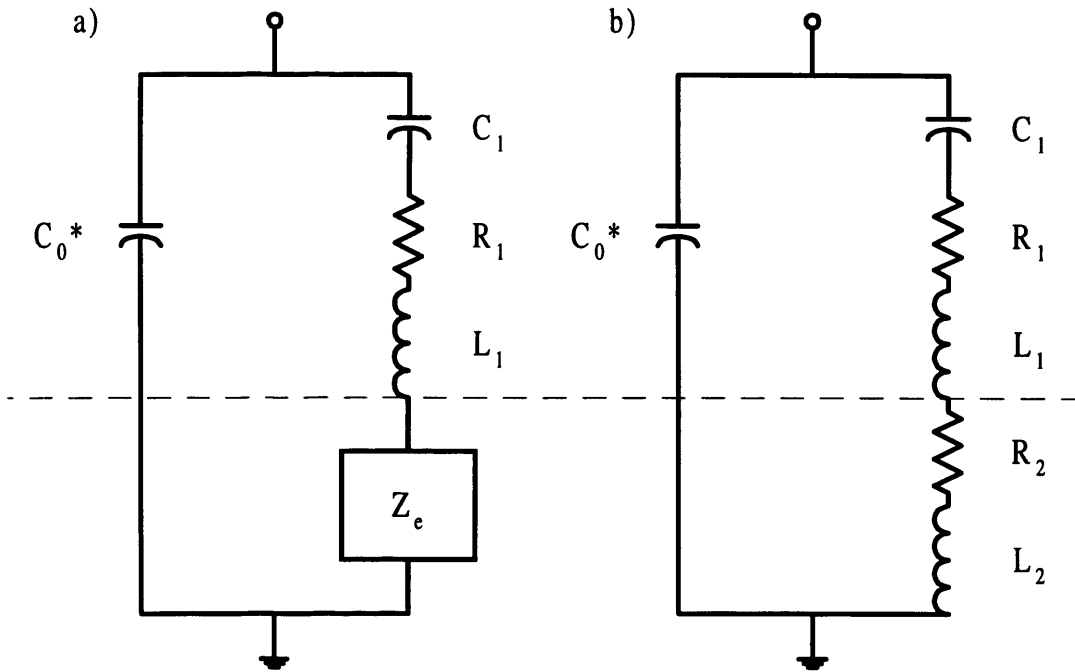


Figure 2.11: Modified Butterworth-Van Dyke equivalent circuit model of a perturbed AT-cut thickness shear mode resonator: (a) with complex impedance element Z_e , and (b) with motional inductance L_2 and resistance R_2 .

2.3.4 Transmission line model

A transmission line (or distributed) model is used to represent the propagation of energy of the transverse shear waves within the quartz and contacting medium [54]. The model uses a transformer to convert the electrical energy supplied to the crystal into the acoustic variables, stress T and velocity v . These acoustical variables are analogous to the electrical variables voltage and current, respectively. Surface perturbations cause acoustic impedances that modify the progression of acoustic energy within the transmission line; the resultant acoustic energy is then converted back into electrical energy at the transformer.

The model (shown in Figure 2.12) consists of an electrical input and two acoustic ports, representing the faces of the crystal. Generally, only one face of the thickness shear mode resonator is exposed to a perturbation, the other being exposed to air. The face exposed to air is considered as a stress-free boundary since the masses of the electrodes are neglected for simplicity. A stress-free boundary is equivalent to short-circuiting one of the acoustic ports.

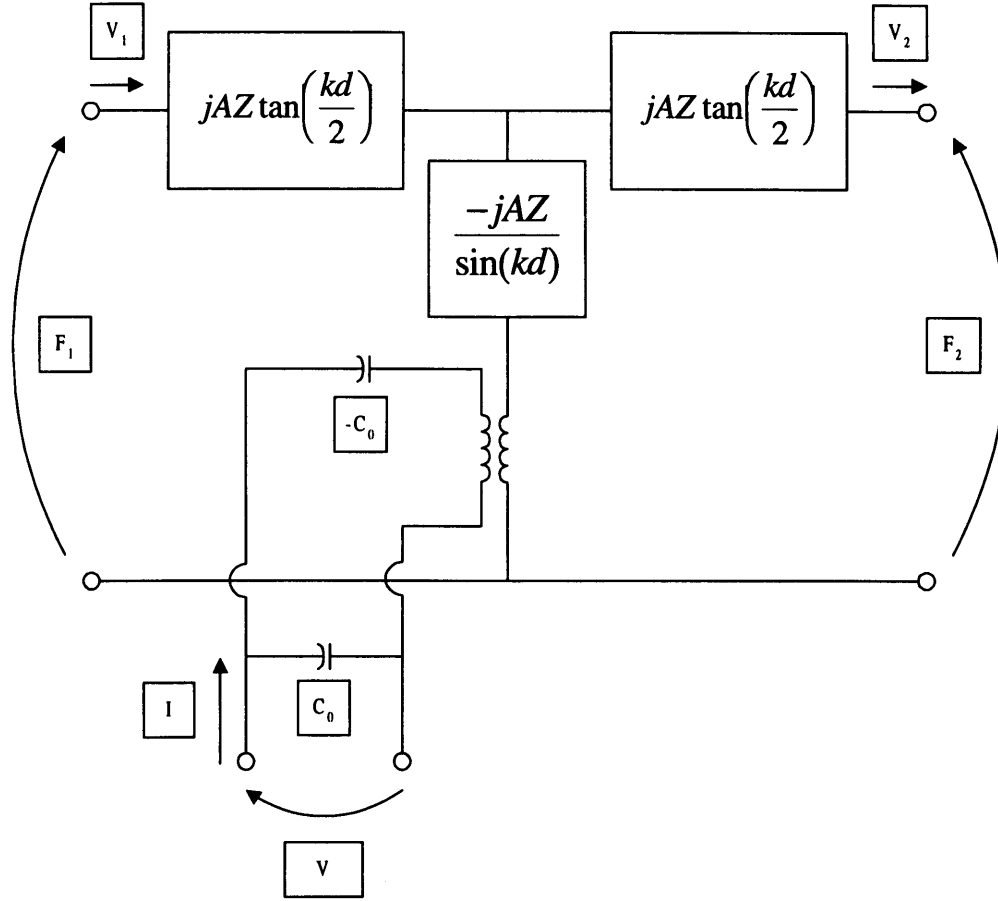


Figure 2.12: Distributed equivalent-circuit model to describe the near-resonant electrical characteristics of a TSM resonator.

Surface mechanical impedance arising from a surface perturbation can be placed across the other boundary. The transmission line model relates the electrical impedance, Z_e , to the surface mechanical impedance, Z_s , and the characteristic shear wave impedance of the quartz, Z_q , with the following equation:

$$Z_e = \frac{N\pi}{4K^2\omega_s C_0} \left(\frac{Z_s}{Z_q} \right) \left[1 - \frac{j \frac{Z_s}{Z_q}}{2 \tan\left(\frac{\pi\omega}{2\omega_s}\right)} \right]^{-1} \quad (2.26)$$

It is interesting to note that, for a crystal oscillating in air, both acoustic ports can be terminated with a short circuit. The transmission line model then reduces to the simpler Butterworth-Van Dyke model, Equation 2.19 [52].

2.3.5 Comparison of the lumped element and transmission line models

Parameters extracted using the transmission line and lumped element models have been compared when using thickness shear mode quartz resonators with different surface perturbations. It was found that these parameters did not differ relatively by more than 3% for most practical sensor configurations operating at the fundamental resonance [55]. It can be seen, by comparing Equations 2.26 and 2.19, that for small ratios of Z_s to Z_q , the equation for the transmission line model will reduce to that for the lumped element model. If the ratio of Z_s to Z_q does not exceed 0.1, the lumped element model always predicts responses within 1% of those for the transmission-line model. Ratios in excess of 0.1 occur when studying thick films in solution, as can be the case when studying electroactive polymer films.

2.4 PHYSICAL MODELS

A quartz thickness shear mode resonator can be considered as a source of transverse acoustic shear waves that radiate into the contacting medium. These transverse waves may become entirely damped by the medium or reflect off interfaces, i.e. overlayer/liquid or overlayer/air interfaces. Reflected transverse waves can interfere with those outgoing from the oscillating crystal either destructively (interference) or constructively (coherence).

2.4.1 Ideal mass layer

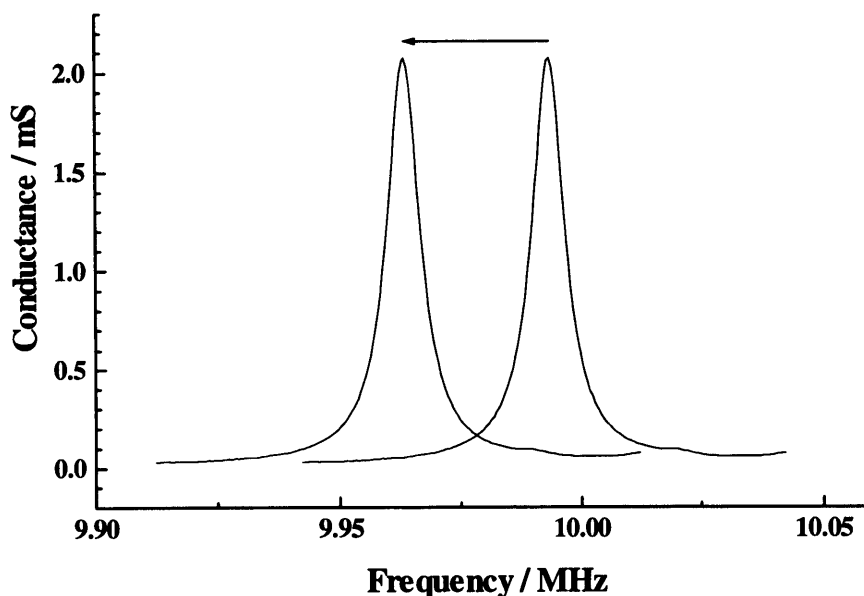


Figure 2.13: Electrical conductance vs. frequency plot for a TSM resonator, demonstrating the effect of ideal mass layer addition.

The addition of a mass to the resonator surface has the effect of increasing the inertial mass of the oscillating system. The effect that this has on the resonator's electrical response can be seen in Figure 2.13. This electrical response can be approximated using the Butterworth-Van Dyke equivalent electrical circuit with the addition of an inductor to the motional arm.

As with the Sauerbrey equation, the assumption is made that zero phase shift of the acoustic wave occurs throughout the ideal mass layer's thickness. This means that no damping or phase shift of the acoustic wave occurs within an ideal mass layer, therefore no interference or coherence phenomena of the acoustic wave can occur. This approximation can be applied when the overlayer is rigid and sufficiently thin (see Figure 2.14).

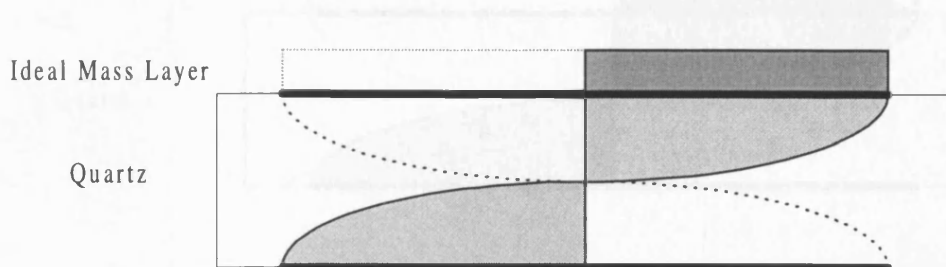


Figure 2.14: Cross sectional view of an AT-cut quartz thickness shear mode resonator with an ideal mass layer attached to one surface. The figure shows the acoustic wave propagation in the crystal and through the mass layer.

The surface mechanical impedance at the oscillator surface arising from the addition of a mass layer can be given by [46]:

$$Z_s = j\omega\rho_s \quad (2.27)$$

where ρ_s is defined as the mass per unit area of the ideal mass layer, given by:

$$\rho_s = h_s\rho_{iml} \quad (2.28)$$

where h_s and ρ_{iml} are the thickness and density, respectively, of the ideal mass layer.

2.4.2 Finite viscoelastic layer

A force exerted on a *rigid* body exclusively results in the acceleration of that body, an assumption that was used in the previous section, when analysing ideal mass layers. However, when a force is exerted upon a viscoelastic body, some of the force is used to accelerate the body and some causes deformations within the body. These deformations can

be either elastic, when the energy of the deforming force is stored in the body and regained when the body returns to its original shape, and/ or viscous, when the body is deformed by the force and the energy is lost due to friction within the body, and, therefore, ultimately lost as heat. When a viscoelastic overlayer is placed upon a TSM resonator, force is exerted upon the layer in the form of transverse acoustic shear waves. Transverse acoustic waves undergo phase shift and attenuation when propagating through viscoelastic layers (see Figure 2.15).

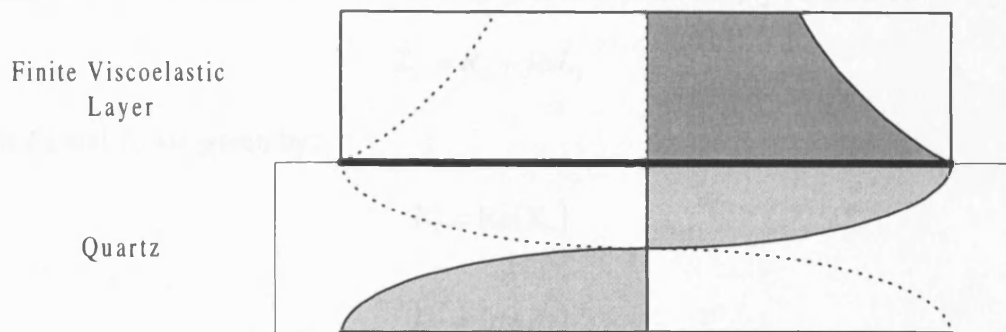


Figure 2.15 Cross-sectional view of a TSM resonator with the top surface in contact with a finite viscoelastic layer.

If the decay length of the transverse wave propagating into this layer is larger than the viscoelastic layer thickness it is considered to be a *finite* viscoelastic layer. When the propagating acoustic wave reaches the outer surface of the finite viscoelastic layer it is reflected at the upper interface and propagates back to the resonator/viscoelastic layer interface. Reflected transverse waves can interfere with waves from the oscillating crystal either destructively (interference) or constructively (coherence). The resultant motion of the resonator is translated into the measured impedance response. The surface mechanical impedance at the oscillator surface, resulting from the addition of a finite viscoelastic layer is given by [56]:

$$Z_s = (G\rho_f)^{1/2} \tanh(\gamma h_f) \quad (2.29)$$

where:

$$\gamma = j\omega \left(\frac{\rho_f}{G} \right)^{1/2} \quad (2.30)$$

G is the finite viscoelastic layer's shear modulus. ρ_f and h_f are the film density and thickness respectively. γ is denoted as the complex wave propagation constant. Equation 2.29 can be combined with Equation 2.19 to obtain the electrical motional impedance that arises from a viscoelastic film on a TSM resonator. Z_e comprises real and imaginary components, where the real part, R_2 , represents power dissipation in the film and the imaginary part, L_2 , represents energy storage. Mathematically, it is difficult to extract real elements for R_2 and L_2 from the complex Z_e due to the hyperbolic tangent function in Equation 2.29. Therefore the electrical impedance is more simply defined as:

$$Z_e = R_2 + j\omega L_2 \quad (2.31)$$

where R_2 and L_2 are given by:

$$R_2 = \text{Re}(Z_e) \quad (2.32)$$

$$L_2 = \text{Im}(Z_e) \quad (2.33)$$

2.4.3 Semi-infinite Newtonian liquid

Viscous coupling causes liquid at the crystal/liquid interface to move synchronously with the quartz resonator and fluid is entrained by the transverse wave which is radiated into the medium (see Figure 2.16).

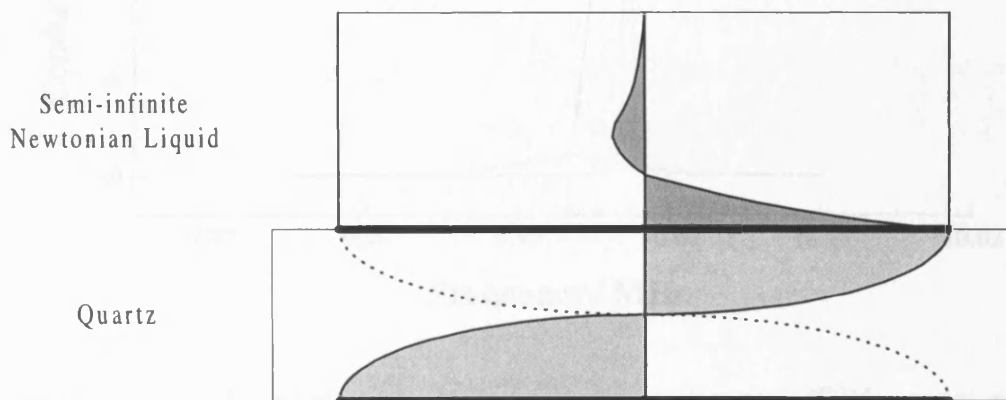


Figure 2.16: Cross-sectional view of a TSM resonator with the top surface in contact with a semi-infinite Newtonian liquid.

The additional inertial mass of viscously entrained fluid has the effect of increasing the kinetic energy of the oscillating system and causes the resonant frequency of the oscillator to shift to lower frequencies, in an analogous fashion to the case of a rigid mass

deposited on a crystal surface. However, unlike the example of a rigid mass, the acoustic shear wave does not penetrate very far into a Newtonian fluid. The transverse wave quickly becomes damped due to frictional forces proportional to the fluid's density and viscosity. Hence, some of the energy of a crystal oscillating in a fluid is used to overcome frictional forces arising from the fluid. This is analogous to a pendulum swinging in water; if the amplitude of the oscillation is to be maintained, energy must be supplied, in order to overcome the frictional forces, proportional to water's density and viscosity, which oppose the pendulum's motion. Frictional losses are reflected in the crystal impedance electrical response curve by severe damping of the resonance peak, also shown in Figure 2.17. The resonant frequency has been shown to vary linearly with $(\rho_l \eta_l)^{1/2}$, as described in Section 2.1.5. More recently, equivalent circuit elements have been computed which approximate the near resonant crystal impedance response for a TSM resonator exposed to Newtonian liquids [57-59].

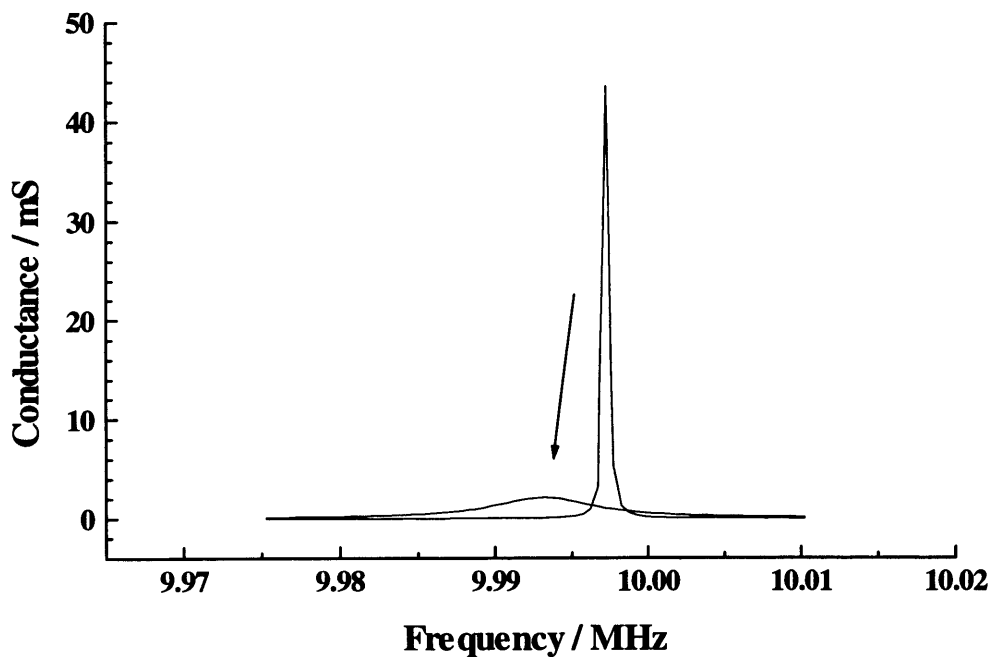


Figure 2.17: Electrical conductance vs frequency data for a TSM resonator, demonstrating the effect of immersion of one face in a Newtonian liquid.

A Newtonian fluid is defined as a fluid in which the shear stress and the gradient in fluid velocity are related by a constant, independent of amplitude or frequency [60]. Newtonian liquids impede the motion of TSM resonators. Equation 2.29 shows the mechanical impedance at the quartz surface due to immersion of one face of the resonator in a liquid.

$$Z_s = \left(\frac{\omega \eta_l \rho_l}{2} \right)^{1/2} (1 + j) \quad (2.34)$$

where η_l and ρ_l are the Newtonian liquid's viscosity and density respectively. Equation 2.29 shows that Z_s comprises equal real and imaginary components. It can be combined with Equations 2.23 and 2.24 to yield the motional impedance elements arising from liquid loading of a smooth TSM resonator.

$$R_2 = \frac{N\pi}{4K^2 \omega_s C_0 Z_q} \left(\frac{\omega_s \rho_l \eta_l}{2} \right)^{1/2} \quad (2.35)$$

$$\omega L_2 = \frac{N\pi}{4K^2 \omega_s C_0 Z_q} \left(\frac{\omega_s \rho_l \eta_l}{2} \right)^{1/2} \quad (2.36)$$

The distance that a transverse acoustic wave propagates into a contacting medium is known as the decay length. The decay length of a transverse acoustic wave in a Newtonian liquid is given by:

$$\delta = \left(\frac{2\eta_l}{\omega \rho_l} \right)^{1/2} \quad (2.37)$$

A Newtonian liquid is said to be *semi-infinite* when the thickness of the fluid layer exposed to the oscillator is larger than the decay length, δ , of the transverse wave propagating into that fluid. The transverse wave decay length, for a 10 MHz TSM resonator immersed in water can be calculated from Equation 2.32 as 0.18 μm . In most practical cases the thickness of the fluid layer above the resonator is far in excess of 0.18 μm , therefore, these cases are known as *semi-infinite* Newtonian fluids.

2.5 MULTI-LAYER PHYSICAL MODELS

Real systems studied with the TSM resonator often consist of more than one layer. It is possible to create many combinations of layers and derive equations that approximate the surface mechanical impedance these layers produce at the oscillator. Outlined below are examples of multilayer models that have been chosen for use in the study of electroactive polymer films.

When compiling a multi-layer model it is important to note whether a phase shift of the acoustic wave occurs in any of the layers except the outer layer. When no phase shift occurs in the 'lower' layers, combination of surface mechanical impedance is simply

additive. However, if phase shift does occur in the lower layers, a more complicated combination procedure is required, as discussed below.

2.5.1 Ideal mass layer + semi-infinite Newtonian liquid

The surfaces of TSM resonators are often not hydrodynamically smooth (see Section 2.2.3). Surface roughness can cause liquid trapping, leading to an increase in the dependence of the imaginary component of Z_s . This offset has been shown to be proportional to the density of the trapped fluid. When modelling rough crystals, the effect of surface roughness on the surface mechanical impedance is approximated by treating the trapped fluid as an ideal mass layer [46].

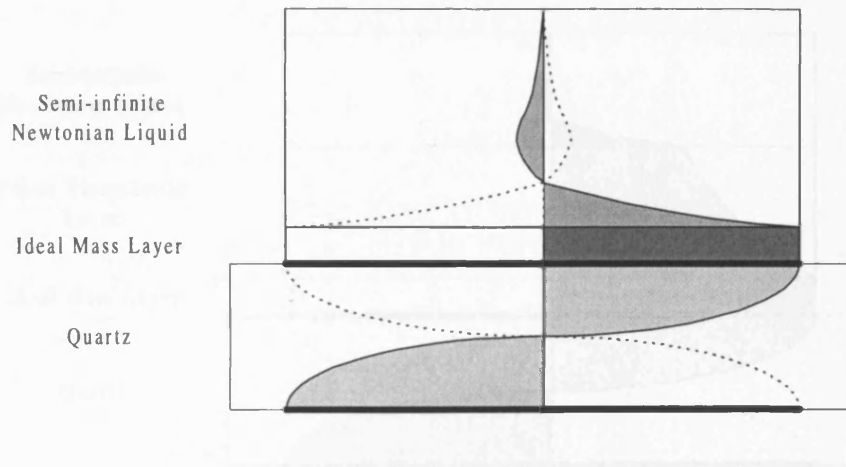


Figure 2.18: Cross-sectional view of a TSM resonator with the top surface in contact with an ideal mass layer and a semi-infinite Newtonian liquid.

The propagation of the acoustic wave within an ideal mass layer and a contacting Newtonian layer is shown in Figure 2.18. As there is no acoustic wave shift within an ideal mass layer, the composite surface mechanical impedance is purely the sum of the two impedances considered separately [46]. Hence, combining Equations 2.29 and 2.34 yields:

$$Z_s = j\omega\rho_s + \left(\frac{\omega\rho_l\eta_l}{2}\right)^{1/2} (1+j) \quad (2.38)$$

Equations 2.23 and 2.24 can be combined with Equation 2.38 to yield the electrical elements R_2 and L_2 for the composite electrical impedance of a combined ideal mass layer and semi-infinite Newtonian liquid:

$$R_2 = \frac{N\pi}{4K^2\omega_s C_0 Z_q} \left(\frac{\omega_s\rho_l\eta_l}{2}\right)^{1/2} \quad (2.39)$$

$$L_2 = \frac{N\pi}{4K^2\omega_s^2 C_0 Z_q} \left[\left(\frac{\omega_s \rho_l \eta_l}{2} \right)^{1/2} + \omega_s \rho_s \right] \quad (2.40)$$

2.5.2 Ideal mass layer + finite viscoelastic layer + semi-infinite Newtonian liquid

It is useful to use a three-layer model to describe the surface mechanical impedance imposed by *in situ* electreactive polymer films at a TSM resonator surface. An ideal mass layer is used to describe the effect of the surface roughness, a finite viscoelastic layer approximates a polymer film and the contacting electrolyte solution is represented by a semi-infinite Newtonian Liquid. It is shown in Figure 2.19 how the acoustic wave decays through the layers.

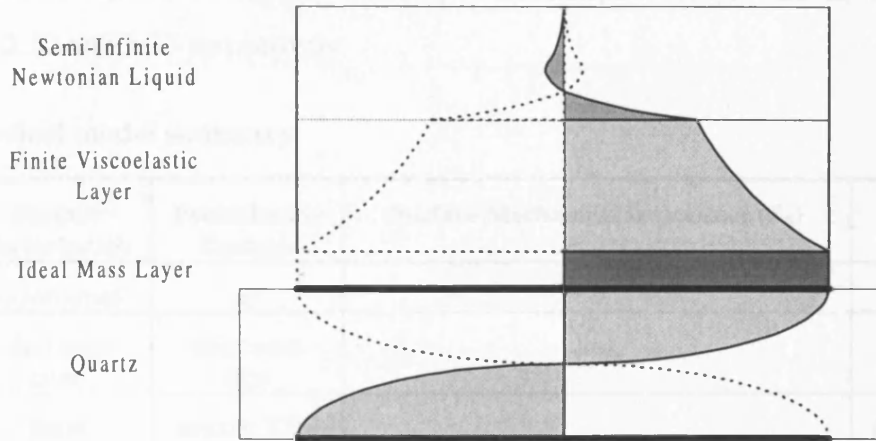


Figure 2.19: Cross-sectional view of a TSM resonator with the top surface in contact with an ideal mass layer, a finite viscoelastic layer and a semi-infinite Newtonian liquid.

Due to the phase shift that the transverse wave undergoes within the finite viscoelastic layer, it is not correct to simply add the surface mechanical impedance of the separate layers together. The total surface mechanical impedance can be described by the equation [61]:

$$Z_s = j\omega_s \rho_s + Z_a \left[\frac{Z_b \cosh(\gamma h_f) + Z_a \sinh(\gamma h_f)}{Z_a \cosh(\gamma h_f) + Z_b \sinh(\gamma h_f)} \right] \quad (2.41)$$

where:

$$Z_a = (\rho_f G)^{1/2} \quad (2.42)$$

$$Z_b = \left(\frac{\omega \rho_l \eta_l}{2} \right)^{1/2} (1 + j) \quad (2.43)$$

In Equation 2.41 it can be noted that the term $j\omega_s \rho_s$, that describes the surface mechanical impedance of an ideal mass layer, where acoustic phase shift does not occur, is simply added to the more complicated combination of terms describing the surface mechanical impedance of a finite viscoelastic layer and semi-infinite Newtonian liquid where phase shift does occur. The total surface mechanical impedance is dependant on the Newtonian liquid's density, ρ_l , and viscosity, η_l , and on the finite viscoelastic film's density, ρ_f , thickness, h_f , and shear modulus, G .

The resultant electrical impedance of the TSM resonator comprises of the electrical components R_2 and L_2 as described in Equation 2.31, where R_2 and L_2 are given by Equations 2.32 and 2.33 respectively.

2.5.3 Physical model summary

Model	Surface Perturbation	Perturbation Example	Surface Mechanical Impedance (Z_s)	Variable Parameters
1	unperturbed	air	0	none
2	ideal mass layer	thin metal film	$j\omega_s \rho_s$	ρ_s
3	finite viscoelastic layer	smooth TSM resonator coated with thin polymer film	$(G\rho_f)^{1/2} \tanh(\gamma h_f)$	G', G'', ρ_f, h_f
4	semi-infinite Newtonian liquid	smooth TSM resonator immersed in water	$\left(\frac{\omega \eta_l \rho_l}{2} \right)^{1/2} (1 + j)$	ρ_l, η_l
5	ideal mass layer + semi-infinite Newtonian liquid	rough TSM resonator immersed in water	$j\omega_s \rho_s + \left(\frac{\omega \rho_l \eta_l}{2} \right)^{1/2} (1 + j)$	ρ_s, ρ_l, η_l
6	ideal mass layer + finite viscoelastic layer + semi-infinite Newtonian liquid	rough TSM resonator coated with thin polymer film immersed in water	$j\omega_s \rho_s + Z_a \left[\frac{Z_b \cosh(\gamma h_f) + Z_a \sinh(\gamma h_f)}{Z_a \cosh(\gamma h_f) + Z_b \sinh(\gamma h_f)} \right]$	$\rho_s, G', G'', \rho_f, h_f, \eta_l, \rho_l$

Table 2.1: Summary of the physical models and related variable parameters for different surface perturbations of the TSM resonator.

Table 2.1 shows a summary of the fitting models detailed in the previous sections. Each type of perturbation is designated a ‘model number’ which will be used for reference purposes throughout this thesis. Column 2 provides a physical description of the perturbation model while column 3 provides a physical example.

2.6 ACOUSTIC EFFECTS

2.6.1 Harmonics

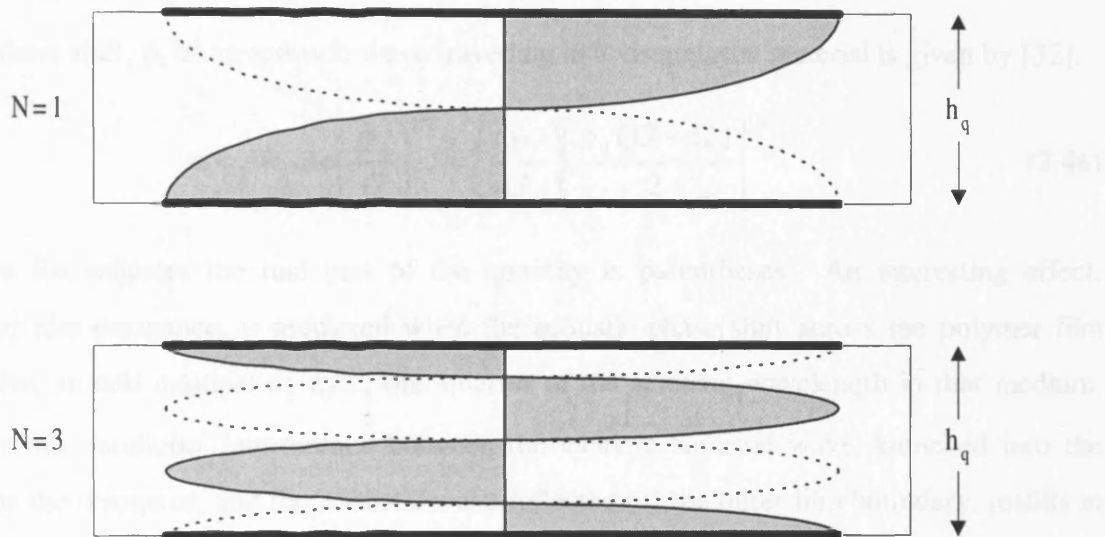


Figure 2.20: Shear displacement profiles across the resonator thickness for the fundamental and the third-harmonic resonances.

The sensitivity of TSM resonators increases with the use of crystals with a higher oscillating frequency. However, the fundamental resonant frequency is inversely proportional to the crystal thickness, see Equation 2.1. Therefore high frequency crystals become increasingly thin and fragile. One solution is to excite higher harmonics within the crystal. This can be done via application of a high frequency driving potential across the crystal surfaces, as long as the following two resonant conditions are satisfied:

$$h_q = N \left(\frac{\lambda}{2} \right) \quad (2.44)$$

$$f_N = \frac{NV_q}{2h_q} \quad (2.45)$$

Where N is an integer, h_q is the crystal thickness, λ is the acoustic wavelength and V_q is the speed of the wave in the quartz. The resonant frequency is denoted by f_N . A more detailed analysis indicates that surface electrodes can only excite odd harmonics (see Figure 2.20). Therefore, N must be an odd integer.

The use of higher harmonics is helpful to obtain unique solutions when extracting physical parameters from crystal impedance responses, since, for example, an overlayer's thickness and density will not change as the frequency is increased.

2.6.2 Film resonance

The phase shift, ϕ , of an acoustic wave travelling in a viscoelastic material is given by [32]:

$$\phi = \omega h_f \operatorname{Re} \left(\frac{\rho_f}{G} \right)^{1/2} = \left(\frac{\omega h_f}{G} \right) \left[\frac{\rho_f (|G| + G)}{2} \right]^{1/2} \quad (2.46)$$

Where Re indicates the real part of the quantity in parentheses. An interesting effect, termed film resonance, is predicted when the acoustic phase shift across the polymer film becomes an odd multiple of $\pi/2$, one quarter of the acoustic wavelength in that medium. Under this condition, interference between the incident acoustic wave, launched into the film by the resonator, and the acoustic wave reflected off the outer film boundary, results in maximal extraction of electrical energy from the source. Film resonance has been reported for a few electroinactive polymers exposed to air or vapour [62-64], by manipulating the acoustic phase shift through the polymer shear modulus.

An essential factor required to observe film resonance is an adequate reflection magnitude at the film/liquid interface, necessary to provide sufficient interference effects for resonance to occur. The reflection coefficient, R_i , at the polymer/liquid interface is given by:

$$R_i = \frac{Z_l - Z_f}{Z_l + Z_f} \quad (2.47)$$

where the liquid impedance, Z_l , is given by Equation 2.34 and the characteristic film impedance, Z_0 , is given by:

$$Z_0 = (G\rho_f)^{1/2} \quad (2.48)$$

In the electrochemical context, exposure of the polymer to an electrolyte solution means that the acoustic reflection coefficient at the outer film boundary is unknown, variable, and

undoubtedly smaller than that in the vapour phase case. Whether film resonance will then occur at all is an open question. Until recently, there has been only one report of film resonance in a liquid environment, involving the temperature dependant swelling of a polymer brush [65].

2.7 POLYMER VISCOELASTICITY

2.7.1 Stress and strain

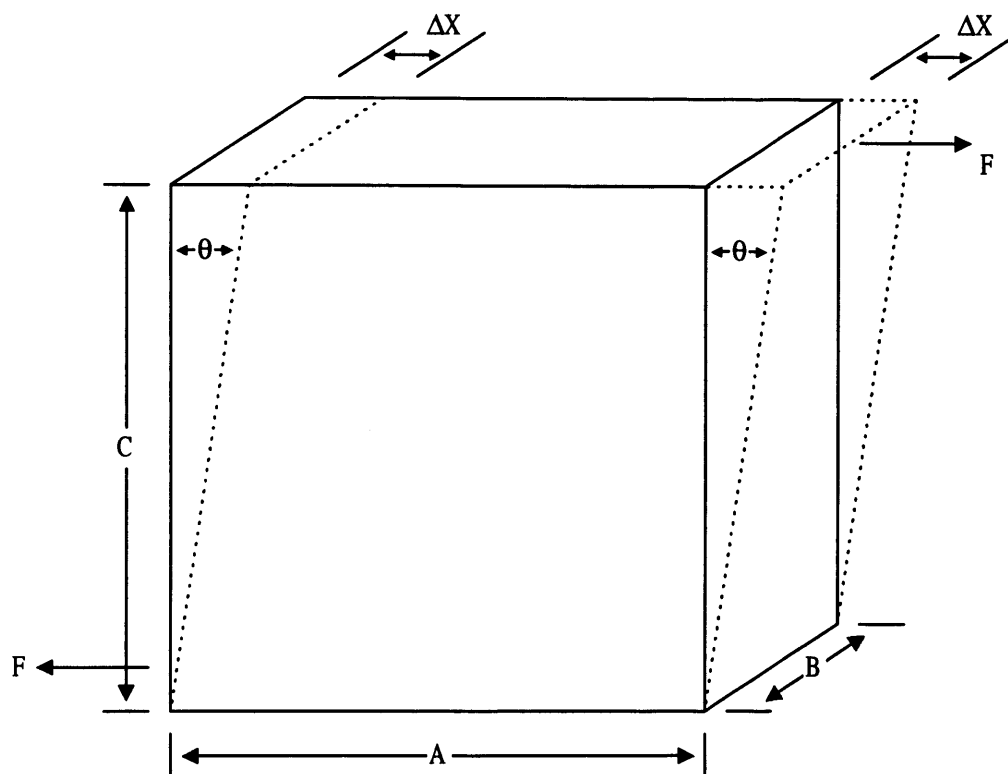


Figure 2.21: Shear in a three dimensional body.

Newtonian mechanics describe the relationship between force acting upon a rigid body and the acceleration that that body undergoes. However, no consideration is given to the internal structure or forces within the body. A body which is in equilibrium may be acted upon by many forces as long as the vector sum of forces is zero, in this case the body is said to be stressed. If the requirement for the body to be rigid is removed, deformation may occur, and the body is termed as being strained [32, 54, 66, 67].

Due to the fact that stress and strain are necessarily coupled phenomena, the magnitude of stress is defined as the force per unit area over which the force acts. The nature of the deformation also depends upon the orientation of the area with respect to the applied stress. A shear stress is defined as that which tends to cut, whilst compressive

stresses tends to push particles together and tensile stresses tends to pull them apart or dilate. There are therefore two basic types of deformation: these are simple shear, shown in Figure 2.21, which yields a change in shape but no change in volume, and bulk compression (or its opposite, dilation) which yields a change in volume with no change in shape. The molecular rearrangements that must occur to accommodate simple shear and compression (or dilation) are different in each case. Physical measurement of the two phenomena should therefore yield different information about the molecular motions and interactions of the material.

The relationship between shear stress and strain is a fundamental material property and is often used as a means of characterisation. Deformations that are reversible upon removal of the perturbing stress are known as elastic deformations. Elastic deformations occur with a linear relationship between stress, T , and strain, S :

$$T \propto S \quad (2.49)$$

Deformations that are irreversible upon removal of the perturbing stress are known as viscous deformations. Viscosity is a measure of the flow resistance of a substance. Viscous deformations occur with a linear relationship between stress and the rate of strain:

$$T \propto \partial S / \partial T \quad (2.50)$$

Materials that are rigid usually exhibit elastic behaviour. Soft materials and liquids are usually viscous. Amorphous polymers, like liquids, have no regular internal structure. However, unlike liquids, the chain structure of polymers gives rise to molecules of large size and molecular weight, which inhibits their flow and exhibits a deformation response that is a combination of both viscous and elastic behaviour. The term that has been given to such behaviour is *viscoelasticity*. The way in which an amorphous polymer behaves in response to the force of an applied stress is dependant upon a number of variables including temperature, pressure, time frame (i.e., frequency) and nature (i.e., shear vs. compressive) of the stress. Due to the nature of the crystal impedance technique used to study polymers in this thesis, the focus herein lies upon the relationships between *shear* stress and strain. Following Figure 2.21, shear stress is defined as the applied force per unit area:

$$\sigma_s = \frac{F}{AB} \quad (2.51)$$

where σ_s is the shear stress, F is the applied force and A and B define the area over which the force is acting as shown in Figure 2.21. Similarly, shear strain is given by:

$$\gamma_s = \frac{\Delta X}{C} = \tan \theta \quad (2.52)$$

where γ_s is defined as the shear strain, ΔX and C are defined in Figure 2.21, related to θ by simple trigonometry.

Viscoelastic properties of materials are described by a complex modulus. The shear modulus, G , is represented by:

$$G = \frac{\sigma_s}{\gamma_s} = \frac{1}{J} \quad (2.53)$$

where J is the shear compliance.

2.7.2 The glass-transition

When a soft, rubbery, amorphous polymer is cooled, a point known as the *glass-transition temperature*, T_g , can be reached where non-crosslinked polymeric materials undergo marked changes in properties associated with local molecular motion. Energy is required for motion of polymer chain segments to occur with respect to one another. The energy demand for this type of motion is usually met by the thermal energy of the system. However, if the temperature is low enough, sufficient thermal energy may not be available for local segmental motion to occur.

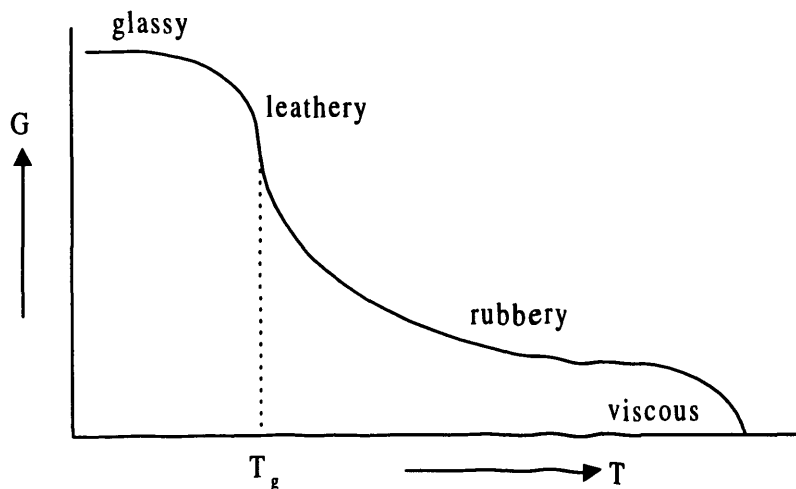


Figure 2.22: Shear modulus as a function of temperature for an amorphous non-crosslinked polymer.

At temperatures below the glass-transition temperature amorphous polymers have many of the properties associated with ordinary inorganic glasses, including hardness, stiffness, brittleness, and transparency. Large-scale molecular motion cannot occur.

Instead chain segments move against the local restraints of secondary bond forces, in a similar way to atoms vibrating in a crystal lattice, the major difference being that amorphous, glassy polymers lack the regularity of a crystalline state. As the temperature is increased, the glass transition is marked by the onset of liquid like motion of larger molecular segments and rotation around the bonds of the polymer backbone. This type of motion is characteristic of the rubbery state in general. More free volume is required for this liquid-like motion of the rubbery state than for motion of the glassy state, hence detection of a higher volume expansion coefficient in the glass transition region is a convenient and common method for determining the glass transition temperature.

Other physical properties of the polymer can be used to determine the glass transition including refractive index and internal friction. In Figure 2.22 it is shown that polymer shear modulus, an important material characteristic of primary interest in this work, can also be used. The glass transition can sometimes occur over a large temperature range of several degrees. This range can be increased by several factors, including heterogeneities in the polymer, presence of plasticiser such as solvent, or a distribution of molecular weights.

2.7.3 Time-temperature equivalence

A rise in temperature increases the molecular and segmental motion of polymers, allowing the system to approach equilibrium more quickly, following a mechanical perturbation. This is conveniently expressed by:

$$a_T = \frac{\tau(T)}{\tau_0(T_0)} \quad (2.54)$$

where a_T is the ratio of the relaxation time, τ , of a particular response at temperature, T , to its value, τ_0 , at a suitably chosen reference temperature, T_0 . For most amorphous polymers the shift factor, a_T , does not vary with τ , so that changes in temperature only shift the distribution of relaxation times but do not otherwise alter it.

When the reference temperature chosen is the glass transition temperature of the material, general expressions for the dependence of a_T on temperature have been derived. One of the most successful of these is the Williams-Landel-Ferry (WLF) equation [68]:

$$\log a_T = \frac{-17.44(T - T_g)}{51.6 + T + T_g} \quad (2.55)$$

Equation 2.54 can be used over a temperature range of T_g to $(T_g + 100)$ K.

2.7.4 Dynamic experiments

The time delay of the mechanical properties of amorphous polymers adds additional complications to the characterisation of their material properties. If a simple harmonic stress is applied to a viscoelastic material, strain lags behind applied stress by a phase angle whose tangent measures the internal friction responsible for energy loss within the sample. Strain that is in phase with the applied stress is an indication of the energy storage within the sample.

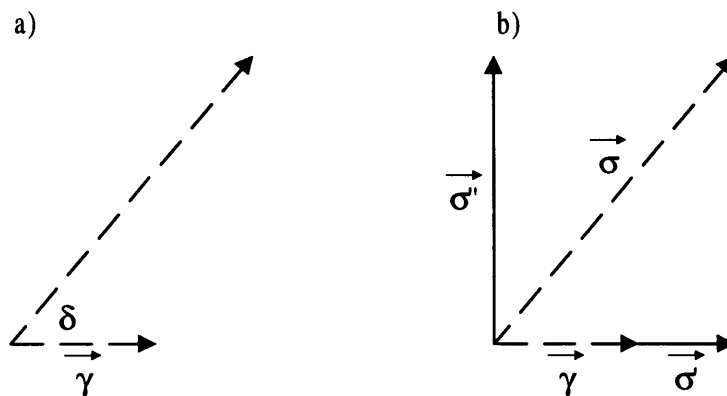


Figure 2.23: a) Orientation of stress and strain vectors in a dynamic experiment. b) Stress decomposed.

A convenient way of visualising the relationship between shear strain and stress during a dynamic experiment is with rotating vectors, see Figure 2.23, part a). The magnitude of the stress vector, σ , represents the maximum of the stress applied to the sample. It rotates anti-clockwise in the figure with an angular frequency, ω . The maximum strain is represented by the vector, γ , and as mentioned previously, the strain lags behind the stress by some amount denoted as the loss angle, δ . The actual sinusoidal stress and strain experienced by the sample is represented by the projection of those rotating vectors onto a suitable axis such as the y axis. Figure 2.23, part b) displays how the component of the stress which is in phase with the strain, σ' , can be shown by projecting σ onto γ . Projection of σ on the axis perpendicular to γ yields the component of the stress that is 90° out of phase with the stress, σ'' . The in-phase and out-of-phase shear moduli are given by:

$$G' = \frac{\sigma'}{\gamma} \quad (2.56)$$

$$G'' = \frac{\sigma''}{\gamma} \quad (2.57)$$

The nomenclature of complex numbers is used as a simple method to represent orthogonal vectors: G'' is made the imaginary part and G' the real part. The complex shear modulus is given by:

$$G = G' + jG'' \quad (2.58)$$

G' , also termed the storage modulus, is a measure of the energy stored and recovered per cycle of sinusoidal shear stress and G'' , also termed the loss modulus, is a measure of energy dissipated or lost as heat due to internal friction per stress cycle. Figure 2.24 shows how these material characteristics vary with perturbation frequency and characteristic polymer relaxation time. Thus, the measured modulus value is dependent on both the temperature of the sample and the frequency of the perturbation. At high frequencies (or low temperatures), the time period for which stress is applied, T_s , is much shorter than the relaxation time ($T_s \ll \tau$). The polymer chains do not have time to move with respect to one another and the polymer behaves elastically. If the frequency is decreased (or the temperature increased) until $T_s \gg \tau$, non-crosslinked polymer chains have time to move with respect to each other and the sample behaves viscously. When $T_s \approx \tau$ the polymer behaves viscoelastically and the polymer is close to its glass transition temperature.

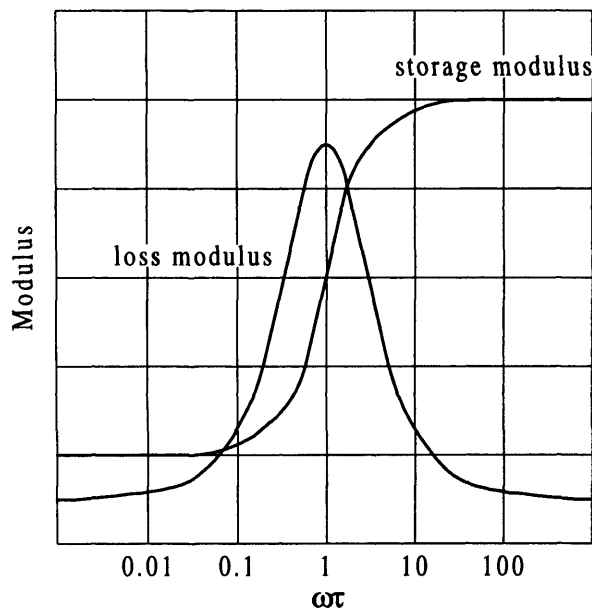


Figure 2.24: Variation of loss and storage moduli with the product of frequency and relaxation time.

The glass transition is a second order transition (as opposed to a first order transition such as melting), associated with polymer relaxation processes. Therefore, the temperature at which the glass transition is observed is also highly frequency dependent, often occurring at temperatures several tens of degrees higher than glass transition temperatures measured statically. Under dynamic conditions, the glass transition temperature is termed the *dynamic* glass transition temperature, T_{α} , occurring when $\omega\tau = 1$, as shown in Figure 2.24.

2.7.5 Models of viscoelastic behaviour

Viscoelastic behaviour can be modelled with combinations of ideal elastic and viscous elements. The ideal elastic element is a spring which obeys Hooke's law, shown in Figure 2.25a, where the stress is proportional to the strain as described by Equation 2.49. The elastic deformation is instantaneous and independent of time.

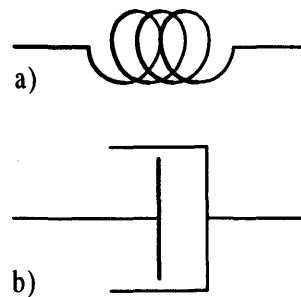


Figure 2.25: a) A spring - mechanical analogue that represents an ideal elastic element.

b) A dashpot - mechanical analogue that represents an ideal viscous element.

The ideal viscous element, representative of a Newtonian liquid, is a dashpot, shown in Figure 2.25b. The dashpot has a constant viscosity, which gives rise to a deformation linear with time, while the stress is applied. Upon removal of the applied stress, the deformation due to a dashpot is unrecoverable, since the input energy is lost as heat. Stress is proportional to the rate of strain as described in Equation 2.50.

Spring and dashpot elements can be combined in two ways. When they are connected in series, the resulting element is known as the Maxwell element. The Maxwell element responds both viscously and elastically to an applied stress. Upon application of stress the spring elongates instantaneously and the dashpot slowly yields. When the stress is removed, the spring recovers but the dashpot does not.

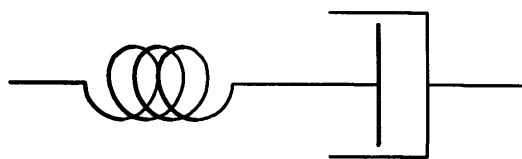


Figure 2.26: A Maxwell element.

Parallel combination of the spring and dashpot elements gives rise to the Voigt element, Figure 2.26. The Voigt element exhibits retarded elastic or viscoelastic behaviour upon application of a stress as the dashpot acts as a damping resistance to the establishment of equilibrium of the spring.

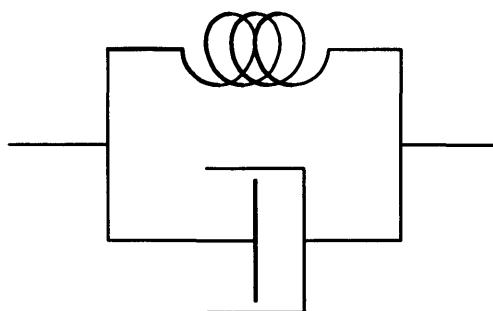


Figure 2.27: A Voigt element.

The Voigt model, Figure 2.27, is more representative of the viscoelastic response of a tangled mass of polymer chains than the Maxwell element. However, often polymer behaviour is most accurately modelled using combinations of both elements, with a distribution of relaxation times.

2.8 REFERENCES

1. P. Curie and R. Curie, C.R. Acad. Sci. 91:294 (1880).
2. C. Lu and A. W. Czanderna (Eds), Application of Piezoelectric Quartz Crystal Microbalances, Elsevier, Amsterdam, (1984).
3. M. R. Deakin and D. A. Buttry, Anal. Chem. 61:A1147 et seq. (1989).
4. J. W. L. R. Strutt, The Theory of Sound, Dover, New York, (1945).
5. G. Z. Sauerbrey, Z. Phys. 155:206 (1959).
6. D. A. Buttry and M. D. Ward, Chem. Rev. 92:1355 (1992).
7. R. Schumacher, Angew. Chem. Int. Ed. Engl. 29:329 (1990).
8. N. Oyama and T. Ohsaka, Prog. Poly. Sci. 20:761 (1995).
9. T. Nomura and A. Minemura, Nippon Kagaku Kaishi:1261 (1980).

10. S. Bruckenstein and M. Shay, *Electrochim. Acta* **30**:1295 (1985).
11. K. K. Kanazawa and J. G. Gordon, *Anal. Chim. Acta* **175**:99 (1985).
12. K. K. Kanazawa and J. G. Gordon, *Anal. Chem.* **57**:1770 (1985).
13. D. Z. Shen, L. H. Nie, and S. Z. Yao, *J. Electroanal. Chem.* **367**:31 (1994).
14. D. Z. Shen, L. H. Nie, and S. Z. Yao, *J. Electroanal. Chem.* **360**:71 (1993).
15. Z. H. Mo, L. H. Nie, and S. Z. Yao, *J. Electroanal. Chem.* **316**:79 (1991).
16. S. Bruckenstein and A. R. Hillman, *J. Phys. Chem.* **92**:4837 (1988).
17. S. Bruckenstein, P. Krtil, and A. R. Hillman, *J. Phys. Chem. B* **102**:4994 (1998).
18. A. R. Hillman, D. C. Loveday, and S. Bruckenstein, *J. Electroanal. Chem.* **274**:157 (1989).
19. A. R. Hillman, N. A. Hughes, and S. Bruckenstein, *Analyst* **119**:167 (1994).
20. M. J. Henderson, A. R. Hillman, E. Vieil, and C. Lopez, *J. Electroanal. Chem.* **458**:241 (1998).
21. M. Skompska and A. R. Hillman, *J. Electroanal. Chem.* **433**:127 (1997).
22. M. Skompska and A. R. Hillman, *Far. Trans.* **92**:4101 (1996).
23. Y. B. Mo, E. Hwang, and D. A. Scherson, *J. Electrochem. Soc.* **143**:37 (1996).
24. A. R. Hillman, M. J. Swann, and S. Bruckenstein, *J. Phys. Chem.* **95**:3271 (1991).
25. A. R. Hillman, D. C. Loveday, and S. Bruckenstein, *J. Electroanal. Chem.* **300**:67 (1991).
26. A. R. Hillman, D. C. Loveday, M. J. Swann, S. Bruckenstein, and C. P. Wilde, *Far. Trans.* **87**:2047 (1991).
27. A. R. Hillman, N. A. Hughes, and S. Bruckenstein, *J. Electrochem. Soc.* **139**:74 (1992).
28. A. R. Hillman, D. C. Loveday, M. J. Swann, S. Bruckenstein, and C. P. Wilde, *Analyst* **117**:1251 (1992).
29. A. R. Hillman and S. Bruckenstein, *Far. Trans.* **89**:3779 (1993).
30. A. R. Hillman and S. Bruckenstein, *Far. Trans.* **89**:339 (1993).
31. M. J. Henderson, A. R. Hillman, and E. Vieil, *J. Electroanal. Chem.* **454**:1 (1998).
32. D. S. Ballantine, R. M. White, S. J. Martin, A. J. Ricco, E. T. Zellers, G. C. Frye, and H. Wohltjen, *Acoustic Wave Sensors*, Academic Press, New York, (1997).
33. J. G. Miller and D. I. Bolef, *J. Appl. Phys.* **39**:4589 (1968).
34. C. S. Lu and O. Lewis, *J. Appl. Phys.* **43**:4385 (1972).
35. R. Schumacher, G. Borges, and K. K. Kanazawa, *Surf. Sci.* **163**:L621 (1985).

36. A. Muller, M. Wicker, R. Schumacher, and R. N. Schindler, *Ber. Bunsenges. Phys. Chem.* 92:1395 (1988).
37. W. Stockel and R. Schumacher, *Ber. Bunsenges. Phys. Chem.* 91:345 (1987).
38. C. Zhang, S. Schranz, R. Lucklum, and P. Hauptmann, *IEEE Trans. Ultrason. Ferro. Freq. Cont.* 45:1204 (1998).
39. K. E. Heusler, A. Grzegorzewski, L. Jäckel, and J. Pietrucha, *Ber. Bunsenges. Phys. Chem.* 92:1218 (1988).
40. E. P. EerNisse, *J. Appl. Phys.* 43:1330 (1972).
41. E. P. EerNisse, *J. Appl. Phys.* 44:4482 (1973).
42. L. V. Rajakovic, B. A. Cavicvlasak, V. Ghaemmaghami, K. M. R. Kallury, A. L. Kipling, and M. Thompson, *Anal. Chem.* 63:615 (1991).
43. A. L. Kipling and M. Thompson, *Anal. Chem.* 62:1514 (1990).
44. M. Thompson, C. L. Arthur, and G. K. Dhaliwal, *Anal. Chem.* 58:1206 (1986).
45. M. Thompson, G. K. Dhaliwal, C. L. Arthur, and G. S. Calabrese, *IEEE Trans. Ultrason. Ferro. Freq. Cont.* 34:127 (1987).
46. S. J. Martin, G. C. Frye, A. J. Ricco, and S. D. Senturia, *Anal. Chem.* 65:2910 (1993).
47. B. A. Martin and H. E. Hager, *J. Appl. Phys.* 65:2630 (1989).
48. M. D. Ward and E. J. Delawski, *Anal. Chem.* 63:886 (1991).
49. C. Gabrielli, M. Keddani, and R. Torresi, *J. Electrochem. Soc.* 138:2657 (1991).
50. S. J. Martin, V. E. Granstaff, and G. C. Frye, *Anal. Chem.* 63:2272 (1991).
51. C. E. Reed, K. K. Kanazawa, and J. H. Kaufman, *J. Appl. Phys.* 68:1993 (1990).
52. V. E. Granstaff and S. J. Martin, *J. Appl. Phys.* 75:1319 (1994).
53. W. G. Cady, *Piezoelectricity*, McGraw-Hill, New York, (1946).
54. J. F. Rosenbaum, *Bulk Acoustic Wave Theory and Devices*, Artech House, Boston, (1988).
55. R. W. Cernosek, S. J. Martin, A. R. Hillman, and H. L. Bandey, *IEEE Trans. Ultrason. Ferro. Freq. Cont.* 45:1399 (1998).
56. S. J. Martin and G. C. Frye, , *IEEE*, New York, 1991, p. 393.
57. H. Muramatsu, E. Tamiya, and I. Karube, *Anal. Chem.* 60:2142 (1988).
58. D. Z. Shen, M. S. Huang, L. H. Nie, and S. Z. Yao, *J. Electroanal. Chem.* 371:117 (1994).
59. T. A. Zhou, L. H. Nie, and S. Z. Yao, *J. Electroanal. Chem.* 293:1 (1990).
60. F. M. White, *Viscous Fluid Flow*, McGraw-Hill, New York, (1974).

61. H. L. Bandey, A. R. Hillman, M. J. Brown, and S. J. Martin, *Far. Disc.* 107:105 (1997).
62. D. S. Ballantine, *Anal. Chem.* 64:3069 (1992).
63. D. Johannsmann, J. Gruner, J. Wesser, K. Mathauer, G. Wegner, and W. Knoll, *Thin Solid Films* 210:662 (1992).
64. A. Domack and D. Johannsmann, *J. Appl. Phys.* 80:2599 (1996).
65. A. Domack, O. Prucker, J. Ruhe, and D. Johannsmann, *Phys. Rev. E* 56:680 (1997).
66. J. J. Aklonis and W. J. MacKnight, Introduction to Polymer Viscoelasticity, Wiley-Interscience, New York, (1983).
67. F. W. Billmeyer, Textbook of Polymer Science, Wiley, New York, (1984).
68. M. L. Williams, F. R. Landel, and J. D. Ferry, *J. Am. Chem. Soc.* 77:3701 (1955).

CHAPTER 3

EXPERIMENTAL

3.1 INTRODUCTION

This chapter describes the electrochemical and crystal impedance instrumentation and the methodologies employed to record and interpret *in situ* crystal impedance spectra of the surface immobilised electroactive polymer films studied in this thesis.

3.2 QUARTZ THICKNESS SHEAR MODE (TSM) RESONATOR PREPARATION

Minimisation of surface roughness effects, discussed in Sections 2.2.3 and 2.5, required the use of polished crystals [1]. Bare, AT-cut, quartz wafers with a $<1 \mu\text{m}$ alumina abrasive finish were purchased from International Crystal Manufacturing (ICM) Co., Oklahoma City, USA. These disc shaped crystals have a diameter of 14 mm and are approximately 0.2 mm thick. Their fundamental oscillating frequency, in the thickness shear mode, is 10 MHz. The polished quartz surfaces were pre-treated with a (3-mercaptopropyl)trimethoxysilane underlayer, necessary to provide a good adhesion between the gold electrodes and the smooth quartz substrate. The crystals were cleaned by soaking them in an aqua regia bath for thirty minutes, following this they were rinsed with water. The underlayer was applied by immersing the crystals in a refluxing solution containing 1:1:50 (3-mercaptopropyl)trimethoxysilane: water: propan-2-ol, for 15 minutes. The crystals were rinsed with propan-2-ol and then the (3-mercaptopropyl)trimethoxysilane layer was cured in an oven maintained at 108°C (ensuring that the temperature did not exceed 115°C). Gold electrodes were evaporated onto the crystals through a keyhole shaped mask. Piezoelectric and electroactive areas are 0.21 cm^2 and 0.23 cm^2 respectively.

3.3 ELECTROCHEMICAL INSTRUMENTATION

Electrochemical experiments were carried out in a standard 3-electrode cell (see Figure 3.1). The working electrode was one of the gold electrodes on the surface of the quartz crystal. This is exposed to electrolyte solution by gluing the crystal across an aperture at the base of the electrochemical cell. Dow-Corning 3145 RTV non-corrosive adhesive/sealant was used to glue the crystals to the cell bases. The counter electrode was planar platinum gauze, with a surface area much larger than the surface area of the working electrode. The cell was designed such that the counter electrode could be arranged parallel

to the base of the cell, to present a uniform electric field to the working electrode, enabling a uniform polymer film to be grown at the surface. The reference electrode used was a silver/silver ion $\text{Ag}/0.1 \text{ mol dm}^{-3} \text{ AgNO}_3$ double junction reference electrode [2].

Due to the water sensitivity of electro-generated 3-hexylthiophene radicals, moisture was excluded from the cell. Solutions were degassed with argon prior to the experiment to displace dissolved oxygen. During an experiment the cell was kept under positive pressure of argon by passing a stream of the gas over the surface of the electrolyte solution and allowing it to escape through a bubbler.

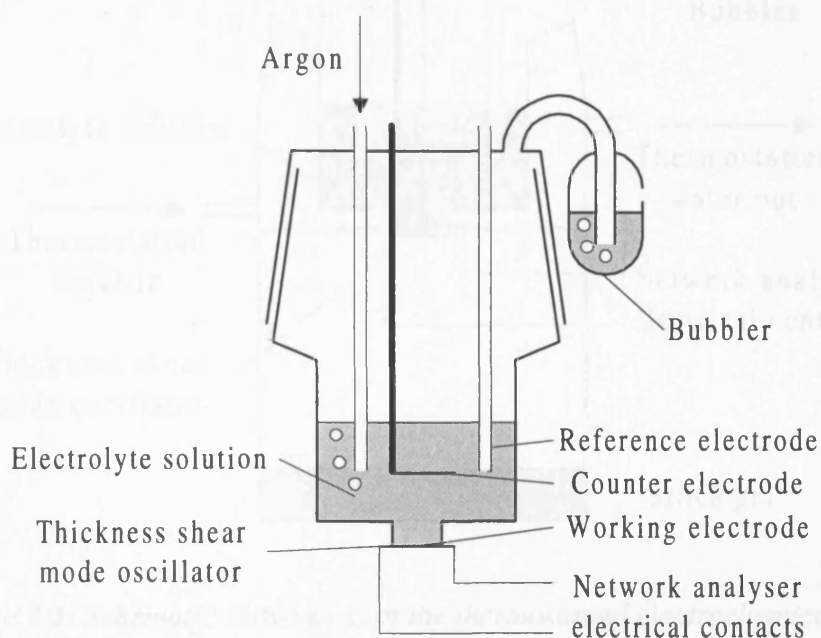


Figure 3.1: Schematic illustration of the electrochemical cell.

Electrochemical measurements were made using an Autostat™ potentiostat and Miniscan™ potential sweep generator (Thompson Electrochem Ltd.). Current transients and cyclic voltammograms were recorded on a series 60000™ X-Y chart recorder (Advance Byran). Measurements were made at room temperature ($20 \pm 2^\circ\text{C}$) or maintained at a preset temperature using a thermostatted cell where stated.

3.3.1 Temperature control

The thermostatted electrochemical cell was maintained at the desired temperature using a water jacket (see Figure 3.2), through which water (containing anti-freeze) of controlled temperature was pumped using a Techne Tempunit™ (TU-16D). Temperatures lower than room temperature were accessible using a Techne refrigerated bath (RB-5). Silica gel was placed in the sealed compartment indicated in Figure 3.2 to avoid condensation of water

onto the underside of the TSM resonator. The temperature at the crystal surface was confirmed using a Eirelec (MT 100 KC) thermometer.

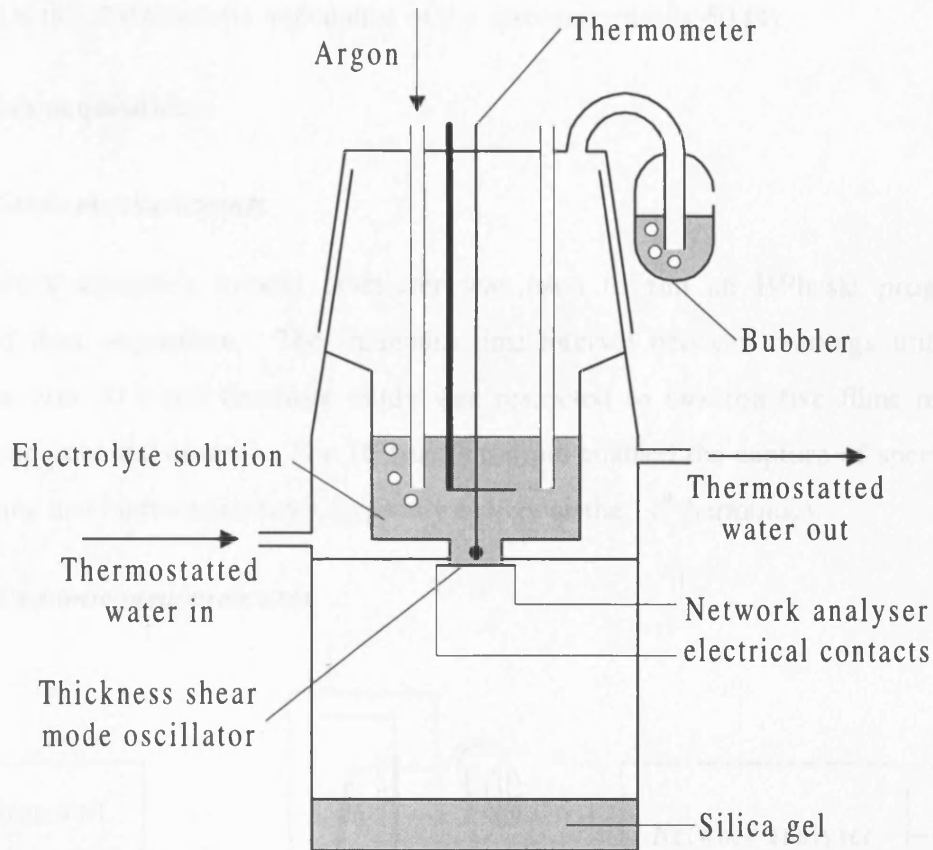


Figure 3.2: Schematic illustration of the thermostatted electrochemical cell.

3.4 CRYSTAL IMPEDANCE MEASUREMENT

3.4.1 Instrumentation

A Hewlett Packard HP8751A network analyser operating in reflectance mode, utilising a HP8512A transmission/reflection test unit, was employed to measure crystal impedance spectra [1, 3, 4]. The test unit was connected to the TSM resonator using a 50 Ω coaxial cable. The network analyser was used to apply an alternating potential of controlled amplitude across the electrodes of the TSM resonator. This could be achieved at a range of frequencies in the vicinity of crystal resonance. The reflected signal was measured and recorded. The frequency dependent ratio of the reflected to incident signal is denoted as the 'scattering parameter', S_{11} . S_{11} is a complex quantity containing magnitude ratio and phase relation information between the incident and reflected signals. The input impedance is found from S_{11} using:

$$Z_s(f) = Z_0 \left(\frac{1 + S_{11}(f)}{1 - S_{11}(f)} \right) \quad (3.1)$$

where Z_0 is the characteristic impedance of the system (typically 50Ω).

3.4.2 Data acquisition

3.4.2.1 Static measurements

The network analyser's in-built computer was used to run an HPbasic program that controlled data acquisition. The minimum time interval between readings utilising this procedure was 30 s and therefore study was restricted to electroactive films maintained under static potential control. The HPbasic program enabled the capture of spectra at the fundamental and higher harmonics (typically as high as the 11th harmonic).

3.4.2.2 Dynamic measurements

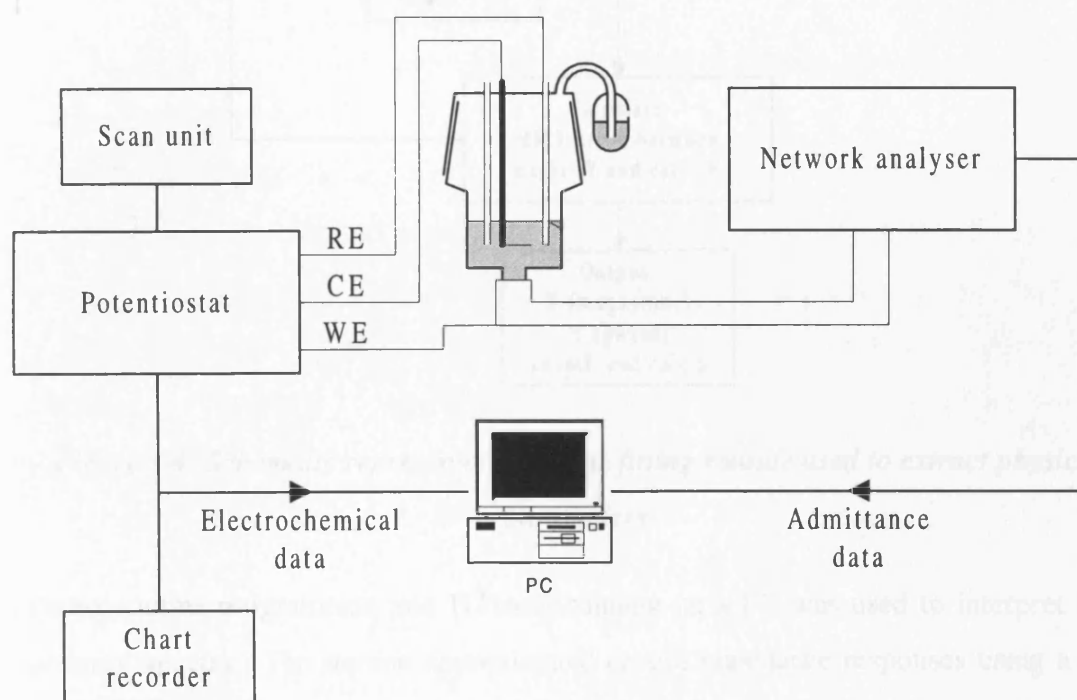


Figure 3.3: Experimental instrumentation.

In order to capture spectra with greater temporal resolution, network analyser data acquisition was controlled using an IBM compatible personal computer (PC), running HP VEE, which was linked to the analyser using a HP-IB interface card (HP 82341C) and cable (HP 10833C) (see Figure 3.3). This program was capable of recording fundamental

resonance spectra (as well as electrochemical data) every 1 s, which permitted the investigation of electroactive films under dynamic potential control.

3.5 CRYSTAL IMPEDANCE INTERPRETATION

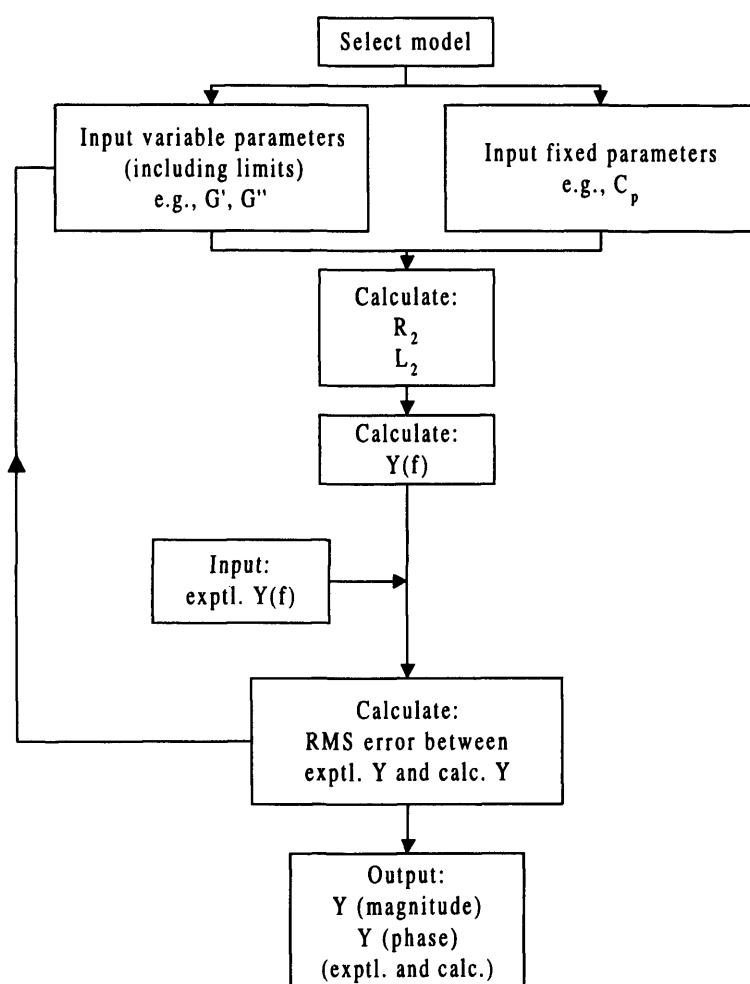


Figure 3.4: Schematic representation of the fitting routine used to extract physical parameters.

A fitting routine programmed into HTbasic running on a PC was used to interpret crystal impedance spectra. The routine approximated crystal impedance responses using a model selected from those summarised in Table 2.1, representative of the system under investigation. A schematic representation of the iterative process is shown in Figure 3.4. After selection of the appropriate model initial parameters within that model are chosen to 'seed' the data fit, these parameters can be maintained constant or allowed to vary. If they are varied, upper and lower limits can be selected. From the initial input variables a theoretical impedance response is calculated using the selected model. The theoretical response is compared to the experimental data. The difference between the two is then

determined in terms of a root mean square (RMS) error. The fitting routine then varies the selected parameters until a data fit with smaller RMS error is calculated. This process continues until the error between the theoretical and experimental responses is small as compared to a pre-set target and the impedance plots appear almost identical. At this point the variable parameters are determined to an appropriate level of precision.

3.5.1 Extraction of electrical parameters

Extraction of equivalent circuit electrical parameters allows us to compare different surface perturbations of the TSM resonator. The electrical parameters of the quartz resonator are determined from the crystal impedance response of the mounted but uncoated device exposed to air. These parameters are then held constant when attempting to fit the electrical response of the perturbed device. This allows extraction of all the circuit elements except Z_e , as described by:

$$Z_m = R_1 + j\omega L_1 + \frac{1}{j\omega C_1} + Z_e \quad (3.2)$$

where Z_e is the additional impedance arising from a surface perturbation defined in Equations 2.19 and 2.22.

The electrical resistance and inductance of the TSM resonator exposed to a surface perturbation are described by Equations 2.23 and 2.24. A change in ωL_2 is inversely proportional to a frequency shift and R_2 is proportional to the maximum impedance.

TSM resonators can be exposed to a combination of physical perturbations. In these cases it is desirable to distinguish between electrical impedances arising from each physical component. Figure 3.5 highlights two examples of particular interest in the electrochemical context. Figure 3.5a shows the modified Butterworth-Van Dyke model, proposed by Martin *et al* [5], which approximates the electrical response of a TSM resonator coated with a rigid mass layer, immersed in a liquid. The electrical parameters, R_L and L_L , arising from the presence of liquid can be extracted by comparing the responses of the uncoated crystal in air and exposed to liquid. The resonator can then be coated with a rigid mass layer, such as a gold film, and immersed in the liquid, the additional response is now due only to the rigid gold film and hence L_S can be extracted.

Figure 3.5b shows the Modified Butterworth-Van Dyke model for a non-rigid film exposed to a liquid, such as a polymer film exposed to an electrolyte solution. The liquid parameters can be extracted as described above. However, since the polymer film is non-

rigid, an additional resistance, representative of energy losses within the film, is necessary in the model.

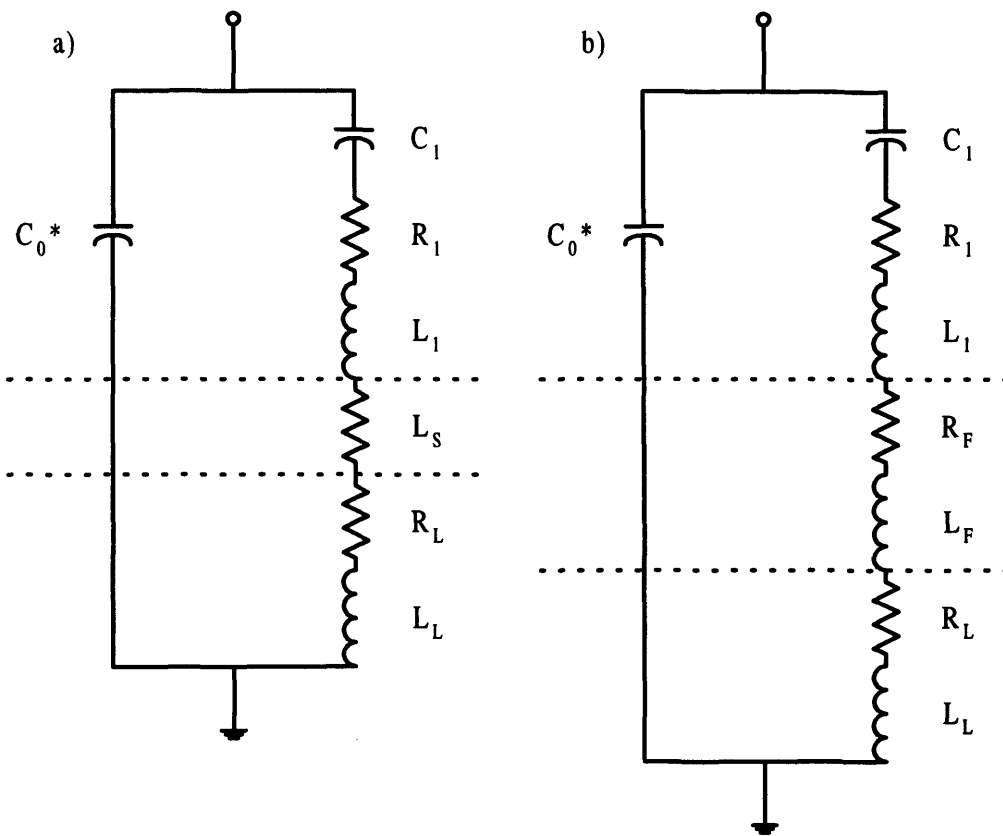


Figure 3.5: Modified Butterworth-Van Dyke equivalent circuit for a TSM resonator with surface perturbations; a) a rigid mass layer and contacting liquid b) a non-rigid mass layer and contacting liquid.

The model in Figure 3.5b is accurate only when the resistive losses within the film are small, i.e., when the film is either thin or rigid. This is due to the fact that the energy that is available to be dissipated by the liquid is dependent on how much is lost in the film. When the contacting film is thick and non-rigid, energy available for the liquid to dissipate may be much less than for the uncoated TSM resonator exposed to liquid. In this case the values of R_L and L_L will be smaller than expected.

$$R_2 = R_L + R_F \quad (3.3)$$

$$L_2 = L_L + L_F \quad (3.4)$$

Equations 3.3 and 3.4 indicate that the electrical elements of the modified Butterworth-Van Dyke equivalent circuit are additive, where R_L and L_L are electrical

resistance and inductance arising from the contacting liquid and R_F and L_F are electrical resistance and inductance arising from the overlayer.

3.5.2 Extraction of physical parameters

Physical parameters are extracted from crystal impedance spectra using the models described in Section 2.5. The variable physical parameters for each model are listed in Table 2.1. It has been found that electroactive polymer films exposed to electrolyte solution can be accurately approximated using a three component model [1], denoted as model 6 in Table 2.1. A similar modelling technique was employed in this study. Crystal parameters were attained from the response of the uncoated crystal in air. A measure of the ideal mass layer thickness, h_q , and contacting electrolyte density viscosity product, $\rho_l \eta_l$, was accomplished by comparing the responses for the bare crystal in air and exposed to electrolyte using model 5 in Table 2.1. Newtonian liquids yield crystal responses with equal real and imaginary components. In contrast, ideal mass layers yield responses with only real components. The difference between the real and imaginary components of the crystal response of a crystal immersed in a Newtonian liquid can therefore be ascribed solely to the entrapped, rigidly coupled, material within the surface features of the crystal surface. Finally, film parameters were determined via measurements on the polymer-coated crystal in electrolyte. Thus, an excessive number of parameters are never fitted on the basis of a single data set.

3.5.2.1 Uniqueness of data fit

In the case of simple models, such as for the model describing the surface perturbation of an ideal mass layer, a unique data fit is obtained because there is one equation and one variable. For more complicated models, such as for a polymer film exposed to electrolyte solution, additional information is required.

3.5.2.1.1 Chemical knowledge

Knowledge of the chemical and/or physical properties of the system can be helpful to reduce the number of unknown physical parameters and to disregard data fits which yield unfeasible parameters. For example, the thickness of a polymer film attached to the electrode surface may be estimated using the procedure described in Section 3.6.2. Also estimations of the polymer film density can be made when the density of the monomer, bathing solvent and electrolyte are known (see Chapter 5).

3.5.2.1.2 Harmonics

An important feature of the use of higher harmonics is that the number of measured parameters increases faster than the number of fitted parameters. Specifically, although the shear modulus components of polymer overlayers may be frequency dependent, film thickness and density must be frequency independent. This allows the choice of either holding these latter two parameters constant (thereby decreasing the number of fitted parameters) or of allowing them to ‘float’ in measurements at different frequencies (thereby using their constancy (or otherwise) as a measure of uniqueness of fit).

3.6 POLY(3-HEXYLTHIOPHENE) DEPOSITION STUDIES

3.6.1 Film preparation

PHT films were deposited via potentiodynamic electrochemical polymerisation of 3-hexylthiophene onto the exposed Au electrode of 10 MHz AT-cut quartz crystals. Potential limits were 0.0 - 1.5 V for the first cycle and 0.0 - 1.2 V thereafter. The scan rate used was 20 mV s⁻¹. The deposition solution contained 3.7 mmol dm⁻³ HT (Aldrich, used as supplied) and 0.1 mol dm⁻³ tetraethylammonium hexafluorophosphate (Aldrich, >99%) in propylene carbonate. The polymer film thickness was controlled by the number of cycles used for deposition.

3.6.2 Estimation of surface coverage

At scan rates of 20 mV s⁻¹ (and lower), the charge passed was independent of potential sweep rate, v . Therefore, at these sweep rates, all of the film was electroactive. PHT surface coverage, $\Gamma/\text{mol cm}^{-2}$, was calculated using the integral of the current response (Q_{red}) passed during the cathodic scan.

3.7 POLY(3-HEXYLTHIOPHENE) OXIDATION STATE STUDIES

PHT films were prepared as described in Section 3.6. When the film had been grown to the desired thickness the Au/PHT electrodes were transferred to background electrolyte solution containing either 0.1 mol dm⁻³ tetraethylammonium hexafluorophosphate in propylene carbonate or 0.1 mol dm⁻³ tetraethylammonium hexafluorophosphate in dichloromethane, as stated.

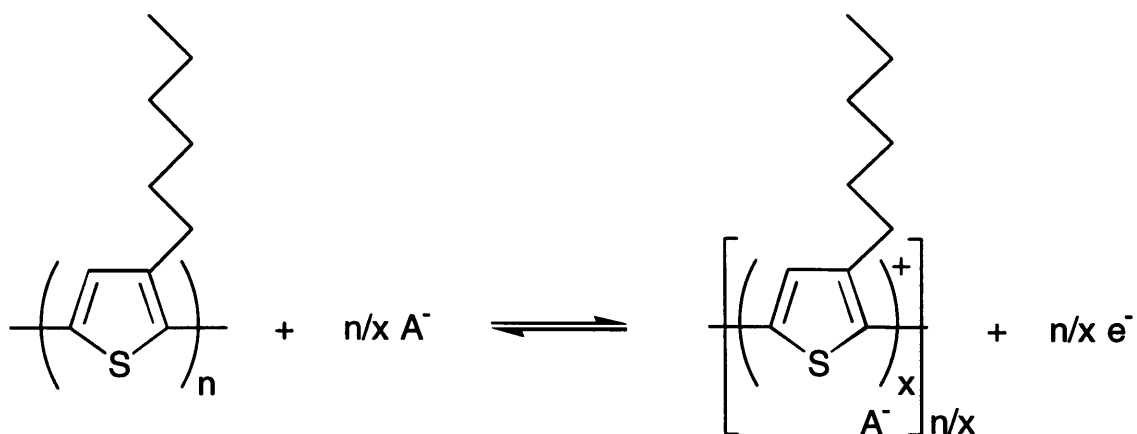


Figure 3.6: PHT redox chemistry.

3.7.1 Static potential control

Crystal impedance measurements were made sequentially at fixed potential at fundamental (10 MHz), third, fifth, seventh, ninth and eleventh harmonics, using the procedure described in Section 3.4.2.1. Static potentials were applied to the film at ascending (0.0, 0.4, 0.5, 0.6, 0.9 V) followed by descending (0.6, 0.4, 0.2, 0.0 V) intervals. The film was held at each potential for 2 mins before crystal impedance measurements were recorded at each harmonic.

3.7.2 Dynamic potential control

Crystal impedance measurements were recorded at the fundamental harmonic using the procedure described in Section 3.4.2.2. Dynamic potentials were applied to the film at known scan rate, v .

3.8 CHEMICALS

Chemical	Supplier	Purity
Propylene carbonate	Aldrich	99.7%, anhydrous
Dichloromethane	Fisons	Reagent grade Distilled over CaH ₂
Tetraethylammonium hexafluorophosphate	Aldrich	99%
3-hexylthiophene	Aldrich	99+%

Table 3.1: List of the chemicals used in this study

3.9 REFERENCES

1. H. L. Bandey, A. R. Hillman, M. J. Brown, and S. J. Martin, *Far. Disc.* **107**:105 (1997).
2. R. Greef, R. Peat, L. M. Peter, D. Pletcher, and J. Robinson, *Instrumental Methods in Electrochemistry*, Ellis Horwood, New York, (1990).
3. A. Glidle, A. R. Hillman, and S. Bruckenstein, *J. Electroanal. Chem.* **318**:411 (1991).
4. A. R. Hillman, M. J. Brown, and S. J. Martin, *J. Am. Chem. Soc.* **120**:12968 (1998).
5. S. J. Martin, V. E. Granstaff, and G. C. Frye, *Anal. Chem.* **63**:2272 (1991).

CHAPTER 4

RESONANCE EFFECTS IN POLY(3-HEXYLTHIOPHENE) FILMS

4.1 INTRODUCTION

This chapter reports the novel observation of mechanical resonance effects in electroactive polymer films. The principal effect, often termed “film resonance”, occurs at a special situation when the acoustic phase shift caused by shear deformation of a thin film corresponds to one quarter of the wavelength of sound in that medium (see Section 2.6.2). The expression *film resonance* has a very different meaning to the term *crystal resonance*. Crystal resonance occurs when the wavelength of the acoustic wave within a *TSM resonator* is twice the thickness of the quartz. Film resonance occurs when the resonant frequencies of the quartz oscillator (crystal resonance) and the contacting film (film resonance) are identical. Under this particular condition there is a dramatic change in the energy transfer between the quartz resonator and the polymer film. Although observed for films that have been immobilised on TSM resonators and exposed to the gas phase, this phenomenon had not been observed previously for the very different case of an electroactive film exposed to a liquid phase electrolyte solution. In the latter case, the situation is not nearly so clear-cut. For film resonance to occur, in electroactive polymer films exposed to liquid electrolyte solution, there must be sufficient reflection magnitude of the propagating acoustic wave at the film/liquid interface (see Section 2.6.2). Since it is known that electrochemically deposited films are often inhomogeneous, with polymer/solution interfaces that are not always clearly defined [1], it is not immediately obvious whether or not immersed electroactive films will exhibit acoustic film resonance effects. The results presented herein provide unequivocal evidence that film resonance effects do occur in electrolyte immersed electroactive polymer films, and that one must consider the possibility of film resonance when analysing viscoelastic films using TSM resonators.

The event of film resonance, occurring at multiple excitation harmonics, is also presented in this chapter. In the succeeding paragraphs it is shown how observation of this event can yield data which may be manipulated such that it provides important indicative information concerning the frequency dependence of the overlaying viscoelastic film's shear modulus. A simple method, used and presented in Section 4.4, utilises the frequency dependence of thickness at which film resonance occurs to this end. It is worth noting that

this technique utilises raw crystal impedance data and does not depend upon the application of complicated modelling procedures. It also provides substantial confirmation of interpretations inferred from the data modelling procedures practised throughout this thesis.

Finally, the new phenomenon of peak splitting is presented, which can occur at film resonance. In this case, the conductance spectrum is highly damped and exhibits two distinct peaks as a consequence of the combination of the resonator and film motional impedances. Peak splitting may only be observed when the conductance spectrum arising from the motional impedance of the crystal is relatively broad compared to that of the film. Novel experimental results presented in this chapter have, in part, prompted the development of new theoretical analysis of crystal impedance spectra; these are discussed in Section 4.4.

4.2 EXPERIMENTAL

PHT films were deposited potentiodynamically using a scan rate, $\nu = 20 \text{ mV s}^{-1}$, and potential limits of 0.0-1.5 V in cycle 1 and 0.0-1.2 V thereafter (as described in Section 3.6). After each polymerisation cycle, the potential was held at 0.0 V to assure that equilibrium was reached. Crystal impedance measurements were then recorded at the fundamental, third, fifth, seventh, ninth and eleventh harmonics. Full characterisation of the uncoated TSM resonator was achieved prior to each experiment using crystal impedance measurements recorded whilst the crystal was exposed to air and background electrolyte solution respectively, according to the procedure described in Section 3.5.

4.3 RESULTS

Figure 4.1 shows sequential cyclic voltammograms resulting from electropolymerisation of 3-hexylthiophene, according to the procedure described in Section 4.2. This procedure results in the deposition of a PHT film onto the exposed gold electrode of a TSM resonator. At scan rates $\nu \leq 20 \text{ mV s}^{-1}$ (for which film redox conversion is complete) the reduction peak charge density can be used to estimate the coverage, Γ , of the deposited film (see Section 3.6).

The dependency of the reduction peak charge density, Q_r , upon the number of deposition cycles is displayed in Figure 4.2. Q_r is linearly dependent upon the number of deposition cycles performed between the limits of 1 to 30 cycles. For films deposited using more than 30 polymerisation cycles the reduction peak charge becomes less dependent upon the cycle number.

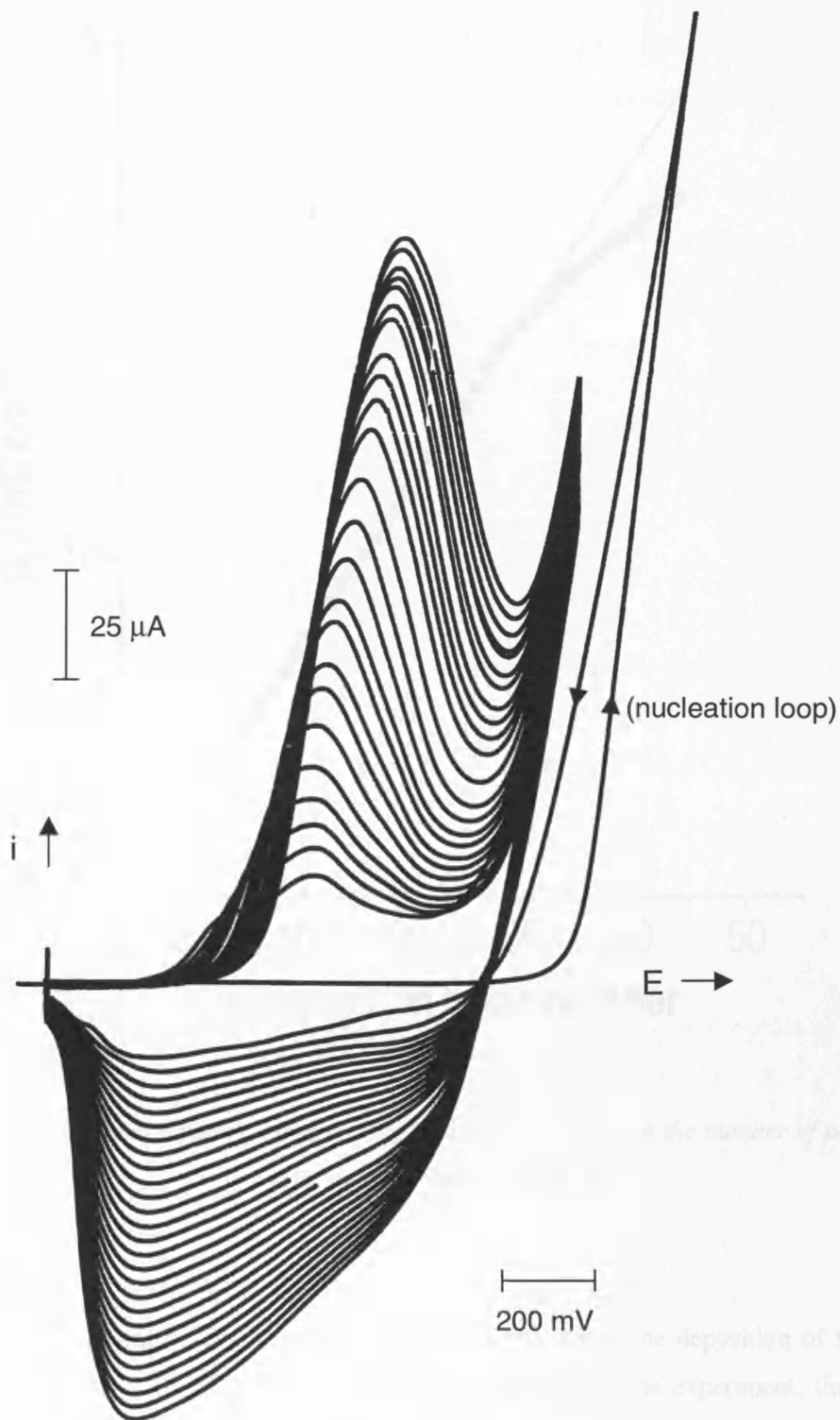


Figure 4.1: Sequential cyclic voltammograms resulting from the deposition of a PHT film, deposited according to the procedure described in Section 4.2.

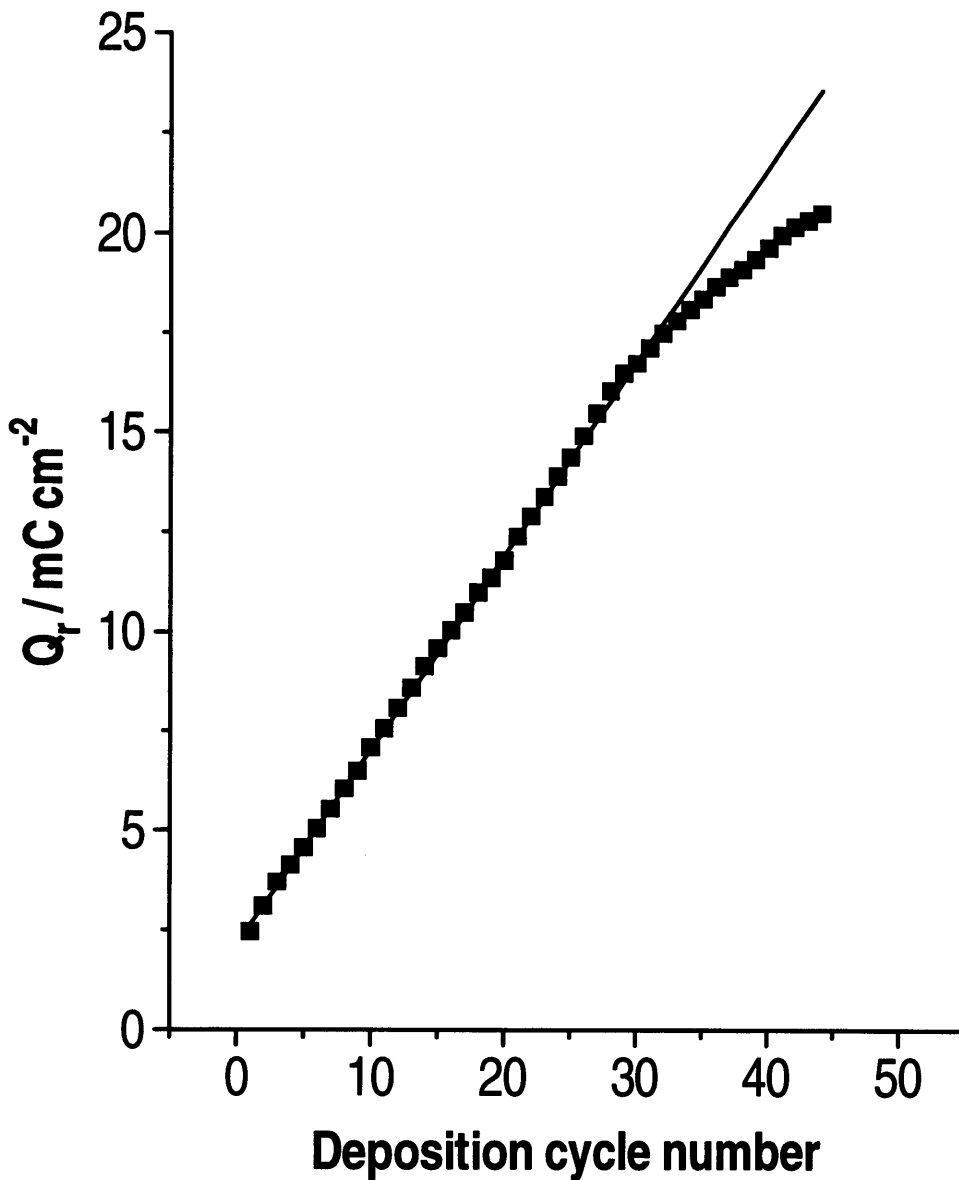


Figure 4.2: Reduction peak charge density (Q_r) dependency upon the number of potential cycles used for film deposition.

4.3.1 Impedance analysis

Figure 4.3 shows fundamental frequency data acquired during the deposition of the PHT film of Figure 4.1. From the outset and for the majority of the experiment, the crystal impedance spectra are typical of those commonly reported for viscoelastic films: for the first 41 deposition cycles, the resonant frequency ($f_{U_{max}}$) and conductance (U_{max}) systematically decrease. However, this does not continue: the trend in frequency shift is reversed and then U_{max} reaches a minimum at ca. 41 deposition cycles. At this point the film is said to be in

resonance with the underlying oscillator. At >41 cycles the peak position exhibits an *increase* in both $f_{U_{max}}$ and U_{max} . This is characteristic behaviour of film resonance (see below), and is clearly not consistent with simple models of a viscoelastic film [2].

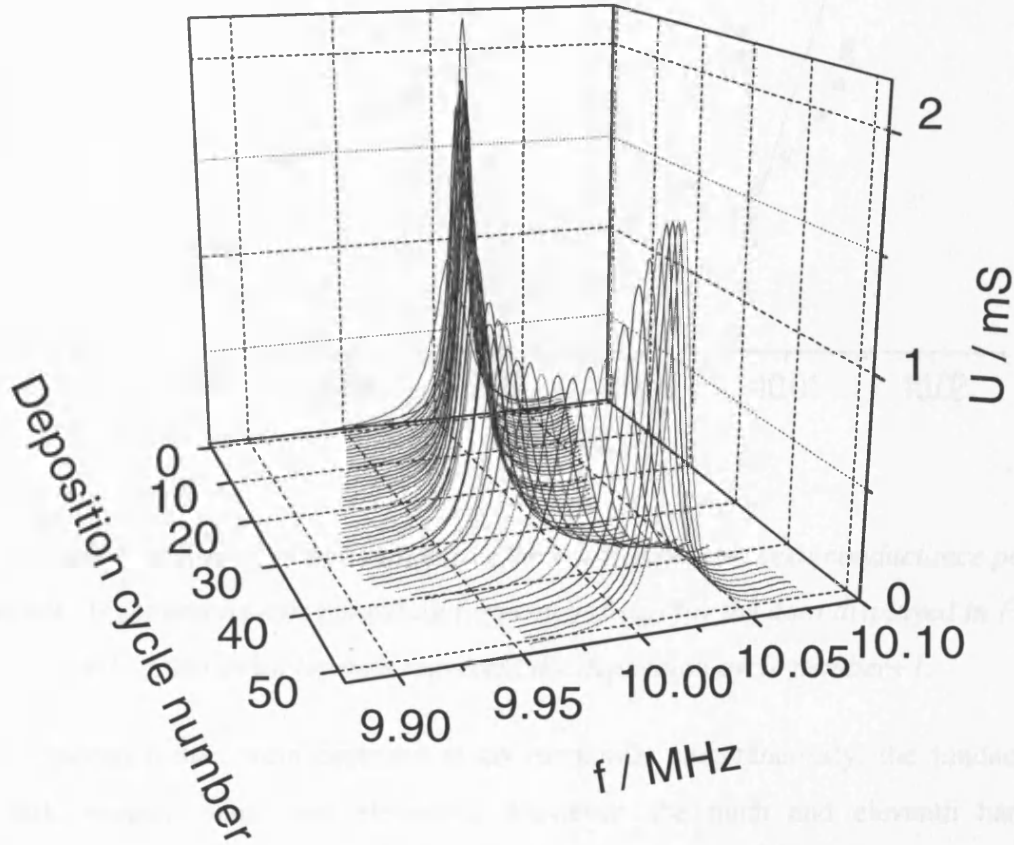


Figure 4.3: Fundamental harmonic (nominally 10 MHz) raw crystal conductance spectra, which were acquired during the deposition of the PHT film of Figure 4.1.

The peak frequency and conductance values of Figure 4.3 are more clearly displayed in Figure 4.4. From this plot it is apparent that the initial deposition cycle results in massive damping of the resonant-peak (Data point legend 2, Figure 4.4). This phenomenon is assigned to the formation of polymer nucleation sites upon the electrode surface [3]. These sites comprise “blobs” of polymer, which are extremely viscoelastic and therefore contribute to high power dissipation from the quartz resonator. In the succeeding deposition-cycles, a more uniform, and therefore more highly packed and rigid, film is formed as spaces between the polymer “blobs” are filled (Data point legends 3-9, Figure 4.4).

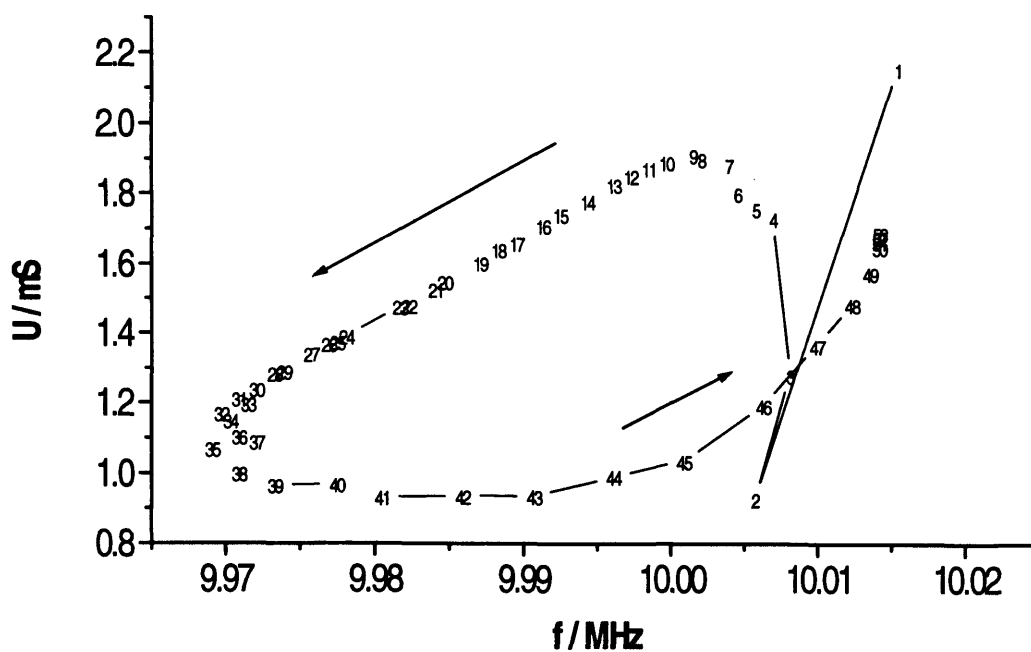


Figure 4.4: Parametric plot that displays the relationship between conductance peak magnitude (U_{max}) and its corresponding frequency ($f_{U_{max}}$) for the data displayed in Figure 4.1. Data point legends represent the deposition cycle number+1.

Crystal impedance data were captured at six harmonics simultaneously: the fundamental, third, fifth, seventh, ninth and eleventh. However, the ninth and eleventh harmonic conductance spectra became so damped as the film was deposited that the network analyser's peak tracking routine, running on the in-built computer, lost track of the conductance peak and hence the data was not successfully recorded.

Figures 4.5, 4.7 and 4.9 show analogous raw crystal impedance data to those captured under identical conditions to Figure 4.3 at higher harmonics; 30, 50 and 70 MHz respectively. The most striking difference between these data is that, at the higher harmonics, the conductance peaks become much more damped at the point of resonance. Also, the point of maximum damping (or point of resonance) occurs after a slightly different number of deposition cycles for each harmonic. Maximum damping occurs at ca. 30 deposition cycles at the seventh harmonic, at 37 deposition cycles for the fifth harmonic, 40 deposition cycles for the third harmonic and 41 deposition cycles for the fundamental harmonic. This can be seen more clearly in Figures 4.4, 4.6, 4.8 and 4.10, which detail the frequency dependence of the conductance peak maximum at 10, 30, 50 and 70 MHz respectively.

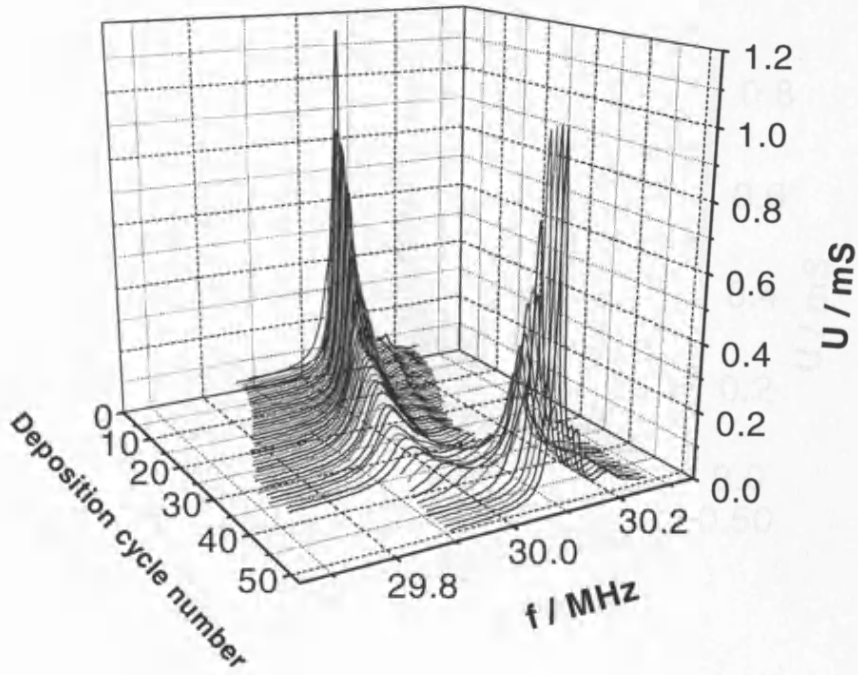


Figure 4.5: Third harmonic (nominally 30 MHz) raw crystal conductance spectra, acquired during the deposition of the PHT film of Figure 4.1.

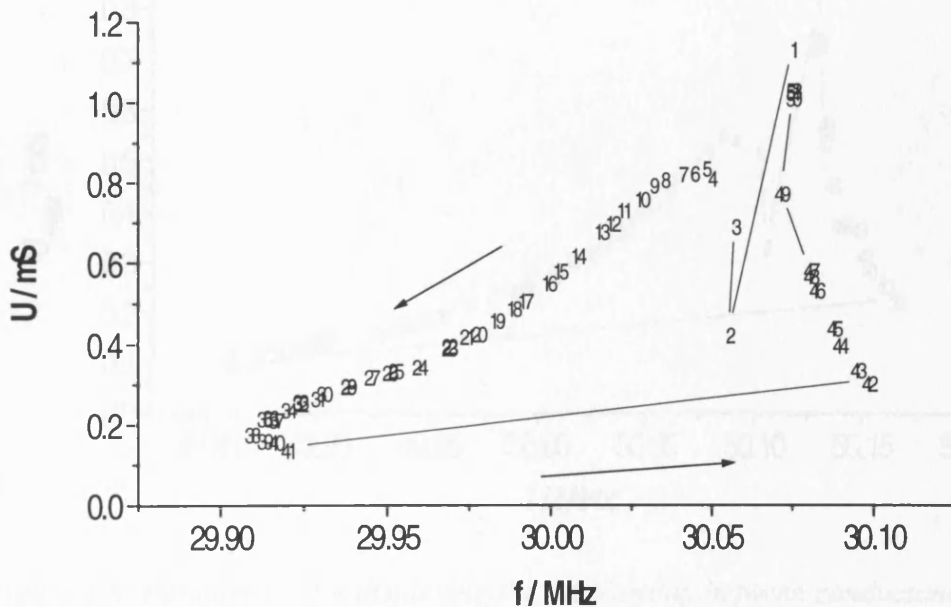


Figure 4.6: Parametric plot displaying the relationship between conductance peak magnitude (U_{max}) and its corresponding frequency ($f_{U_{max}}$) for the third harmonic data displayed in Figure 4.5. Data point legends represent the deposition cycle number+1.

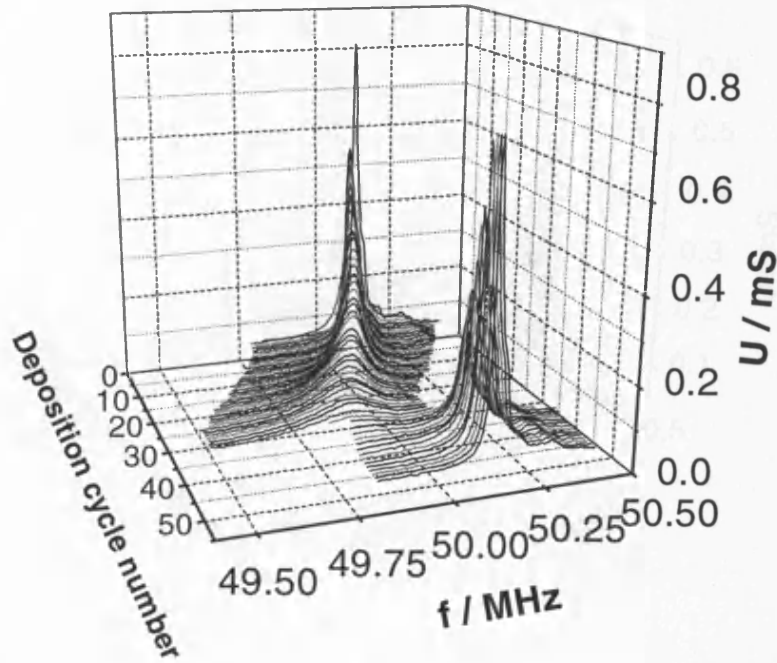


Figure 4.7: Fifth harmonic (nominally 50 MHz) raw crystal conductance spectra, acquired during the deposition of the PHT film of Figure 4.1.

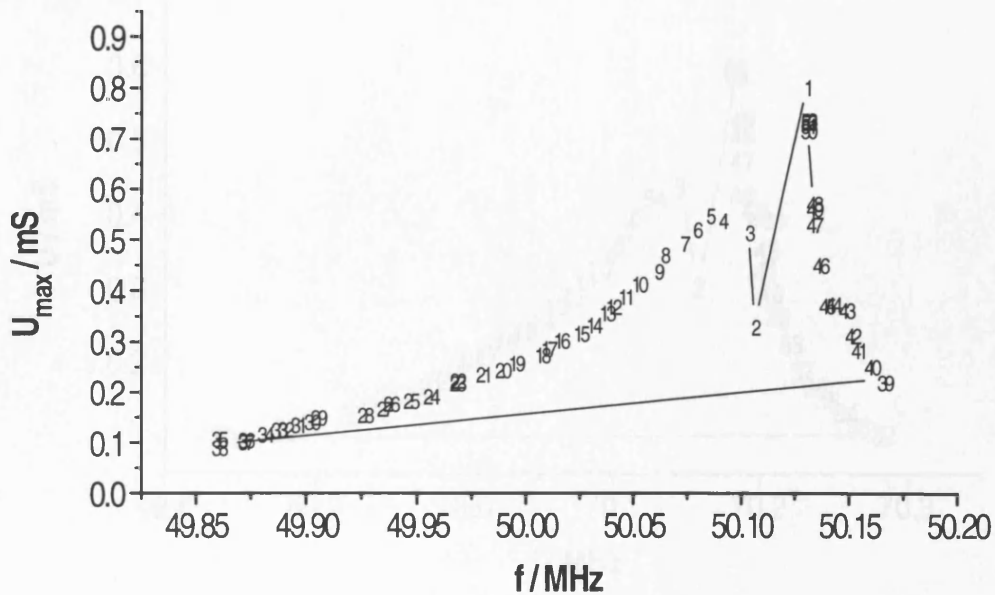


Figure 4.8: Parametric plot displaying the relationship between conductance peak magnitude (U_{max}) and its corresponding frequency ($f_{U_{max}}$) for the fifth harmonic data displayed in Figure 4.7. Data point legends represent the deposition cycle number+1.

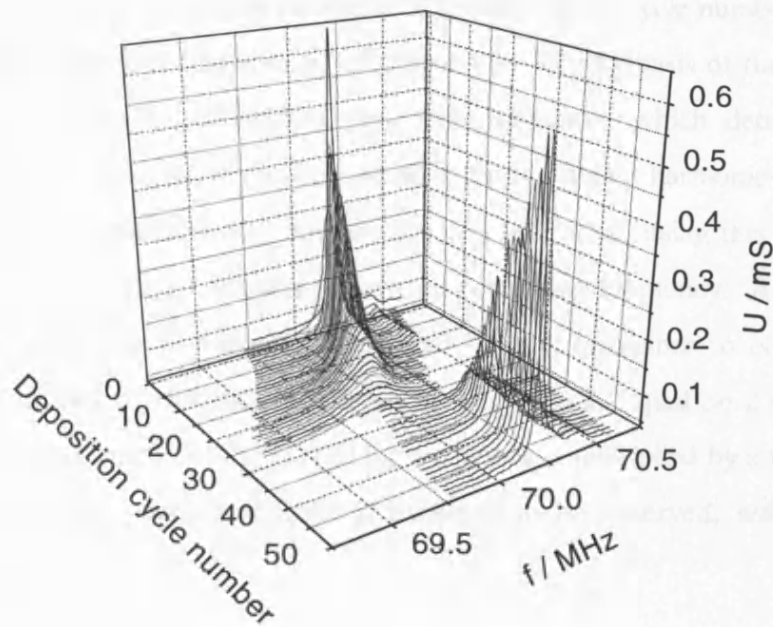


Figure 4.9: Seventh harmonic (nominally 70 MHz) raw crystal conductance spectra, acquired during the deposition of the PHT film of Figure 4.1.

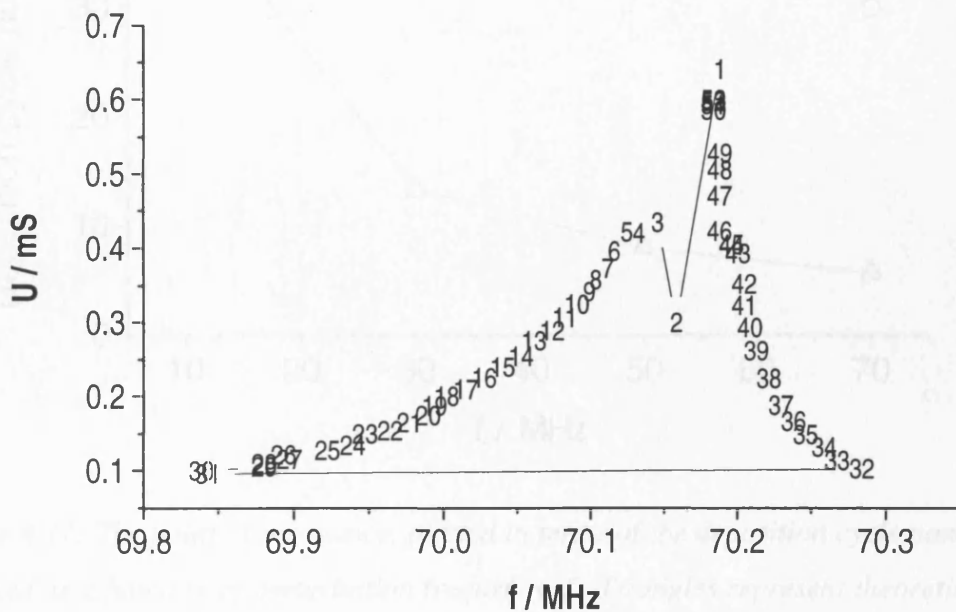


Figure 4.10: Parametric plot displaying the relationship between conductance peak magnitude (U_{max}) and frequency ($f_{U_{max}}$) for the seventh harmonic data displayed in Figure 4.9. Data point legends represent the deposition cycle number+1.

The point of resonance can be plotted in terms of the deposition cycle number and displayed as a function of perturbation frequency, f (Figure 4.11). On the basis of the observation of film resonance at 10 MHz, theoretical data were simulated which detail the point of resonance, in terms of the deposition cycle number, for the higher harmonics (30, 50 and 70 MHz), according to Equation 2.46. An assumption made when using this equation is that the shear modulus of the film, G , is independent of perturbing frequency. A consequence of this assumption is that the film thickness required for film resonance to occur is inversely proportional to applied perturbation frequency (Section 2.6.2, Equation 2.46). Therefore, for example, if the magnitude of the perturbing frequency is multiplied by a factor of 3, then the point (thickness) at which resonance is expected to be observed, will necessarily be divided by a factor of 3.

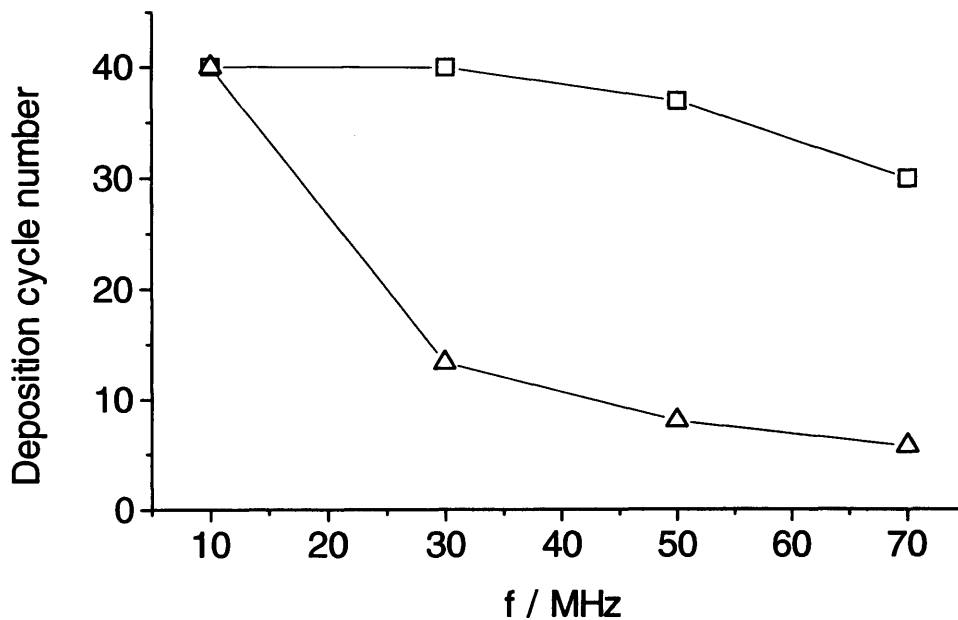


Figure 4.11: The point of resonance, plotted in terms of the deposition cycle number, is displayed as a function of perturbation frequency, f . Triangles represent theoretical data (calculated using the point of resonance at 10 MHz). Squares represent experimental data.

Upon observation of Figure 4.11, it is clear that the experimental data disagree with simulated theoretical data rather markedly. A reasonable explanation for this behaviour is that the shear modulus term, G , which also appears in Equation 2.46, is frequency dependent. This unpredicted dependence of the point of film resonance upon frequency

provided the impetus for studying G as a function of frequency in greater detail. The data resulting from this study are displayed in Chapters 5 and 6.

4.3.2 Peak splitting

This section presents the phenomenon of peak splitting. Due to slight differences in deposition process and procedure, crystal impedance spectra, which clearly display peak splitting, were more apparent in some deposition experiments than in others. The data set displayed in this section was chosen to display the phenomenon of peak splitting most clearly.

In Figure 4.12 typical raw crystal impedance spectra, recorded at 50 MHz, are plotted as a function of the number of potentiodynamic deposition cycles used to deposit the film under investigation. As the film is deposited, and the film thickness increases, the resonant peak becomes more damped and shifts to lower frequencies. At 26 cycles in Figure 4.12, two highly damped resonant peaks are clearly apparent. This feature, called peak splitting, will form a key discussion point later in the text.

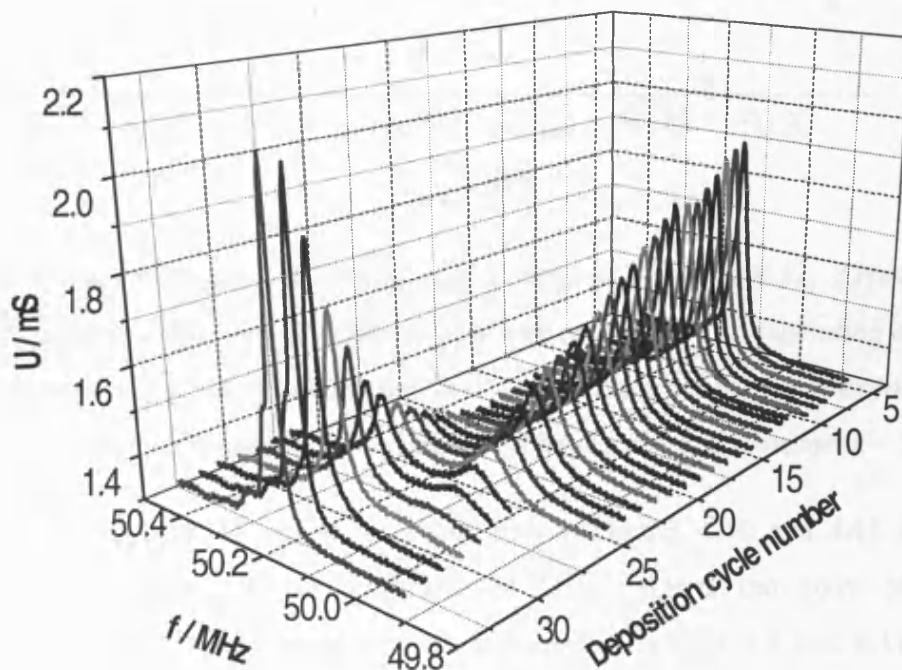


Figure 4.12: 5th harmonic (50 MHz) raw crystal impedance spectra acquired during the deposition of a PHT film. For presentational purposes the frequency axis runs from right-to-left.

The peak maxima, corresponding to the data of Figure 4.12, are more clearly displayed in Figure 4.13. The initial progression of the resonant peak is very similar to those displayed in Figures 4.4, 4.6, 4.8 and 4.10. However, the data of Figure 4.12 permit the observation of two peaks at the vicinity of film resonance. This is exemplified, in Figure 4.13, by the data labelled with data legends 26-30, which display a primary peak diminishing at ca. 50 MHz whilst a secondary peak is increasing at ca. 50.2 MHz. At data point 31, of Figure 4.13, the primary peak is undetectable and the secondary peak dominates the conductance spectrum.

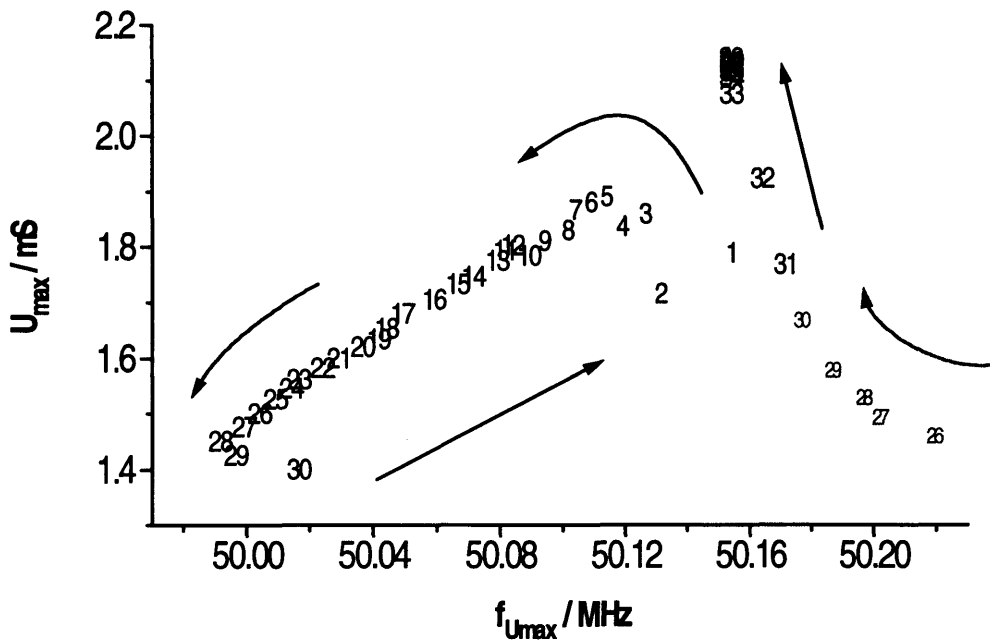


Figure 4.13: Dependence of U_{max} upon f_{Umax} for the data of Figure 4.12. Arrows and data labels indicate the direction of resonant peak movement and corresponding deposition cycle number+1 respectively. Duplicate data labels, displayed in a smaller font, indicate the position of the second peak and its direction of movement.

The features of Figures 4.8 and 4.9 are mirrored in Figures 4.10 and 4.11 respectively, which display data recorded at nominally 70 MHz. Here, the point of resonance (corresponding to the conductance minima displayed in Figures 4.9 and 4.11) occurs at deposition cycles 29 and 27. This is consistent with the notion of frequency dependent shear modulus values, as postulated in the preceding paragraphs.

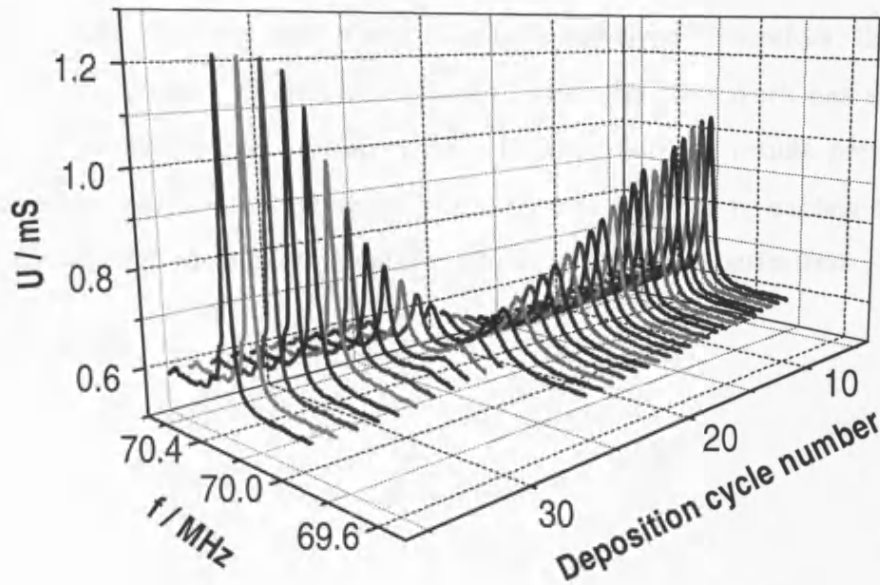


Figure 4.14: 7th harmonic (70 MHz) raw crystal impedance spectra acquired during the deposition of a PHT film. For presentational purposes the frequency axis runs from right-to-left.

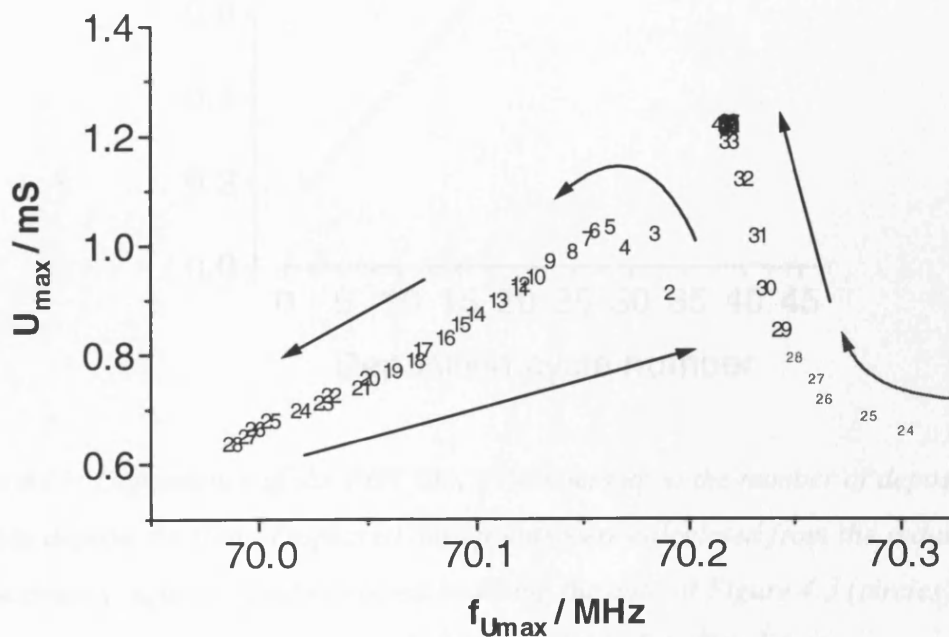


Figure 4.15: Dependence of U_{max} upon $f_{U_{max}}$ for the data of Figure 4.14. Arrows and data labels indicate the direction of resonant peak movement and corresponding deposition cycle number+1 respectively. Duplicate data labels, displayed in a smaller font, indicate the position of the second peak and its direction of movement.

4.4 DISCUSSION

In this chapter some very new phenomena have been displayed. Therefore, this discussion section is necessarily rather qualitative in places. However, this work has the important consequence of prompting much future work. In particular, the results presented herein have provided the impetus for the development of new theories to explain the observed effects and demand that further investigations into these effects be performed.

4.4.1 Data analysis

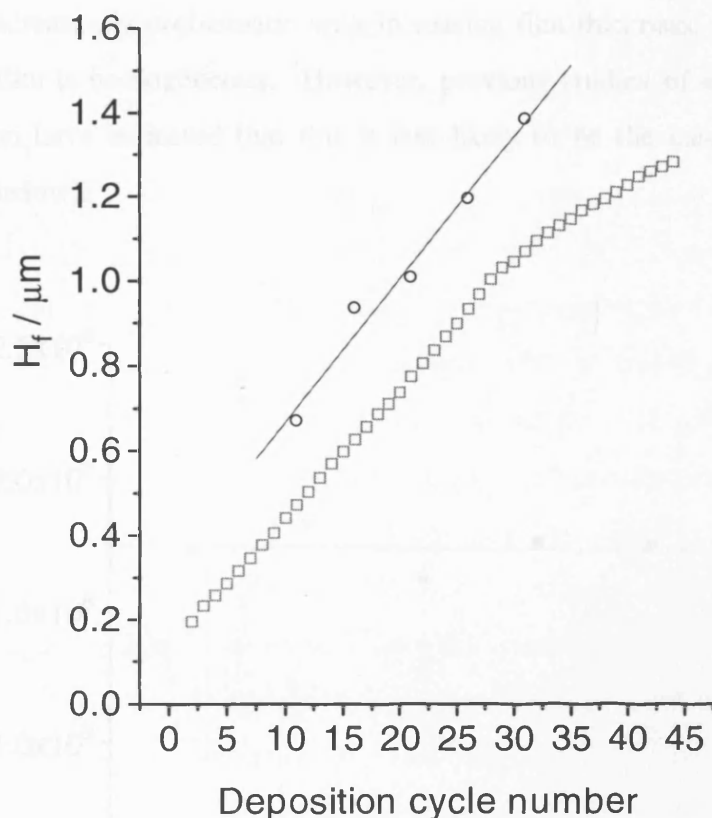


Figure 4.16: Dependence of the PHT film's thickness upon the number of deposition cycles used to deposit the film. Displayed data points were calculated from the reduction peak charge density (squares) and extracted by fitting the data of Figure 4.3 (circles) – the solid line represents a least squares fit of the fitted data.

The data of Figure 4.3 were fitted using the procedure described in Section 3.5.2. In Figure 4.16 film thickness values extracted using the model, represented by Figure 2.19 and Equation 2.41, are compared to film thickness values which were calculated using the reduction peak charge and the method described in Section 3.6.2. This method yields film

thickness values, which are calculated using the assumption that the polymer's density is equal to the density of the pure monomer. This assumption ignores the effects of swelling which occur in polymer films immersed in solvent electrolytes. Therefore, the film thickness calculated using the reduction peak charge is expected to be lower than that extracted from crystal impedance data. This is quite clearly seen in Figure 4.16.

Figure 4.17 displays G' values which have been extracted by fitting the pre-resonant, fundamental harmonic, crystal impedance data of Figure 4.3. For the initial 30 deposition cycles, G' exhibits a consistent value of approximately 1.75×10^8 dynes cm^{-2} . The modelling of crystal impedance data arising from PHT films deposited using 35 deposition cycles and over became increasingly problematic with increasing film thickness. The model assumes that the PHT film is homogeneous. However, previous studies of electroactive polymer films in solution have indicated that this is less likely to be the case as the thickness is increased (see below).

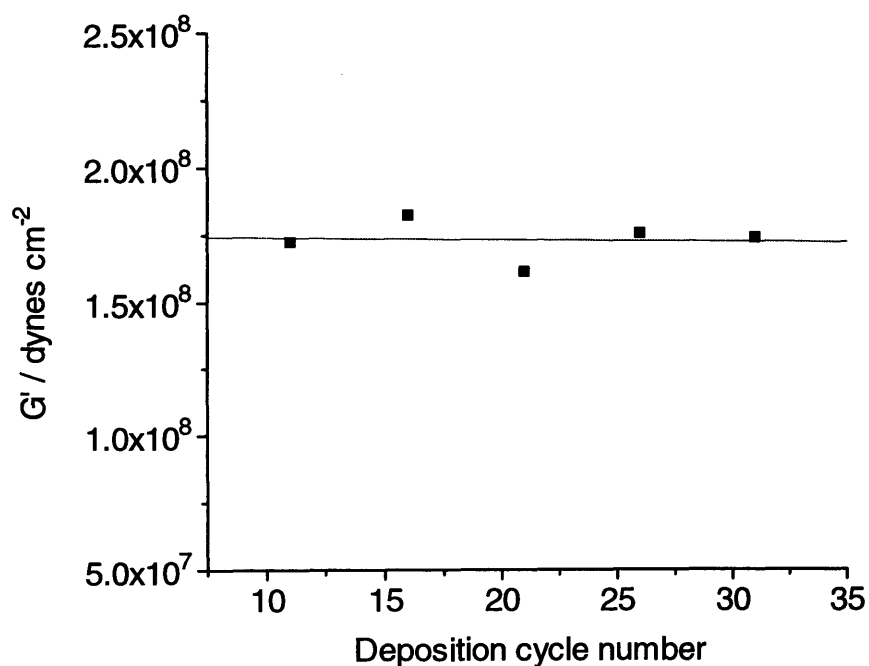


Figure 4.17: Dependence of the PHT film's shear storage modulus (G') upon the number of deposition cycles used to deposit the film. The displayed data points were extracted by fitting the data of Figure 4.3 (squares) – the solid line represents a least squares fit of the fitted data.

Shear loss modulus, G'' , data could not be extracted from the fundamental harmonic data since G'' is more than an order of magnitude smaller than G' in this instance. This is discussed in more detail in Section 5.3.2.

The Butterworth Van Dyke equivalent circuit, which was introduced in Section 2.3.1, was used to extract electrical parameters of the TSM resonator arising from the presence of the PHT film on its surface. R_F and ωL_F represent the electrical resistance and inductance respectively, arising from the presence of the polymer film. The procedure for extracting these parameters is described in Section 3.5.1.

Theoretical R_F versus ωL_F data have been simulated for the physical example of a PHT film exposed to propylene carbonate (PC) electrolyte solution, oscillating at the fundamental harmonic, using Equation 2.41 in conjunction with Equations 2.32 and 2.33. In Figure 4.18 this data has been plotted parametrically and overlaid upon the experimental data. The theoretical plots were calculated for homogeneous films, i.e. with G' and G'' values invariant with deposition cycle number and with spatial location within the film. Thus, for a similarly homogeneous PHT film, the experimental points should superimpose on a single theoretical line corresponding to the appropriate G' and G'' values.

Despite systematic variation of G' and G'' across the physically reasonable range of values, this could not be achieved. This can be interpreted as indicating that $G = G' + jG''$ for PHT films is a function of film thickness when more than 30 deposition cycles are used to deposit the film, according to Figure 4.17. Hence, the locus of experimental points will evolve from one theoretical curve to another with increasing film thickness in parametric plots such as in Figure 4.18. In other words, not one theoretical curve, calculated using the assumption that the film is homogeneous, could exactly overlay experimental data arising from the crystal impedance analysis of an inhomogeneous film. For example, experimental data, arising from an inhomogeneous film, may follow the path of a fairly rigid film in the early deposition stages but then “jump” to the path of a different theoretical curve, perhaps corresponding to a softer film, in later deposition stages.

Spatial variation of film properties, although not discussed commonly, is physically reasonable and is entirely consistent with generally accepted views of polymer adsorption. More specifically, it is consistent with previously observed variations of G values with thickness, prior to the onset of any resonance effects [3, 4]. It is also expected on the basis of neutron reflectivity-derived spatial distributions of polymer and solvent within electroactive polymer films [1, 5].

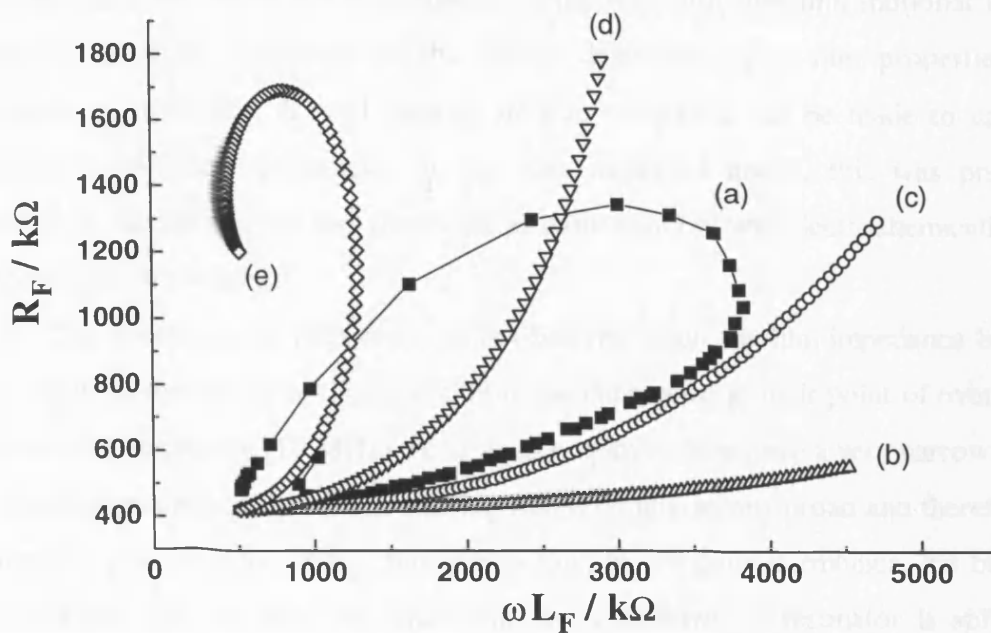


Figure 4.18: Parametric plot for the electropolymerisation of 3-hexylthiophene at the crystal fundamental frequency (10 MHz): (a) experimental data; (b-d) theoretical plots for growth of homogeneous films where (b) $G'=5 \times 10^8$, $G''=5 \times 10^8$ (c) $G'=9 \times 10^7$, $G''=9 \times 10^7$ (d) $G'=5 \times 10^7$, $G''=5 \times 10^7$ (e) $G'=2 \times 10^7$, $G''=2 \times 10^7$.

Data modelling of the PHT film, deposited using less than 35 deposition cycles, indicates that the film generally has a relatively high shear storage modulus. The point of resonance, predicted using Equation 2.46, on the basis of this data, occurs at considerably greater film thickness than that which is actually observed. An explanation for this observation is that thicker films tend to be inhomogeneous and more diffuse at the polymer/electrolyte interface. Therefore, film resonance is observed at a much lower film thickness.

4.4.2 Peak splitting

The phenomenon of peak splitting has previously received very little attention in the literature. The results presented herein have therefore driven (rather than responded to established) theory. Recently, Martin *et al* have derived a lumped element equivalent-circuit model which approximates the electrical response of a TSM resonator with a contacting viscoelastic film [6]. Development of this model has been prompted in part by the work presented in this chapter and is a very good example of experiment and theory working in tandem, with much positive synergy.

The response of the thickness shear mode resonator, with a contacting viscoelastic overlayer, depends upon the combination of the resonator and film motional impedances. Since the resonant frequency of the film is dependent upon film properties including thickness, h_f , modulus, G , and density, ρ_f , film resonance can be made to approach the resonator's resonant frequency. In the data displayed above, this was predominantly achieved by increasing the film thickness, as more material was electrochemically deposited on the electrode surface.

The double peak response is only observed when the film impedance bandwidth is comparable to the width of the quartz motional impedance at their point of overlap. At the fundamental frequency (10 MHz) the crystals employed here have a very narrow bandwidth, the impedance arising from the overlaying film is comparatively broad and therefore a single admittance peak results. When film loss is low, or at higher harmonics, the bandwidth of the resonator and the film are equivalent, the impedance of resonator is split when the impedances of the film and resonator overlap. This translates to the observation of two conductance peaks, examples of which can be seen in Figures 4.12 and 4.14.

The recent discovery of the peak splitting phenomenon prompts more experiments. The bandwidth of the resonator's response appears to be crucial in observing double peaks, since the impedance of the crystal has to be wider than the impedance of the contacting film in order to be able to be split. Good quality TSM quartz resonators are deliberately manufactured with bandwidths as small as possible. Perhaps the use of crystals with a much wider bandwidth would facilitate the observation of the peak splitting event, especially at the fundamental harmonic. Instrumentation that is more readily capable of measuring a large frequency range would also be an advantage. Usually, crystal impedance instrumentation is configured to locate the resonant peak, then automatically crop conductance spectra and therefore enable spectra to be captured with higher resolution. This procedure may cause double peak observation to be missed.

The importance and possible implications of the peak splitting phenomenon are not yet fully understood. Presently, experimental data containing double peak conductance spectra have not been fitted to a mathematical model. It is apparent from the data presented herein, that peak splitting occurs over a very narrow range of film parameters. Hence, successful modelling of crystal impedance spectra that simultaneously exhibit two resonant peaks will unequivocally yield important information about the contacting film. It is also conceivable that such modelling will pinpoint film parameters more accurately than current

data fitting programs (detailed in Section 3.5.2), especially if the double peak resonance is observed at multiple harmonics.

4.5 CONCLUSIONS

Crystal impedance data, recorded *in situ* during the electrodeposition of PHT films, have for the first time demonstrated that mechanical resonance effects can occur in electroactive polymer films exposed to a liquid contacting medium. These are manifested by dramatic changes in the resonator electrical response when the film thickness approaches $\frac{1}{4}$ of the acoustic wavelength in the medium. In particular, trends in the peak conductance and resonant frequency shift are reversed. Fitted shear moduli immediately prior to film resonance, together with parametric $f_{U_{max}}$ versus U_{max} plots, indicate the possibility of structural inhomogeneity and thus spatially variant shear moduli. Observation of the occurrence of film resonance at multiple harmonics has also lead to the conclusion that PHT films, electrochemically deposited under the conditions described here, are structurally inhomogeneous.

Analysis of parametric plots that display the relationship between conductance peak magnitude (U_{max}) and frequency ($f_{U_{max}}$) as film thickness is increased, accomplished here via electrochemical polymerisation, is very novel. This area of research requires much further development. In particular, the evolution of additional modelling programs could be initiated which would attempt to approximate parametric plots arising from the deposition of electrochemical films. This type of data modelling procedure could be used to monitor the deposition of electrochemical films and assess their quality *in situ*. To date, modelling routines assume that deposited films are structurally homogeneous. In the electrochemical context this tends not to be the case.

Future data modelling research could focus upon approximating crystal impedance responses arising from inhomogeneous films exposed to electrolyte solution. At present this modelling procedure is avoided due to the large number of unknown variable parameters presented by an inhomogeneous film. Observation and data modelling of film resonance and peak splitting phenomena at multiple excitation harmonics could help to elucidate some of these unknown parameters.

The phenomenon of peak splitting has been observed at the point of film resonance for PHT films exposed to electrolyte solution. Two highly damped conductance peaks were apparent at higher harmonics. However, they were not detected at the fundamental

harmonic, indicating that at the fundamental harmonic the impedance bandwidth of the crystal was too narrow for peak splitting to be observed.

This chapter has presented some very new phenomena: film resonance and peak splitting. Furthermore, these effects have been observed for electrochemically deposited films *in situ*. Observation of these occurrences prompts further experiments and development of their theoretical interpretation.

4.6 REFERENCES

1. R. W. Wilson, R. Cubitt, A. Glidle, A. R. Hillman, P. M. Saville, and J. G. Vos, J. Electrochem. Soc. 145:1454 (1998).
2. D. S. Ballantine, R. M. White, S. J. Martin, A. J. Ricco, E. T. Zellers, G. C. Frye, and H. Wohltjen, Acoustic Wave Sensors, Academic Press, New York, (1997).
3. H. L. Bandey, A. R. Hillman, M. J. Brown, and S. J. Martin, Far. Disc. 107:105 (1997).
4. H. L. Bandey, A. R. Hillman, and S. J. Martin, in Chemical and Biological Sensors and Analytical Electrochemical Methods (A. J. Ricco, M. A. Butler, P. Vanysek, G. Horvai, and A. F. Silva, eds.), The Electrochemical Society, Pennington, NJ, 1997, p. 218.
5. R. M. Richardson, M. J. Swann, A. R. Hillman, and S. J. Roser, Far. Disc. 94:295 (1992).
6. S. J. Martin, H. L. Bandey, R. W. Cernosek, and A. R. Hillman, Anal. Chem. submitted (1999).

CHAPTER 5

MANIPULATION OF ELECTROACTIVE POLYMER FILM VISCOELASTICITY: THE ROLES OF APPLIED POTENTIAL AND FREQUENCY

5.1 INTRODUCTION

This chapter describes an exploration of polymer dynamics within thin electroactive polymer films externally maintained in electronically conducting or insulating states. The general goals are an understanding of the way in which film material characteristics (here represented by film shear modulus) respond to (i) their environment (here, a liquid electrolyte) and (ii) external control parameters (here, the variation of polymer charge density, as dictated by the applied electrochemical potential). This is broadly complementary to the majority of work on such materials, which tends to focus on electronic properties *per se*. The link between the two is the fact that redox-driven changes in electronic characteristics ('doping' and 'undoping') require polymer structural changes that are in turn markedly influenced by polymer dynamics. Therefore a proper understanding of polymer dynamics is an important pre-requisite for the design of polymer-based interfacial modifications. In the context of materials science, it is important to note that the importance of bulk viscoelastic characteristics of polymers has long been appreciated [1, 2], to the extent that molecular interpretations of the macroscopic phenomena have been discussed at length [3]. However, the analogous phenomena for *thin films* of polymers - the focus of this study - have not received such attention.

The majority of TSM-based studies of polymer films have been rather limited: most commonly they are restricted to qualitative diagnosis of film (non-)rigidity, and there are a few examples of film shear moduli determinations [4-6]. In this study a more ambitious approach has been adopted, with the ultimate objective of *a priori* control and *in situ* manipulation of film shear modulus and dynamics. This capability would have direct implications in sensing, molecular recognition, controlled release and separation science, as well as indirect generic benefits in interfacial design.

The intermediate goal *en route* is a systematic understanding of the parameters that govern film shear modulus. Qualitatively, the shear modulus is recognised to depend upon physicochemical parameters that may be intrinsic to the polymer, a feature of its environment or amenable to external control. The immediate objective is an understanding of the roles film charge (Q) and the frequency regime ($f = 2\pi/\omega$) in which the system

operates. Film charge is a variable of natural choice, since it can be readily manipulated through the applied electrochemical potential (E): it is seen as a primary driver of film composition - most obviously ion and solvent content - and structure. Operating frequency as a delimiter of film dynamics is a much under-explored variable: the vast majority of studies in this area are based upon TSM device responses at their fundamental frequency, typically 5 or 10 MHz. Here use of higher harmonics is made to effect simultaneous measurements at a range of frequencies; this is relatively rare for viscoelastic measurements of electroactive polymer films and offers significant insights into materials properties.

Film composition (mobile species populations) and structure (polymer reconfiguration) may be under either thermodynamic or kinetic control, according to the electrochemical control function and other parameters. In this chapter attention is restricted to static measurements at fixed $Q(E)$. Here the film is at redox equilibrium although the question of equilibrium with regard to non-electrochemical processes (such as solvation and polymer reconfiguration) is more complex.

5.2 EXPERIMENTAL

The experimental instrumentation and procedures are described in Chapter 3. PHT films were deposited according to Section 3.6.1 using a total of 6 cyclic potential scans. Following deposition, the Au/PHT electrodes were transferred to a background electrolyte solution containing 0.1 mole dm^{-3} tetraethylammonium hexafluorophosphate in propylene carbonate. Cyclic voltammetry (0.0-0.9 V, scan rate 2 mV s^{-1} ; see Figure 5.1, below) indicated chemically reversible behaviour. Static potentials were applied to the film according to the protocol described in Section 3.7.1. The temperature was thermostatted at 25°C.

5.3 RESULTS

5.3.1 Raw spectra

Figure 5.1 shows a typical voltammogram for a PHT film upon redox cycling in 0.1 mole dm^{-3} TEAPF₆ / propylene carbonate. It shows all the characteristics generally found for poly(thiophene)-type films [7], with p-doping / undoping (see Figure 1.10) occurring during the positive- / negative-going half cycle. The conditions under which this voltammogram was obtained, primarily slow potential scan rate, allow complete redox conversion of the film. This is signified by linearity of peak currents with potential scan rate for scan rates $\nu \leq$

20 mV s^{-1} . Consequently, it is possible to use the integrated peak currents as a reliable measure of the polymer coverage, $\Gamma = Q/nFA$, with the doping level taken to be $n = 0.35$ [8].

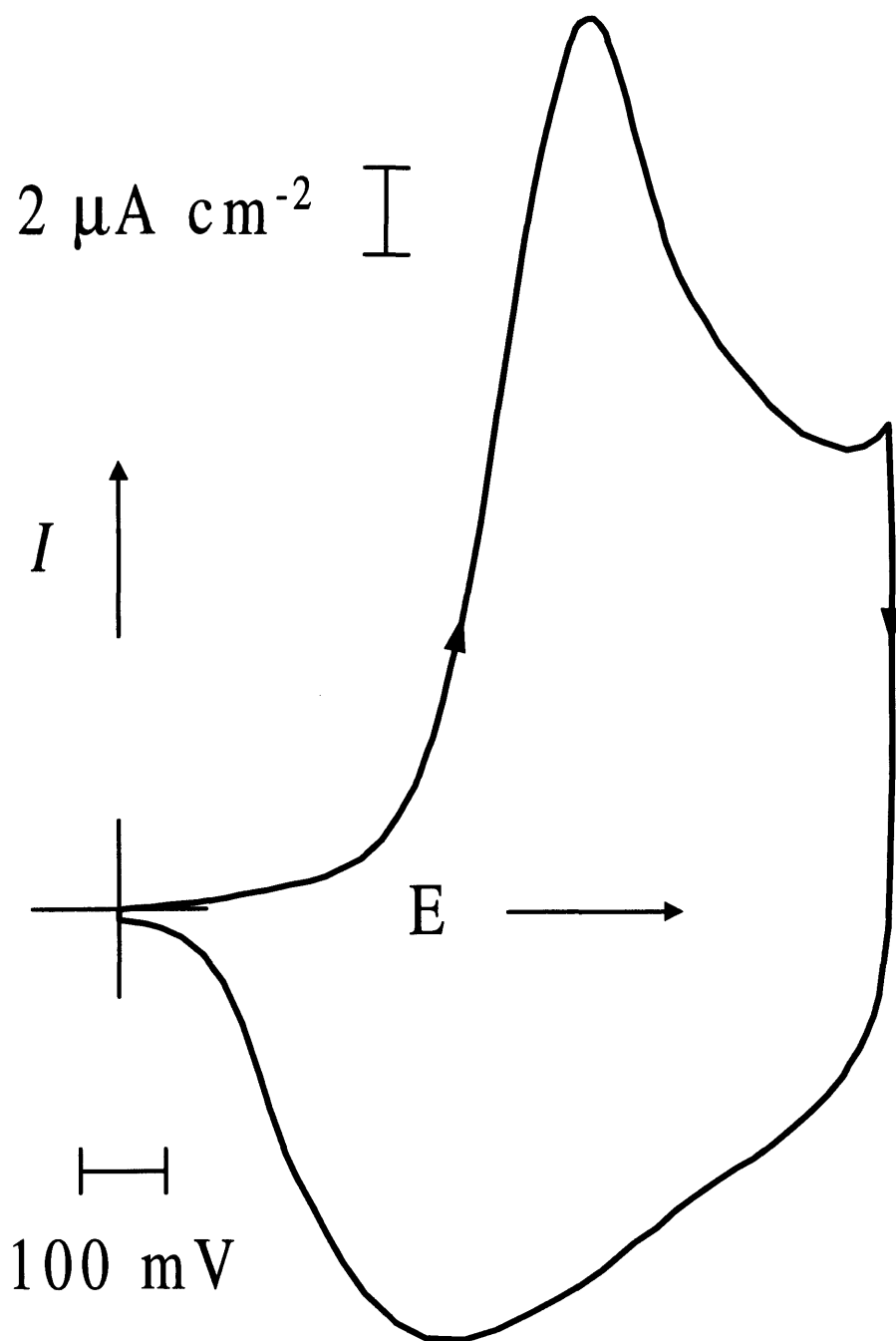


Figure 5.1: Cyclic voltammogram of a PHT film ($\Gamma = 0.22 \mu\text{mol cm}^{-2}$) exposed to 0.1 mole dm^{-3} TEAPF₆/propylene carbonate. Scan rate: 2 mV s^{-1} . At scan rates, ν , $\leq 20 \text{ mV s}^{-1}$ peak currents are linear with scan rate, indicating complete redox conversion.

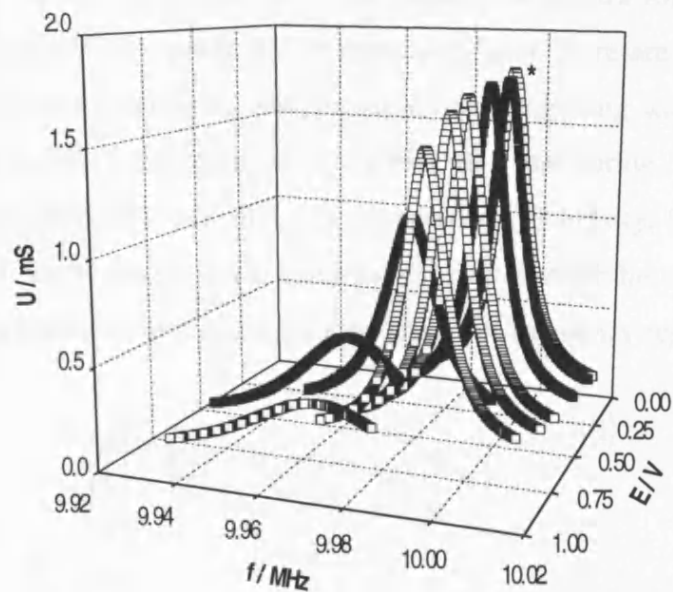


Figure 5.2: Raw crystal impedance spectra for the PHT film of Figure 5.1 exposed to $0.1 \text{ mole dm}^{-3} \text{ TEAPF}_6 / \text{propylene carbonate}$. Open symbols: data acquired at progressively more positive applied potentials, commencing at 0 V; filled symbols: data acquired at progressively more negative potentials, commencing at 0.9 V. Data taken at the fundamental frequency (nominally 10 MHz). The asterisk adjacent to one of the spectra refers to (Figure 5.7).

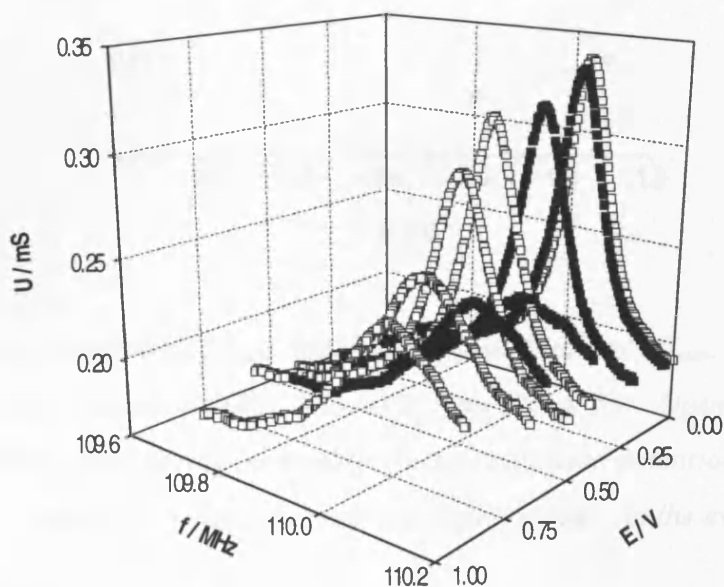


Figure 5.3: Raw crystal impedance spectra for the film of Figure 5.2 taken under identical conditions, except at the eleventh harmonic (nominally 110 MHz).

Figures 5.2 and 5.3 show representative crystal impedance spectra for this PHT film as a function of the applied (fixed) potential. Within each figure there are two sets of spectra, acquired at progressively increasing and progressively decreasing applied potentials, i.e. during ‘doping’ of a fully reduced (uncharged) PHT film and during ‘undoping’ of a fully oxidized (positively charged) PHT film. In the interests of brevity, figures for all of the harmonics acquired are not shown: the fundamental and eleventh harmonics are chosen to represent the spread of behaviour occasioned by choice of frequency regime.

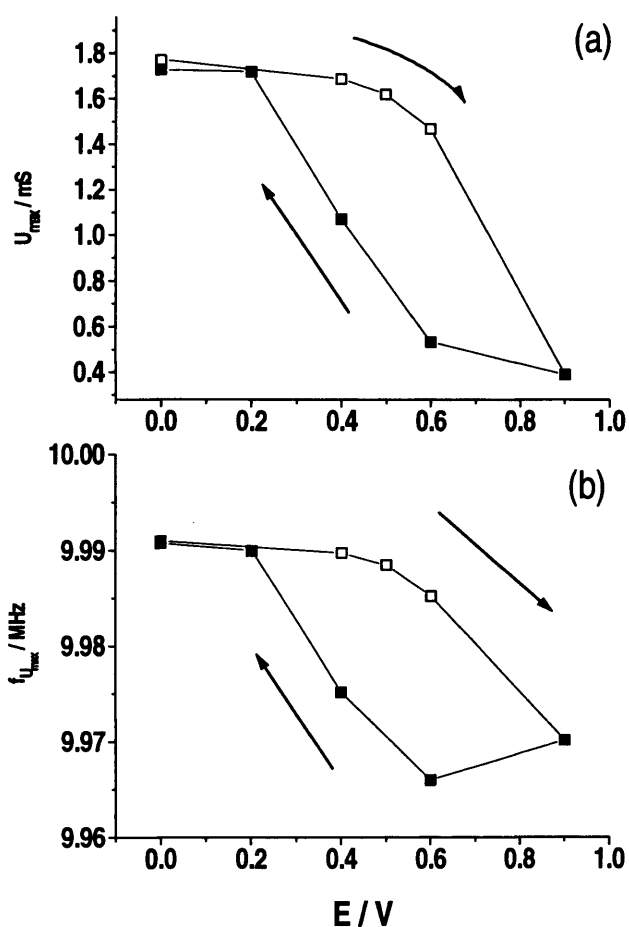


Figure 5.4: Peak conductance (U_{max} ; panel a) and peak frequency ($f_{U_{max}}$; panel b) variations with applied potential at 10 MHz; data taken from Figure 5.2. Open (filled) symbols represent data acquired during increasing (decreasing) fixed potential sequence. Lines connecting adjacent points are merely a guide to the eye.

On the basis of the data, one can make four qualitative observations. First, there are obvious viscoelastic changes: the doped polymer is associated with greater energy loss (lower peak admittance). Second, these effects are clearly a function of frequency. Third, in these and all other data sets (other films, harmonics and choices of potential program)

'asymmetry' of the crystal frequency responses is observed during the oxidative and reductive half cycles. This will be a key discussion point later in the text. Fourth, appropriate combinations of film thickness, applied potential and frequency lead to film resonance effects (discussed in Section 2.6.2) [8], in which the peak admittance and frequency show dramatic variations. To illustrate the breadth of the behaviour observed, data which are (Figure 5.3) / are not (Figure 5.2) complicated by these phenomena are shown; the model (detailed in Section 2.5.2) is capable of handling such effects.

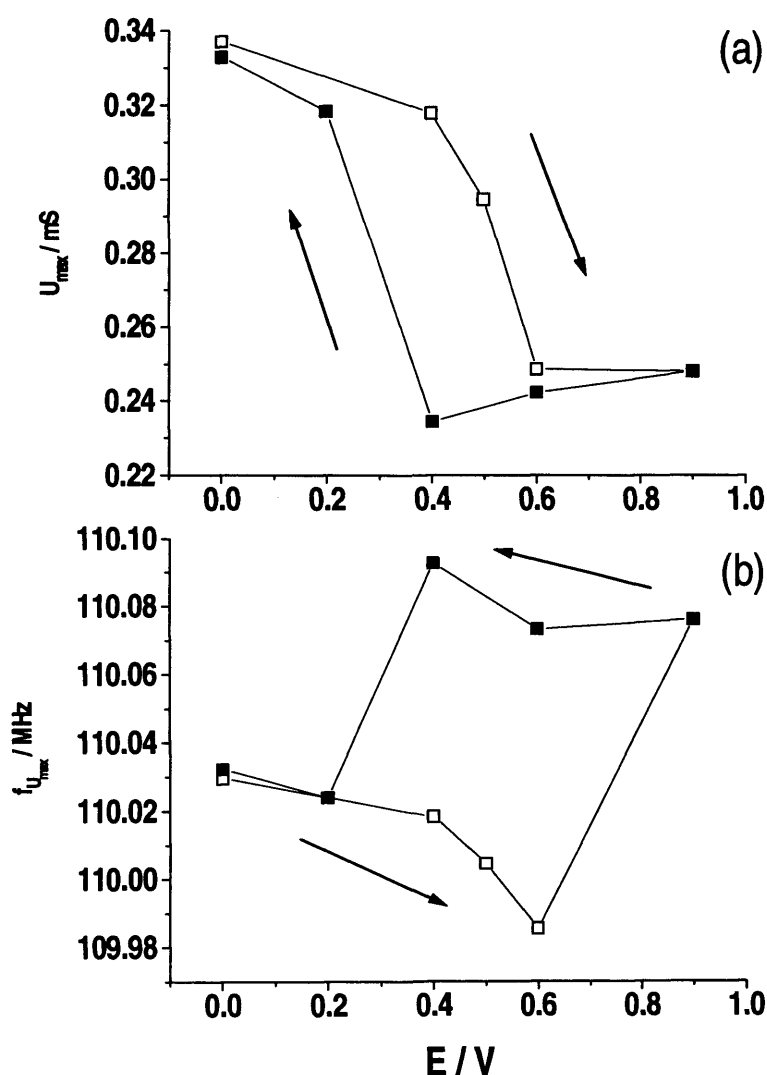


Figure 5.5: Peak conductance (U_{max} ; panel a) and peak frequency (f_{max} ; panel b) variations with applied potential at 110 MHz; data taken from Figure 5.3. Open (filled) symbols represent data acquired during increasing (decreasing) fixed potential sequence. Lines connecting adjacent points are merely a guide to the eye.

Figures 5.4 and 5.5, respectively, summarise some of the key features of Figures 5.2 and 5.3, through the potential variations of resonant admittance (Figures 5.4a and 5.5a) and resonant frequency (Figures 5.4b and 5.5b). The most prominent features of the data shown here are the pronounced hysteresis in all cases, and the fact that it appears in 'reverse' fashion for the 110 MHz resonant frequency data. The latter is a consequence of resonance effects [8].

Since the responses are not single valued with potential, it is immediately clear that global equilibrium is not established, even on the rather extended time scales (equilibration for 2 minutes at each potential) employed here. The question then arises as to whether this is a failure to establish equilibrium of the redox state or of other associated processes. Figure 5.6 shows a plot of the injected charge (Q) as a function of potential associated with the experiments of Figures 5.2 and 5.3 (and their analogues at intervening harmonics). Whilst it is true that there is some hysteresis, i.e. redox equilibrium is not fully established, the extent of this hysteresis is nowhere near as marked as in the viscoelastic responses. One can therefore conclude, at a qualitative level, that the film viscoelastic characteristics are under effective control by intrinsically *non*-electrochemical processes that are a consequence of the electrochemical oxidation / reduction of the polymer.

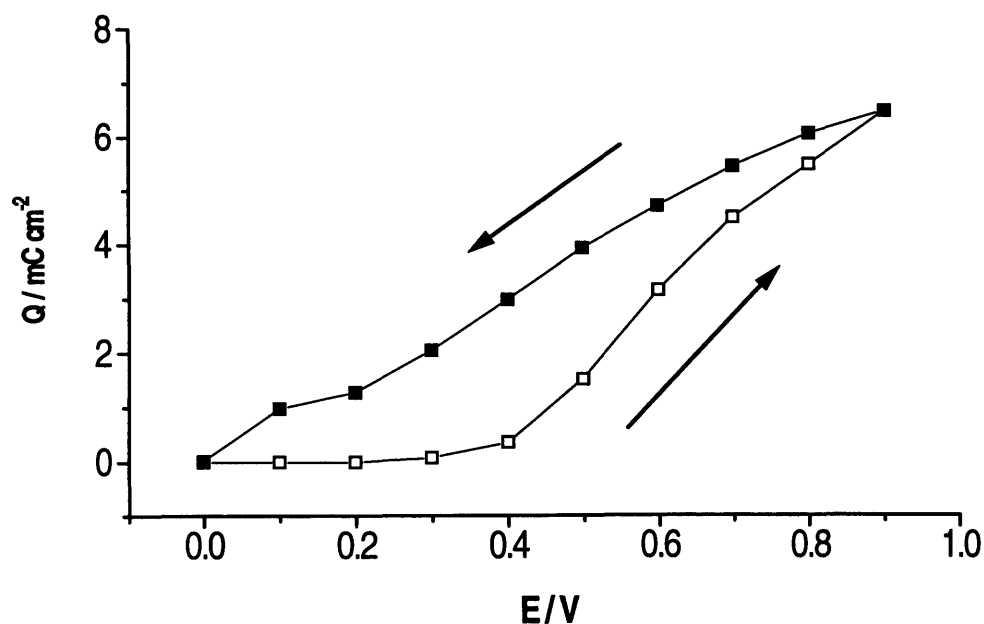


Figure 5.6: Plot of charge (Q) vs potential (E) for the PHT film of Figures 5.1-5.5. The charge data were acquired by progressively incrementing the potential in the intervals used for the experiments in Figures 5.2-5.5. Open (filled) symbols represent data acquired during increasing (decreasing) fixed potential sequence.

5.3.2 Fitted data

5.3.2.1 General observations

The objective of this study is to determine quantitative shear modulus data and to explore their variations with applied potential and operating frequency, i.e. $G(E, \omega)$. In order to achieve this, the data of Figures 5.2 and 5.3 (and their various analogues at different harmonics) needs to be fitted to the model represented by Figure 2.19 and Equation (2.41). The procedure for this has been outlined in Section 3.5.2. A typical fit is shown in Figure 5.7.

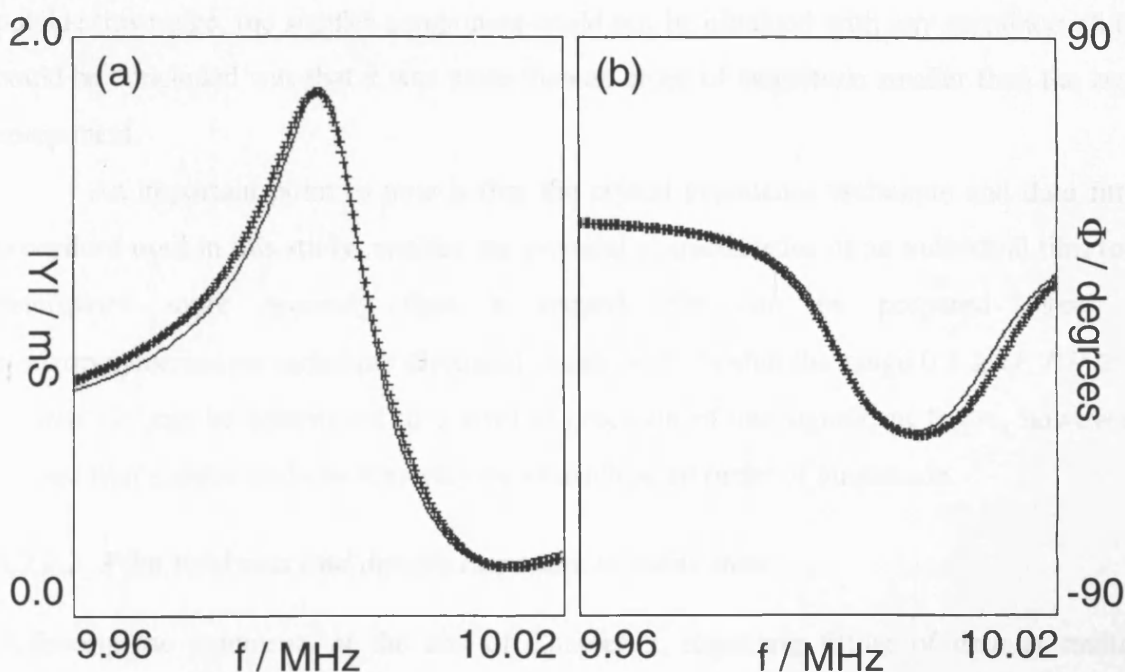


Figure 5.7: Typical fits to the amplitude ($|Y|$; panel a) and phase (Φ ; panel b) data for a crystal impedance spectrum. The data (points) are taken from the spectrum marked with * in Figure 5.2. The lines represent the best fits.

In many cases the phase crossed zero by an appreciable margin and, due to the combination of peak width and measurement interval, it was possible to encompass both the peak and its high / low frequency 'wings'. In such cases, fitting was straightforward and commonly better than represented by Figure 5.7. The limiting features in terms of fitting were broadening and much diminished phase changes for acoustically thicker and 'softer' films. In such cases, the fits were less good than that in Figure 5.7, notably in the 'wings' of the

peak. As a more subtle point, although one would anticipate that this would become highly problematical at higher frequency (i.e. for the higher harmonics, for which the film might appear semi-infinite), the frequency dependence of shear modulus (see below) increases the decay length in the film, thereby diminishing the effect.

Some general observations, relevant to the correlations made later in the text, are appropriate with regard to the reliability (reproducibility) of G' and G'' values. It was always possible to get reliable (reproducible) values of the larger component of G , regardless of the starting values used to seed the fitting algorithm. However, the reliability of the smaller component was dependent upon the relative values of G' and G'' , i.e. the loss tangent. When $0.1 \geq G''/G' \geq 10$, both components were reliably obtainable. However, outside this range, the smaller component could not be obtained with any certainty; all that could be concluded was that it was more than an order of magnitude smaller than the larger component.

An important point to note is that the crystal impedance technique and data fitting procedure used in this study, enables the physical characteristics of an individual film to be determined more precisely than a second film can be prepared using the electropolymerisation technique discussed in this text. Within the range $0.1 \geq G''/G' \geq 10$, G' and G'' can be determined to a level of precision of one significant figure, however, a second film's shear modulus may vary by as much as an order of magnitude.

5.3.2.2 Film thickness and density responses to redox state

Following the comments at the end of Chapter 3, regarding fitting of data at multiple harmonics, the film thickness and density parameters were allowed to 'float' (within physically reasonable bounds) in the data fitting routine for each frequency. Data for the film density (ρ_f) and thickness (h_f) as functions of applied potential are shown in Figures 5.8 and 5.9 respectively. In each figure, data are shown at four frequencies: the fundamental, third harmonic, fifth harmonic and seventh harmonic (nominally 10, 30, 50 and 70 MHz, respectively).

Naturally, the film composition and dimensions - here represented by film density and thickness - are independent of the excitation frequency with which they were probed (although the same is not true for the modulus; see below). (The only apparent violation of this would be the situation where the range of frequencies employed, taking account of their effect on G , and the film thickness were such that one moved between the acoustically 'thin' and acoustically 'thick' cases within a single data set. In the latter case, corresponding to h_f

$\gg \omega^{-1}(G/\rho_f)^{1/2}$, the TSM would perceive the film as being of ‘infinite’ extent, i.e. a bulk medium; this less interesting regime was not explored.) As the data show, the fitted film density and thickness at any given potential are, within experimental uncertainty, independent of the crystal harmonic (operating frequency) involved. These consistent values of ρ_f and h_f strongly support the validity of the fitting procedures.

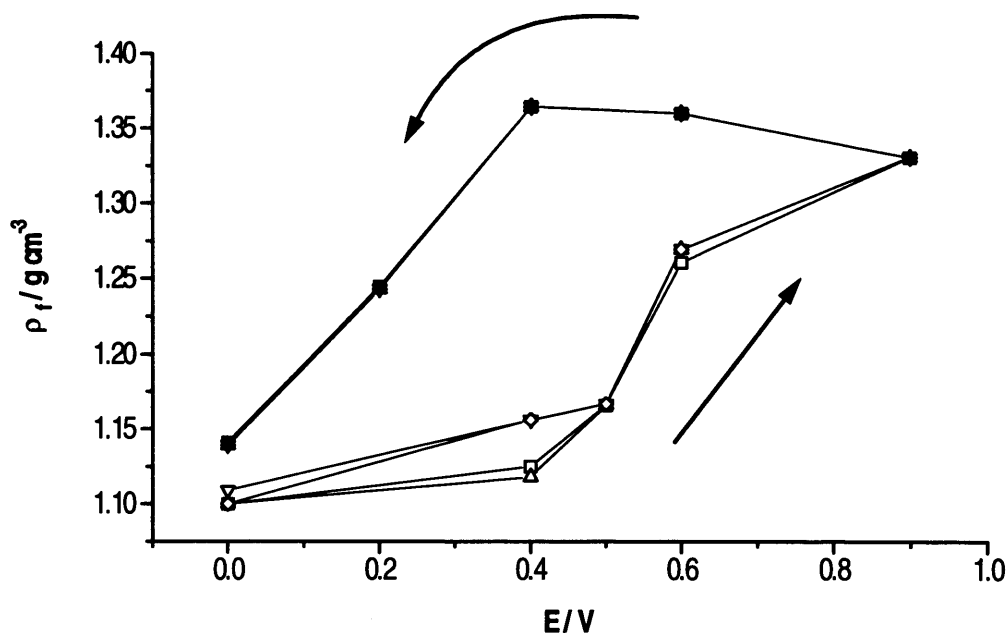


Figure 5.8: Fitted film density values as functions of applied potential for the data of Figure 5.2 (\square , \blacksquare) and its third (Δ , \blacktriangle), fifth (∇ , \blacktriangledown) and seventh (\diamond , \blacklozenge) harmonic analogues. Open (filled) symbols represent data acquired during increasing (decreasing) fixed potential sequence.

Beyond this ‘validation’ role, the ρ_f and h_f data provide further clues to the physical origins of the hysteresis seen in the TSM responses of Figures 5.2 and 5.3 (and analogues). First it is helpful to note the densities of the components present in the system. One would anticipate that the density of the pure undoped polymer (containing no charge-balancing anions) would be similar to that of the monomer, 0.936 g cm^{-3} (as supplied). The density of the solvent is 1.189 g cm^{-3} (as supplied). As an approximation to the density of the dopant anion, the density of its conjugate acid is used, estimated from a solution value to be ca. 2.0 g cm^{-3} [9].

Data analogous to those shown in Figure 5.8, but for a number of films, always showed the same trends. Absolute values of film densities lay in the range $1.00 (\pm 0.10) \text{ g cm}^{-3}$ for the reduced (undoped) polymer and $1.25 (\pm 0.10) \text{ g cm}^{-3}$ for the oxidised polymer. These variations are believed to be real, and to reflect variations in film density, according

to minor variations in deposition, handling or ageing circumstances. The relative magnitude of the density increase upon complete oxidation was always ca. 25%. Taking the data of Figure 5.8 as representative, one can deduce that the reduced polymer (at 0 V) contains a little solvent; this is consistent with the non-rigid behaviour of the film.

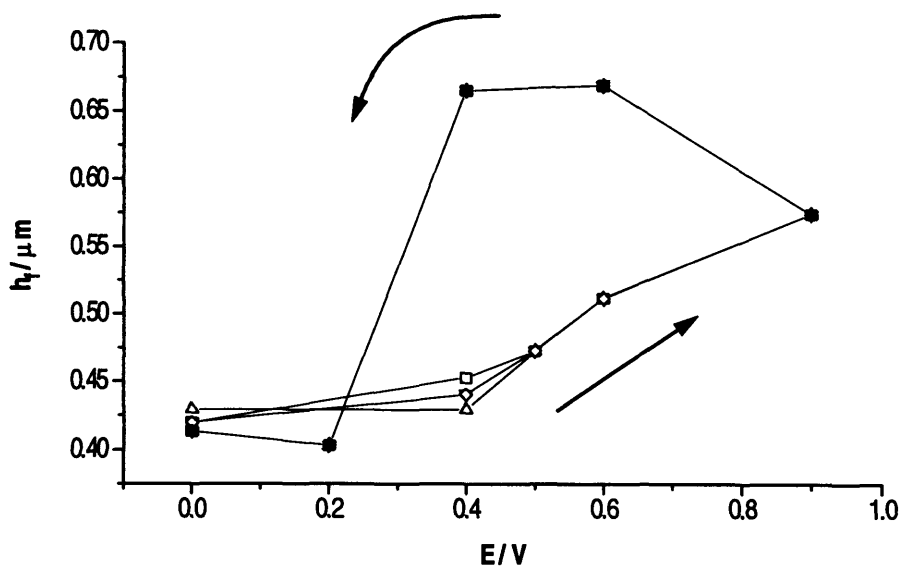


Figure 5.9: Fitted film thickness values as functions of applied potential for the data of Figure 5.2 and its third, fifth and seventh harmonic analogues. Symbols as in Figure 5.8.

Qualitatively, the increase in density upon doping (see Figure 5.8) is consistent with the entry of a dense balancing anion ('dopant'). However, the associated thickness increase (see Figure 5.9) is too large to be associated with anion entry alone; rather, it signals substantial concomitant solvent entry. Qualitatively, the magnitudes of the density and thickness increases allow one to estimate the relative amounts of solvent and dopant entering the film. At the level of precision available, volume of mixing effects are ignored, which would be small compared to the magnitude of the effects seen in Figures 5.7 and 5.8.

Denoting the undoped film, the solvent and the dopant, respectively, by the subscripts of 'f,RED', 'PC' and 'A', it is straightforward to show that the density of the fully oxidised film

$$\rho_{f,OX} = \frac{\rho_{f,RED}h_{f,RED} + \rho_{PC}h_{PC} + \rho_A h_A}{h_{f,RED} + h_{PC} + h_A} \quad (5.1)$$

where the ' ρ_i ' values denote the component densities (see above) and the ' h_i ' values denote the contributions to the total film thickness of the individual (subscripted) species. The intention here is *not* to imply that each film component occurs in a series of separate layers, but that each component of the oxidised film (i.e. polymer, solvent and salt) contributes

towards its thickness. The experimental data (Figures 5.8 and 5.9) provide $\rho_{f,OX}$, $\rho_{f,RED}$, $h_{f,RED}$, and $(h_{f,RED} + h_{PC} + h_A) (=h_{f,OX})$. There are two unknowns, h_{PC} and h_A , in Equation (5.1), so two pieces of information are needed. In addition to Equation (5.1), the masses of anion and polymer can be related via the doping stoichiometry. Specifically, since the doping level is 0.35:

$$\frac{\rho_A h_A}{\rho_{f,RED} h_{f,RED}} = 0.35 \frac{RMM(A)}{RMM(HT)} = 0.31 \quad (5.2)$$

Using this in Equation (5.1) yields $h_{PC}/h_{f,RED} = 0.48$, i.e. complete oxidation of the fully reduced polymer results in solvent transfer that swells the film by 48%. The observed swelling, $(h_{PC} + h_A) / h_{f,RED} \approx 0.63$ (see Figure 5.9). Hence $h_A/h_{f,RED} \approx 0.15$, i.e. anion entry (to maintain electroneutrality upon oxidation of the polymer) swells the film by 15%. Crudely, since each anion contains 7 ‘heavy’ atoms, and is associated with 33 ‘heavy’ atoms in the polymer (three monomer units each containing 11 ‘heavy’ atoms), this is physically reasonable.

The responses of Figures 5.7 and 5.8 show significant hysteresis, rather like those in the raw TSM responses (see Figures 5.2 - 5.5), and certainly much greater than in Q vs E plots (see Figure 5.6). This leads one inexorably to the conclusion that the film viscoelastic characteristics (see Figures 5.9 and 5.10, below) are governed not by charge variations *per se*, but rather by the dramatic solvation changes they engender. The hysteresis, in the response to potential changes, of the various parameters is then a consequence of slow solvent transfer and/or polymer reconfiguration that facilitates it.

5.3.2.3 Film shear modulus responses to redox state

5.3.2.3.1 Effect of potential

Plots of shear modulus components as functions of applied potential for four harmonics are shown in Figures 5.10 (G') and 5.11 (G''). In panels a and b, respectively, the moduli are plotted against applied potential and the resultant injected anodic charge. No G'' data are shown at the fundamental frequency, since these loss modulus values were too small to determine reliably ($G''/G' < 0.1$; see above).

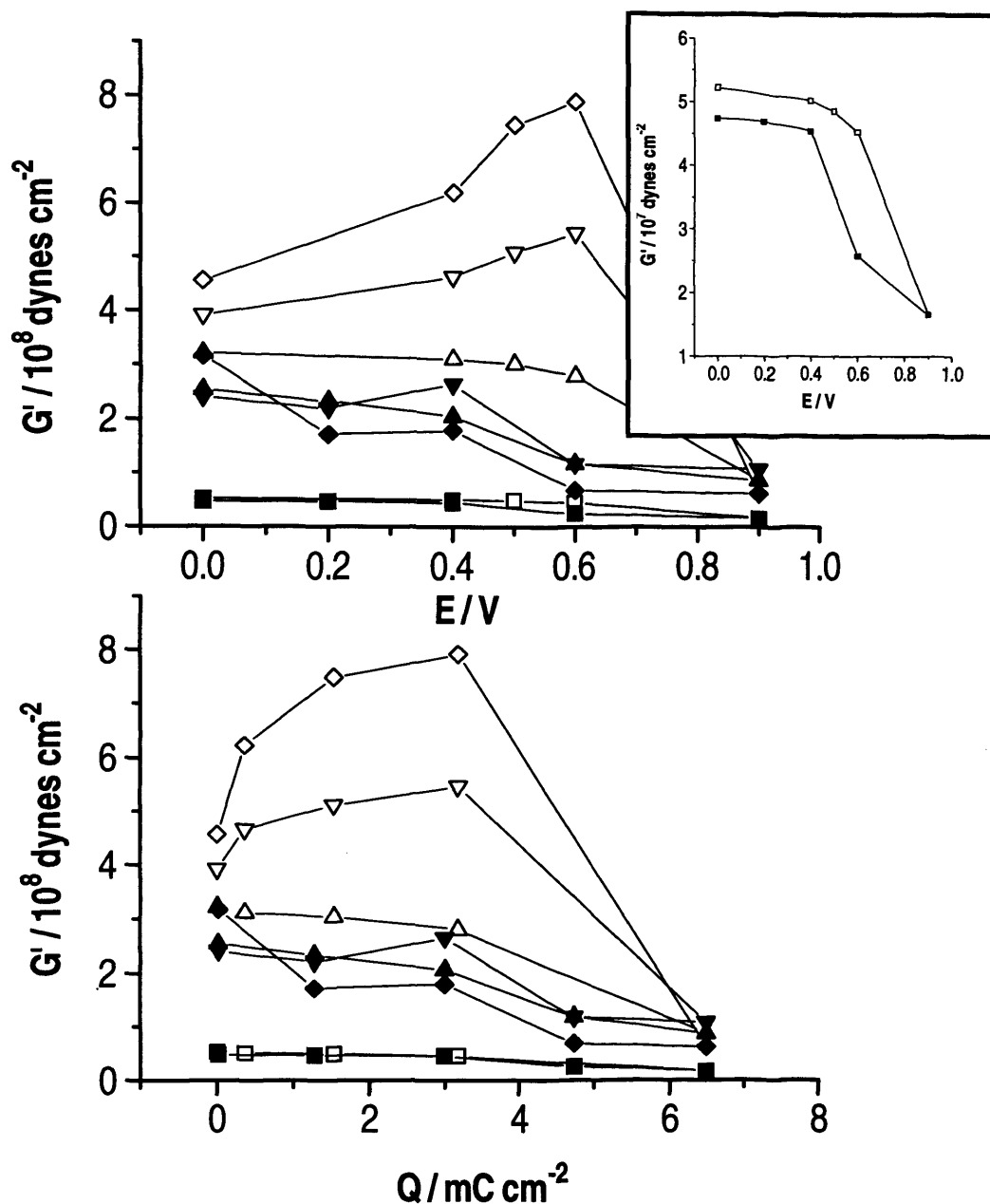


Figure 5.10: Plots of fitted storage modulus, G' , as a function of potential (panel a) and charge density (panel b) for the data of Figure 5.2 and its third, fifth and seventh harmonic analogs. Inset shows expanded view of G' at 10MHz. Symbols as in Figure 5.8.

A number of observations can be made. First, individual shear modulus components show hysteresis with respect to both potential and charge. This is more obvious pictorially for the higher frequency data, for which the shear moduli are larger, but the inset to Figure 5.10 highlights that this is true for all the data obtained. One can therefore conclude that, despite a little irreversibility (in a thermodynamic sense) of the charge injection / removal process, the shear moduli at a given potential, determined on the time scale of these measurements, reflect the immediate prior history of the film. Such history effects have been postulated

and discussed previously in the context of mobile species transfers and polymer reconfigurational processes [10]. The film density and thickness data of Figures 5.8 and 5.9 unequivocally indicate that solvent swelling/deswelling is far from equilibrium on the time scale of these measurements. Thus, the film shear moduli reflect not the film charge state *per se*, but rather the solvation state which it subsequently dictates.

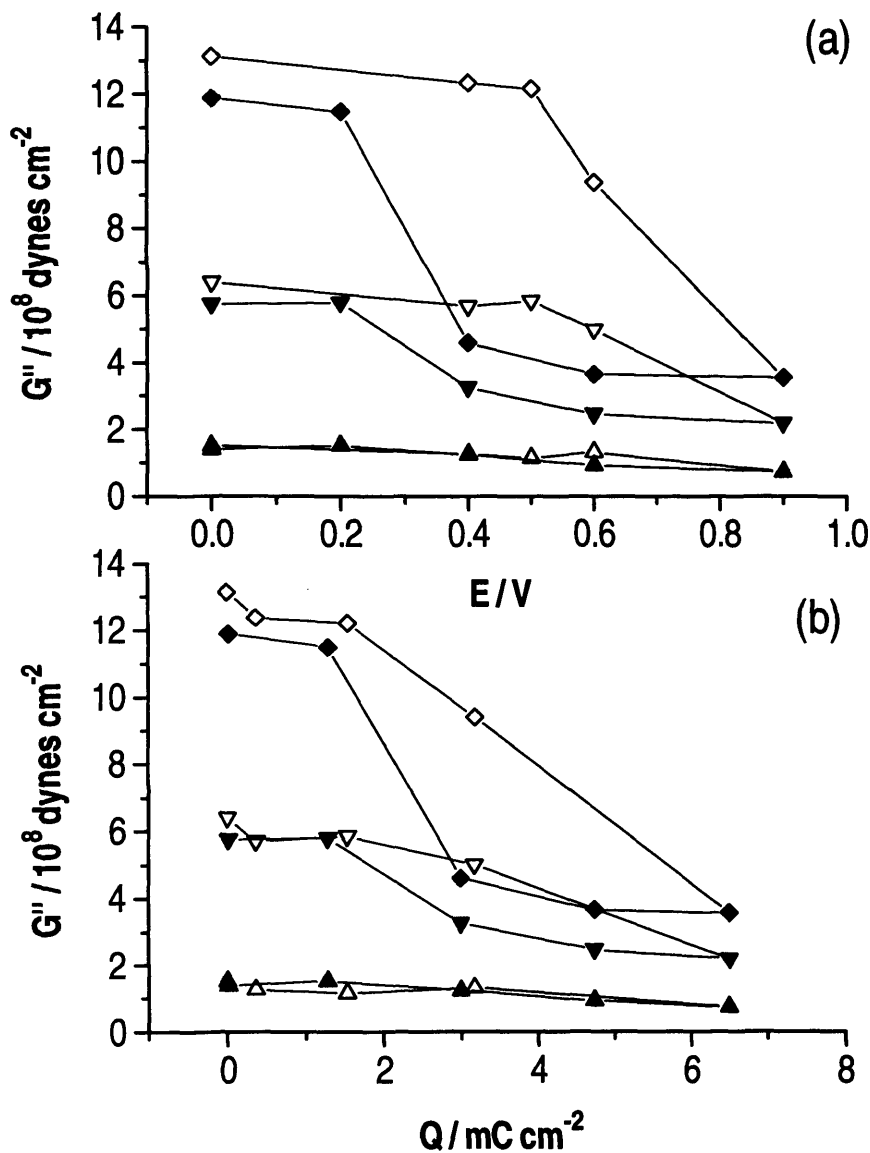


Figure 5.11: Plots of fitted loss modulus, G'' , as a function of potential (panel a) and charge density (panel b) for the data of Figure 5.2 and its third, fifth and seventh harmonic analogues. Symbols as in Figure 5.8.

This is entirely plausible, since solvents act as ‘plasticisers’ of polymeric materials. In the present context solvent transfers are extremely slow, most likely due to associated polymer reconfigurational processes which have large activation barriers. The ability of the system to achieve its ‘equilibrium’ state at the extreme of the potential excursion - but not at

intermediate values - may be due to the build-up of large electrostatic forces that trigger the reconfiguration.

Second, the oxidised (doped) polymer has significantly lower storage and loss moduli values than the reduced (undoped) polymer. This is a consequence of the entry of the solvent, which softens the film and 'lubricates' the movement of the polymer chains past each other. The direction of solvent transfer, and thus the change in shear modulus components, is readily explainable: the solvent is polar and is a better solvent for the charged (*cf* uncharged) polymer.

Third, the direction of the hysteresis in the shear modulus components mirrors that of the solvent transfers. During polymer oxidation the modulus values stay higher than one would anticipate their equilibrium values to be (based on charge). This is a consequence of the kinetic failure of solvent to *enter* the film and thus soften it. As one approaches the positive end of the potential excursion, one has a film whose charge state is largely 'oxidised', but whose solvation state is still broadly that of the reduced polymer. Analogously, during polymer reduction the modulus values stay lower than one would anticipate their equilibrium values to be (based on charge). This is now a consequence of the kinetic failure of solvent to *leave* the film. Thus, as one approaches the negative end of the potential excursion, one has a film whose charge state is largely 'reduced', but whose solvation state is still broadly that of the oxidized polymer.

Finally, the shear moduli are markedly frequency dependent. This leads to the second major objective of this study.

5.3.2.3.2 *Effect of frequency*

Qualitative inspection of Figures 5.10 and 5.11 clearly indicates that the shear moduli for PHT films in all oxidation / solvation states increase significantly with frequency, G'' more so than G' . This general behaviour is consistent with material in the glass transition region [3]. The goal of this study is to quantify this behaviour.

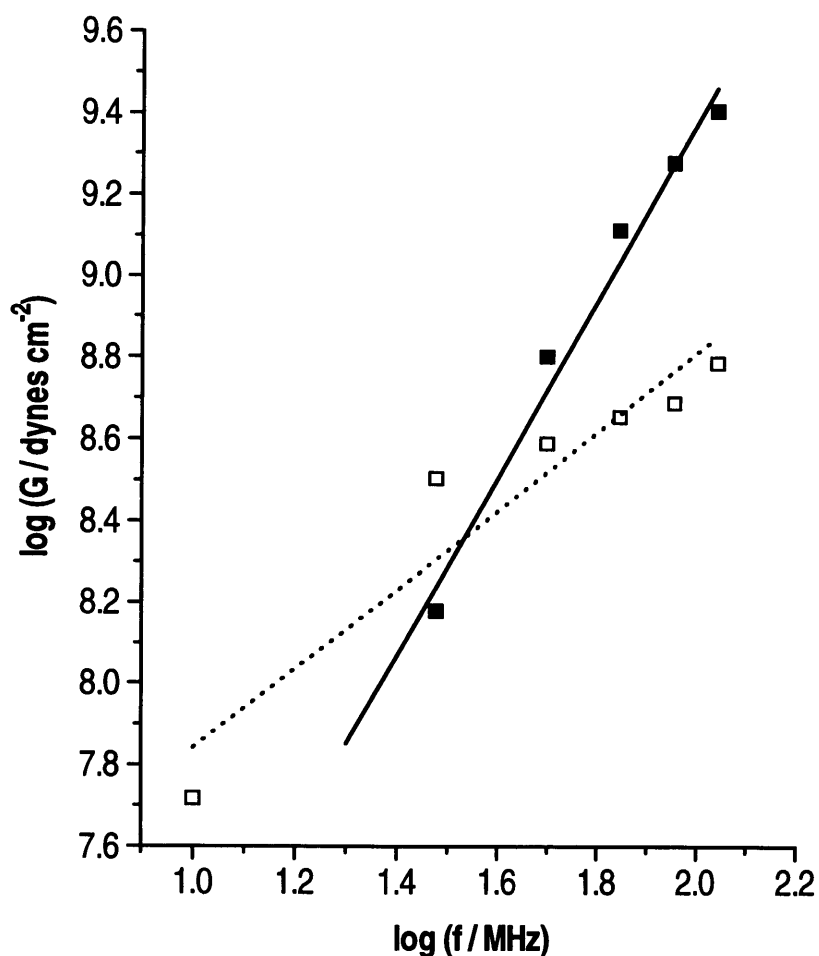


Figure 5.12: Plots of (a) $\log G'$ (\square) and (b) $\log G''$ (\blacksquare) vs $\log(f)$ for the fitted shear modulus components of Figures 5.10 and 5.11 and their analogs at 90 and 110 MHz at $E = 0$ V. Lines represent least squares fits of the data (see text).

Figure 5.12 shows the shear modulus components for the reduced film ($E = 0$ V) as a function of frequency, plotted on logarithmic axes. Since the plots appear broadly linear, least squares fits are shown to an equation of the form $\log(G) = a + b \log(f)$. For the G' data $b = 0.97 (\pm 0.15)$ ($R = 0.95$; $n = 6$) and for the G'' data $b = 2.19 (\pm 0.18)$ ($R = 0.99$; $n = 5$). Although there is clearly scatter on the data and there is only a one order of magnitude spread in the frequency regime, these data imply $G' \propto \omega$ and $G'' \propto \omega^2$.

Figure 5.13 shows the corresponding plots for the oxidized film ($E = 0.9$ V). The situation here is less straightforward. Specifically, the G' data are non-monotonic with frequency, showing a maximum storage modulus at ca. 50 MHz, and the G'' values are not linear. (The lines drawn on the plot are not an attempt to fit the data, but rather lines of slope 1 and 2 for G' and G'' , respectively, to allow comparison with the behaviour of the reduced film.)

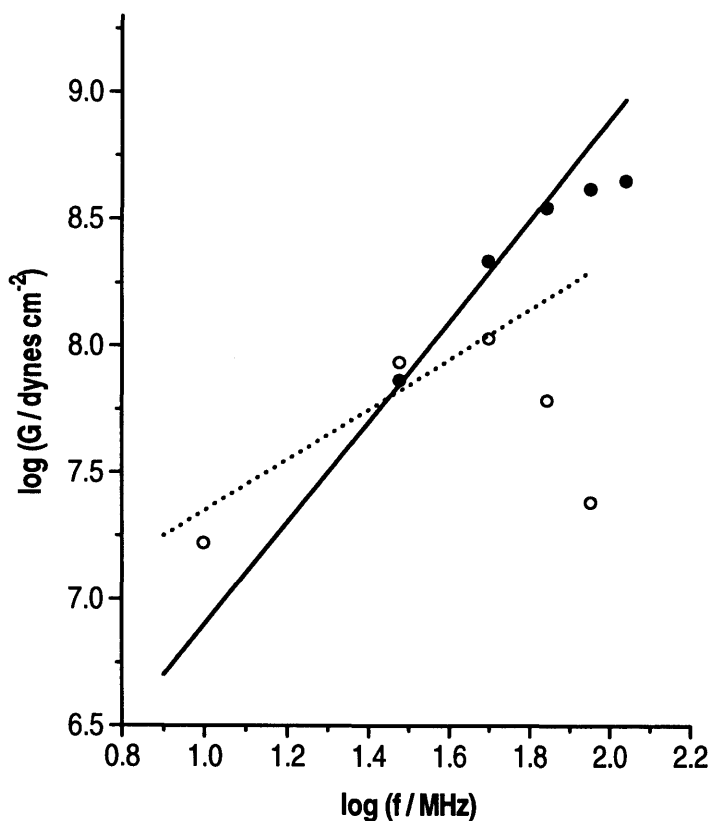


Figure 5.13: Plots of (a) $\log G'$ (O) and (b) $\log G''$ (●) vs $\log(f)$ for the fitted shear modulus components of Figures 5.10 and 5.11 and their analogs at 90 and 110 MHz at $E = 0.9V$. Dashed and full lines, respectively, are of slope 1 and 2 (see text).

5.4 DISCUSSION

The long-term goal of this study is the manipulation of film shear moduli. En route to this, the immediate goal is to rationalise $G(\omega, E)$, i.e. the frequency and potential (charge) variations of the shear modulus. In general terms, despite a huge volume of literature (discussed elsewhere [1-3]) on the viscoelastic characteristics of *bulk* polymers, there has been relatively little progress for *thin films*. Here the ability of the simple Voigt and Maxwell models are tested, which have been widely used for bulk materials, to explain the functional variations of G' and G'' .

5.4.1 Constitutive relations

The goal of this section is to derive a model for the polymer's viscoelastic properties as a function of excitation frequency and oxidation state (doping). The frequency dependence of modulus is modelled by postulating a *constitutive relation*, i.e., a relationship between stress (T) and strain (S) for a material. When a stress is applied to a material, it results in a

combination of elastic deformation (reversible energy storage) and dissipation (irreversible energy loss).

Purely elastic deformation results in a constitutive relationship given by Hooke's law: $T = \mu S$, where μ is the stiffness of the material. This constitutive relationship is commonly represented by an ideal spring. Purely viscous dissipation arises in a Newtonian fluid, described by the constitutive relationship: $T = \eta(dS/dt)$, where η is the viscosity, t is the time, and dS/dt is the strain rate. This behaviour is commonly represented by an ideal 'dashpot' - a plunger in a fluid. A polymer is a complicated material that includes both elastic deformation and viscous dissipation i.e. it is viscoelastic.

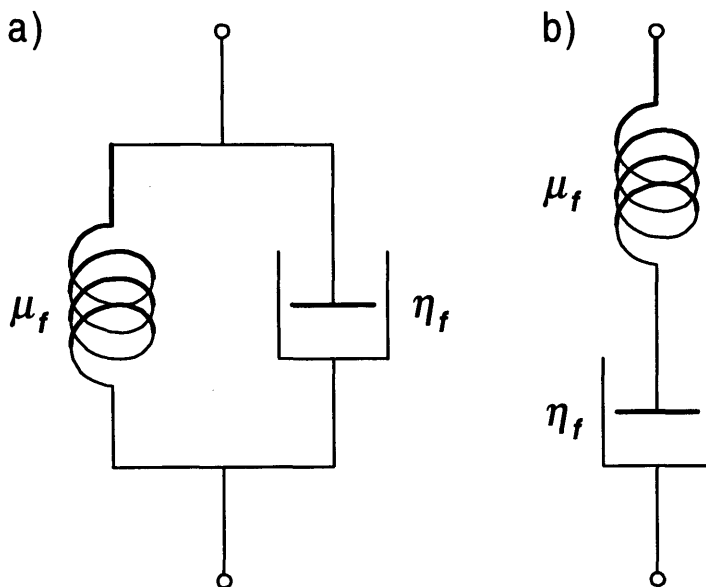


Figure 5.14: Two-element models leading to constitutive relationships for a polymer: (a) Voigt model, (b) Maxwell model.

The viscoelastic behaviour of a polymer can be approximated by various combinations of springs and dashpots [2]. The manner in which they are connected gives rise to a unique frequency dependence that can be tested experimentally. If the simplest approximations are considered that account for both energy storage and dissipation, there are two possibilities: a series and a parallel combination of spring and dashpot.

The Voigt model, Figure 5.14a, consists of a *parallel* combination of spring and dashpot. This combination implies equal strains across the two elements, while the stresses are additive. This gives rise to the following constitutive relation:

$$\mathbf{G} = \frac{T}{S} = \mu_f + j\omega\eta_f \quad (5.3)$$

where it is explicitly shown that μ and η refer to a film, via the use of a subscript 'f', \mathbf{G} is the resulting complex shear modulus and $j = \sqrt{-1}$. The equation can be expressed in the form

$$\mathbf{G} = \mu_f(1 + j\omega\tau) \quad (5.4)$$

where $\tau = \eta_f/\mu_f$ is a characteristic relaxation time.

The Maxwell model, Figure 5.14b, consists of a *series* combination of the spring and dashpot. This combination implies that the stresses across each element are the same, while the strains are additive. This gives rise to the constitutive relation:

$$\mathbf{G} = \frac{T}{S} = \left(\frac{1}{\mu_f} + \frac{1}{j\omega\eta_f} \right)^{-1} \quad (5.5)$$

With a little algebraic manipulation, Equation (5.5) can be expressed in the form:

$$\mathbf{G} = \mu_f \left(\frac{(\omega\tau)^2}{1 + (\omega\tau)^2} + j \frac{\omega\tau}{1 + (\omega\tau)^2} \right) \quad (5.6)$$

where the symbols have the same significance as above. For each model, G' and G'' , respectively, are identified with the real and imaginary components of expressions (5.4) and (5.6).

5.4.2 Frequency dependence of shear modulus

The Voigt model predicts a very simple frequency dependence, illustrated in Figure 5.15a. The storage modulus is independent of frequency ($G' = \mu_f$), while the loss modulus is proportional to frequency ($G'' = \omega\eta_f$).

The Maxwell model predicts a somewhat more complicated frequency dependence, illustrated in Figure 5.15b. G' increases monotonically with frequency, saturating at μ_f , while G'' goes through a peak (maximum value of $\mu_f/2$) at $\omega\tau = 1$. The low frequency ($\omega\tau \ll 1$) limiting characteristics are quadratic and linear respectively for G' and G'' .

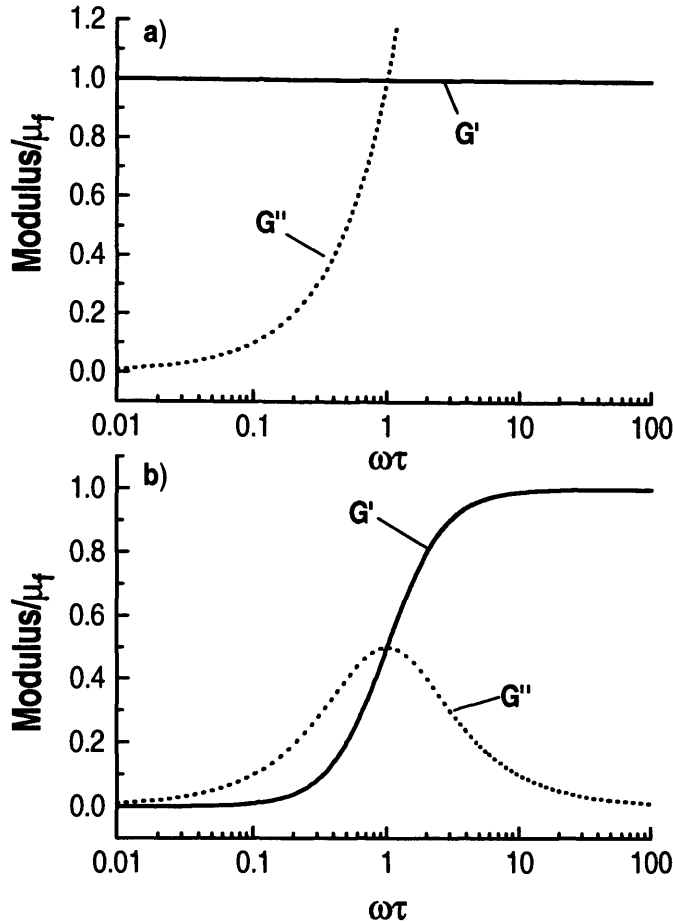


Figure 5.15: Frequency dependencies of the storage (G') and loss (G'') moduli predicted by (a) the Voigt model and (b) the Maxwell model.

The Maxwell model exhibits behaviours more in line with what is commonly observed with a polymer. When a polymer is deformed slowly (compared with the time for segmental chain motion), applied stress is taken up by inter-chain movements, i.e., chains slip past one another. This results in viscous dissipation predominating. When the polymer is deformed rapidly, the chains do not have time to move past one another; instead, the strain is taken up by deformation of the individual polymer chains. This results in elastic storage predominating. The Maxwell model gives both of these extremes. At low frequencies (when $\omega\tau \ll 1$) viscous dissipation predominates, while at high frequencies (when $\omega\tau \gg 1$) elastic storage predominates. The frequency dependence of the Maxwell model, shown in Figure 5.15b, illustrates a *glass-to-rubber transition*. Low $\omega\tau$ gives a low storage modulus (G'), corresponding to a rubbery polymer, and high $\omega\tau$ gives a large G' , corresponding to a glassy polymer. Between these limits, the elastic and viscous components match, so that G'' is maximum. (This model can be improved to more closely describe the behaviour in

the rubbery regime by adding a spring in parallel to the Maxwell elements with a modulus that matches that of a rubbery polymer - approximately 10^7 dynes cm^{-2} .)

5.4.3 Solvent effects

A central feature of these - and indeed any other *in situ* electrochemical - experiments is the presence of solvent. Anecdotally, it is generally acknowledged that solvent penetrates surface-immobilised polymer films, although the extent to which this occurs, the rate at which it happens and the effects it includes are subject to some debate. One must therefore consider what effect solvent permeation might have on the polymer films considered here, and how this might be manifested through film viscoelastic characteristics.

The glass to rubber transition exhibited by the Maxwell model can also be induced by varying relaxation time (τ) at fixed frequency (effectively ω). Since $\tau = \eta/\mu_f$, this parameter can be controlled either through the modulus or viscosity of the polymer. It is well known that the glass-to-rubber transition in a glassy polymer can be induced either by increasing the temperature or through solvent absorption [1, 2]. In either case, the polymer viscosity - and hence τ - is decreased, thereby inducing a glass-to-rubber transition. The glassy regime may thus be associated with either high frequency, low temperature, or pure (solvent-free) polymer. The rubbery regime may also be associated with low frequency, high temperature, or high solvent concentration in the polymer.

The effect of solvent absorption can be modelled by postulating [1] that polymer viscosity (as represented by the viscous element η_f in the Maxwell model) varies because incorporated solvent contributes 'free volume' to the material. This free volume 'lubricates' the interaction between polymer chains, thereby decreasing the viscosity. If the amount of free volume increases linearly with the amount of incorporated solvent, then the observed viscosity in the presence of solvent incorporation (η_f) will be decreased from its value ($\eta_{f,0}$) in the absence of solvent according to:

$$\eta_f = \eta_{f,0} \exp(-kV_s) \quad (5.7)$$

where k is the plasticization constant and V_s is the free volume fraction of the absorbed solvent. According to the Maxwell model (see above), this decrease in η_f causes the relaxation time (τ) to decrease and G' and G'' to decrease (for $\omega\tau < 1$).

Cursory comparison of Figure 5.15a with the data of Figures 5.10-5.13 shows that the Voigt model is inappropriate: it simply fails to predict any variation of G' with ω . Qualitatively, the increasing values of G' and G'' with frequency (see Figures 5.10 and

5.11) are consistent with the Maxwell model (Figure 5.14b) in the rubbery regime (when $\omega\tau < 1$). Quantitatively, the power law variations (Figures 5.12 and 5.13) are not explained by the Maxwell model. More sophisticated (multi-element) spring and dashpot models may be more successful, but these are not pursued here on the grounds that such models would involve a proportionate increase in the number of fitting parameters, so that uniqueness of fit would become an issue.

The variations of shear moduli components with potential are more complex and interesting. The experimental protocol involved measurements at fixed potentials and a prior “hold” at the selected potential with the intent of allowing pre-equilibration before data acquisition. Thus, a film maintained at any given potential would be expected to have a unique composition and structure appropriate to that applied potential. Simplistically, one would then expect the shear moduli, at any specified frequency, to be single valued at any given potential. The fitted data (Figures 5.8-5.11) are clearly inconsistent with this view. That this is *not* a feature of the fitting procedures is clearly indicated by the presence of hysteresis in the raw data (see Figures 5.2-5.5). Possible reasons for the observed hysteresis are therefore explored.

One possibility is that, despite similar globally averaged composition, the films may have *spatial variations* within them that reflect their prior history (here, direction of approach to a given potential). The quartz resonator is most sensitive to the state of the film nearest the electrode. Hence, spatial variation of viscoelastic properties could then lead to the hysteresis in the shear modulus responses to applied potential shown in Figures 5.10a and 5.11a. Since the decay length for displacement in the film varies inversely with frequency (see above), the hysteresis from this source would increase with frequency, as is indeed observed. Such variations could pertain to the oxidation state (doping level) and/or the local solvent concentration. They might particularly be expected when a significant fraction of the film is in the reduced state (for which the conductivity is low) due to potential variations across the film.

A subsidiary question is *how might such spatial variations arise?* For ‘conducting’ polymers, the electronic and ionic conductivities of the two redox states (doped and undoped) are very different. For different redox switching directions this leads to different conversion mechanisms, e.g. homogeneous throughout the film, from the inside outwards or from the outside inwards; this point has been explored for poly(3-methylthiophene) films [11].

The other possible causes of hysteresis considered here are associated with failure to establish equilibrium film composition on the time scale (minutes) of the experiment. Most obviously, this might be associated with slow charge transport or slow solvent transport. Note that these situations *need not* be associated with spatial compositional inhomogeneity (see above), i.e. the film may be spatially uniform, but have non-equilibrium, ion and/or solvent populations.

In case of slow ion transfer, the charge and shear modulus response to potential would show equivalent hysteresis. Although there is some hysteresis in the Q vs E plot (see Figure 5.6), this effect is much less pronounced than in the G' and G'' vs E plots (see Figures 5.10a and 5.11a). That failure to establish charge equilibrium is not the predominant cause of the shear modulus hysteresis is confirmed by the presence of hysteresis in the G' and G'' vs Q plots (see Figures 5.10b and 5.11b).

In the case of slow solvent transfer, the hysteresis in G' and G'' vs E plots would greatly exceed that in the Q vs E plots. This is exactly what is found (see Figures 5.10b and 5.11b), indicating that the rate of solvent equilibration between film and the solution is slow compared with the experimental time scale. It is interesting in this respect to note that the film density and thickness data (see Figures 5.8 and 5.9), which were acquired sequentially for the different harmonics, show no temporal 'drift'. Thus, one can conclude that the film solvent population at each potential is not changing significantly on the time scale of these measurements. One could postulate various models for the rate of solvent transfer, and use the time dependence of shear modulus variation as a measure of solvent transfer in order to determine the appropriate rate parameter; such investigations would involve much longer time scale observations than used here.

One interesting supplementary question is the origin of the maxima in the shear modulus values at partial redox conversion. This may be due to the interplay of two opposing effects that increase, but in a functionally different manner, upon film oxidation: electrostatic stiffening and solvent plasticisation. At low doping levels, the former appears to predominate, since there is insufficient driving force to cause significant solvent entry. At higher doping levels, there is a significant driving force for solvent entry for the latter to predominate.

There has been one study reported on the 'electroplastic behaviour' of PHT [12], in which values of $G' \approx 8 \times 10^9$ dynes cm^{-2} and $G'' \approx 6 \times 10^8$ dynes cm^{-2} (based on $\tan \delta \approx 0.07$) were found. However, the material used in that study was very different to the material used in this one. First, the 'films' were sufficiently thick (ca. 0.1 mm) to be considered as

bulk material, whereas thin ($< 1 \mu\text{m}$) films were studied here. Second, most of the samples studied by Shiga *et al* were of chemically (*cf.* electrochemically) prepared polymer. Third, their technique used freestanding films exposed to air, not solvent. Consequently, their polymers had G values indicative of ‘glassy’ materials, whereas the films analysed in this study have G values indicative of viscoelastic materials. Fourth, the simple mechanical nature of their measurements meant that the frequency range studied was 0.1-100 Hz, i.e. many orders of magnitude lower than in this study. Furthermore, the *in situ* nature of this study has allowed the effect of polymer charge state to be studied in a systematic manner.

Finally some general observations can be made on the variations of shear modulus determined here. The data presented here indicate that PHT films exposed to propylene carbonate solutions are viscoelastic and rather ‘lossy’. The primary effect of oxidation is to cause the entry of solvent, which plasticises the film; however there are kinetic limitations associated with solvent transfer. This situation can be qualitatively visualised using the scheme-of-squares model illustrated in Figure 5.16. This type of model has been used to describe slow redox driven solvent transfer in *rigid* electroactive films at TSM resonators; there the principal manifestations were in the gravimetric response, optimally demonstrated though hysteresis in ΔM vs Q plots. Here, the underlying mobile species transfers are identical, but the principal manifestations of slow solvent transfer are in the viscoelastic response, which is demonstrated here through hysteresis in G vs Q plots.

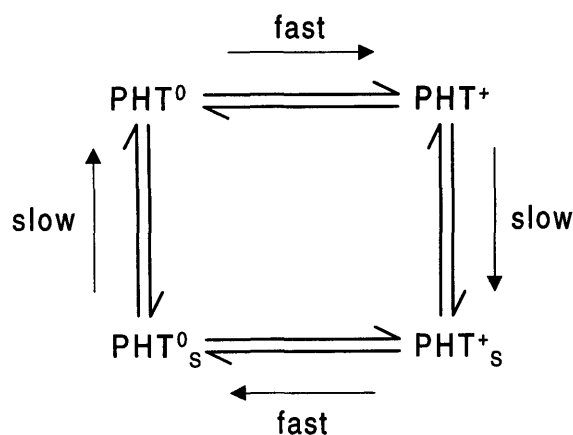


Figure 5.16: Scheme-of-squares model for PHT in two oxidation states (indicated by superscripts ‘0’ and ‘+’), each of which may exist in a solvated form (PHT_s^0 and PHT_s^+) and an unsolvated form (PHT^0 and PHT^+). Redox state changes (doping / undoping) are represented by ‘horizontal’ translations and solvation state changes are represented by ‘vertical’ translations in the diagram.

5.5 CONCLUSIONS

Quartz crystal impedance measurements are a rich source of information on electroactive polymer film rheological properties, parameterised through shear moduli. Thin films of poly(3-hexylthiophene) (PHT) exposed to propylene carbonate electrolyte solutions are viscoelastic at 25°C, and show film mechanical resonance effects. The storage and loss moduli vary significantly with applied potential and operating frequency (in a range 10 - 110 MHz). The p-doped film is substantially softer than the undoped film and G' and G'' variations with potential can show maxima at partial p-doping. Both storage and loss moduli for undoped PHT films increase monotonically with frequency in the range studied, but for doped PHT films the storage modulus goes through a maximum at ca. 50 MHz under the conditions employed. A Voigt model is qualitatively incompatible with these observations, and a Maxwell model can qualitatively explain some features.

Even in fixed potential - nominally 'equilibrium' - experiments there is dramatic hysteresis in shear modulus values determined during stepwise doping and undoping. From the $G-Q-E$ relationship, one can deduce that this is a consequence of extremely slow solvent transfer between the film and the solution phase. Qualitatively, this can be modelled using a scheme of squares representation involving doped and undoped PHT, both in solvated and unsolvated forms, in which redox transformations (coupled electron/ion transfer) are much faster than the associated solvation changes (solvent transfer). These non-equilibrium solvation states may or may not be associated with spatial compositional heterogeneity.

On the basis of the data obtained it has been shown that appropriate selection of operating frequency, applied potential and time scale offer the prospect of manipulating film viscoelastic parameters in a controllable manner over several orders of magnitude, from 'rubbery' to near 'glassy' behaviour.

5.6 REFERENCES

1. J. Ferry, Viscoelastic Properties of Polymers, John Wiley & Sons, Inc., New York, (1961).
2. J. J. Aklonis and W. J. MacKnight, Introduction to Polymer Viscoelasticity, Wiley-Interscience, New York, (1983).
3. W. W. Graessley, Faraday Symposia of the Chemical Society:7 (1983).
4. V. E. Granstaff and S. J. Martin, J. Appl. Phys. 75:1319 (1994).
5. R. Lucklum, C. Behling, R. W. Cernosek, and S. J. Martin, Journal of Physics D-Applied Physics 30:346 (1997).

6. H. L. Bandey, A. R. Hillman, M. J. Brown, and S. J. Martin, *Far. Disc.:*105 (1997).
7. Handbook of Conducting Polymers, Marcel Dekker, Inc., New York, (1986).
8. A. R. Hillman, M. J. Brown, and S. J. Martin, *J. Am. Chem. Soc.* 120:12968 (1998).
9. CRC Handbook of Chemistry and Physics, CRC Press, Cleveland, (1975).
10. A. R. Hillman and S. Bruckenstein, *J. Chem. Soc., Far. Trans.* 89:339 (1993).
11. F. Chao and M. Costa, *Synth. Met.* 39:97 (1990).
12. T. Shiga and A. Okada, *J. Appl. Polym. Sci.* 62:903 (1996).

CHAPTER 6

MANIPULATION OF POLYMER FILM VISCOELASTICITY: THE EFFECT OF TEMPERATURE

6.1 INTRODUCTION

The previous chapter explored an effective way of manipulating the shear modulus of thin PHT films, immersed in propylene carbonate (PC) electrolyte solution, by adjusting the applied potential and frequency. An additional way of controlling the shear modulus of a polymer is by altering its temperature. Decreasing a polymer's temperature has a similar effect on the measured shear modulus to increasing the frequency at which it is perturbed. Hence, by decreasing/ increasing the temperature and increasing/ decreasing the perturbing frequency, one can gain access to a significantly expanded range of the polymer's material properties. This is established practice for the manipulation of bulk polymer properties [1, 2]. Williams, Landel and Ferry extensively investigated the relationship between temperature and frequency, for *bulk* polymers, and formulated the equation now known as the WLF equation [3]. An attempt is made here to apply the principles of the WLF equation to the analogous situation of thin electroactive *films* exposed to electrolyte solution.

6.2 EXPERIMENTAL

PHT films were deposited and then transferred to background electrolyte in an identical manner to that described in Section 5.2 of the previous chapter. The temperature was thermostatted at 25°C using the electrochemical cell shown in Figure 3.2. Cyclic voltammetry (0.0-0.9 V, scan rate 2 mV s⁻¹: see Figure 4.1 in Chapter 4) indicated chemically reversible behaviour. Static potentials were then applied to the film according to the protocol described in Section 3.7.1. Once this was completed, a second cyclic voltammogram assured that negligible irreversible change had occurred within the film during the previously applied static potential program. This procedure was subsequently repeated at temperatures of 5, 50 and 90°C.

6.3 RESULTS

Large amounts of raw crystal impedance data were recorded for PHT films exposed PC electrolyte solutions at a variety of film oxidation states, frequencies and temperatures. Raw

crystal impedance spectra were recorded at a total of 9 redox states (including data acquired at progressively more positive and negative applied potentials during the fixed potential sequence) between potential limits of 0.0 V and 0.9 V. Each of these readings was recorded at 4 temperatures and 6 separate frequencies. This led to the accumulation of over 200 spectra that required detailed and time consuming data fitting analysis.

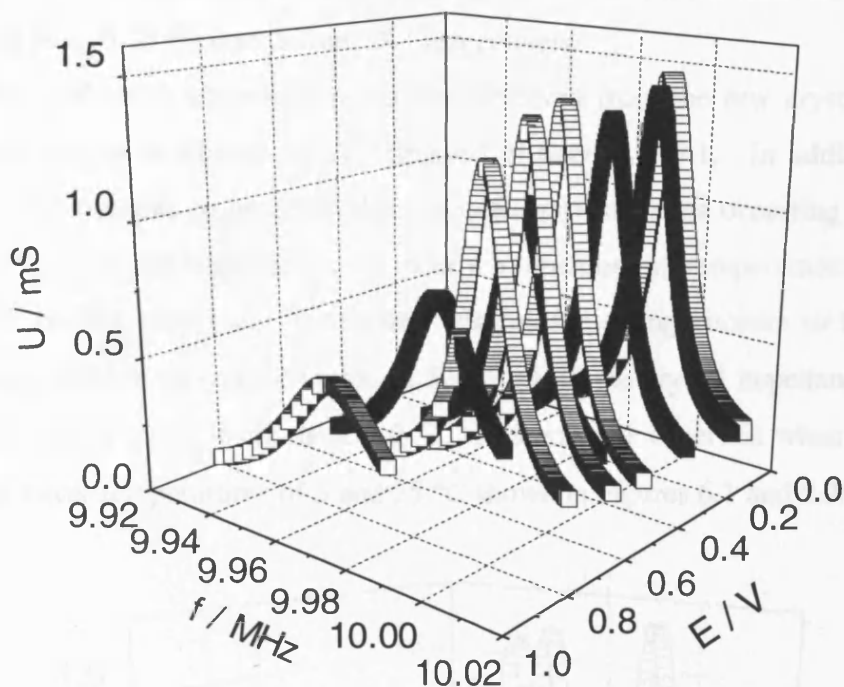


Figure 6.1: Raw crystal impedance spectra for a PHT film exposed to 0.1 mol dm^{-3} TEAPF₆ – propylene carbonate. Open symbols: data acquired at progressively more positive applied potentials, commencing at 0 V; filled symbols: data acquired at progressively more negative applied potentials, commencing at 0.9 V. Data taken at the fundamental frequency (nominally 10 MHz) and at 5 °C.

The data set presented here was recorded using the same film that was analysed in the preceding chapter. Therefore, raw crystal impedance data arising from measurements made on this film at the four temperatures studied, appear almost identical to those presented in Chapter 5 and are not repeatedly shown here. Similarly, following full analysis of the crystal impedance spectra, the dependence of film density and thickness upon applied potential is similar to those shown in Figures 5.8 and 5.9 respectively.

Figures 6.1 and 6.2 show representative crystal impedance spectra for this PHT film as a function of the applied (fixed) potential. Within each figure there are two sets of spectra, acquired at progressively increasing and progressively decreasing applied

potentials, *i.e.* during “doping” of a fully reduced (uncharged) PHT film and during “undoping” of a fully oxidised (positively charged) PHT film. In the interests of brevity, figures for all of the frequencies and temperatures studied are not shown here. Data recorded at 5 °C and 50 °C, at the fundamental frequency, are chosen to represent the spread of behaviour occasioned by choice of temperature. Crystal impedance spectra recorded for the same PHT film, thermostatted at 25 °C, at the fundamental and eleventh harmonics can be seen in Figures 5.2 and 5.3 respectively.

Similar qualitative observations may be observed from the raw crystal impedance data displayed in this section to those displayed in Section 5.3.1. In addition to those observations, it is possible to ascertain that viscoelastic phenomena occurring in PHT films exposed to PC electrolyte solutions are clearly a function of temperature. Figure 6.2 indicates that, on this time scale, irreversible viscoelastic change occurs to the PHT film once it has been held in its oxidised state at 50 °C, since the crystal impedance spectra do not return to their original positions at 0.0 V. This was not observed when the film was maintained at lower temperatures of 5 and 25 °C shown in Figures 6.1 and 5.2 respectively.

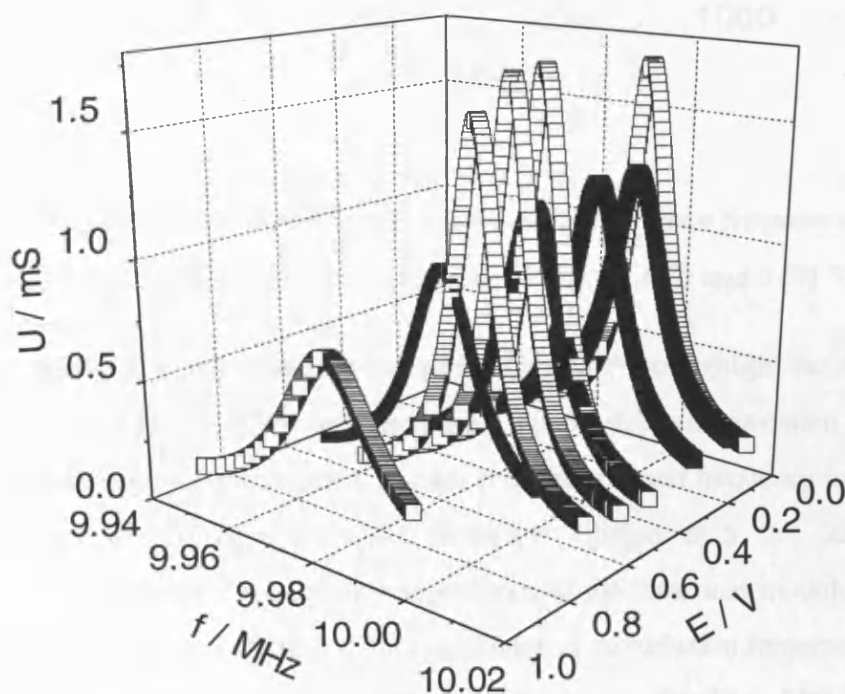


Figure 6.2: Raw crystal impedance spectra for a PHT film exposed to 0.1 mol dm^{-3} TEAPF_6 – propylene carbonate. Open symbols: data acquired at progressively more positive applied potentials, commencing at 0 V; filled symbols: data acquired at progressively more negative applied potentials, commencing at 0.9 V. Data taken at the fundamental frequency (nominally 10 MHz) and at 50 °C.

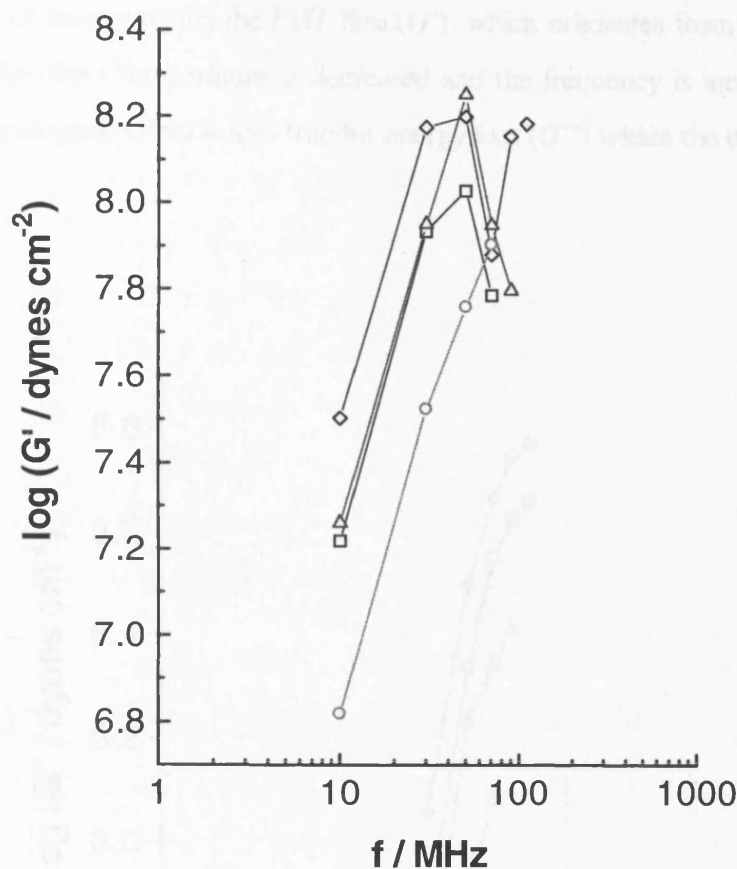


Figure 6.3: Dependence of shear storage modulus, $\log G'$, upon frequency, f , for an oxidised ($E=0.9V$) PHT film at 90 (\circ), 50 (Δ), 25 (\square) and 5 (\diamond) $^{\circ}C$.

The fitted data presented in this chapter were specifically chosen to highlight the dependence of the shear modulus of thin PHT films upon frequency, temperature and oxidation state. Figure 6.3 displays the relationship between shear *storage* modulus, G' , and frequency for the oxidised PHT film immersed in propylene carbonate electrolyte solution, at 5, 25, 50 and 90 $^{\circ}C$. Similarly, Figure 6.4 displays the frequency dependence of the shear *loss* modulus, G'' , also at the four different temperatures studied. The magnitudes of perturbation frequencies applied to the oscillator were the fundamental, nominally 10 MHz, and 30, 50, 70 and 90 MHz. Where shear modulus data were not displayed corresponding to all of the frequencies studied, this was because that particular component, either G' or G'' , was an order of magnitude smaller than its counterpart, either G'' or G' respectively.

General trends within Figures 6.3 and 6.4 indicate that, as one might expect, heating the PHT film causes it to be considerably softened. As displayed in the previous chapter,

it is also apparent that increasing the applied frequency leads to polymer film stiffening. These trends are generally reflected throughout the data presented in this chapter. Figure 6.3 shows how the *storage* of energy within the PHT film (G'), which originates from the TSM oscillator, is increased as the film's temperature is decreased and the frequency is increased. Figure 6.4 shows how the analogous effect is also true for energy *loss* (G'') within the overlaying PHT film.

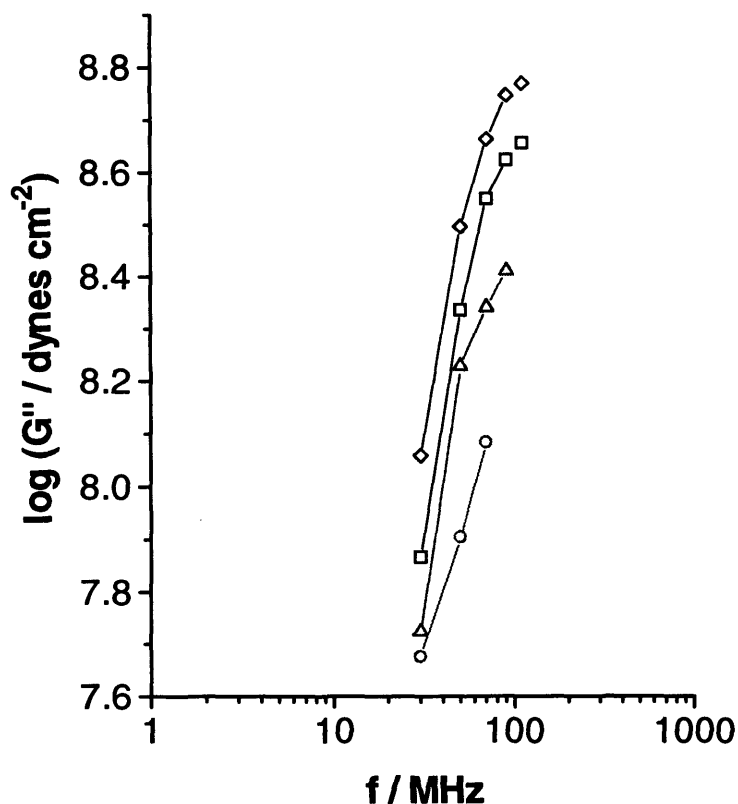


Figure 6.4: Dependence of shear loss modulus, $\log G''$, upon frequency, f , for an oxidised ($E=0.9V$) PHT film at 90 (O), 50 (Δ), 25 (\square) and 5 (\diamond) °C.

It is important to note the extensive range of polymer viscoelastic properties displayed in Figures 6.3, 6.4 and broadly throughout the data presented herein. In Figure 6.3 $\log(G' / \text{dynes cm}^{-2})$ varies from 6.8 to approximately 8.2 within the temperature and frequency range that could be reliably analysed using the crystal impedance data fitting procedures. Similarly, $\log(G'' / \text{dynes cm}^{-2})$ ranges from approximately 7.7 to 8.8. In other words the polymer's properties are ranging between those of a rubbery solid and those of a glassy

solid. Such enormous variations in polymer viscoelastic properties unequivocally indicate that the polymer is within its glass transition region under these conditions.

6.4 DISCUSSION

The immediate aim of this work is to rationalise $G(\omega, T)$, i.e. the frequency and temperature variations of the PHT film's shear modulus. This is complementary to the aims of Chapter 5 which were to rationalise $G(\omega, E)$ and makes a significant contribution towards the global goal of the manipulation of film shear moduli. The fitted data presented in the previous section, which have arisen from raw crystal impedance data measured for PHT films immersed in PC electrolyte solutions, effectively display four segments of a PHT shear modulus master curve, which arise from the four polymer temperatures studied. In this section it is shown how these segments can be overlaid to (partially) obtain a master curve, within the limits of the frequency and temperature range applied.

6.4.1 The Williams, Landel and Ferry (WLF) equation

The WLF equation was introduced in Section 2.7. According to this equation, changing a polymer's temperature has the inverse effect on relaxation time (and therefore measured shear modulus) to altering the perturbation frequency. Hence, the shift factor, a_T , allows one to translate temperature changes into changes in frequency and *vice versa*. In order to calculate a_T using the WLF equation it is necessary to know the glass transition temperature of the polymer being studied. In this case the glass transition temperature is unknown.

Many factors govern the glass transition temperature, T_g , of polymers including chain length, degree of cross-linking, plasticisation due to the presence of solvent and electrolyte or the rigidification of the polymer backbone, for example due π -electron delocalisation or the introduction of charged sites. Consequently, it is necessary to shift the data displayed in Figures 6.3 and 6.4 manually in order to gain insight into the shape of the shear modulus master curve. The relative magnitudes of the shifts can be used to increase understanding of the magnitude of the glass transition temperature of the PHT film.

Figures 6.5 and 6.6 show how the data of Figures 6.3 and 6.4, respectively, can be aligned to form a section of shear modulus master curve. This was also achieved for the PHT film in its reduced state in Figures 6.7 and 6.8.

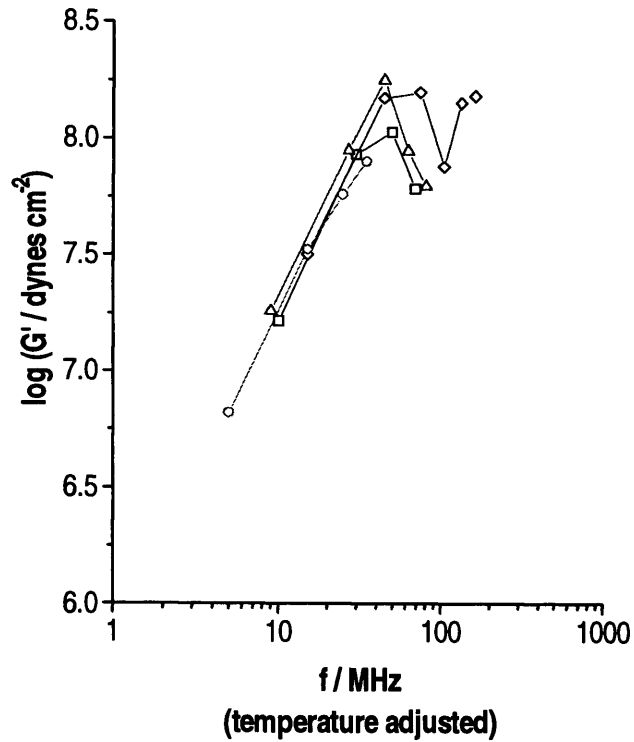


Figure 6.5: Dependence of shear storage modulus, $\log G'$, upon (temperature adjusted) frequency, f , for an oxidised ($E=0.9V$) PHT film at 90 (O), 50 (Δ), 25 (\square) and 5 (\diamond) °C.

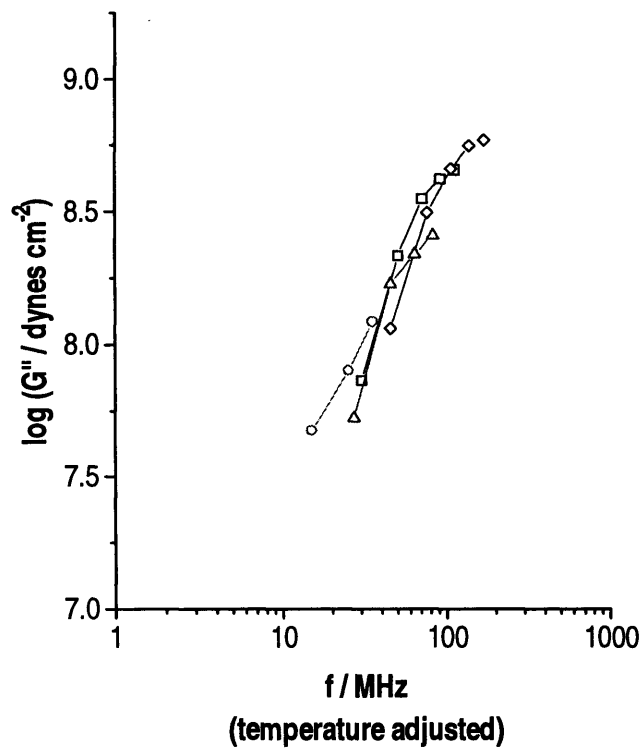


Figure 6.6: Dependence of shear loss modulus, $\log G''$, upon (temperature adjusted) frequency, f , for an oxidised ($E=0.9V$) PHT film at 90 (O), 50 (Δ), 25 (\square) and 5 (\diamond) °C.

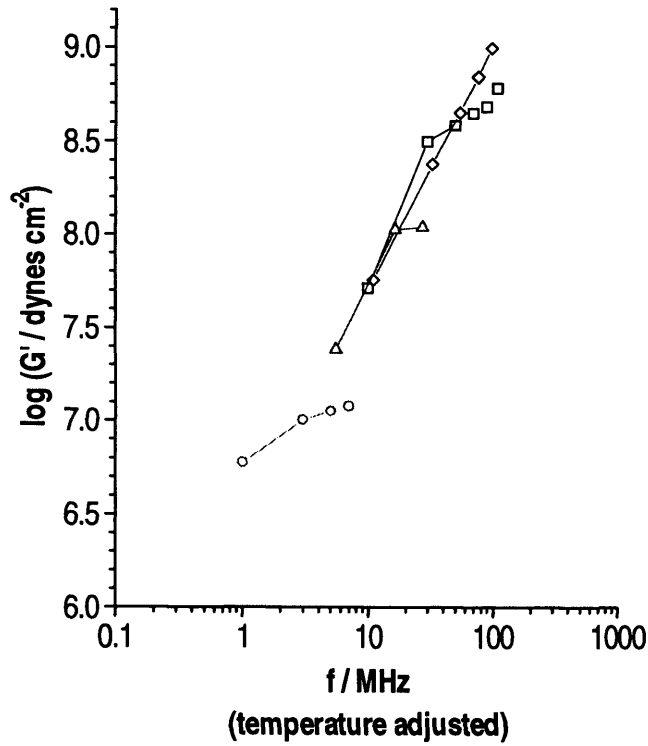


Figure 6.7: Dependence of shear storage modulus, $\log G'$, upon (temperature adjusted) frequency, f , for a reduced ($E=0.0V$) PHT film at 90 (\circ), 50 (Δ), 25 (\square) and 5 (\diamond) $^{\circ}C$.

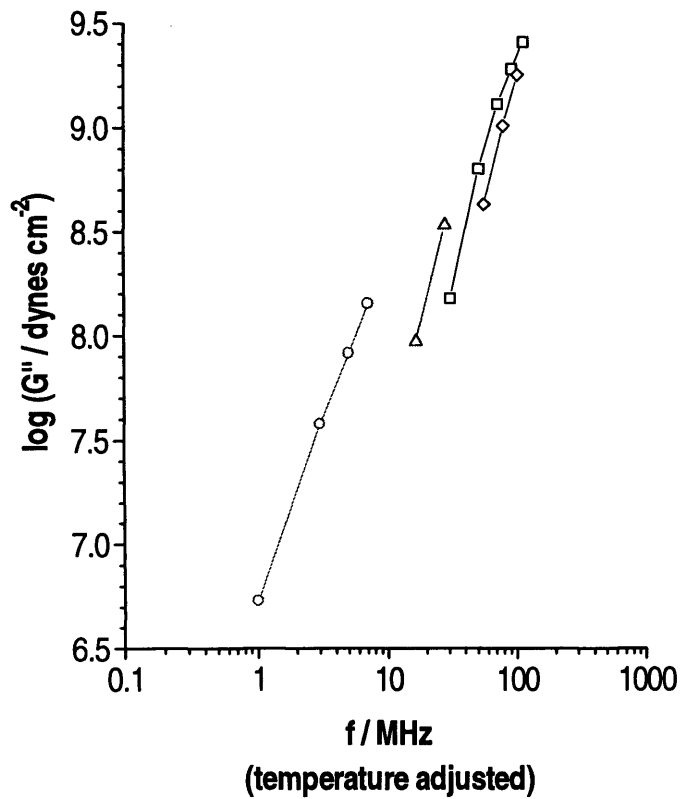


Figure 6.8: Dependence of shear loss modulus, $\log G''$, upon (temperature adjusted) frequency, f , for a reduced ($E=0.0V$) PHT film at 90 (\circ), 50 (Δ), 25 (\square) and 5 (\diamond) $^{\circ}C$.

The factors used to adjust the position of the film shear modulus data on the frequency axis, for the film in both its oxidised and reduced states at each temperature studied, are displayed in Table 6.1. The reference temperature chosen in these examples is 25 °C for both of the film oxidation states. Hence, the shift factor for both reduced and oxidised films, which are maintained at 25 °C, is 1. However, the shift factors are non-identical for the polymer in its oxidised and reduced states at all temperatures other than, by choice, at 25 °C. This indicates that the glass transition occurs at different temperatures when the polymer is maintained in oxidised and reduced states.

Temperature of polymer / °C	Frequency shift factor for reduced film	Frequency shift factor for oxidised film
5	1.1	1.5
25	1	1
50	0.55	0.9
90	0.1	0.5

Table 6.1: Summary of the coefficients used to shift shear modulus data on the frequency axis, according to the temperature at which the polymer is maintained, in order to obtain a shear modulus master curve.

This is reiterated in Figures 6.9 and 6.10, which highlight the differences between temperature adjusted shear modulus data (G'' and G' respectively), for the film in both its oxidised and reduced states. These figures show that the oxidised film has a shear modulus master curve that is noticeably shifted to higher frequencies in comparison to the master curve corresponding to the reduced film. This is equivalent to saying that the glass transition temperature, T_g , of the polymer is decreased when the film is oxidised. In the previous chapter many possible explanations were discussed for the PHT film softening that occurs upon oxidation, which would equally explain the decrease in its T_g observed here. The most obvious is that oxidation causes an ingress of solvent which plasticises the film, allowing polymer segmental motion to occur more easily, and therefore lowering the glass transition temperature.

6.4.2 Estimation of the glass transition temperature

The glass transition temperature, T_g , of electropolymerised PHT films immersed in propylene carbonate electrolyte solution is unknown and is undoubtedly different for each thin film produced due to slight variations in the polymerisation procedure. When T_g is

unknown, an estimation of its magnitude can be made using the WLF equation in conjunction with the combination of the log of two shift factors arising from shear modulus data recorded at two different temperatures. These shift factors are listed in Table 6.1. The formula used to estimate T_g is shown in Equation (6.1). To fulfil the need to select a “standard” temperature, the shift factor arising from data recorded at 25 °C (298 K) is defined as unity. Hence the difference between the shift factors at T_1 and at 298 K can be used to yield T_g .

$$\log(a_{T_1}) + \log(1) = \left[\frac{-17.44(T_1 - T_g)}{51.6 + T_1 + T_g} \right] + \left[\frac{-17.44(298 - T_g)}{51.6 + 298 + T_g} \right] \quad (6.1)$$

The form of Equation 6.1 means that it does not give precise values of T_g ; nevertheless it does give a reasonable estimation of T_g . Solving Equation 6.1 for T_g provides a quadratic equation that in this case yields two possible T_g values of approximately 40 and 90 °C. Since huge variations in the polymer shear modulus are observed at temperatures much lower than 90 °C it is reasonable to disregard this value of T_g . The T_g value of approximately 40 (± 10) °C results when shift factors corresponding to $T_1=5, 50$ and 90 °C are used.

Analysis of this kind has not been attempted before using data derived from crystal impedance measurements on thin electro-polymerised films immersed in solution. However, dynamic measurements taken for *dry* PHT films yielded glass transition temperatures of approximately 30 °C [4]. The T_g value calculated using Equation 6.1 is consistent with these results, which indicates that the methodology and data presented here are viable.

Upon observation of Figures 6.9 and 6.10 one can see that quantitatively there is a notable shift in the shear modulus master curves upon film oxidation. Hence, one would expect there to be a difference in the T_g of oxidised and reduced PHT films. However, numerically this shift is too small to be calculated using the procedure outlined above.

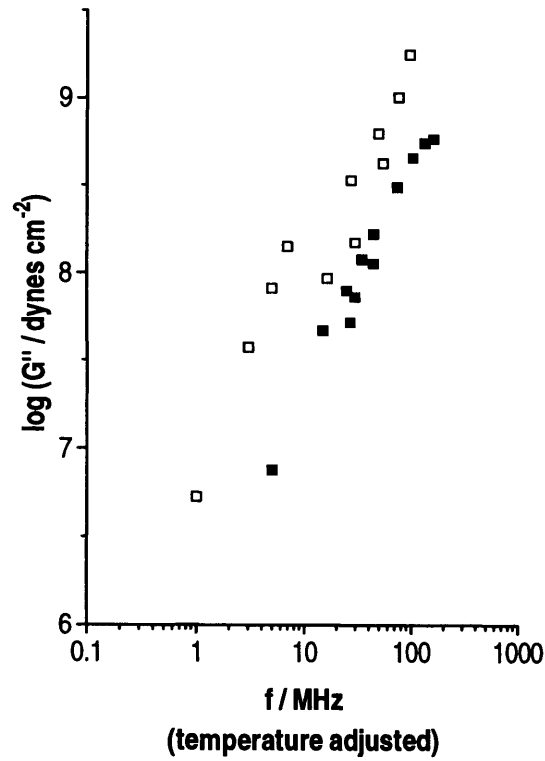


Figure 6.9: Dependence of shear loss modulus, $\log G''$, upon (temperature adjusted) frequency, f , for a PHT film in its reduced ($E=0.0V$) (\square) and oxidised ($E=0.9V$) (\blacksquare) states.

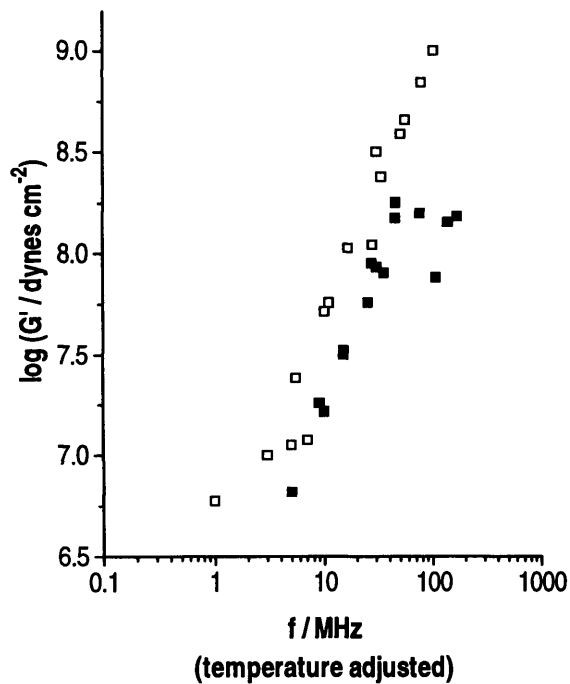


Figure 6.10: Dependence of shear storage modulus, $\log G'$, upon (temperature adjusted) frequency, f , for a PHT film in its reduced ($E=0.0V$) (\square) and oxidised ($E=0.9V$) (\blacksquare) states.

6.5 CONCLUSIONS

The conclusions reached at the end of this chapter extend the conclusions attained at the end of the previous chapter; quartz crystal impedance measurements provide invaluable information on the rheological properties of thin electroactive polymer films, *in situ*. Of primary importance in this work, these preliminary studies have shown that it is possible to access a larger proportion of an electroactive polymer film's viscoelastic properties by adjusting the polymer temperature in conjunction with the applied perturbation frequency, ω

The system studied and experimental instrumentation used here permit the investigation of the shear moduli of thin PHT films between the temperatures of 5 and 90 °C. Within this temperature range a huge PHT shear modulus variation was observed, which alone indicates that the polymer is within its glass transition region. Combination of data recorded at different temperatures with those recorded at separate frequencies yields the opportunity to construct a shear modulus master curve. From the frequency shifts required to construct this curve, one can gain insight into the T_g of thin PHT immersed in electrolyte solution. This method yielded a PHT glass transition temperature of approximately 40 °C. However, this method of T_g calculation is not numerically accurate enough to quantify the difference in T_g between oxidised and reduced films, even though a difference in the T_g of oxidised and reduced films is apparent from the observation of the master curves of these films.

There is much scope for future work. It would be interesting to compare the glass transition temperature resulting from direct measurement of PHT polymer dynamics, such as is the case with crystal impedance measurements, with T_g values resulting from methods that indirectly probe polymer dynamics. Examples of such techniques include coulometry, which would detect a discontinuity in heat capacity at T_g , or a.c. impedance that could detect a change in the film conductivity at T_g .

6.6 REFERENCES

1. J. J. Aklonis and W. J. MacKnight, Introduction to Polymer Viscoelasticity, Wiley-Interscience, New York, (1983).
2. J. Ferry, Viscoelastic Properties of Polymers, John Wiley & Sons, Inc., New York, (1961).
3. M. L. Williams, F. R. Landel, and J. D. Ferry, *J. Am. Chem. Soc.* 77:3701 (1955).
4. T. Shiga and A. Okada, *J. Appl. Polym. Sci.* 62:903 (1996).

CHAPTER 7

MANIPULATION OF ELECTROACTIVE POLYMER FILM VISCOELASTICITY: THE ROLE OF SOLVENT

7.1 INTRODUCTION

The dependency of electroactive polymer films' electrochemical responses upon polymer dynamics has been discussed in Chapter 5 [1]. Here the effects of solvent-polymer interactions are explored, which are known to directly influence polymer dynamics. These effects have been monitored and quantified using the crystal impedance technique and data fitting procedures (described in Chapter 3). Measurements were made on electroactive PHT films maintained under dynamic (*kinetic*) electrochemical control in the presence of two solvents with contrasting solvation properties: propylene carbonate (PC) and dichloromethane (DCM). In contrast, the studies conducted in the previous chapters concentrated on static electrochemical measurements of PHT films at (quasi) redox equilibrium and therefore under *thermodynamic* control.

7.2 EXPERIMENTAL

PHT films were prepared as described in Section 3.6.1 via potentiodynamic electrochemical polymerisation of 3-hexylthiophene from a deposition solution containing 3.7 mmol dm⁻³ HT and 0.1 mol dm⁻³ tetraethylammonium hexafluorophosphate (TEAPF₆) in PC. The PHT film was prepared using 6 potentiodynamic cycles and then transferred to 0.1 mol dm⁻³ TEAPF₆ in PC background electrolyte solution, as described in Section 3.7. Following transferral the film was redox cycled at $\nu = 10 \text{ mV s}^{-1}$ (potential limits of 0.0 V and 1.0 V) until a steady state response was attained at which point crystal impedance spectra were acquired every second during a complete redox cycle (see Section 3.7.2).

The film was then held in its reduced state (0.0 V) for ca. 30 s until equilibrium electrochemical (no current flow) and crystal impedance (no change in peak frequency and admittance) responses were attained. Crystal impedance spectra were acquired every second following a positive (0.0 V to 1.0 V) instantaneously applied potential step until no current flow or change in peak frequency or admittance were observed. A negative potential step (1.0 V to 0.0 V) was then applied to the film and crystal impedance spectra were recorded until no further change was observed.

The film was transferred to a second background electrolyte solution containing 0.1 mol dm^{-3} TEAPF₆ dissolved in DCM. The procedure (described above) for acquiring steady state crystal impedance spectra of the same PHT film was repeated in this medium for both cyclic voltammograms ($\nu = 10 \text{ mV s}^{-1}$) and instantaneously applied potential steps (potential limits of 0.0 V and 1.0 V).

7.3 PROPYLENE CARBONATE ELECTROLYTE SOLUTIONS

The experimental results displayed in this section originate from measurements made on the prepared PHT film exposed to PC background electrolyte solutions.

7.3.1 Cyclic voltammetry experiments

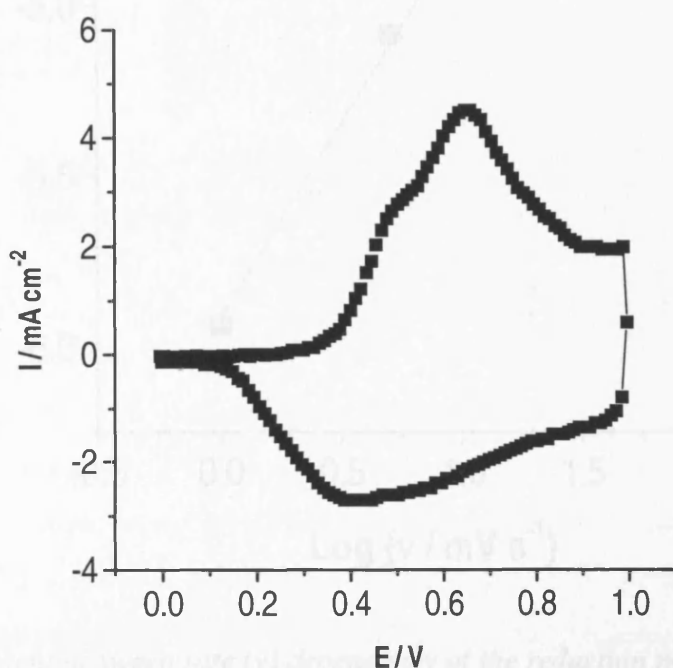


Figure 7.1: Cyclic voltammogram of a PHT film ($\Gamma = 0.23 \mu\text{mol cm}^{-2}$) exposed to 0.1 mol dm^{-3} TEAPF₆ / propylene carbonate. Scan rate: 10 mV s^{-1} .

Figure 7.1 displays a typical voltammogram for a PHT film upon redox cycling in 0.1 mol dm^{-3} TEAPF₆ / propylene carbonate at scan rate, $\nu = 10 \text{ mV s}^{-1}$. It is apparent from this voltammogram that significant electrochemical reaction of the polymer during the oxidative half scan commences at 0.4 V, this feature will form a key discussion point later in the text. A linear relationship between $\log(\nu)$ and $\log(I_{pred})$ with a slope of approximately 1 (1.1 ± 0.05), for scan rates lower than 20 mV s^{-1} , is illustrated in the plot of Figure 7.2, indicating that complete redox conversion is achieved for cyclic electrochemical experiments of PHT

films of similar thickness in PC electrolyte solutions when scan rates of 20 mV s^{-1} and below are used. Integration of peak currents therefore yields a reliable measure of polymer coverage, $\Gamma=Q/nFA$, as previously described in Chapter 5.

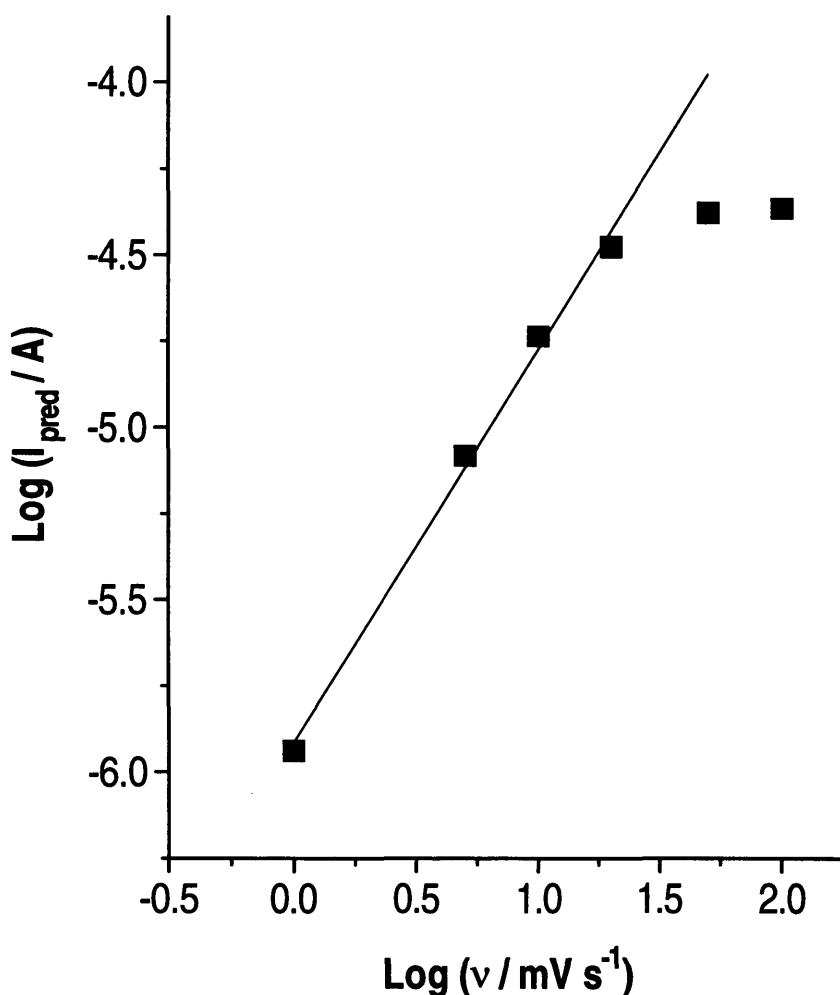


Figure 7.2: Potential sweep rate (v) dependency of the reduction peak current density (I_{pred}) for a PHT film ($\Gamma = 0.22 \mu\text{mol cm}^{-2}$) exposed to 0.1 mol dm^{-3} TEAPF₆ / propylene carbonate. At sweep rates $v \leq 20 \text{ mV s}^{-1}$ peak currents are linear with scan rate, indicating complete redox conversion. The line (of slope 1.1) represents a least squares fit of the data.

Figure 7.3 shows a plot of injected charge density (Q) as a function of potential, corresponding to the experiment of Figure 7.1. In similarity to the situation described above, charge injection does not occur during the anodic half scan until 0.4 V has been reached. There is appreciable hysteresis in the Q vs E plot (see Figure 7.3). Maximum charge injection of 1.75 mC cm^{-2} corresponds to a polymer coverage of $\Gamma = 0.23 \mu\text{mol cm}^{-2}$ ($n = 0.35$).

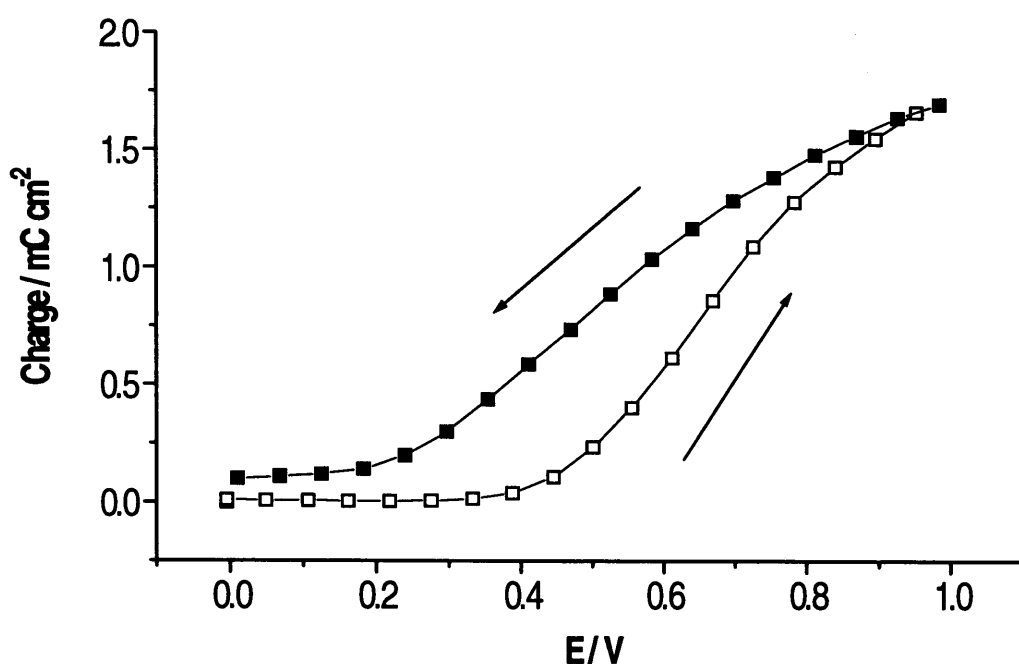


Figure 7.3: Plot of charge density (Q) vs potential (E) for the PHT film of Figure 7.1. Open (filled) symbols represent data acquired during increasing (decreasing) potential; scan rate 10 mV s^{-1} .

Figure 7.4 shows crystal impedance data for the cyclic electrochemical experiment of Figure 7.1. Spectra were acquired every second (corresponding to 10 mV intervals). However, for presentational purposes, only spectra recorded every 5 seconds (corresponding to 50 mV intervals) are shown. Panel (a) displays the raw data acquired during the oxidative half cycle of Figure 7.1 associated with “doping” of the completely reduced (uncharged) PHT film. During oxidation the conductance peak shifts to lower frequencies and becomes more damped; the direction of this peak movement is indicated in the figure with an arrow. Analogously, panel (b) displays the raw crystal impedance data acquired during the subsequent reductive half cycle of Figure 7.1, associated with “undoping” of the completely oxidised (positively charged) PHT film. In this case, the conductance peak shifts back to its original position for the undoped film.

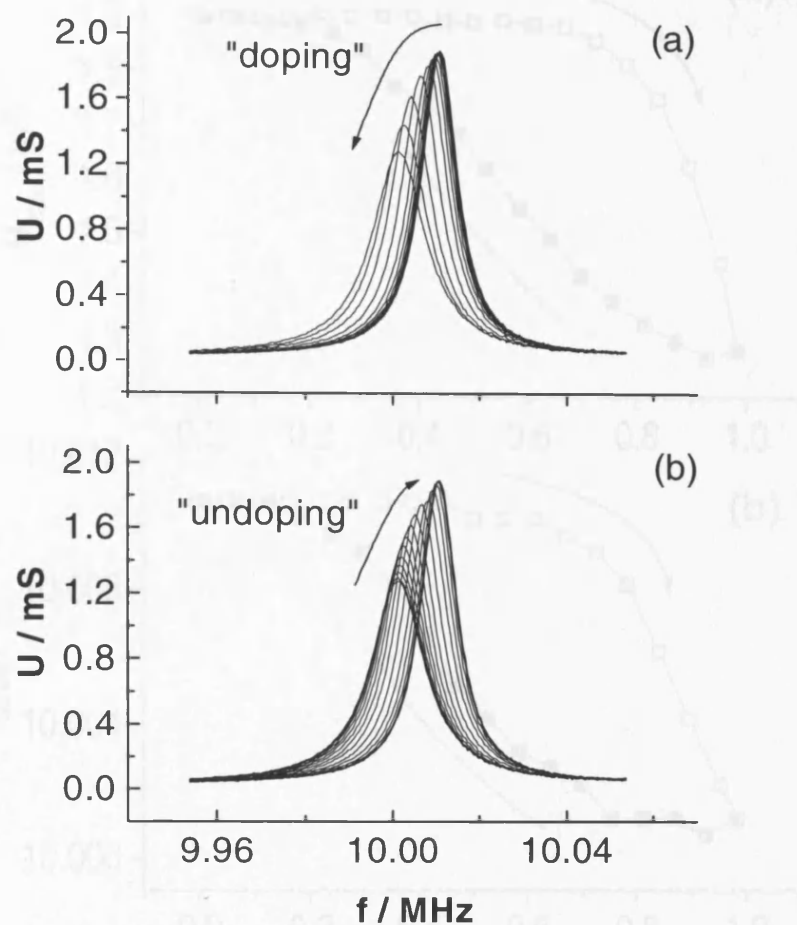


Figure 7.4: Raw crystal impedance spectra for the PHT film of Figure 7.1 exposed to 0.1 mol dm^{-3} TEAPF₆ / propylene carbonate. Spectra recorded during increasing (panel a) and decreasing (panel b) potentials; scan rate 10 mV s^{-1} . Data taken at fundamental frequency (nominally 10 MHz).

The peak positions of the raw crystal impedance data of Figure 7.4 are displayed in Figure 7.5, which summarises some key features of the variations with applied potential (E) of peak conductance, U_{max} (panel a), and the corresponding frequency, f_{Umax} (panel b). Both variables (U_{max} and f_{Umax}) exhibit significant hysteresis with E . However, when it is considered that global equilibrium was not reached on the extended time scales of the experiments in chapter 5, it is not surprising that equilibrium was not attained on the considerably shorter time scales of this experiment (100 s for complete redox conversion).

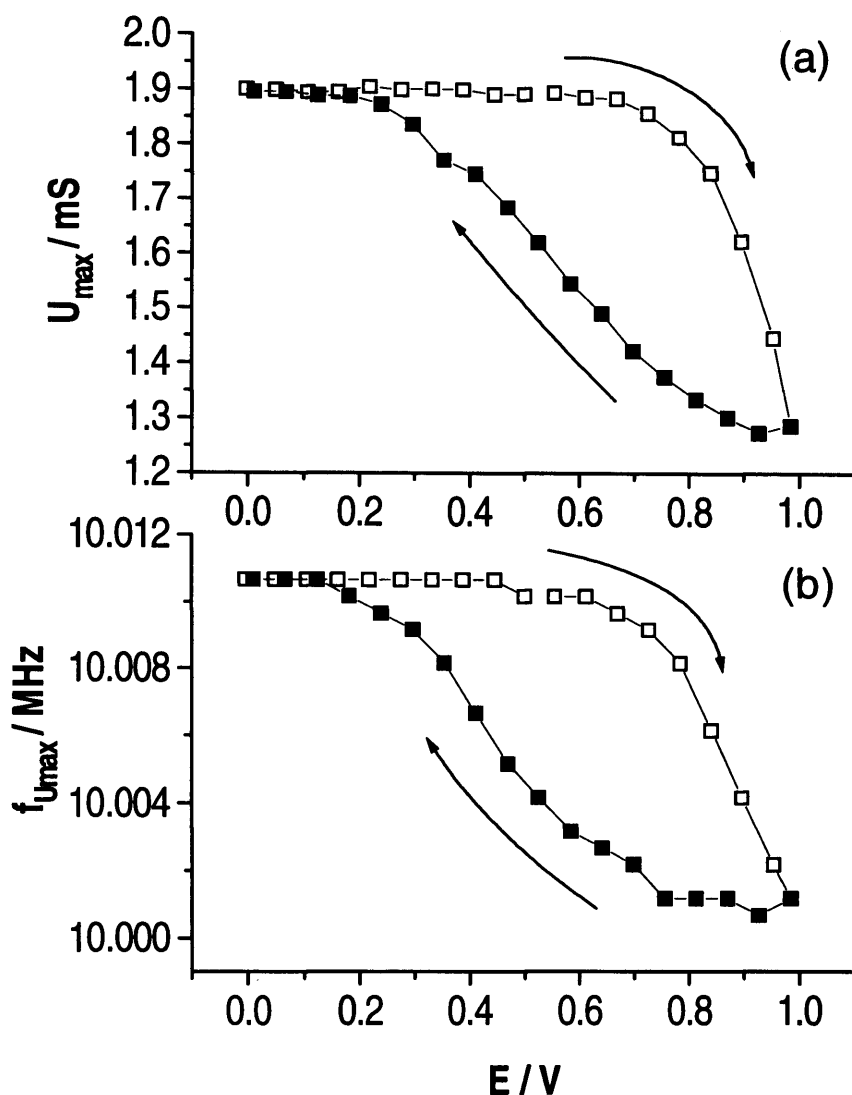


Figure 7.5: Peak conductance (U_{max} ; panel a) and peak frequency ($f_{U_{max}}$; panel b) variations with applied potential at 10 MHz; data taken from Figure 7.4. Open (filled) symbols represent data acquired during increasing (decreasing) potential; scan rate 10 mV s^{-1} .

Despite the hysteresis highlighted in the Q vs. E plot of Figure 7.3, significant hysteresis is also prominent in plots of U_{max} vs. Q (Figure 7.6a) and $f_{U_{max}}$ vs. Q (Figure 7.6b). This indicates that the viscoelastic changes inferred from the shifts in the conductance peak's position and shape upon redox cycling are not simply related to the amount of charge stored in the polymer. Significant decrease in both U_{max} and $f_{U_{max}}$ does not occur until over half (ca. 1 mC cm^{-2}) of the maximum charge (1.75 mC cm^{-2}) is stored in the film during the oxidative half cycle. However, on the return (reductive) half cycle, close to linear relationships between Q , U_{max} and $f_{U_{max}}$ are observed.

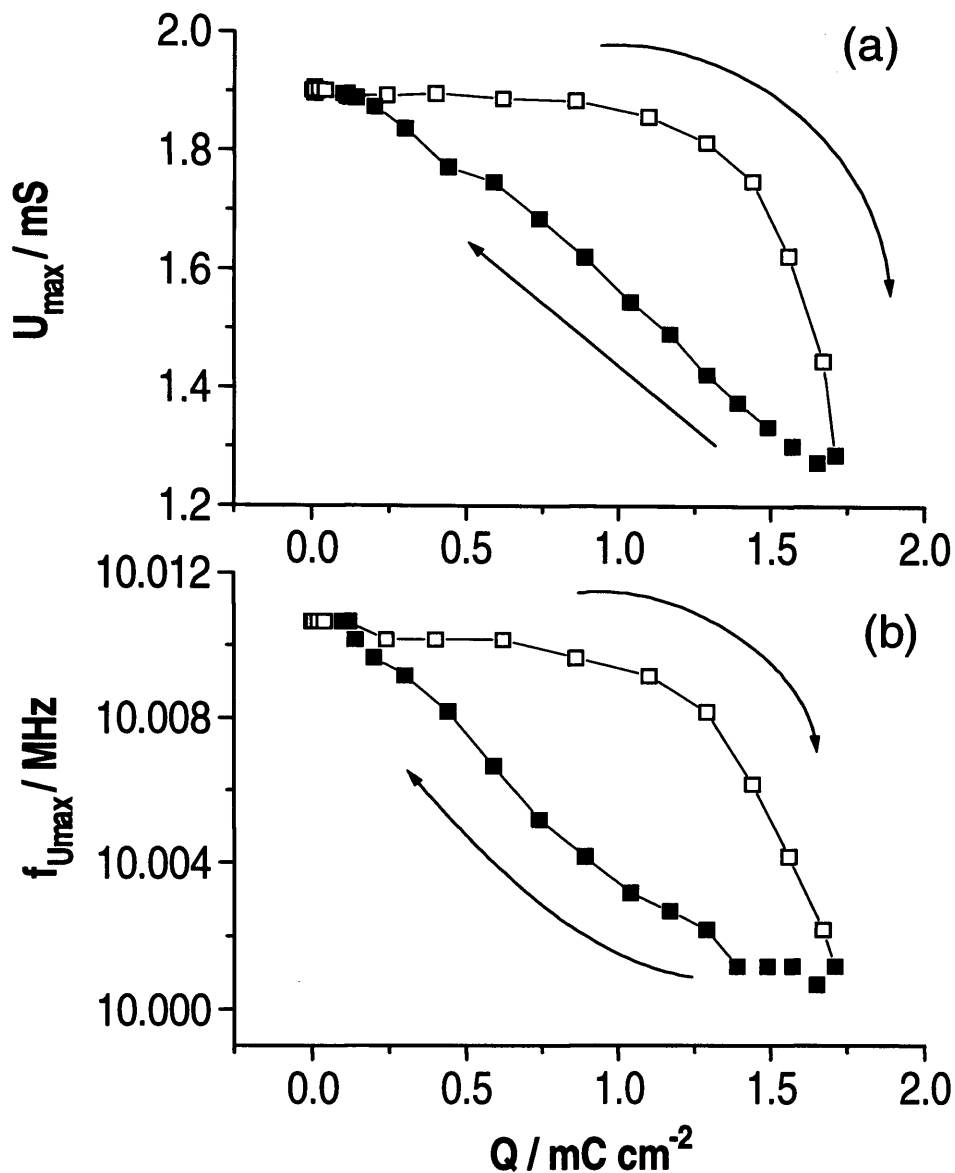


Figure 7.6: Peak conductance (U_{max} ; panel a) and peak frequency ($f_{U_{max}}$; panel b) variations with charge at 10 MHz; data taken from Figure 7.4. Open (filled) symbols represent data acquired during increasing (decreasing) potential; scan rate 10 mV s^{-1} .

Figure 7.7 shows the dependence of U_{max} upon $f_{U_{max}}$ during the redox cycle of Figure 7.1. The lack of hysteresis in this plot indicates that the relationship between U_{max} and $f_{U_{max}}$ is independent of scanning direction, despite the fact that the potential (time) dependent distribution of points along the pathway described by their relationship is non-linear. In other words, the viscoelastic changes which occur within the polymer upon “doping” and “undoping” are identical, even though their potential (time) and charge dependencies vary.

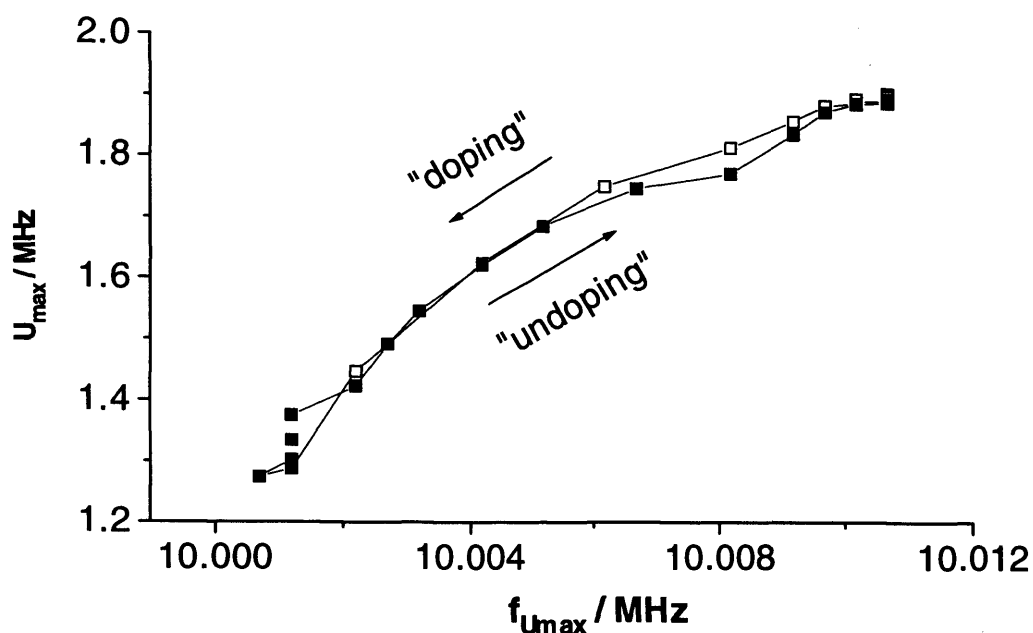


Figure 7.7: Frequency at peak conductance ($f_{U_{max}}$) dependence of peak conductance (U_{max}) for the data of Figure 7.4. Open (filled) symbols represent data acquired during increasing (decreasing) potential; scan rate 10 mV s^{-1} .

7.3.2 Potential step experiments

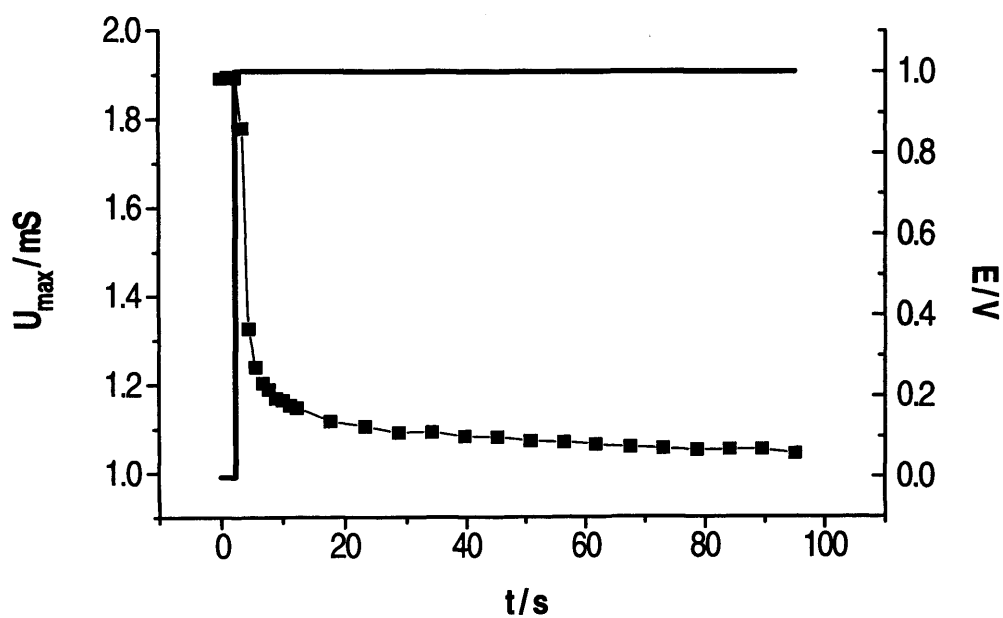


Figure 7.8: Time dependence of peak conductance, U_{max} , (left axis, squares) and applied potential, E , (right axis, solid line) during a potential step oxidation.

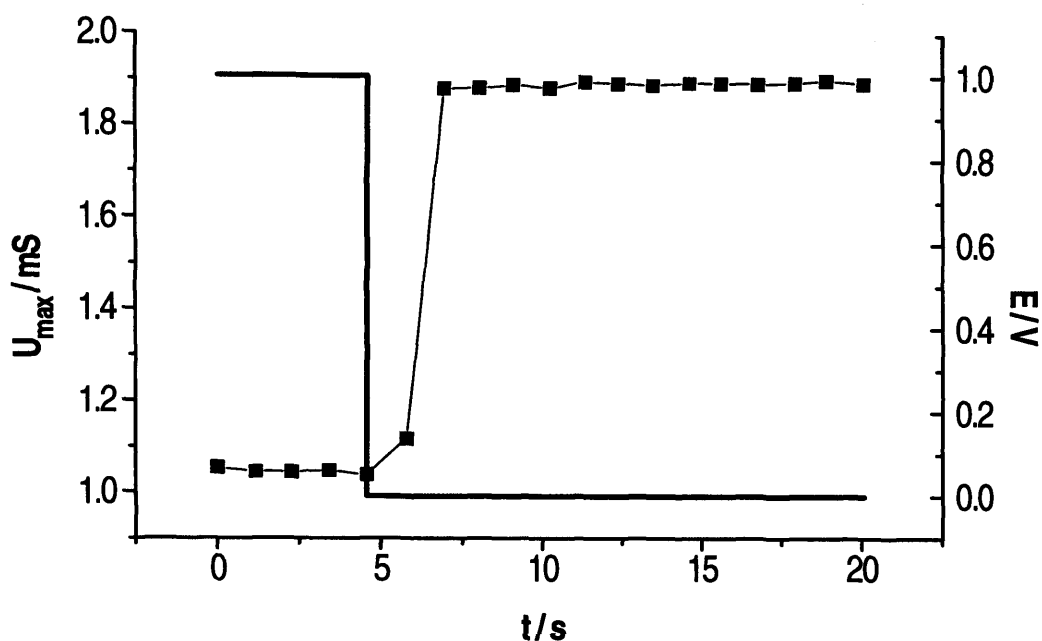


Figure 7.9: Time dependence of peak conductance, U_{max} , (left axis, squares) and applied potential, E , (right axis, solid line) during a potential step reduction.

Figures 7.8 and 7.9 show the dependencies of peak conductance, U_{max} , upon time following a positive and negative potential step respectively. Figure 7.8 indicates that the *decrease* in U_{max} (and hence the *increase* in film viscoelasticity) upon oxidation occurs much more slowly than the reverse process occurring upon reduction (Figure 7.9). When the potential is stepped from 0.0 V to 1.0 V (Figure 7.8) U_{max} falls from a value of 1.90 mS to 1.05 mS over a period of approximately 90 s. (Note that during the cyclic voltammetry experiments the minimum peak conductance value (U_{max}) reached was approximately 1.3 mS (Figure 7.6). However, the total time that a potential of at least 1 V was applied to the film was considerably shorter during the cyclic voltammetry experiment (Section 7.3.1) than in the potential step experiments displayed here. When the potential is stepped back from 1.0 V to 0.0 V (Figure 7.9) U_{max} rises from a value of 1.05 mS to 1.9 mS in approximately 2 s. This behaviour suggests that propylene carbonate ingress and the associated polymer reconfiguration are more difficult (slower) than solvent egress and its associated polymer reconfiguration (discussed more fully in Section 7.6).

7.4 DICHLOROMETHANE ELECTROLYTE SOLUTIONS

The experimental results displayed in this section originate from measurements made on the same PHT film studied in Section 7.3 transferred to a dichloromethane electrolyte solution (see Section 7.2 for experimental details).

7.4.1 Cyclic voltammetry experiments

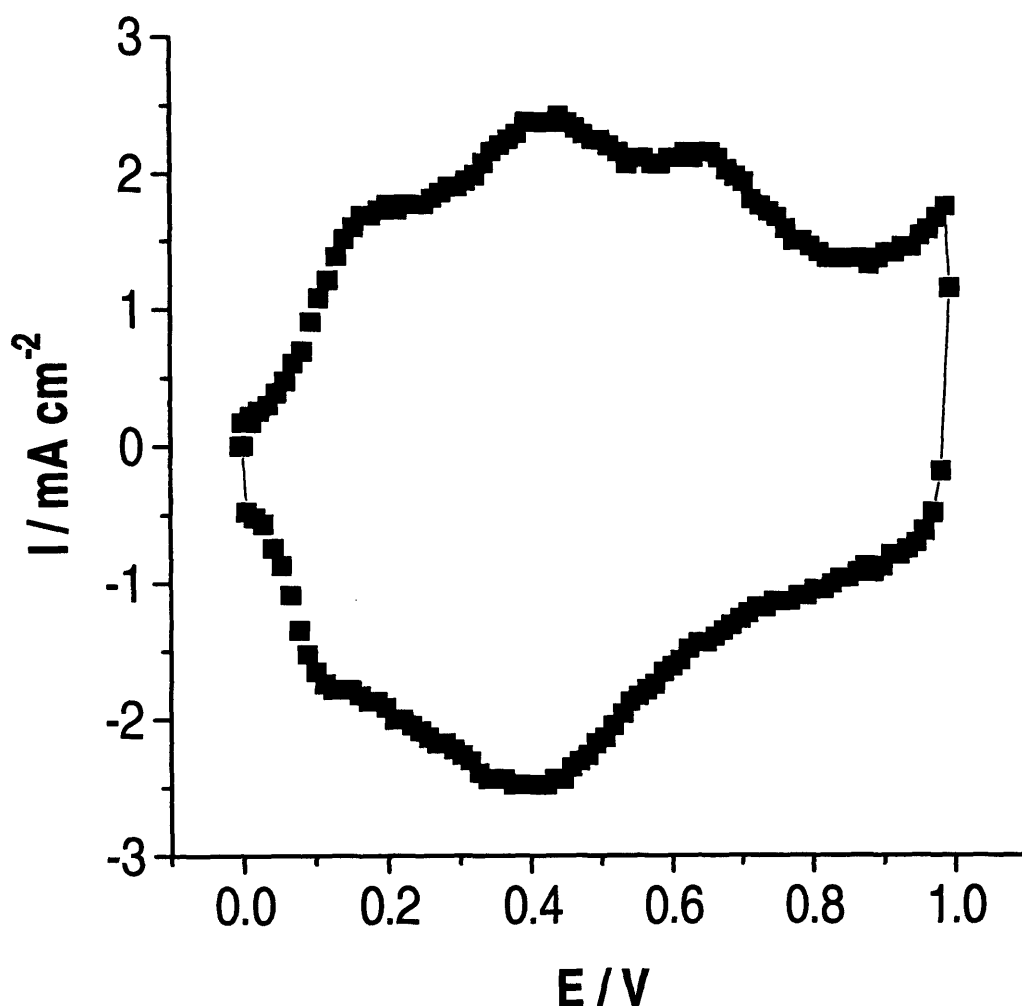


Figure 7.10: Cyclic voltammogram of the PHT film of Figure 7.1 ($\Gamma = 0.23 \mu\text{mol cm}^{-2}$) exposed to 0.1 mol dm^{-3} TEAPF_6 / dichloromethane. Scan rate: 10 mV s^{-1} .

Figure 7.10 shows a typical cyclic voltammogram acquired from the PHT film of Figure 7.1 immersed in an electrolyte solution containing 0.1 mol dm^{-3} TEAPF_6 / dichloromethane. The voltammogram is quite different from that of Figure 7.1, notably because the threshold for significant oxidation is about 0.1 V during the oxidative half cycle, in contrast to 0.4 V for the same film immersed in PC electrolyte solution (Figure 7.1).

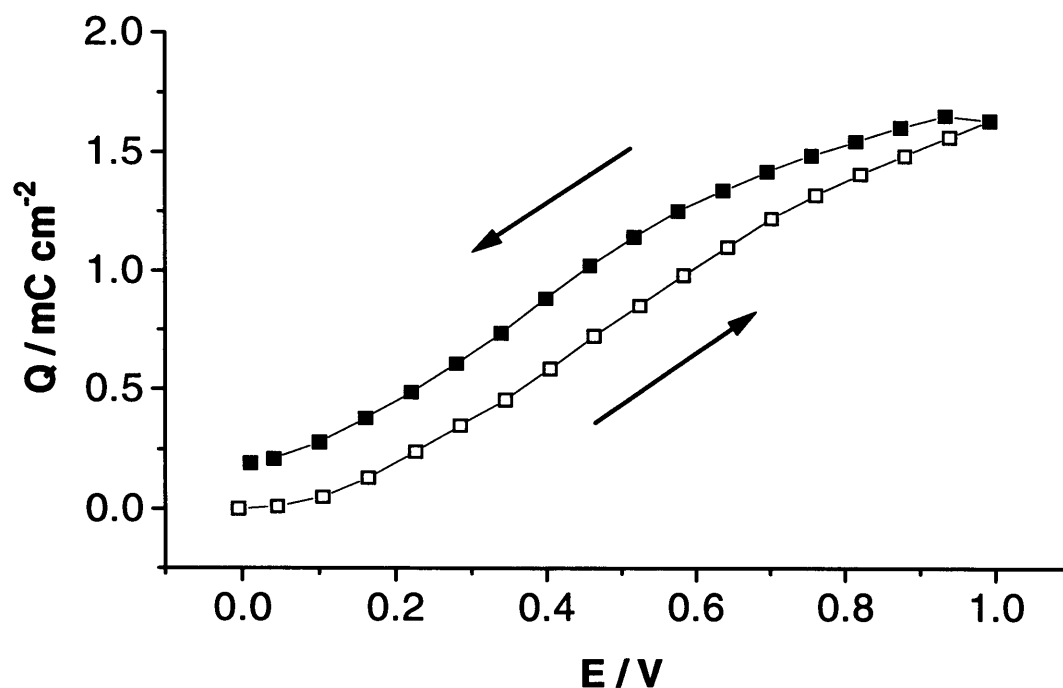


Figure 7.11: Plot of charge density (Q) vs potential (E) for the PHT film of Figure 7.10. Open (filled) symbols represent data acquired during increasing (decreasing) potential; scan rate 10 mV s^{-1} .

From the corresponding plot of Q vs E (Figure 7.11) for the PHT film (exposed to DCM electrolyte solution) it is also clear that charge injection becomes significant at 0.1 V. The plot displays appreciably less hysteresis than its counterpart measured in PC (Figure 7.3). The maximum charge stored in the film is identical to that stored in the same PHT film exposed to PC electrolyte solution, indicating that complete redox conversion is also achieved at scan rates of 10 mV s^{-1} (and below) in DCM electrolyte solutions.

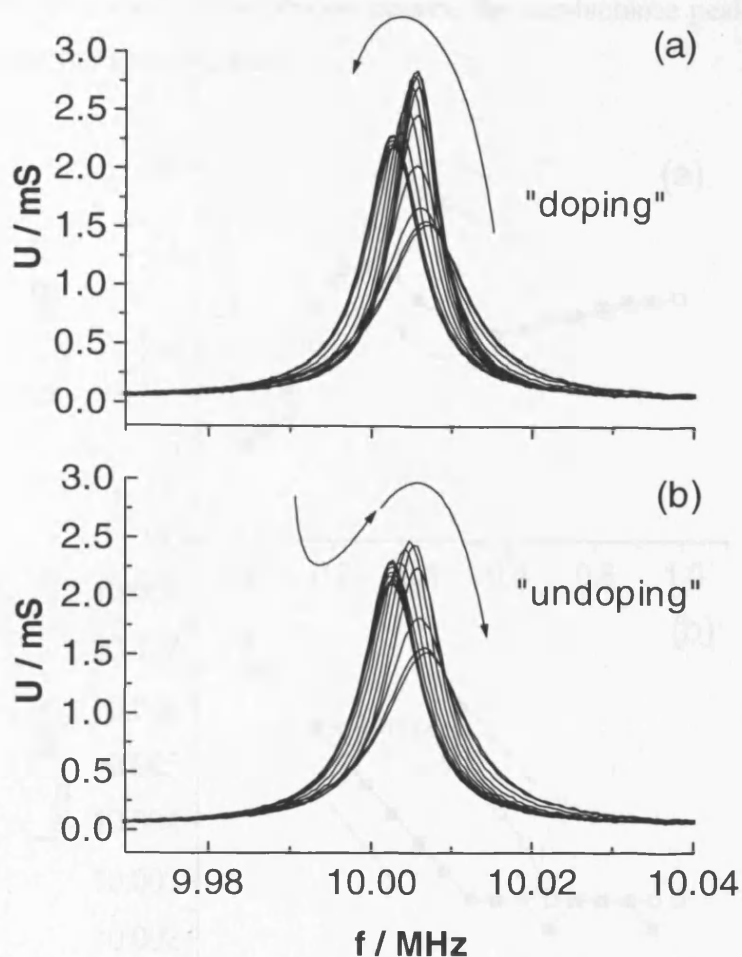


Figure 7.12: Raw crystal impedance spectra for the PHT film of Figure 7.10 exposed to 0.1 mol dm^{-3} TEAPF₆ / dichloromethane.

Figure 7.12 shows crystal impedance data for the cyclic electrochemical experiment of Figure 7.10. Spectra were acquired every second (corresponding to 10 mV intervals). However, for presentational purposes only spectra recorded every 5 seconds (corresponding to 50 mV intervals) are shown. Panel (a) displays the raw data acquired during the oxidative half cycle of Figure 7.10 associated with “doping” of the completely reduced (uncharged) PHT film. During oxidation the conductance peak shifts to lower frequencies, the peak conductance briefly becomes less damped, initially rising sharply to higher values. As more positive potentials are applied, the conductance peak becomes more damped, whilst its position on the frequency axis continues to decrease. The direction of this peak movement is indicated in the figure with an arrow. Analogously, panel (b) displays the raw crystal impedance data acquired during the subsequent reductive half cycle of Figure 7.10, associated with “undoping” of the completely oxidised (positively charged)

PHT film. In this case, the reverse process occurs, the conductance peak shifts back to its original position for the undoped film.

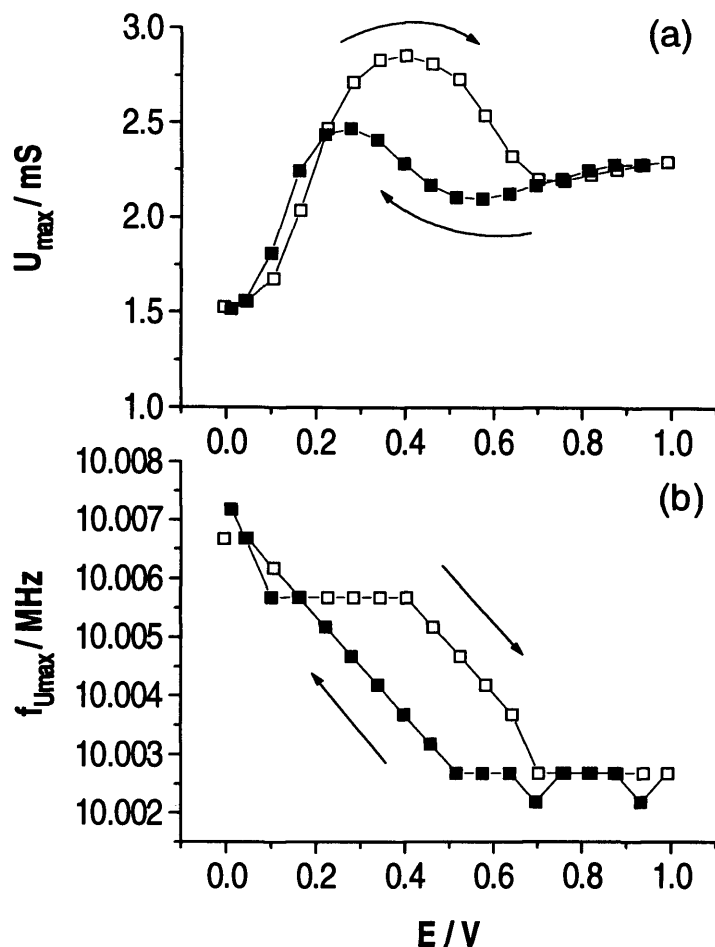


Figure 7.13: Peak conductance (U_{max} ; panel a) and peak frequency ($f_{U_{max}}$; panel b) variations with applied potential at 10 MHz; data taken from Figure 7.12. Open (filled) symbols represent data acquired during increasing (decreasing) potential; scan rate 10 mV s^{-1} .

The peak positions of the raw crystal impedance data of Figure 7.12 are displayed in Figure 7.13, which summarises some key features of the variations with applied potential (E) of peak conductance, U_{max} (panel a), and the corresponding frequency, $f_{U_{max}}$ (panel b). From this plot the sharp rise in peak conductance is apparent, commencing at about 0.1 V as charge is injected into the film. Hysteresis is minimised when the data of Figure 7.13 are plotted as a function of charge density (Q) (Figure 7.14). The peak conductance maxima both occur at ca. 0.6 mC cm^{-2} however, the maximum value of U_{max} is considerably lower during the reductive half cycle.

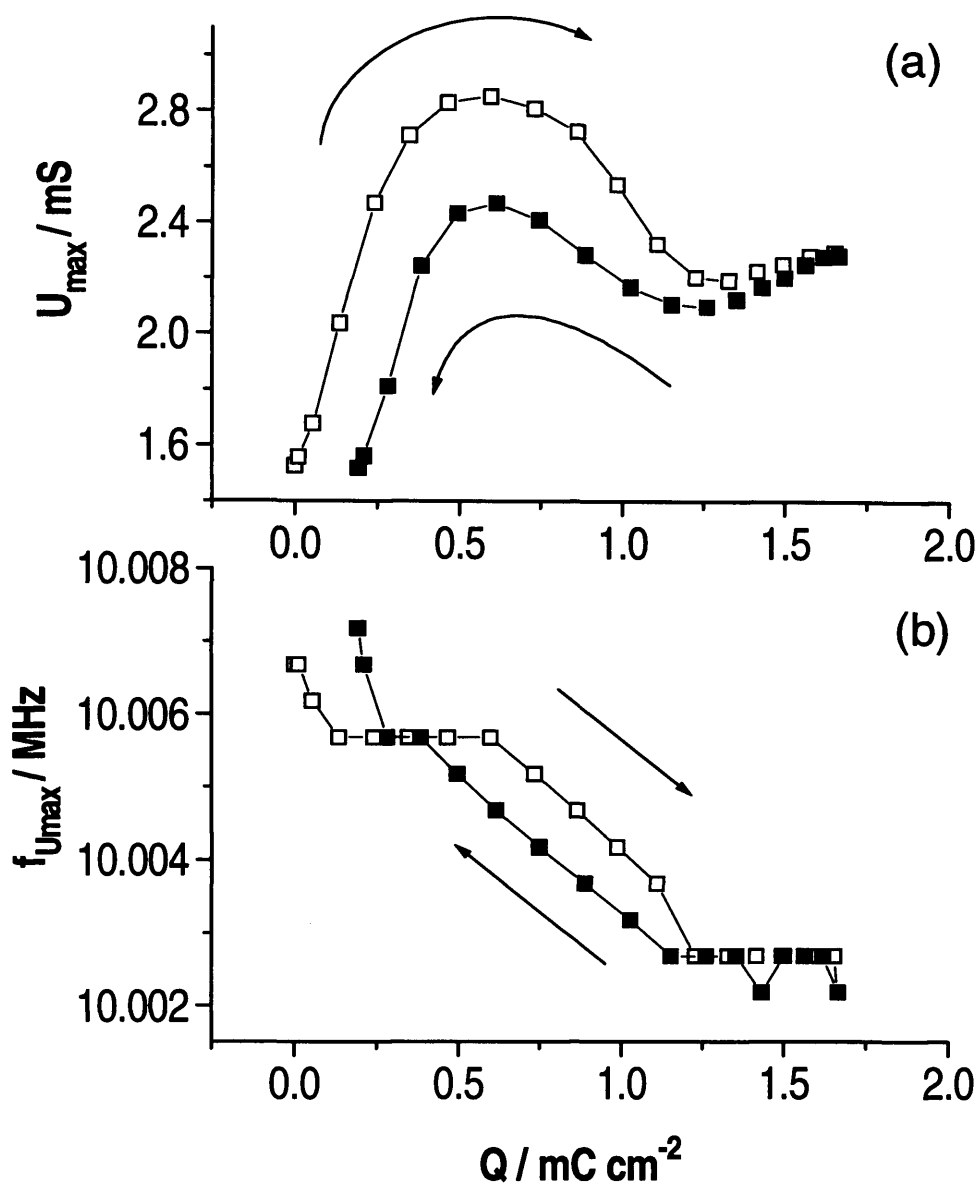


Figure 7.14: Peak conductance (U_{max} ; panel a) and peak frequency ($f_{U_{\text{max}}}$; panel b) variations with charge at 10 MHz; data taken from Figure 7.12. Open (filled) symbols represent data acquired during increasing (decreasing) potential; scan rate 10 mV s^{-1} .

The plot of U_{max} vs $f_{U_{\text{max}}}$ (Figure 7.15) clearly shows that the peak conductance rises dramatically with little change in frequency at about 10.0055 MHz during both the “doping” and “undoping” processes. The relationship is clearly very different from that of the same PHT film exposed to PC electrolyte solutions (Figure 7.7). A notable difference between the plots arises from the presence of hysteresis in the case for the film immersed in DCM electrolyte (Figure 7.15), not present in the corresponding plot for the same PHT film immersed in PC (Figure 7.7). This indicates that the viscoelastic pathways of “doping” and “undoping” are non-identical.

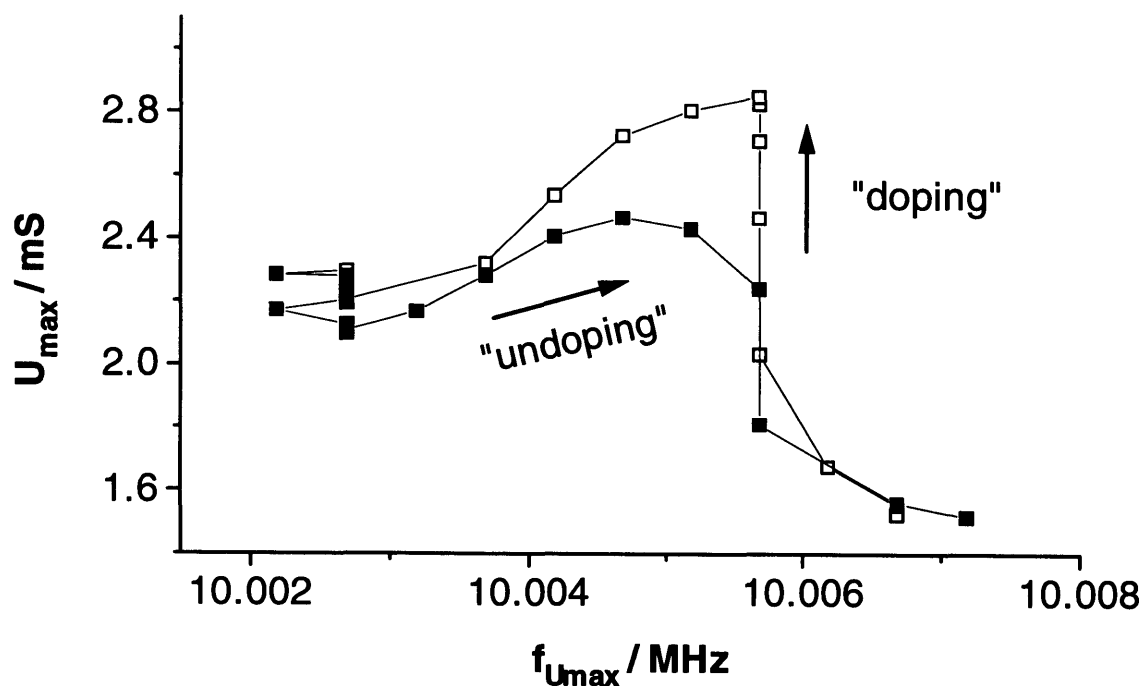


Figure 7.15: Frequency at peak conductance ($f_{U_{max}}$) dependence of peak conductance (U_{max}) for the data of Figure 7.12. Open (filled) symbols represent data acquired during increasing (decreasing) potential; scan rate 10 mV s^{-1} .

7.4.2 Potential step experiments

Figures 7.16 and 7.17 show the dependence of peak conductance, U_{max} , upon time following a positive and negative potential step respectively. Figure 7.16 indicates that the *increase* in U_{max} (and hence the *decrease* in film viscoelasticity) from 1.5 mS to approximately 2.3 mS takes place in 3 s when the applied potential is instantaneously stepped from 0.0 V to 1.0 V. (During cyclic voltammetry experiments the value of U_{max} reached when 1.0 V was applied to the film was also approximately 2.3 mS even though the total time spent at 1.0 V was considerably shorter.) When the potential is stepped back from 1.0 V to 0.0 V (Figure 7.17) U_{max} falls from a value of approximately 2.3 mS to 1.5 mS in a period of 3 s. Since the times taken for U_{max} to reach steady values are approximately equal and relatively short (3 s) for both the oxidation and reduction processes. This suggests that solvent ingress and egress (as well as the associated polymer reconfigurations) are relatively easy (cf. propylene carbonate ingress/polymer reconfigurations shown in Section 7.3.2).

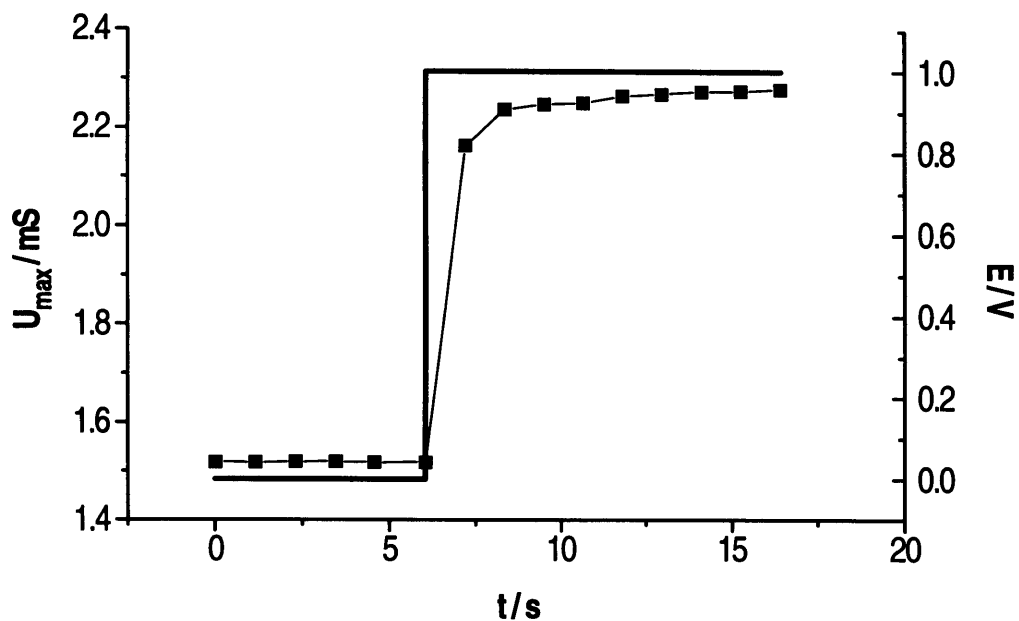


Figure 7.16: Time dependencies of peak conductance, U_{max} , (left axis, squares) and applied potential, E , (right axis, solid line) during a potential step oxidation.

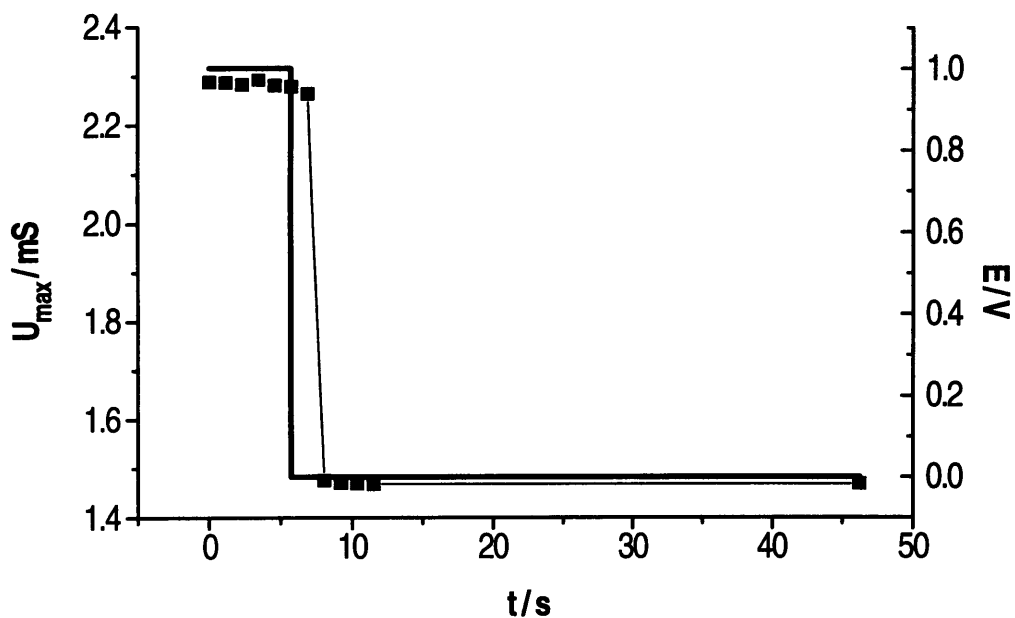


Figure 7.17: Time dependencies of peak conductance, U_{max} , (left axis, squares) and applied potential, E , (right axis, solid line) during a potential step reduction.

A further point to note is that during these potential step experiments U_{max} values apparently moved monotonically between their quasi equilibrium levels (at the potential limits). This

contrasts with the observation of peak conductance maxima recorded during cyclic voltammetry experiments at intermediate doping levels (Section 7.4.1). It is, however, impossible to determine if this is actually the case since the temporal resolution of the crystal impedance instrument used is 1 s and peak conductance maxima may appear and decay on much faster time scales. A more detailed discussion of this point is presented in Section 7.6.

7.5 DATA MODELLING

In this section are displayed film physical parameters extracted from the raw crystal impedance data of Figures 7.4 and 7.13, using similar fitting procedures to those described in Chapter 5 (Section 5.3.2.1) and outlined in Section 3.5.2.

7.5.1 Poly(3-hexylthiophene) films exposed to propylene carbonate

The same general trends are observed for the data of the PHT film studied in this section and for the PHT film for which data was presented in Chapter 5; both films have similar surface coverage: $\Gamma = 0.23$ and $0.22 \mu\text{mol cm}^{-2}$, respectively. The film density, ρ_f , (Figure 7.18) lies within the previously stated range (Chapter 5) of $1.00 (\pm 0.10) \text{ g cm}^{-3}$ for the reduced (undoped) polymer and $1.25 (\pm .010) \text{ g cm}^{-3}$ for the oxidised (doped) polymer.

Figure 7.19 displays the thickness change (h_f) of the polymer with applied potential, E . As in Chapter 5 the deduction has been made that the thickness increase upon oxidation is too large to be caused by anion entry alone; these considerable thickness increases are assigned to solvent swelling. Applying Equations 5.1 and 5.2 indicates, that within experimental uncertainty, solvent entry upon complete oxidation of the fully reduced PHT film induces swelling of about 150% of the original film thickness, and anion entry (necessary to maintain electroneutrality) causes film swelling of about 15%. The PHT film studied in Chapter 5 also showed large thickness changes upon oxidation. These thickness changes arise from solvent entry, which is believed to govern the viscoelastic changes observed during redox conversion of PHT films exposed to propylene carbonate electrolyte solutions (see below).

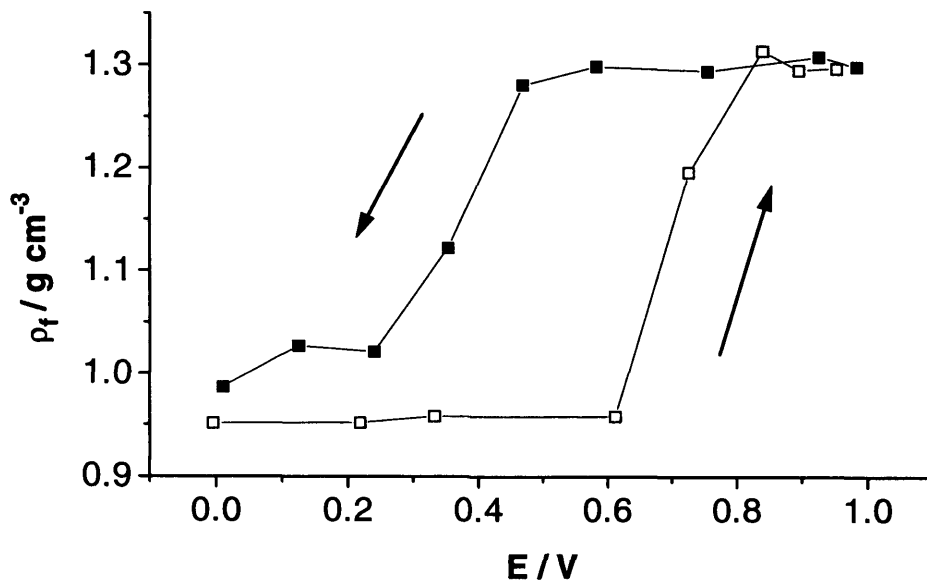


Figure 7.18: Fitted film density values as a function of applied potential for the data of Figure 7.4, corresponding to cyclic voltammetry of a PHT film exposed to PC electrolyte solution. Open (filled) symbols represent data acquired during increasing (decreasing) potential; scan rate 10 mV s^{-1} .

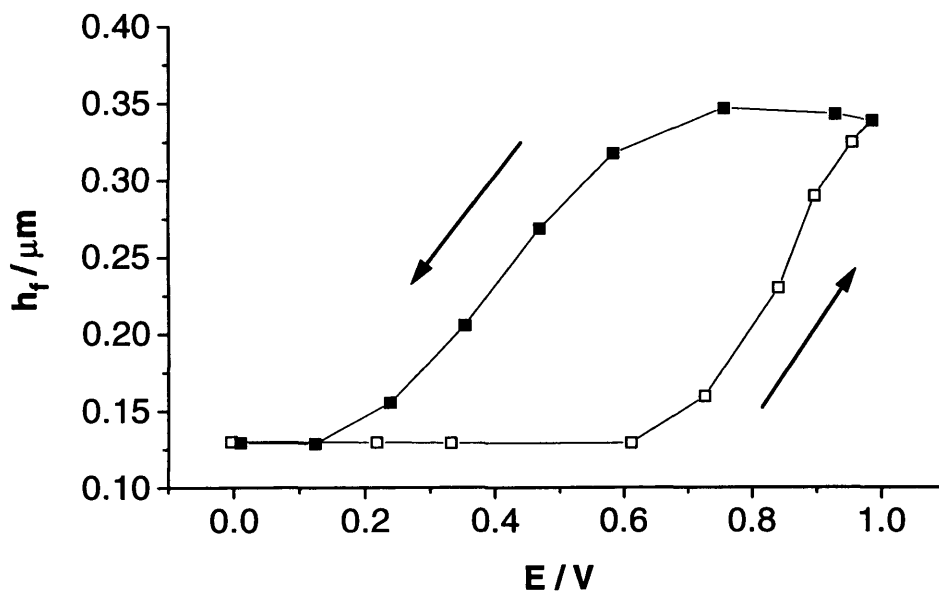


Figure 7.19: Fitted film thickness values as a function of applied potential for the data of Figure 7.4, corresponding to cyclic voltammetry of a PHT film exposed to PC electrolyte solution. Open (filled) symbols represent data acquired during increasing (decreasing) potential; scan rate 10 mV s^{-1} .

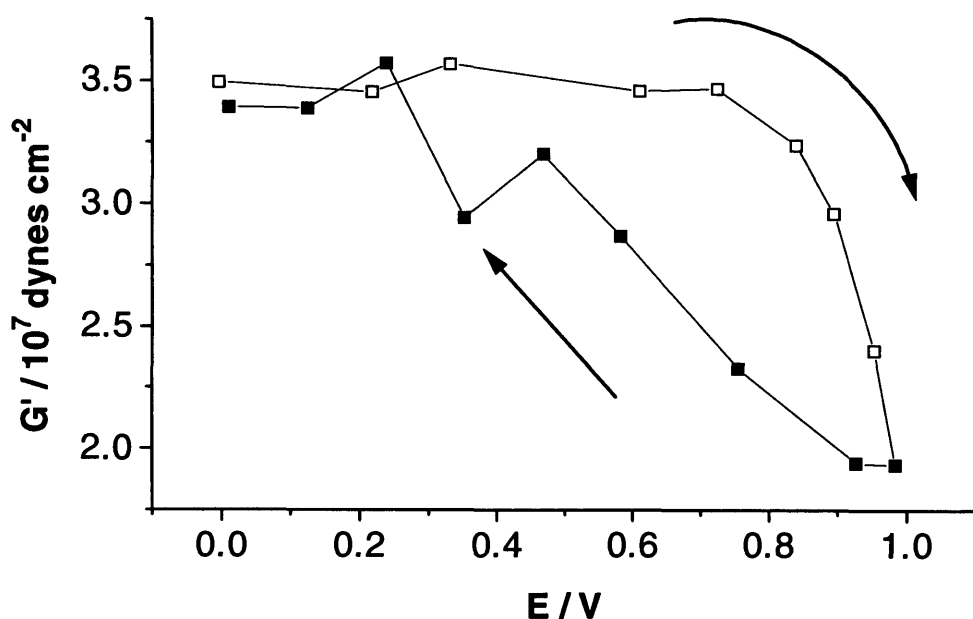


Figure 7.20: Plot of fitted storage modulus, G' , as a function of potential for the data of Figure 7.4, corresponding to cyclic voltammetry of a PHT film exposed to PC electrolyte solution. Open (filled) symbols represent data acquired during increasing (decreasing) potential scan; scan rate 10 mV s^{-1} .

Figure 7.20 shows shear storage modulus data (G') extracted from fitting the data of Figure 7.4. G' decreases dramatically as the applied potential is increased (during the oxidative half cycle) and returns to its original value when the potential is reduced to 0.0 V (during the reductive half cycle). The dramatic softening observed upon oxidation does not occur until the applied potential, E , has reached 0.7 V. During the reductive cycle the modulus increases more linearly as the applied potential is reduced.

The PHT film studied in this chapter is more compact than that studied in Chapter 5, this difference is believed to arise from slight differences in the film deposition procedure. This may be due to an inability to totally exclude moisture from the polymerisation solution using the experimental apparatus described in Chapter 3.

7.5.2 Poly(3-hexylthiophene) films exposed to dichloromethane

Film physical parameters are shown in this section which have been extracted from the data of Figure 7.12 using identical fitting procedures to those used above (described in Chapter 5, Section 5.3.2.1 and outlined in Section 3.5.2). The film density, ρ_f (Figure 7.21), and film thickness, h_f (Figure 7.22) both increase with applied potential. However, a major

difference between those plots and the analogous plots for the same film exposed to PC electrolyte solutions is the lack of hysteresis in DCM.

The PHT film studied in DCM electrolyte solutions undergoes thickness increases by a total of about 75% upon oxidation. Using Equations (5.1) and (5.2), introduced in Chapter 5, it can be calculated that 25% of this thickness increase is due to the incorporation of charge balancing anions and 50% is due to solvent ingress. Following the arguments detailed in Section 5.3.2.2, this thickness increase is reasonable.

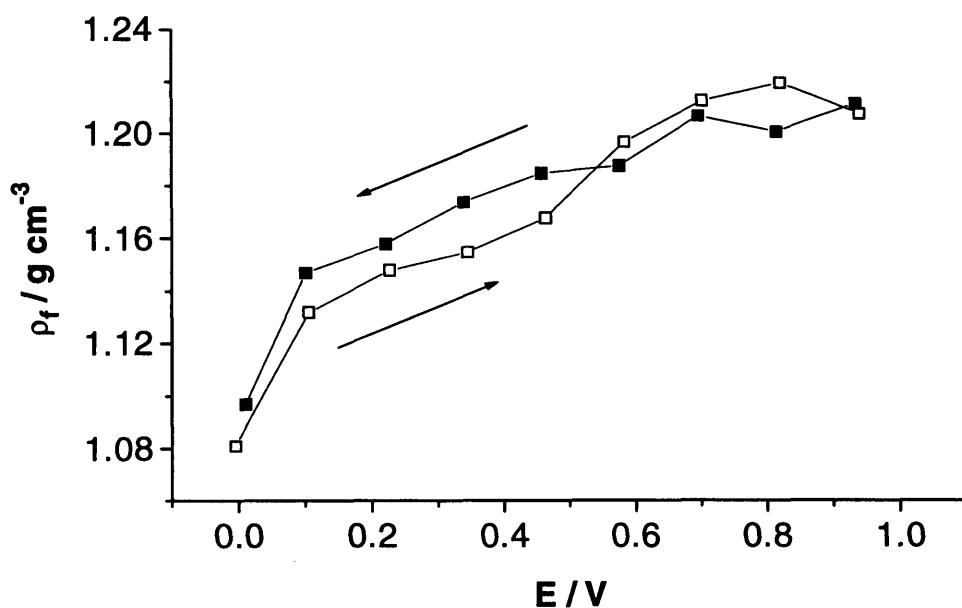


Figure 7.21: Fitted film density values as a function of applied potential for the data of Figure 7.12, corresponding to cyclic voltammetry of a PHT film exposed to DCM electrolyte solutions. Open (filled) symbols represent data acquired during increasing (decreasing) potential; scan rate 10 mV s⁻¹.

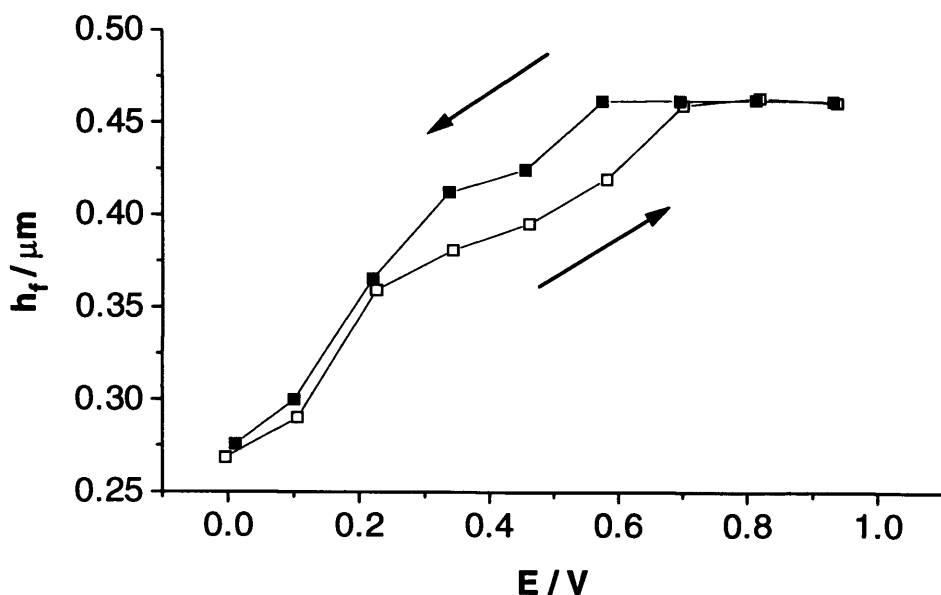


Figure 7.22: Fitted film thickness values a function of applied potential for the data of Figure 7.12, corresponding to cyclic voltammetry of a PHT film exposed to DCM electrolyte solutions. Open (filled) symbols represent data acquired during increasing (decreasing) potential; scan rate 10 mV s^{-1} .

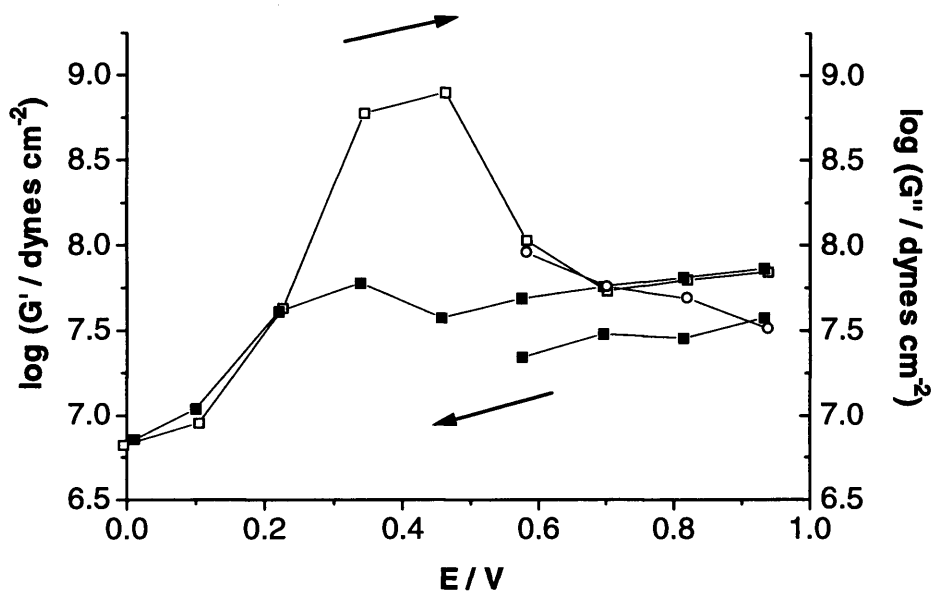


Figure 7.23: Plot of the fitted storage modulus, G' (expressed as $\log G'$, left axis) and fitted loss modulus, G'' (expressed as $\log G''$, right axis), as a function of applied potential for the data of Figure 7.12, corresponding to cyclic voltammetry of a PHT film exposed to DCM electrolyte solutions. Open (filled) symbols represent data acquired during increasing (decreasing) potential; scan rate 10 mV s^{-1} .

The shear modulus data of Figure 7.23 displays dramatic differences compared to data from the same PHT film exposed to PC electrolyte solutions (Figure 7.20). In PC solutions, PHT films are most rigid in the reduced state and less rigid in their oxidised state. Opposite trends are observed when the film is exposed to DCM electrolyte solutions. In DCM solutions there is also a wider range of G' variation. Figure 7.23 indicates the dependence of the PHT film shear storage modulus (G') upon applied potential (E). The film exposed to DCM is highly softened when in its reduced state (0.0 V), with $G' \approx 6 \times 10^6$ dynes cm^{-2} . Upon oxidation G' increases dramatically, reaching a maximum of $G' \approx 5 \times 10^8$ dynes cm^{-2} at approximately 0.4 V. As the applied potential is increased further, the shear modulus decreases, but at 1.0 V it remains at $G' \approx 1 \times 10^8$ dynes cm^{-2} .

In Chapter 5 (Section 5.3.2.1) it is stated that the smaller component of G cannot be reliably obtained when $0.1 \geq G''/G' \geq 10$. At potentials lower than 0.6 V G'' is more than an order of magnitude smaller than G' and hence G'' has not been plotted in Figure 7.23. At potentials above 0.6 V, G'' becomes a significant component of G and can be reliably obtained. G'' exhibits shear modulus values of approximately 3.2×10^7 dynes cm^{-2} when the PHT film, exposed to DCM electrolyte solutions, is at potentials greater than 0.6 V and hence largely in its oxidised form.

7.6 DISCUSSION

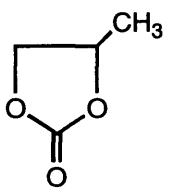
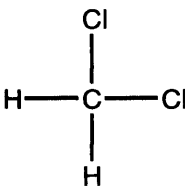
Name	Structure	Relative permittivity ϵ	Density $\rho_l / \text{g cm}^{-3}$	Viscosity $\eta_l / \text{g cm}^{-1} \text{s}^{-1}$
Propylene carbonate		65.1	1.19	0.0247
Dichloromethane		9.08	1.33	0.00430

Table 7.1: Table of DCM and PC physical constants.

The solvation properties of PC and DCM are very different (see Table 7.1). With the aid of crystal impedance data and the physical information inferred from their interpretation (via the modelling procedure) polymer solvation arguments are used to explain the differences

observed between the electrochemical behaviour of the PHT film exposed to polar (PC) and non-polar (DCM) electrolytic solvents.

The PHT film in its reduced (uncharged) state is expected to be relatively non-polar. In fact the addition of the hexyl group to the thiophene backbone was originally intended to increase polymer solubility in common organic solvents [2]. It is therefore reasonable to assume that PC ($\epsilon \approx 65$) will be a relatively poor solvent for the uncharged film and DCM ($\epsilon \approx 9$) will be a relatively good one. However, the oxidised film contains a high concentration of charged species. Under these conditions one would expect PC to be a good solvent and DCM to be a poor solvent. This hypothesis is affirmed by the raw and fitted crystal impedance data.

If one considers the raw crystal impedance data recorded for the film exposed to PC electrolyte solutions, it is apparent that the conductance spectrum for the oxidised (1.0 V) film is much more damped and shifted to lower frequencies than that of the reduced (0.0 V) film (Figure 7.4). This is clearer when observing the peak position as a function of charge density (Q) (Figure 7.6). This is consistent with the idea that the film becomes more viscoelastic as a consequence of oxidation-induced solvent entry.

The fitted data indicate that the *oxidised* PHT film immersed in PC electrolyte solution is denser, thicker, and softer than the same film in its *reduced* state. A value of 0.9 g cm^{-3} is estimated as the density for a dry (undoped) PHT film (based on the assumption that the polymer has a similar density to the hexylthiophene monomer). Since the density of pure PC is relatively high (1.2 g cm^{-3}), the inferred density, thickness and plasticisation increases are easily rationalised as outcomes of solvent ingress occurring upon film oxidation. Solvent ingress is believed to be driven by activity arguments [3-5]. In particular, solvent associated with entry of charge balancing anions and “free” solvent, which enters the film as it becomes more lyophilic (in this case when both the oxidised film and the bathing electrolyte are polar media).

An opposing situation has been discovered when the PHT film is exposed to DCM solutions. The raw spectra (Figure 7.12) recorded at 0.0 V are more damped than those recorded at 1.0 V which indicate that the reduced (0.0 V) film is more viscoelastic than the oxidised (1.0 V) film. This is shown more clearly in Figure 7.14 where the peak position is plotted as a function of charge density (Q). Fitted crystal impedance spectra show that the shear modulus for the reduced (0.0 V) film exposed to DCM electrolyte solutions is lower than that for the oxidised (1.0 V) film. This is consistent with the hypothesis that the

oxidised (polar) film exposed to (non-polar) DCM electrolyte solution is less lyophilic than the reduced (non-polar) film, and therefore less plasticised.

The PHT film exposed to DCM electrolyte solutions undergoes interesting viscoelastic changes upon partial oxidation. Figure 7.13 shows a massive increase in peak conductance, U_{max} , during the oxidative half cycle with increasing applied potential between the values of 0.1 V and 0.4 V. At 0.4 V U_{max} peaks. Between the values of 0.4 V and 0.7 V, U_{max} decreases with increasing applied potential. These changes are interpreted using the modelling procedures as large increases in the shear storage modulus G' with concomitant thickness and density increases. G' peaks at 0.4 V and continues to decrease until 0.7 V is reached (Figure 7.23). The rise and fall of G' at partial oxidation may be a consequence of opposing effects which increase, but in a functionally different manner, upon film oxidation: electrostatic stiffening and solvent plasticisation (introduced in Chapter 5). As charge is initially injected into the PHT film, a sharp increase in the shear modulus is observed. The formation of conjugated double bonds (required for the formation of charge carrying polarons and/or bipolarons, discussed in Chapter 1) leads to rigidification of the polymeric backbone. However, solvent entry (either associated with charge balancing anions or driven in by activity arguments) would tend to negate the manifestations of this effect. It is therefore reasonable to hypothesise that the maximum in G' which occurs during partial doping of the PHT film in DCM solutions originates from a combination of these effects. At low doping levels, electrostatic stiffening appears to predominate, causing substantial polymer shear storage modulus (G') increases. At higher potentials, significant driving force for solvent entry tends to counteract the effects of electrostatic stiffening.

The shear loss modulus is much smaller than the shear storage modulus ($G'' \ll G'$) at potentials lower than 0.6 V. However, when $E > 0.6$ V, G'' becomes significant enough to be accurately determined. This can be partly attributed to the fact that the magnitude of G' is smaller at these potentials. However, G'' is a measure of the energy losses occurring within the polymer overlayer. At potentials greater than 0.6 V, PHT is largely in its oxidised state when exposed to DCM solutions. In this state the energy losses due to friction within the film are likely to be higher. This could arise from electrostatic stiffening of the polymer chains and/or the fact that the film becomes lyophobic in its oxidised form.

Polymer solvation arguments can be used to explain some of the major differences in the observed electrochemical responses of the PHT film exposed to PC and DCM electrolyte solutions. The reduced film, immersed in DCM, is highly solvated (affirmed by the storage shear modulus, $G' \approx 6 \times 10^6$ dynes cm^{-2}). Polymer reconfiguration, required to

accommodate charge injection and the formation of polaronic states, will therefore be highly facilitated by the increased proportion of “free volume” afforded by this degree of solvation. Consequently, charge injection occurs at a relatively low applied potential of 0.1 V during the oxidative scan as compared to 0.4 V when exposed to PC solutions. The reduced form of PHT exposed to PC solutions is comparatively unsolvated ($G' \approx 4 \times 10^7$ dynes cm^{-2}) polymer reconfiguration is therefore relatively difficult (compared to the analogous situation in DCM) and charge injection does not occur until 0.4 V is reached.

The charge dependence of solvent ingress, responsible for film plasticisation, for the PHT film exposed to PC solutions is interesting. The majority of plasticisation occurs at doping levels corresponding to charge injection of above 1 mC cm^{-2} (i.e., 60% of the maximum observed doping level) during the oxidative half cycle. Until this doping level is reached the shear modulus remains relatively constant. However, on the return (reductive) half cycle the plasticisation level exhibits a linear relationship with charge (Figure 7.6). Behaviour like this is expected when there is an energy barrier to solvent entry. Hence, high doping levels (found at higher potentials) are necessary to provide sufficient driving force for solvent ingress. On the return (reductive) half cycle there is apparently no barrier to solvent egress. The polarity of the polymer film, and the amount of charge balancing anions present, dictate how much solvent remains present in the film.

	Insulating	Conducting
Poorly solvated	Reduced PHT film in PC	Oxidised PHT film in DCM
Highly solvated	Reduced PHT film in DCM	Oxidised PHT film in PC

Figure 7.24: Schematic representation of polymer properties arising from redox manipulation of a PHT film immersed in PC or DCM. (Darker shading represents more hindered subsequent redox conversion.)

The results of the potential step experiments (and indeed more general trends in the electrochemical behaviour of PHT) can be understood by considering a 2 by 2 matrix of polymer properties (Figure 7.24). These properties are the conductivity of the polymer and its degree of solvation. If the reduced film immersed in PC electrolyte solution is considered first, its properties are that it is non-conducting (electron movement is difficult) and that it is non-solvated (polymer reconfiguration is difficult). Figure 7.8 shows the effect of these two properties exemplified by the *long* time required for the peak conductance, U_{max} , to reach its equilibrium value (i.e., for the film to become fully solvated) following an instantaneously applied *oxidative* potential step.

A situation with the opposite extreme of properties (a highly solvated and conducting film) occurs when the oxidised PHT film is exposed to PC electrolyte solution (Figure 7.9). The effect of this combination of film and solvent properties is indicated by the *short* time required for U_{max} to reach its equilibrium value following an instantaneously applied *reductive* potential step. This is indicative of relatively fast electron movement and polymer reconfiguration (solvent egress).

Examples which present properties intermediate to those described above are when the PHT film is immersed in DCM electrolyte solution. Combinations of a solvated *non-conducting* polymer (for the case of reduced PHT film exposed to DCM) and poorly solvated *conducting* polymer (for the case of oxidised PHT film exposed to DCM) are shown. These examples have more “symmetric” responses, exhibiting *fast* U_{max} equilibration times following either an oxidative (Figure 7.16) or reductive (Figure 7.17) instantaneously applied potential step. This result (combined with the results attained from the same PHT film immersed in PC solutions) tend to suggest that polymer solvation is the key limiting factor.

7.7 CONCLUSIONS

The experiments discussed in this chapter have unequivocally proven that the electrochemical responses of PHT films are highly dependent upon the nature of the solvent they are exposed to. Using crystal impedance analysis it has been possible to show that the observed response variations are related to the degree of solvation of the polymer and hence its viscoelasticity. Highly solvated PHT, either in its reduced form (exposed to DCM electrolyte solutions) or in its oxidised form (exposed to PC electrolyte solutions), exhibited fast electrochemical response and polymer reconfiguration processes which are believed to have been facilitated by high polymer chain mobility (arising from their highly solvated

state). This was exemplified by low shear storage modulus (G') values extracted from modelling the crystal impedance spectra measured for these films.

In contrast, electrochemical responses measured for a poorly solvated PHT film (specifically, the reduced PHT film exposed to PC electrolyte solution) exhibited hindered electrochemical and polymer reconfiguration responses. These slow responses were believed to be due to the difficulty of polymer reconfigurations, required for the oxidation process to proceed, arising from polymer chains with poor mobility. Exemplified by relatively high G' values extracted from modelling the crystal impedance responses of these films.

7.8 REFERENCES

1. M. J. Brown, A. R. Hillman, M. J. Martin, R. W. Cernosek, and H. L. Bandey, *J. Mater. Chem.*, *in press*, (1999).
2. J. Roncali, *Chem. Rev.* 92:711 (1992).
3. A. R. Hillman, D. C. Loveday, M. J. Swann, S. Bruckenstein, and C. P. Wilde, *Analyst* 117:1251 (1992).
4. S. Bruckenstein and A. R. Hillman, *J. Phys. Chem.* 95:10748 (1991).
5. A. R. Hillman, D. C. Loveday, and S. Bruckenstein, *J. Electroanal. Chem.* 300:67 (1991).

CHAPTER 8

GENERAL CONCLUSIONS AND SCOPE FOR FUTURE WORK

8.1 GENERAL CONCLUSIONS

The crystal impedance technique has been used throughout this thesis to determine the viscoelastic properties of thin electroactive polymer films. Raw crystal impedance spectra permit *qualitative* determination of the departure from film rigidity and extent of its viscoelastic contribution. *Quantitative* determination of the viscoelastic contribution is provided via the use of detailed modelling routines. These approximate the electrical response of the TSM resonator using equivalent electrical circuits, such as the Butterworth Van Dyke and transmission line models. Use of the transmission line model warrants the extraction of film physical parameters such as thickness and density, h_f and ρ_f respectively, and shear *storage* and *loss* moduli, G' and G'' respectively.

The focus of this study has been upon the viscoelastic effects of overlaying films, comprising poly(3-hexylthiophene) (PHT), upon the electrical responses of TSM resonators. The novel discovery is reported that *in situ* PHT films exhibit mechanical film resonance effects. Film resonance occurs when the thickness of the film approaches $\frac{1}{4}$ of the acoustic wavelength in that medium. Resonance effects had not previously been reported for liquid contacting media, such as the case of electroactive polymer films exposed to electrolyte solution. The observation of these effects confirms the possibility film resonance must be considered when crystal impedance spectra are analysed. It also confirms that the polymer/ electrolyte interface is sharp enough to allow adequate reflection of the propagating acoustic shear wave for film resonance to occur.

Parametric plots of the extracted electrical parameters R_F and ωL_F , which arise from crystal impedance spectra measured throughout the deposition process, have been compared with those of theoretically derived electrical parameters. These theoretical data were simulated using the assumption that the deposited film is homogeneous and therefore that the shear modulus is constant throughout the film thickness. It was discovered that the parametric curve arising from electrochemically polymerised PHT films could not be overlaid upon theoretically derived curves, which assumed structural homogeneity. This implies that PHT films, electrochemically deposited using the procedures described in this thesis, are inhomogeneous. In general, the films are relatively compact and homogeneous in the early deposition stages and become more diffuse (and therefore less homogeneous) in latter deposition stages. Therefore, the locus of experimental points evolves from one

theoretical curve to another, in this case from that of a more rigid film to that of a less rigid film, with increasing film thickness.

For the first time, the phenomenon of peak splitting has been observed at film resonance. This has led to the development of new theory that explains the effect as a combination of resonator and film motional impedances. The double peak response is only seen when the film impedance bandwidth is comparable to the width of the quartz motional impedance at their point of overlap. Hence, two conductance peaks are most easily observed at higher crystal harmonics when the bandwidth of the resonator and the film are similar.

Film resonance responses, which were recorded at higher crystal harmonic resonant frequencies, indicated that the film thickness at which resonance occurred was not inversely proportional to the harmonic number. This is contrary to theory based predictions, which apply the assumption that the PHT film's shear modulus is frequency independent. The variation between data derived from this model and those measured experimentally suggest that the shear modulus of thin PHT films is frequency *dependent*. This gives new insight into PHT polymer film dynamics. Realisation of this fact prompted more detailed analysis of the frequency dependence of shear modulus.

Data modelling of impedance spectra recorded at higher crystal harmonics was used to more meticulously explore the frequency dependence of the shear moduli of thin PHT films, *in situ*. By examining crystal impedance spectra recorded at higher resonant harmonics, the number of measured parameters is increased more than the number of unknown parameters, since the thickness and density of the film remain constant. This reinforces the validity of the modelling procedure and allows one to determine the extent of the shear modulus frequency dependence. The measured shear modulus of PHT increased with increasing perturbation frequency and varied over an order of magnitude in a frequency range of 10-90 MHz.

The shear moduli of thin PHT films were examined as a function of their oxidation state. It was revealed that oxidation (doping) of PHT causes the film to become considerably softened, which is most likely caused by the ingress of solvent, in this case propylene carbonate. G' and G'' can also show maxima at partial p-doping. Interestingly, even in fixed potential experiments, there is dramatic hysteresis in shear modulus values determined during stepwise doping and undoping. Qualitatively, this can be modelled using a scheme of squares representation in which redox transformations are much faster than the associated solvation changes.

The PHT film was also studied whilst immersed in dichloromethane electrolyte solutions. As opposed to the situation of PHT films immersed in PC, films immersed in DCM are more rigid in their oxidised state than in their reduced state. This has been explained by the fact that oxidised PHT is relatively polar, more easily solvated and therefore plasticised by more polar solvents such as PC rather than non-polar solvents such as DCM. It was discovered that more highly solvated PHT films have much faster electrochemical response times. This is ascribed to the fact that solvated films have a relatively high polymer chain mobility and therefore the diffusion of charge balancing counterions is less hindered.

Overall, it has been shown that electroactive polymer film dynamics, parameterised through shear moduli, can be effectively studied using the crystal impedance technique and associated data modelling procedures. It has been shown how it is possible to manipulate electroactive films shear moduli in a variety of ways, including variation of the perturbation frequency, temperature, applied potential and contacting electrolyte. This will undoubtedly have important implications upon the manufacture of electroactive film based devices since the electrochemical response of polymer films is dependent upon polymer film dynamics.

8.2 FUTURE WORK

The data fitting models used to analyse crystal impedance spectra within this thesis assume that the electroactive film in contact with the TSM resonator is homogeneous. However, it is becoming increasingly obvious that electroactive polymer films, deposited *in situ*, are often not homogenous. Therefore, it is important to develop a model that describes inhomogeneous electroactive polymer films. However, it is likely that the number of unknown parameters in such a model would be quite considerable and therefore the probability of obtaining a unique data fit would be small. A useful exercise would be to generate a library of parametric plots of R_F vs. ωL_F that would enable comparison of different types of film homogeneity (for example a film that becomes progressively viscoelastic as its thickness increases) with data acquired experimentally.

There are two main types of inhomogeneity that occur in electroactive polymer films. The first type is structural inhomogeneity that may arise due to the way the film is deposited or due to the uneven distribution of oxidised/ reduced sites at intermediate redox compositions. The other type is transient inhomogeneity and may arise, for example, when the film is partially oxidised but the oxidation states are *temporarily* non-uniformly distributed throughout the film thickness. This could result from the occurrence of a redox

wave that propagates through the film upon redox switching perhaps due to the hindered diffusion of counterions or solvent. It would be interesting to further explore both of these phenomena using the crystal impedance technique.

The phenomenon of peak splitting provides the impetus for much future investigation. Although a theoretical model has been derived which qualitatively explains the effect in dry films, it has yet to be extended for application to films immersed in solution. This would allow the extraction of qualitative information concerning *in situ* electroactive films from experimental data. Since peak splitting occurs over such a narrow range of film thickness it could be an important feature that would assure a unique fit, especially if a model describing inhomogeneous films were to be employed.

The effect of solvent upon electroactive film shear modulus has been explored in this work. However, interactions between the polymer and solvent can also be manipulated via substitution of polymer side chains. There is much scope for this type of investigation, particularly whilst studying polythiophenes. In this work the presence of the hexyl side chain, on the thiophene chains of PHT, played a crucial role in determining the shear modulus of the polymer. The crystal impedance technique would be ideally suited to exploring the effect upon shear modulus of other side groups.

The effect of regioregularity upon polymer shear modulus is also worthy of exploration. Certain polythiophenes that comprise head-to-head or head-to-tail configurations, for example, are known to be electrochemically and spectroscopically dissimilar. However, at this point the significance of the effect of regioregularity upon polymer dynamics is unknown and bears further investigation.

The crystal impedance technique could also be combined with a technique such as a.c. impedance. This could provide an alternative method for determining physical properties of polymer films, such as the glass transition temperature, which could indirectly be investigated by monitoring the change in the film's electrical conductance as the temperature is varied.